EPFL

Thèse n° 10 343

Silicon Nitride Integrated Nonlinear Photonics

Présentée le 11 septembre 2020

à la Faculté des sciences et techniques de l’ingénieur
Laboratoire de photonique et mesures quantiques (STI/SB)
Programme doctoral en photonique

pour l’obtention du grade de Docteur ès Sciences

par

Junqiu LIU

Acceptée sur proposition du jury

Prof. C. S. Brès, présidente du jury
Prof. T. Kippenberg, directeur de thèse
Prof. K. Vahala, rapporteur
Prof. J. Bowers, rapporteur
Prof. L. Thévenaz, rapporteur

École
polytechnique
fédérale
de Lausanne

2020

I am not what happened to me, I am what I choose to become.
— Carl Gustav Jung

Perspective, Perseverance and Power.
— Chen-Ning Franklin Yang

To my parents . . .

Acknowledgements

Including my master thesis, I have been living in Switzerland and working in EPFL for five years. Five years, which sounds long, but when looking back, is just like the blink of an eye. I joined the group of Prof. Tobias J. Kippenberg on June 2015, since I was awarded a scholarship to conduct my master thesis at EPFL. Before I came to Switzerland, I did not know much about EPFL and had never been to “Suisse Romande” (French-speaking region of Switzerland). I chose Tobias’ group because my background matched, and the group’s academic achievements were certainly outstanding. In addition, at that time, I was eager to make my own publication, and I believed that I could only achieve this goal here. That was the start of everything – I finally got my first *Optics Letters* published right after my master thesis defence. Then I continued as a PhD student in Tobias’ group. Today, when I look back, the decision I made to join Tobias’ group is one of the best decisions in my life.

When I am writing my PhD thesis now, I cannot deny that I am proud of what I have achieved during my PhD thesis – the results are completely beyond what I could imagine when I started. And I have to admit that, a key reason for my successful PhD thesis is that I did it in Tobias’ lab. Therefore, first and foremost, I must express my deepest gratitude to my supervisor Prof. Tobias J. Kippenberg. With and from Tobias, I have acquired knowledge in several research topics and mastered a number of research skills. I am also very lucky to participate in several collaboration projects, from which I expand my knowledge and scope from experts in the same or different research fields. I deeply appreciate that Tobias allows me to organize a small team which undertakes several key functions in our group including fabrication and packaging, and I have obtained experience in team management. Beyond this, his supervision on my research projects and mentoring on my soft skills, combining encouragement and rigour, will be my lifelong treasure. I am proud that I am Tobias’ PhD student, and I hope one day Tobias will be proud that he is my PhD supervisor. Keeping this in mind, I shall never stop to pursue higher levels – the end of my PhD thesis is the start of a new endeavour.

I am deeply indebted to Dr. Rui Ning Wang, Dr. Jijun He and Arslan S. Raja, who are the closest colleagues of mine. Together, we form the “DODOS” squad which handles nearly all the fabrication, sample testing and packaging work. My success is a result of the continuous and significant support from these great scientists. Without them, this PhD thesis would look different.

Thanks to the Si_3N_4 fabrication experts Dr. Michael Zervas, Dr. Martin H. P. Pfeiffer, Clemens Herkommer and Tiago Morais, who have taught and shared with me their knowledge and expertise on Si_3N_4 fabrication. Michael is a learned and experienced experts on nano-fabrication. The discussion and guidance I received from Michael cannot be underestimated, without which I would not be able to develop my own Si_3N_4 process in two years. Martin is probably the group member who I have worked with for the longest period. He developed the first Damascene process and came up with several key techniques which are still being used today. The knowledge he passed to me is beyond only fabrication. Clemens was actually my first fabrication teacher. One of my happiest times in this group is the intensive fabrication training with Clemens on February and March 2017. The first lesson I learned from Clemens, was that one must put *dedication* for the work one is doing – great masterpieces will not make themselves, but will be made by their creators. Tiago is probably the one who passed me the most skills on using the fabrication tools. With Tiago we have fabricated a number of wafers together, and I have accumulated a lot of practical experience under his help. These four teachers made me an expert on Si_3N_4 nano-fabrication.

Thanks to our postdocs Dr. Nils J. Engelsen, Dr. Maxim Karpov, Dr. Johann Riemensberger, Dr. Grigory Lihachev, Dr. Wenle Weng, Dr. Itay Shomroni and Dr. Alexey Tikan. With their rich knowledge developed during their PhD theses, these great scientists carry this group to a higher level. In addition, they are very productive, and their contributions are invaluable to the success of nearly all projects in this group. Special thanks to Nils, who has constantly and patiently helped me to improve my English.

Thanks to our PhD student colleagues in the comb team, Guanhao Huang, Tianyi Liu, Anton Lukashchuk, Miles H. Anderson, Mikhail Churaev and Anat Siddharth. These people are the future of LPQM microcomb research, and I am very sure that all of them will have a great success at the end of their PhD theses. A Chinese idioms says “One remaining humble can acquire knowledge from the younger” – I can tell you it is so true. All these people have taught me and broadened my scope in their fields of expertise.

Thanks to my former colleagues Dr. Erwan Lucas, Dr. Hairun Guo, Bahareh Ghadiani, Dr. Romain Bouchand, Dr. Clément Javerzac-Galy, Dr. Ryan Schilling, Dr. Hendrik Schutz and Dr. Alexey K. Feofanov. These people all have helped me to conquer some outstanding challenges in research, and shared with me their knowledge selfishlessly. Special thanks to Erwan and Hairun. Two of my most important results were achieved with the significant contribution from Erwan, a truly spectacular scientist with full set of experimental skills. I could not appreciate more Erwan’s contribution to my PhD thesis. Hairun is an outstanding scientist rich in the knowledge of nonlinear optics. He also gave me valuable guidance on how to manage my research projects and manuscript writing.

Thanks to our international collaborators: the **Purdue** team with Hao Tian and Prof. Sunil A. Bhave; the **Caltech** team with Dr. Qi-Fan Yang, Boqiang Shen, and Prof. Kerry Vahala; the

UCSB team with Dr. Lin Chang, Chao Xiang, Dr. Paul Morton, and Prof. John Bowers; the **CSEM** team with Dr. Victor Brasch, Dr. Ewelina Obrzud, and Prof. Tobias Herr; the **RQC** team with Dr. Andrey Voloshin, Dr. Nikita Kondratiev, Prof. Michael L. Gorodetsky, and Prof.Igor Bilenko; the **IBM Zurich** team with Simon Hönl, Charles Möhl, and Dr. Paul Seidler; and the **MenloSystems** team with Dr. Rafael Probst, Ignacio Baldoni, and Dr. Ronald Holzwarth. It is a great pleasure to see our Si_3N_4 devices used in these institutes and well recognized by our collaborators. Special thanks to Sunil and Hao, from whom I learned a lot about MEMS technology, integrated modulators and isolators.

Thanks to our EPFL collaborators: the **GFO** group with Dr. Flavien Gyger, Dr. Fan Yang, and Prof. Luc Thévenaz; and the **PHOSL** group with Jianqi Hu, Dr. Edgars Nitiss, and Prof. Camille S. Brès. It is a great pleasure that we could together develop the Si_3N_4 photonics technology rooted in EPFL. Special thanks to Flavien and Fan for teaching me and extending my knowledge of Brillouin nonlinearity of Si_3N_4.

Thanks to our local company collaborators: the **MicroR** team with Dr. John D. Jost and Dr. Nikolay Pavlov; and the **Ligentec** team with Dr. Davide Sacchetto, Gabriel Navickaite and Dr. Michael Geiselmann. Special thanks to John and Nikolay. Picking up extra knowledge of crystals and packaging from them is certainly full of joy.

Thanks to my colleagues Dr. Liu Qiu, Mohammad Bereyhi, Alberto Beccari, Sergey Fedorov, Philippe A. Rölli, Amir Youssefi, Terence Blésin, Dr. Dian Tan, Zelin Tan and others. Thanks to my friend Alain Yuji Takabayashi (EPFL), Dr. Wei Liu (now UCLA), and others. Thanks to my EPFL mentor Dr. Toralf Scharf. It is a great pleasure to know and work with these gentlemen, with whom we support and encourage each other.

Thanks to our funding manager and group secretaries Antonella Ragnelli, Kathleen Vionnet, Helene Laurens and Nicole Bouendin. Special thanks to Antonella and Kathleen, who have done great jobs to make this group function well, and have provided priceless support to everyone of us to enjoy better the Swiss life. I simply could not imagine how our group would look like without them.

Thanks to the CMi team with Dr. Philippe Flückiger, Dr. Cyrille Hibert, Dr. Didier Bouvet, Dr. Zdenek Benes, Joffrey Pernollet, Patrick A. Madliger, Julien Dorsaz, Giovanni Monteduro, Rémy Juttin, Dr. Niccolo Piacentini, Miguel Marmelo, Gatera Kumuntu and others. These great engineers maintain the cleanroom tools and support our research activities in the CMi cleanroom. Like I always say, one can never make a delicacy without the people providing cookers, food and seasoning.

感谢我的父母，感谢你们给我无私的爱与支持，这些都是我努力奋斗的动力。最让我自豪的不仅是我今天取得的成就，而是成为你们的儿子，使你们为我骄傲。感谢我的大姑。我至今记忆犹新，那是我们2013年的对话，大姑说“当别人说你不行的时候，你反

应如此剧烈，说明你内心还不够强大”。这句话当时是一棒子敲醒了我，从此以后，我经常跟自己重复这句话，时刻鞭策自己。

Lausanne, 17 June 2020 Junqiu Liu

Abstract

Recently, microresonator-based dissipative Kerr soliton frequency combs ("soliton microcomb") have emerged as miniaturized optical frequency combs. So far, soliton microcombs have been realized in many CMOS-compatible material platforms including silicon nitride (Si_3N_4) that is widely used in CMOS fabrication of microelectronic circuits. For Si_3N_4 photonic integrated circuits (PIC), the optical losses are critical for building soliton microcomb devices with high power efficiency, low power budgets and compact form factors .

This PhD thesis addresses several key topics in the development of ultralow-loss waveguides and microresonators based on Si_3N_4 PIC, critical to integrated soliton microcomb technology. Through careful design and simulations of Si_3N_4 PIC, systematic development of Si_3N_4 wafer-scale fabrication process, and comprehensive characterization of the final Si_3N_4 devices, a novel Si_3N_4 fabrication technology featuring ultralow loss, engineered dispersion and wafer-level yield has been realized. Currently, integrated Si_3N_4 microresonators of Q factors exceeding 30×10^6 (corresponding to a linear optical loss of 1 dB/m) have been routinely achieved. Meanwhile, thermal characterization using a microresonator modulation response measurement which is self-calibrated via the Kerr nonlinearity reveals that, the intrinsic absorption-limited Q factor exceeds 10^9. Using these Si_3N_4 devices, integrated soliton microcombs with unprecedentedly low power budgets and repetition rates down to 10 GHz have been demonstrated, which allow highly compact soliton microcomb modules via hybrid integration with III-V lasers and new applications such as low-noise microwave synthesis. Furthermore, via monolithic integration with aluminium nitride, on-chip piezoelectric actuation of soliton microcombs with megahertz bandwidth has been realized, which can facilitate the realization of soliton-based massively parallel coherent LiDAR. Further beyond the domain of soliton microcombs, this thesis also contributes to other research topics such as the backward stimulated Brillouin scattering in Si_3N_4 and supercontinuum generation for mid-infrared dual-comb spectroscopy. Transferring this Si_3N_4 photonics technology developed during this PhD thesis to standard commercial foundries, and merging it with silicon photonics using heterogeneous integration technology, could significantly expand the scope of today's integrated photonics and seed new applications.

Keywords: silicon nitride, photonic integrated circuit, frequency comb, nonlinear optics, dissipative Kerr soliton, MEMS, micro-nano-fabrication.

Résumé

Récemment, les peignes de fréquences de type Kerr basés sur des microrésonateurs ("microcomb") ont émergés comme des solutions miniaturisées pour générer des microcombs à large enveloppe de spectre et composantes fréquentielles dans les domaines du gigahertz et terahertz. Jusqu'à présent, les solitons microcombs ont été réalisés dans de nombreux matériaux, y compris le nitrure de silicium (Si_3N_4), matériau couramment utilisé dans la fabrication CMOS de circuits microélectroniques. Dans les circuits photoniques Si_3N_4 intégrés (PIC), la réduction des pertes optiques est critique.

Ce doctorat adresse plusieurs sujets clés dans le développement de guides d'ondes à pertes optiques ultra-basses et des microrésonateurs basés sur les circuits photonics intégrés (PIC) en Si_3N_4, qui sont les éléments clés de la technologie des solitons microcombs intégrés. A travers le design et la simulation consciencieuse de PIC Si_3N_4, le développement systématique du procédé de fabrication à l'échelle du wafer, et la charactérisation étendue des appareils finaux, une nouvelle technologie de fabrication de PIC Si_3N_4 a été réalisée, offrant de basses pertes optiques, à dispersion variable, et avec un rendement maximal à l'échelle du wafer. Actuellement, des facteurs Q excédant 30×10^6 (correspondant à une perte optique linéaire de 1 dB/m) sont couramment atteints. En utilisant cette technologie, des solitons microcombs intégrés avec un budget énergétique sans précédent ont été obtenus, et des espacements fréquentiels de 10 GHz seulement, ce qui permet l'intégration hybride de modules de solitons microcombs compactes avec des lasers III-V, ou de nouvelles applications tels que la synthèse de micro-ondes à bas niveau de bruit. En outre, par intégration monolithique avec le nitrure d'aluminium, l'actuation piézoélectrique on-chip de solitons microcombs a été démontrée, ce qui peut faciliter la réalisation de LiDAR cohérent massivement parallèle basé sur des solitons. Au-delà du domaine des solitons microcombs, cette thèse a aussi contribué à d'autres sujets de recherches, tels que la stimulation inversée de diffusion de Brillouin dans le Si_3N_4 et la génération de super-continuum pour la spectroscopie dans l'infrarouge moyen à peignes binaires. Le transfert des technologies développées durant cette thèse vers des fonderies de semi-conducteurs commerciaux standards, et la fusion avec la photonique sur silicium par intégration hétérogène, pourrait étendre la portée de la photonique intégrée actuelle de manière significative et semer les graines pour de nouvelles applications.

Mots-clés : nitrure de silicium, circuits photoniques intégrés, peignes de fréquences, optique non-linéaire, solitons Kerr dissipatifs, MEMS, micro-nano-fabrication.

List of Publications

(* equal contribution)

1. **J. Liu***, H. Tian*, E. Lucas*, A. S. Raja*, G. Likhachev, R. N. Wang, J. He, T. Liu, M. H, Anderson, W. Weng, S. A. Bhave, and T. J. Kippenberg, "**Monolithic piezoelectric control of soliton microcombs**", *Nature* 583, 385 (2020).

2. W. Weng, A. Kaszubowska-Anandarajah, **J. Liu**, P. M. Anandarajah, and T. J. Kippenberg, "**Frequency division using a soliton-injected semiconductor gain-switched frequency comb**", *Science Advances* in press (2020).

3. J. Hu, J. He, **J. Liu**, A.S. Raja, M. Karpov, A. Lukashchuk, T. J. Kippenberg, and C.-S. Brès, "**Reconfigurable radiofrequency filters using versatile soliton microcombs**", *Nature Communications* in press (2020).

4. H. Guo*, W. Weng*, **J. Liu***, F. Yang, W. Hänsel, C. S. Brès, L. Thévanaz, R. Holzwarth, and T. J. Kippenberg, "**Nanophotonic super continuum based mid-infrared dual-comb spectroscopy**", *Optica* in press (2020).

5. E. Nitiss, B. Zabelich, O. Yakar, **J. Liu**, R. N. Wang, T. J. Kippenberg, and C.-S. Brès, "**Broadband quasi-phase-matching in dispersion-engineered all-optically poled silicon nitride waveguides**", *Photonics Research* 8, 1475 (2020).

6. H. Tian, **J. Liu**, B. Dong, J. C. Skehan, M. Zervas, T. J. Kippenberg, and S. A. Bhave, "**Hybrid Integrated Photonics Using Bulk Acoustic Resonators**", *Nature Communications* 11, 3073 (2020).

7. B. Shen*, L. Chang*, **J. Liu***, H. Wang*, Q.-F. Yang*, C. Xiang, R. N. Wang, J. He, T. Liu, W. Xie, J. Guo, D. Kinghorn, L. Wu, Q.-X. Ji, T. J. Kippenberg, K. Vahala, and J. E. Bowers, "**Integrated turnkey soliton microcombs operated at a CMOS-compatible frequencies**", *Nature* 582, 365 (2020).

8. **J. Liu***, E. Lucas*, J. He*, A. S. Raja*, R. N. Wang, M. Karpov, H. Guo, R. Bouchand, and T. J. Kippenberg, "**Photonic microwave oscillators based on integrated soliton microcomb**", *Nature Photonics* (2020).

9. J. Riemensberger, A. Lukashchuk, M. Karpov, W. Weng, E. Lucas, **J. Liu**, and T. J. Kippenberg, "**Massively parallel coherent laser ranging using soliton microcombs**", *Nature* 581, 164 (2020).
10. A. S. Raja*, **J. Liu***, N. Volet, R. N. Wang, J. He, E. Lucas, R. Bouchand, P. Morton, J. Bowers, and T. J. Kippenberg, "**Packaged photonic chip-based soliton micro comb using an ulralow-noise laser**", *Opt. Express* 28, 2714 (2020).
11. F. Gyger*, **J. Liu***, F. Yang*, J. He, A. S. Raja, R. N. Wang, T. J. Kippenberg, and L. Thevanaz, "**Observation of stimulated Brillouin scattering in silicon nitride integrated waveguides**", *Phys. Rev. Lett.* 124, 013902 (2020).
12. M. Karpov, M. H. Pfeiffer, H. Guo, W. Weng, **J. Liu**, and T. J. Kippenberg, "**Dynamics of soliton crystals in optical microresonators**", *Nature Physics* 15, 1071 (2019).
13. T. Wildi, V. Brasch, **J. Liu**, T. J. Kippenberg, and T. Herr, "**Thermally stable access to microresonator solitons via slow pump modulation**", *Opt. Lett.* 44, 4447 (2019).
14. G. Huang, E. Lucas, **J. Liu**, A. S. Raja, G. Lihachev, M. L. Gorodetsky, N. J. Engelsen, and T. J. Kippenberg, "**Thermal-refractive noise in silicon nitride microresonators**", *Phys. Rev. A: Rapid Communications* 99, 061801 (2019).
15. D. Martyshkin, V. Fedorov, T. Kesterson, S. Vasilyev, H. Guo, **J. Liu**, W. Weng, K. Vodopyanov, T. J. Kippenberg, and S. Mirov, "**Visible-near-middle infrared spanning super continuum generation in a silicon nitride waveguide**", *Opt. Mater. Express* 9, 2553 (2019).
16. A. S. Raja*, A. S. Voloshin*, H. Guo*, S. E. Agafonova*, **J. Liu***, A. S. Gorodnitskiy, M. Karpov, N. G. Pavlov, E. Lucas, R. R. Galieve, A. E. Shitikov, J. D. Jost, M. L. Gorodetsky, and T. J. Kippenberg, "**Electrically pumped photonic integrated soliton micrcomb**", *Nature Communications* 10, 680 (2019).
17. E. Obrzud, M. Rainer, A. Harutyunyan, M. H. Anderson, **J. Liu**, M. Geiselmann, B. Chazelas, S. Kundermann, S. Lecomte, M. Cecconi, A. Ghedina, E. Molinari, F. Pepe, F. Wildi, F. Bouchy, T. J. Kippenberg, and T. Herr, "**A Microphotonic Astrocomb**", *Nature Photonics* 13, 31 (2019).
18. **J. Liu***, A. Raja*, M. Karpov, B. Ghadiani, M. H. P. Pfeiffer, N. J. Engelsen, H. Guo, M. Zervas, and T. J. Kippenberg, "**Ultralow-power photonic chip-based soliton frequency combs**", *Optica* 5, 1347 (2018).
19. M. H. P. Pfeiffer, **J. Liu**, A. Raja, T. Morais, B. Ghadiani, and T. J. Kippenberg, "**Ultra-smooth silicon nitride waveguides based on the Damascene reflow process: fabrication and loss origins**", *Optica* 5, 884 (2018).
20. **J. Liu***, A. Raja*, M. H. P. Pfeiffer, C. Herkommer, H. Guo, M. Zervas, M. Geiselmann, and T. J. Kippenberg, "**Efficient light coupling to integrated photonic devices using 2D inverse tapers**", *Opt. Lett.* 43, 3200 (2018).

21. M. H. P. Pfeiffer, C. Herkommer, **J. Liu**, T. Morais, M. Zervas, M. Geiselman, and T. J. Kippenberg, “**Photonic Damascence process for low-loss, high-confinement silicon nitride waveguides**”, *IEEE J. Sel. Top. Quantum Electron.* 24, 1 (2018).

22. M. Anderson, N. G. Pavlov, J. D. Jost, G. Lihachev, **J. Liu**, T. Morais, M. Zervas, M. L. Gorodetsky, and T. J. Kippenberg, “**Highly efficient coupling of crystalline microresonators to integrated photonic waveguides**”, *Opt. Lett.* 43, 2106 (2018).

23. M. Karpov, M. H. P. Pfeiffer, **J. Liu**, A. Lukashchuk, and T. J. Kippenberg, “**Photonic chip-based soliton frequency combs covering the biological imaging window**”, *Nature Communications* 9, 1146 (2018)

24. H. Guo, E. Lucas, M. H. P. Pfeiffer, M. Karpov, M. Anderson, **J. Liu**, M. Geiselmann, J. D. Jost, and T. J. Kippenberg, “**Inter-mode breather solitons in optical microresonators**”, *Phys. Rev. X.* 7, 041055 (2017).

25. M. H. P. Pfeiffer, C. Herkommer, **J. Liu**, H. Guo, M. Karpov, E. Lucas, M. Zervas, and T. J. Kippenberg, “**Octave-spanning dissipative Kerr soliton frequency combs in Si3N4 microresonators**”, *Optica* 4, 684 (2017).

26. M. H. P. Pfeiffer*, **J. Liu***, M. Geiselmann, and T. J. Kippenberg, “**Coupling ideality of integrated planar high-Q microresonators**”, *Phys. Rev. Applied* 7, 024026 (2017).

27. **J. Liu**, V. Brasch, M. H. P. Pfeiffer, A. Kordts, A. N. Kamel, H. Guo, M. Geiselmann, and T. J. Kippenberg, “**Frequency-comb-assisted broadband precision spectroscopy with cascaded diode lasers**”, *Opt. Lett.* 41, 3134 (2016).

Preprint:

1. **J. Liu**, G. Huang, R. N. Wang, J. He, A. S. Raja, T. Liu, N. J. Engelsen, and T. J. Kippenberg, “**High-yield wafer-scale fabrication of ultralow-loss, dispersion-engineered silicon nitride photonic circuits**”, arXiv: 2005.13949 (2020).

2. M. H. Anderson, G. Lihachev, W. Weng, **J. Liu**, and T. J. Kippenberg, “**Zero-dispersion Kerr solitons in optical microresonators**”, arXiv: 2007.14507 (2020).

3. W. Weng, A. Kaszubowska-Anandarajah, J. He, P. D. Lakshmijayasimha, E. Lucas, **J. Liu**, P. M. Anandarajah, and T. J. Kippenberg, “**Gain-switched semiconductor laser driven soliton microcombs**”, arXiv: 2006.10662 (2020).

4. A. Tikan, J. Riemensberger, K. Komagata, S. Hönl, M. Churaev, C. Skehan, H. Guo, R. N. Wang, **J. Liu**, P. Seidler, and T. J. Kippenberg, “**Emergent Nonlinear Phenomena in a Driven Dissipative Photonic Dimer**”, arXiv: 2005.06470 (2020).

5. J. Feldmann, N. Youngblood, M. Karpov, H. Gehring, X. Li, M. Le Gallo, X. Fu, A. Lukashchuk, A. S. Raja, **J. Liu**, C. D. Wright, A. Sebastian, T. J. Kippenberg, W. H. P. Pernice, and H. Bhaskaran, "**Parallel convolution processing using an integrated photonic tensor core**", arXiv: 2002.00281 (2020).

6. A. S. Voloshin*, **J. Liu***, N. M. Kondratiev*, G. V. Likhachev, T. J. Kippenberg, and I. A. Bilenko, "**Dynamics of laser self-injection locked solitonmicrocombs in integrated microresonators**", arXiv:1912.11303 (2019).

7. M. H. Anderson, R. Bouchand, **J. Liu**, W. Weng, E. Obrzud, T. Herr, and T. J. Kippenberg, "**Photonic chip-based resonant supercontinuum**", arXiv: 1909.00022 (2019).

8. P. J. Marchand, J. C. Skehan, J. Riemensberger, J.-J. Ho, M. H. Pfeiffer, **J. Liu**, C. Hauger, T. Lasser, and T. J. Kippenberg, "**Soliton microcomb based spectral domain optical coherence tomography**", arXiv: 1902.06985 (2019)

List of Presentations

1. “Ultralow-Loss Silicon Nitride Photonics”, ACP/IPOC 2020, China (2020).
2. “Monolithic piezoelectric control of soliton microcombs”, IFCS-ISAF, US (2020).
3. “Monolithic piezoelectric control of soliton microcombs”, IEEE RAPID, US (2020).
4. “Monolithic piezoelectric control of soliton microcombs”, ECIO, France (2020).
5. “**(Invited)** Monolithic piezoelectric control of integrated soliton microcombs”, CLEO US (2020).
6. “**(Tutorial)** Introduction to FDTD”, workshop “Computational methods for nonlinear photonics” within the Marie-Curie ITN MICROCOMB, Switzerland (2020).
7. “Heterogeneously integrated silicon-Si_3N_4 frequency combs for data-centre interconnect”, EPFL-IMEC Edge Artificial Intelligence Workshop, Switzerland (2020).
8. “**(Invited)** Microresonator frequency comb”, Annual Meeting of Chinese Association of Science & Technology in Switzerland (2019).
9. “Photonic integrated microwave oscillators based on silicon nitride soliton microcomb”, CLEO US (2019).
10. “Electrically Driven Ultra-compact Photonic Integrated Soliton Microcomb”, CLEO US (2019).
11. “Integrated Si_3N_4 Soliton Microcomb Driven by a Compact Ultra-low-noise Laser”, CLEO US (2019).
12. “**(The Best Student Paper)** Photonic integrated microwave oscillators based on silicon nitride soliton microcomb”, ECIO, Belgium (2019).
13. “Photonic integrated microwave oscillators based on silicon nitride soliton microcomb”, IFCS-EFTF, US (2019).
14. “**(Invited)** Ultralow-power photonic chip-based soliton frequency combs”, Keio Symposium on Microresonator Frequency Comb, Japan (2018).

15. “Ultralow-power photonic chip-based soliton frequency combs”, ECOC, Italy (2018).
16. “Ultralow-power photonic chip-based soliton frequency combs”, OMN 2018, Switzerland (2018).
17. “Ultralow-power photonic chip-based soliton frequency combs”, Advanced Photonics Congress, Switzerland (2018).
18. “Double-inverse tapers for efficient light coupling with arbitrary polarization”, CLEO US (2018).
19. “Photonic Damascene process with reflow step for ultra-smooth Si_3N_4 waveguide”, CLEO US (2018).
20. “**(Tutorial)** Study of Optical Mode Coupling in Nanophotonic Devices Using FDTD Methods”, workshop within the Marie-Curie ITN OMT, Switzerland (2017).
21. “Dispersion characterization of microresonators for broadband Kerr frequency comb generation”, CLEO US (2017).

List of Symbols and Abbreviations

ARDE: aspect ratio dependent etching
APCVD: atmospheric-pressure chemical vapour deposition
AOM: acousto-optic modulator
AWG: arbitrary waveform generator
BPSG: borophosphosilicate glass
BHF: buffer hydrofluoric acid
CMP: chemical mechanical planarization
CME: coupled-mode equation
CD: critical dimension
DKS: dissipative Kerr soliton
DUV: deep ultraviolet
DRO: dielectric resonator oscillator
EBL: electron-beam lithography
EBR: edge bead removal
EPD: end point detection
ECDL: external cavity diode laser
ESA: electrical spectrum analyzer
EOM: electro-optic modulator
ER: etch rate
FSR: free spectral range
FMW: four-wave mixing
FDTD: finite-difference time-domain
FWHM: full-width-at-half-maximum
FMCW: frequency-modulated continuous-wave
GVD: group-velocity dispersion
HDPCVD: high-density-plasma chemical vapour deposition
HTO: high temperature oxide
HWAR: height-to-width aspect ratio
HBAR: high-overtone bulk acoustic wave resonances
HVA: high-voltage amplifier
LLE: Lugiato-Lefever Equation

LER: line edge roughness
LPCVD: low-pressure chemical vapour deposition
LTO: low temperature oxide
NLSE: nonlinear Schrödinger equation
OSA: optical spectrum analyzer
OEO: optoelectronic oscillators
PIC: photonic integrated circuit
PECVD: plasma-enhanced chemical vapour deposition
PVD: physical vapour deposition
PML: perfectly matched layer
PC: polarization controller
PNA: phase noise analyzer
PID: proportional-integral-derivative
PDF: Pound-Drever-Hall
PSD: power spectrum density
RF: radio-frequency
RIE: reactive ion etcher
RBW: resolution bandwidth
RIN: relative intensity noise
SPM: self-phase modulation
SEM: scanning electron micrography
SNR: signal-to-noise ratio
SSB: single-sideband
SBS: stimulated Brillouin scattering
SRS: stimulated Raman scattering
TE: transverse electric
TM: transverse magnetic
TEM: transmission electron micrography
TRN: thermo-refractive noise
VNA: vector network analyser
VCO: voltage-controlled oscillator
WGM: whispering gallery mode
WDM: wavelength-division multiplexer
XPM: cross-phase modulation

Contents

Acknowledgements iii

Abstract (English/Français/Deutsch) vii

List of Publications xi

List of Presentations xv

1 Introduction 1

1.1 Optical frequency comb 1

1.2 Application of Frequency Combs 4

1.3 Miniaturized frequency combs using optical microresonators 9

1.4 Dissipative Kerr solitons 12

1.4.1 Soliton tuning methods 17

1.4.2 Theoretical model 20

1.5 Integrated materials platforms for microcombs 23

1.5.1 Dispersion engineering 26

1.6 Application of soliton microcombs 31

2 Fabrication of Ultralow-Loss Si_3N_4 Integrated Waveguides 39

2.1 Silicon nitride photonic integrated circuits 42

2.1.1 Refractive index of Si_3N_4 45

2.2 Fabrication process overview 48

2.2.1 Fabrication challenges 49

2.2.2 The subtractive process 51

2.2.3 The photonic Damascene process 52

2.3 Deep-UV stepper lithography 54

2.3.1 Reticle 56

2.3.2 BARC and photoresist coating 59

2.3.3 Exposure 60

2.4 Dry etching 62

2.5 Preform reflow 65

2.6 Chemical vapour deposition 67

2.6.1 LPCVD Si_3N_4 film stress and crack prevention 71

2.7 Planarization . . . 75
2.7.1 Etchback . . . 76
2.7.2 Chemical-mechanical polishing . . . 77
2.7.3 CMP dishing effect . . . 79
2.8 Thermal annealing and SiO_2 cladding deposition . . . 80
2.9 Heaters module . . . 82
2.10 Chip release . . . 85
2.10.1 Photolithography . . . 85
2.10.2 Photoresist . . . 88
2.10.3 Deep RIE . . . 90
2.10.4 Grinding . . . 91

3 Design and simulation of Integrated Photonic Circuits 93
3.1 Photonic circuit design using Python's Gdspy package . . . 93
3.2 Finite-difference time-domain method . . . 96
3.3 Inverse taper coupler: simulations . . . 99
3.3.1 FDTD model to simulate inverse taper coupling . . . 104
3.4 Inverse taper coupler: experiments . . . 106
3.4.1 Standard inverse tapers . . . 107
3.4.2 Double inverse tapers . . . 109
3.5 Bus-waveguide-to-microresonator coupling . . . 113
3.5.1 Input-output formalism and coupling ideality . . . 114
3.5.2 Analytical description of a multi-mode coupling section . . . 119
3.5.3 Experimental study of coupling ideality . . . 122
3.5.4 Simulations of coupling ideality . . . 125

4 Chip Characterization and Waveguide Loss Analysis 131
4.1 Characterization of microresonator dispersion and Q . . . 131
4.1.1 Dispersion Characterization with One Diode Laser . . . 131
4.1.2 Dispersion Characterization with Cascaded Diode Lasers . . . 135
4.1.3 Molecular Spectroscopy . . . 137
4.1.4 Dispersion Characterization . . . 138
4.2 Statistical analysis of microresonator Q factors . . . 143
4.2.1 Ringdown measurement . . . 145
4.2.2 Wafer-scale distribution of Q . . . 146
4.2.3 Reflow's impact . . . 148
4.3 Probing the ultimate microresonator Q limited by absorption loss . . . 148
4.4 Metre-long spiral waveguides . . . 154

5 Soliton Generation with Ultralow Power Threshold 155
5.1 Ultralow-power single soliton . . . 155
5.1.1 Solitons of repetition rates below 100 GHz . . . 156
5.1.2 99 GHz soliton generation without EDFA . . . 159

5.1.3 Sub-milliwatt-power soliton generation 162
5.1.4 40 GHz soliton generation without EDFA 164
5.2 Soliton formation via laser self-injection locking 166
5.2.1 Schematic with a laser diode 166

6 Generation and Application of Microwave-Repetition-Rate Solitons 171
6.1 Principle and sample description 173
6.2 K- and X-band soliton generation 175
6.3 Phase noise characterization 177
6.4 Soliton injection-locking 184
6.5 Comparison of microwave oscillators 185
6.6 Fully packaged device: DARPA DODOS deliverable 187

7 Monolithic Piezoelectric Control of Soliton Microcombs 189
7.1 Integrated Aluminium Nitride Actuators on Silicon Nitride Circuits 191
7.1.1 Stress-optic tuning 192
7.1.2 High-overtone bulk acoustic wave resonances 194
7.2 Monolithic piezoelectric control of soliton microcombs 197
7.2.1 Voltage-controlled soliton microcombs 197
7.2.2 Fast soliton actuation and locking 199
7.2.3 Soliton-based parallel LiDAR engine 204

8 Conclusion and Outlook 209
8.1 Novel Si_3N_4 and SiO_2 CVD processes using silicon tetrachloride 209
8.2 Ultra-pure SiO_2 deposition via flame hydrolysis 212
8.3 Beyond lithography limit – patterning nano structures with photolithography . 214

Bibliography 249

Curriculum Vitae 251

1 Introduction

This thesis starts with an introduction to optical frequency combs. First, the principle of optical frequency combs will be illustrated. Conventionally, optical frequency combs are generated with mode-locked lasers. Demonstrated at the beginning of the 21st century, several milestone applications of mode-locked-laser-based optical frequency combs will be briefly reviewed. Shortly after John L. Hall and Theodor W. Hänsch won one half of the Nobel Prize in Physics for their fundamental contributions to optical frequency combs and spectroscopic applications, it was discovered in 2007 that frequency combs can also be generated in optical microresonators driven by continuous-wave (CW) lasers via Kerr nonlinear parametric processes. This type of frequency combs is commonly referred as "**microresonator-based Kerr frequency combs**" or "**microcombs**". The generation scheme of microcombs will be explained, followed by a review of several key works on theoretical description and experimental characterization of the comb formation dynamics in nonlinear microresonators. An overview of the materials platforms and demonstrated system-level applications using microcombs will be provided at the end of this chapter.

1.1 Optical frequency comb

Optical frequency combs [1, 2, 3] have revolutionized timekeeping and metrology over the past decades, and have found a wide variety of applications [4, 5]. In 2005, one half of the Nobel Prize in Physics was awarded to John L. Hall and Theodor W. Hänsch, "*for their contributions to the development of laser-based precision spectroscopy, including the optical frequency comb technique*" [6, 7]. An optical frequency comb is an ultrashort pulse laser source emitting an optical pulse stream with a constant repetition rate f_{rep}. Figure 1.1 illustrates the representation of a frequency comb in the frequency and time domain. In the frequency domain, the optical spectrum of an optical pulse stream has many Fourier frequency components that are equally spaced by f_{rep}. Each line can be considered as a CW laser. Therefore, an optical frequency comb can be viewed as a group of CW lasers whose frequencies are equally spaced

to each other. The optical frequency of the N-th frequency component can be express as

$$f_N = N \times f_{\text{rep}} + f_{\text{ceo}} \tag{1.1}$$

where f_{rep} is the "**repetition rate**" describing the mode spacing ($1/f_{\text{rep}}$ being the pulse interval time), and $0 \le f_{\text{ceo}} < f_{\text{rep}}$ is called the "**carrier-envelope offset frequency**" describing the frequency offset from the zero. The integer number N is typically around 10^4–10^6 depending on the ration of f_N/f_{rep}, thus it bridges an RF or a microwave frequency (100 MHz – 10 GHz) to an optical frequency (100 THz – 1 PHz). Equation 1.1 is important since with N being a large value, it allows frequency conversion from the microwave domain to the optical domain ("**optical frequency synthesis**" [8]), or vice versa ("**optical frequency division**" [9]). In addition to the fact that all the frequency components are harmonically equidistant, the forming of ultrashort optical pulses requires that all these components are phase coherent and share a common phase evolution.

To fully characterize a frequency comb, two parameters in Eq. 1.1 need to be measured, i.e.

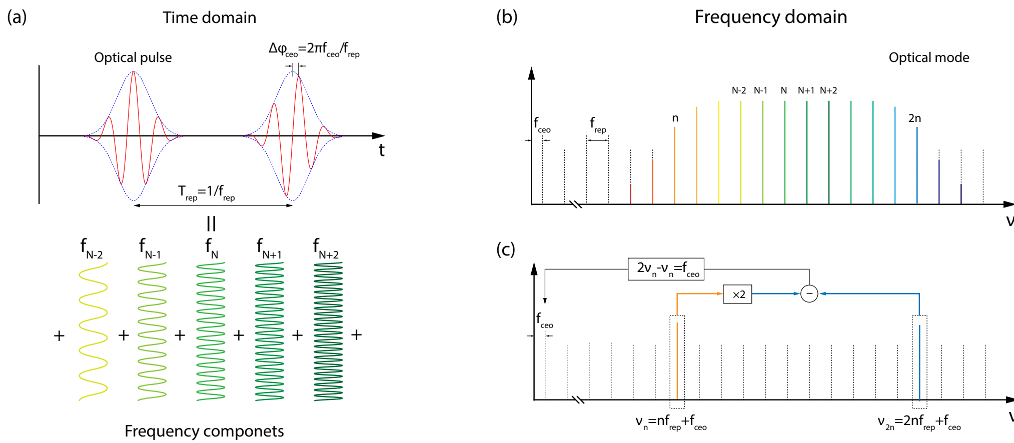

Figure 1.1 – Optical spectrum of an optical frequency comb and the self-referencing scheme to fully stabilize the frequency comb. (a) Representation of a frequency comb in the time domain. (b) Representation of a frequency comb in the frequency domain. In the frequency domain, the frequency comb consists of many frequency lines equidistantly spaced by f_{r}. Each frequency line manifests itself as a c.w. laser. All the c.w. lasers add up to an ultrashort pulse stream, with the pulse repetition rate precisely equal to the line spacing f_{r} in the frequency domain. In addition to f_{r}, the entire comb spectrum has an offset frequency f_0. This offset frequency describes the time evolution of the pulse's carrier-envelope phase. (c) Detection scheme of f_0 using self-referencing. The repetition rate f_{r} is directly measurable by photodetection of the pulse repetition rate using a fast photodiode and analyzing the output microwave spectrum. The detection of f_0 requires the implementation of self-referencing. Upon frequency doubling a frequency line (frequency is $\nu_{\text{N}} = N f_{\text{rep}} + f_0$) to $2\nu_{\text{N}} = 2N f_{\text{rep}} + 2f_0$ and comparing the doubled frequency to the line of frequency $\nu_{2\text{N}} = 2N f_{\text{rep}} + f_0$, the beat signal detected by the photodetector outputs a microwave signal whose carrier frequency is f_0.

f_{rep} and f_{ceo}. To measure f_{rep}, the simplest method is to perform a heterodyne measurement by launching the optical pulse stream to a fast photodetector. The output voltage signal from the photodetector presents an amplitude modulation at a frequency corresponding to the optical frequency beatnote, which is f_{rep} – the frequency difference between two adjacent Fourier frequency components. However, measuring f_{ceo} is challenging. The origin of f_{ceo} comes from the fact that the optical pulse has a group velocity different from the phase velocity within a laser cavity [10]. Therefore, revealed in the time domain, there is a pulse-to-pulse phase slippage between the carrier phase and the pulse envelope [11]. The f_{ceo} is defined as the time derivative of the carrier-envelope phase ϕ_{ceo}, as

$$f_{\text{ceo}} = \frac{1}{2\pi}\frac{d\phi_{\text{ceo}}}{dt} \tag{1.2}$$

There have been multiple techniques proposed and implemented to measure f_{ceo} [10]. Nowadays, the most widely used technique is based on f–$2f$ self-referencing [12, 13]. Figure 1.1(c) shows the principle of f–$2f$ **self-referencing** that requires the frequency comb to have an optical bandwidth exceeding one octave. Octave-spanning bandwidth can be directly achieved using Ti:sapphire lasers [14, 15], but requires external spectrum broadening via supercontinuum generation [16] for other types of lasers (e.g. Er-doped fibre lasers). One comb line (N-th) at the lower frequency side (longer wavelength) is frequency-doubled via a second harmonic generation (SHG). This SHG process multiplies the initial frequency ($\nu_{\text{N}} = N f_{\text{rep}} + f_{\text{ceo}}$) to its double ($2\nu_{\text{N}} = 2N f_{\text{rep}} + 2 f_{\text{ceo}}$). The doubled frequency $2\nu_{\text{N}}$ is then compared to the $2N$-th comb line at the higher frequency side whose frequency is $\nu_{2\text{N}} = 2N f_{\text{rep}} + f_{\text{ceo}}$. By combining these two frequencies and measuring the optical beat signal between these two frequencies using a fast photodetector, the output frequency of the microwave carrier from the photodetector represents the value of f_{ceo}. Therefore, by locking the f_{rep} and f_{ceo} to microwave standards, the entire frequency comb is fully stabilized, and the precise frequency of each comb line can be ambiguously calculated using the known microwave frequency values of f_{rep} and f_{ceo}.

To fully stabilize the frequency comb, i.e. the two key comb parameters f_{rep} and f_{ceo}, typically two actuators within the laser cavity are needed, which allow to control of f_{rep} and f_{ceo}. The standard way is to use piezo-mounted cavity mirror to actuate f_{rep} (i.e. changing the physical length of the laser cavity), and intracavity power modulation to actuate f_{ceo} (i.e. via nonlinear light-matter interaction) [11]. Ideally, the control of one parameter should be independent to the control of the other, i.e. the actuation on f_{rep} is orthogonal to the actuation on f_{ceo}. However this is usually not the case.

When using a fully stabilized frequency comb to measure an optical frequency f_{opt}, the common strategy is to beat this optical frequency with a fully-referenced frequency comb, and measure the beatnote frequency Δf_{beat}. The optical frequency can thus be calculated as

$$f_{\text{opt}} = N \times f_{\text{rep}} + f_{\text{ceo}} + \Delta f_{\text{beat}} \tag{1.3}$$

Since the frequency comb is fully stabilized (i.e. f_{rep} and f_{ceo} are known), the only unknown

parameter here to determine f_{opt} is N. The value of N can be predetermined by directly measuring f_{opt} using a wavelength metre. For example, typically the frequency comb has a $f_{rep} > 200$ MHz, and a good wavelength metre can offer resolution better than 100 MHz (below $f_{rep}/2$). Therefore, the value of N is estimated as the integer part of f_{opt}/f_{rep}. With the knowledge of f_{rep}, f_{ceo}, N and the measured Δf_{beat}, the optical frequency f_{opt} can be ambiguously determined [17].

Originally, frequency combs are built on mode-locked lasers. Yet, not all mode-locked lasers are qualified as frequency combs. Specifically, only the mode-locked lasers fully stabilized can be called as frequency combs. As shown in Eq. 1.1, the full stabilization of a mode-locked laser requires the measurement and control of two comb parameters f_{rep} and f_{ceo}. This is the reason why, despite that the first mode-locked laser was demonstrated back to 1960's [18], the use of "frequency comb" only appears after more than 40 years. Since 2000, frequency comb technology has been rapidly developed and leads to a vast of applications [11], such as optical clocks, spectroscopy, exoplanet searches, low-noise microwave synthesis, and distance measurements. Some representative applications will be illustrated with more details later.

So far, frequency combs have been demonstrated using various kinds of mode-locked lasers which output an average pulse power more than 100 mW, even up to a Watt. These mode-locked lasers can be solid-state lasers (e.g. Ti:sapphire [13], the first studied laser for frequency combs), fibre lasers (e.g. Er- or Yi-doped [19, 20], these are currently the most widely employed lasers for frequency combs), quantum cascade lasers (key for mid-infrared gas sensing and spectroscopy [21]), and others. The center wavelengths of the generated frequency combs range from ultraviolet (via high-harmonic generation of the pump [22], key for ultrafast physics), visible (around 800 nm, key for atomic clocks), near-infrared (around 1.0 μm and 1.55 μm, key for microwave synthesis and metrology), to mid-infrared (above 2 μm, key for spectroscopy). The typical repetition rates vary from slightly below 100 MHz, to more than 10 GHz. Smaller comb repetition rates (few hundreds of megahertz or even below 100 MHz) are intrinsically beneficial for spectroscopy in order to resolve fine structures of atomic or molecular transitions. Larger repetition rates (above 1 GHz to tens of gigahertz) are key for microwave synthesis and astrophysical spectrometer calibration. Intuitively, it is believed that higher repetition rates indicate fewer lines to cover an octave bandwidth, or higher average power per comb line with a constant pulse power. However, the pulse energy is inversely proportional to the repetition rate, thus nonlinear spectral broadening to achieve an octave bandwidth is less efficient for higher repetition rate in the gigahertz domain.

1.2 Application of Frequency Combs

Optical clocks [23, 24, 25]: Time has always had a special position in physics because of its fundamental role in specifying the regularities of nature. It has an extraordinary precision with which it can be measured [25] so far. Atoms and ions are ideal to build clock references. The electromagnetic field bonding the electrons and the atomic nucleus forces the electrons

to circulate around the static nucleus, and is orders of magnitude larger than the possible environmental perturbation. Therefore, atomic transitions between different stable states in isolated systems are sufficiently stable to be a clock reference. In fact, the "second", the unit of time, has been defined since 1967 as the duration that a Cs atom oscillates 9,192,631,770 times between its two hyperfine ground states. Using an inherent atomic transition to define time enables the accuracy of event counting as well as the long-term stability of the clock. Today, the Cs atomic transition in the microwave domain serves as the most accurate time standard with a fractional frequency uncertainty at the level of 10^{-15}. It is expected that the fractional frequency uncertainty and instability can be significantly lower when using atomic transition at optical frequency (e.g. a ground state to an excited state). Though direct counting optical cycles in the optical frequency (~500 THz) is impossible, this can be realized by using an optical frequency comb which divides the optical frequency into countable microwave frequencies. Thus here the frequency comb serves as an optical-to-microwave link.

In the work reported by S. A. Diddams *et al.* [23], an optical clock has been demonstrated using a $^{199}Hg^{+}$ cold ion, a stable CW laser locked to the $^{199}Hg^{+}$ atomic transition, and a self-referenced Ti:sapphire frequency comb. The CW laser of 563 nm wavelength was locked to a narrow (2 Hz linewidth), two-photon, electric-quadrupole transition at 283 nm ($f_{\mathrm{opt}} = 1.064$ PHz) of a laser-cooled and trapped $^{199}Hg^{+}$ ion. This stabilized CW laser served as the reference optical-frequency oscillator and had a short-term (1 to 10 s) fractional frequency instability below 5×10^{-16}. Meanwhile, the Ti:sapphire frequency comb of $f_{\mathrm{rep}} \sim 1$ GHz repetition rate was self-referenced. Both the f_{rep} and f_{ceo} were detected, and f_{ceo} was locked to f_{rep} via a phase-lock loop such that $f_{\mathrm{ceo}} = \beta f_{\mathrm{rep}}$ ($\beta < 1$). The m-th comb line close to the reference CW optical frequency was locked to this CW oscillator, and their beat frequency f_b was detected and locked to f_{rep} via another phase-lock loop such that $f_b = \alpha f_{\mathrm{rep}}$ ($\alpha < 1$). The photodetected comb repetition rate can thus be calculated as $f_{\mathrm{rep}} = f_{\mathrm{opt}}/(m \pm \alpha \pm \beta)$. Therefore, the comb repetition rate f_{rep} was ambiguously referenced to the optical transition of the $^{199}Hg^{+}$ ion at 283 nm, such that this optical frequency was coherently divided down to the 1 GHz microwave frequency as the electronic output from the photodetector. The microwave frequency thus inherits the fractional frequency uncertainty from the optical oscillator, which was measured as 7×10^{-15} in 1 second of averaging, about an order of magnitude better than the value reported in the Cs microwave standard.

Later, in the work reported by T. Rosenband *et al.* [25], two optical clocks based on $^{199}Hg^{+}$ and $^{27}Al^{+}$ respectively were compared and their relative frequency ratio was measured. Two sub-hertz-linewidth lasers were stabilized respectively to the trapped $^{199}Hg^{+}$ and $^{27}Al^{+}$ ions via their four-order harmonics. The respective systematic fractional frequency uncertainty was 1.9×10^{-17} for the $^{199}Hg^{+}$ clock, and 2.3×10^{-17} for the $^{27}Al^{+}$ clock, after great effort spent on reducing the atomic transition frequency uncertainty induced by micromotion and secular motion of the trapped ions in Paul trap (time dilation), Doppler effect, and quadratic Zeeman effect etc. The two clock laser frequencies were then compared to a common, octave-spanning, self-referenced Ti:Sapphire femtosecond comb. The comparison was implemented by phase-locking the comb to one clock laser, and measuring the heterodyne beatnote signal of the other

clock laser with the nearest comb tooth. The frequency ratio of the two optical clocks was measured as ν_{Al}/ν_{Hg} = 1.052871833148990438(55), corresponds to a fractional uncertainty of 5.2×10^{-17}.

In parallel, in the work reported by A. D. Ludlow *et al.* [24], a Sr lattice clock at JILA was remotely compared to a Ca optical clock at NIST Boulder lab via a 4-km phase-noise-cancelled optical fibre link. A self-referenced, octave-spanning optical frequency comb at JILA was phase-locked to the Sr lattice clock laser operating at 698 nm. A CW Nd:YAG laser at 1064 nm was phase-locked to the same frequency comb, transferred to NIST, and frequency-counted against another self-referenced, octave-spanning frequency comb at NIST which was phase-stabilized to the Ca optical clock operating at 657 nm. The Sr lattice clock, built on neutral atoms instead of a single trapped ion, presented a systematic fractional frequency uncertainty evaluation of 1×10^{-16}, surpassing the best evaluations of Cs fountain primary standards

To evaluate the possible limit of fractional frequency uncertainty of optical clock standards, the comparison of two optical frequency combs and measurement of their mutual errors or systematic offsets in the optical frequency combs allow to calculate of the technical limitation for the clock frequency stability. In the work reported by L.-S. Ma *et al.* [26], a rigorous comparison of four frequency comb synthesizers was performed in order to reveal and evaluate the potential limitations of frequency instability in femtosecond mode-locked-laser-based frequency comb synthesizers. The authors demonstrated that optical frequency synthesizers based on femtosecond mode-locked laser combs can operate with a fractional frequency uncertainty of 10^{-19}, which essentially have no fundamental limitations imposed by physics. The key technical limitations identified in their work were the noises induced by the thermal and mechanical fluctuations of their experimental setups, and total integration time.

Low-noise microwave synthesis [9, 27]: Frequency combs can serve as frequency down-converters of an optical frequency to a microwave frequency. This "frequency division" technique using optical frequency combs is the basis for photonic generation of low-noise microwave signals. In this case, a self-reference frequency comb with its carrier-envelope frequency f_{ceo} detected and locked to a microwave reference. Meanwhile, one comb line f_n is phase-locked to an optical frequency reference, which is a c.w. laser frequency-stabilized to an ultra-stable, high-finesse optical cavity [28]. Note that this scheme is similar to the previously described optical clocks where a c.w. laser is phase-locked to an atomic optical transition. Via locking f_{ceo} and f_n, the comb repetition rate can thus be derived as $f_{\text{rep}} = (f_n - f_{\text{ceo}})/n$. The optical reference c.w. laser can achieve a fractional frequency instability at the order of 10^{-16} for averaging times of 1–10 s. As the microwave signal is derived from the division of the optical frequency, this level of fractional frequency instability is preserved. Thus the absolute phase fluctuation is reduced by a scaling factor determined by the optical and microwave frequency (e.g. the division factor n = 500 THz / 10 GHz = 5×10^4). The phase-noise power spectral density (PSD) is intrinsically reduced by n^2. Photodetection of the comb repetition rate generates microwave carriers whose frequencies are the comb repetition rate and its harmonics. Using this method, in the work reported by T. M. Fortier *et al.* [9], a 10 GHz

microwave signal with fractional frequency instability below 8×10^{-16} at 1 s was demonstrated. A self-referenced Ti:sapphire femtosecond laser with 1 GHz repetition rate was used, and the 10 GHz microwave is the 10-th harmonic of the photodetected 1 GHz microwave carrier. Since the expected phase noise level is comparable or even lower than the best microwave oscillators operated at cryogenic temperatures, they built two independent systems, mixed the 10 GHz microwave carriers from each system, and characterized the phase noise of the mixer output.

Recently, in the work reported by X. Xie *et al.* [27], a microwave signal with improved stability was demonstrated via high-fidelity transfer of the frequency stability and the use of cutting-edge photodetection techniques. An ultrastable c.w. laser at 1542 nm was used to stabilize a self-referenced fibre-based frequency comb. A specially designed high-linearity photodiode with flicker phase noise below $-140 f^{-1}$ dBc / Hz (with f being the Fourier offset frequency) was used to detect the pulse repetition rate and to generate the microwave carrier. To increase the signal-to-noise ratio, four fibre-based optical-pulse repetition-rate multipliers were used to redistribute the photocurrent to the harmonic of interest at 12 GHz carrier frequency (comb repetition rate was 250 MHz), and to output a microwave power above 2.5 mW for a d.c. photocurrent of 8 mA. The generated microwave signal featured a fractional frequency uncertainty below 6.5×10^{-16} at 1 s and a timing noise floor below 41 zs $\text{Hz}^{-1/2}$ (phase noise below -173 dBc / Hz for a 12 GHz carrier), the purest microwave signal reported up to date.

Frequency comb spectroscopy [29, 30, 31]: The frequency comb can be used as a broadband light source to directly probe or interrogate a sample exhibiting photon absorption. The photon absorption or nonlinear response of the sample under investigation, due to rotational or rovibrational transitions in atoms and molecules, can be directly characterized with a frequency comb spectrometer. Nowadays, frequency comb spectrometers cover operation spectral range from near-infrared to mid-infrared, using mode-locked lasers or quantum cascade lasers [32] depending on the wavelength. Extending the spectrum down to ultraviolet is currently ongoing, which is realized on nonlinear spectral broadening based on supercontinuum generation or high harmonic generation [22] seeded at near-infrared wavelength. To implement frequency comb spectroscopy, the linear spectroscopy is performed with a single comb line resonant with a transition and all the other lines detuned from resonances. However this scheme suffers from several effects limiting the spectrometer resolution, e.g. the Doppler effect. The Doppler effect can be removed by using the two-photon excitation spectroscopy, which has better spectral resolution and higher spectra efficiency as many pairs of comb lines of the same sum frequency all contribute to the excitation.

Dual-comb spectroscopy [33, 34]: Dual-comb spectroscopy utilizes a pair of frequency combs, and enables mapping of the optical spectra to the radio-frequency domain. This approach enables fast detection, scanning without moving parts, and high spectral resolution. It has today seen significant advances [35], and has also been successfully applied to an increasing portion of the mid-infrared spectroscopy. For a dual-comb spectrometer, the mutual coherence between the two frequency combs critically determines the resolution. Key techniques to

improve the coherence include sophisticated servo controls, detection and active correction of the relative timing or phase fluctuations, or generating two combs in the same laser cavity such that the two combs experience the same system drift.

1.3 Miniaturized frequency combs using optical microresonators

In addition to mode-locked lasers, in the last decade optical frequency comb generation in Kerr nonlinear microresonators driven by c.w. lasers [36, 37] has emerged as a promising approach to access comb repetition rates exceeding 10 GHz. As mentioned, currently achieving higher than 10 GHz repetition rate with bulk lasers is only possible in Ti:sapphire lasers [38], in which a small laser cavity is built and employed. Alternatively, semiconductor mode-locked lasers can have repetition rates from 10 GHz to 100 GHz. The microresonator-based optical frequency comb, where a low-loss, nonlinear, whispering-gallery-mode microresonator [39, 40] is used, is intrinsically beneficial to access the comb repetition rates in the gigahertz to the terahertz domain that are the key frequency ranges for microwave synthesis. This type of frequency comb is nowadays widely referred as "**microcomb**".

The generation scheme of frequency combs in optical microresonators is entirely different from the scheme using mode-locked lasers that rely on the intracavity saturation absorber offering Kerr-lens mode-locking. In an optical microresonator, it is the Kerr nonlinearity that triggers the parametric oscillation for frequency sideband generation [41] from a single-frequency c.w. pump laser. The whispering-gallery-mode (WGM) microresonator confines the light by total internal reflection (TIF) at the interface, thus allows intracavity power build-up. The power enhancement factor, described by the quality factor Q or finesse $\mathscr{F}$, depends on the optical loss of the microresonator, i.e. linewidth κ of the optical resonance. With the resonance frequency ω and free spectral range (FSR, $D_1/2\pi$) of the microresonator, the quality factor is defined as $Q = \omega/\kappa$, and the finesse is defined as $\mathscr{F} = D_1/\kappa$. An intracavity power enhancement factor exceeding 10^5 can be achieved in ultrahigh-Q microresonators ($Q > 10^8$) made of materials exhibiting Kerr nonlinearity, triggering nonlinear parametric process in the microresonator with only sub-milliwatt power coupled from the feed bus waveguide. Figure 1.2(a) illustrate the frequency conversion process induced by the Kerr nonlinearity. When the pump laser's frequency is tuned into a resonance of frequency ν_p, the pump light is coupled into the microresonator. Initially, the degenerate four-wave mixing (FWM) process annihilates two photons at the pump mode and creates a new pair of photons (signal and idler), whose frequencies are ν_s and ν_i respectively. The energy conservation must be satisfied here, thus $2\nu_\mathrm{p} = \nu_\mathrm{s} + \nu_\mathrm{i}$. Within the microresonator, the generated signal and idler photons coincide with other resonances, and their frequencies are spaced to the pump mode with equal frequency difference (but opposite sign). The momentum conservation, also called “phase matching condition", requires $2h\nu_\mathrm{p} n_\mathrm{p}/c = h\nu_\mathrm{s} n_\mathrm{s}/c + h\nu_\mathrm{i} n_\mathrm{i}/c \rightarrow 2\nu_\mathrm{p} n_\mathrm{p} = \nu_\mathrm{s} n_\mathrm{s} + \nu_\mathrm{i} n_\mathrm{i}$, where n_p, n_s and n_i are the effective refractive indices of the pump, signal and idler photons. The difference in these refractive indices accounts the microresonator chromatic dispersion. However, in reality, not only the dispersion but also the nonlinear phase shift should be considered in the phase matching conditions. The nonlinear phase shift comes from the self-phase modulation (SPM) and cross-phase modulation (XPM). When including the nonlinear phase shift, it is found that the phase matching conditions can be satisfied only in microresonator featuring anomalous group-velocity dispersion [42].

If the nonlinear gains for the signal and idlers exceed their respective losses, parametric amplification takes over and generates more sidebands. The threshold input power to the microresonator for parametric amplification scales with $1/Q^2$, thus it can be extremely low for ultrahigh-Q microresonators [41]. Further increasing the input power in the pump mode increases the power of the sidebands and broadens the spectral bandwidth spanned over all frequency lines. The degenerate FWM can induce sidebands in any combination of resonances as long as they are equally spaced with respect to the pump, but all the generated sidebands from the pump are not necessarily equidistant due to the microresonator dispersion. In addition, the non-degenerate FWM can dominate the degenerate FMW and take the leading role for cascaded sideband generation and spectral broadening. The non-degenerate FWM involves four modes with different frequencies, and can happen for any four modes as long as the phase matching condition is fulfilled. Therefore, the FWM processes, degenerate and non-degenerate, can result in a vast array of new sidebands, but also makes precise description and prediction of the entire comb formation dynamics complicated [43]. As each non-degenerate FWM process takes place individually, these new sidebands do not necessarily exhibit precisely equidistant frequency spacing and constant phase difference. In this sense, the intracavity waveform is not necessarily a pulse stream. The formation of "dissipative Kerr solitons" [44, 45], which are ultrashort pulses circulating inside the microresonator, will be discussed later.

The cascaded FWM process finally stops when the comb spectrum bandwidth exceeds a certain value, determined by the microresonator anomalous GVD. Though the frequency

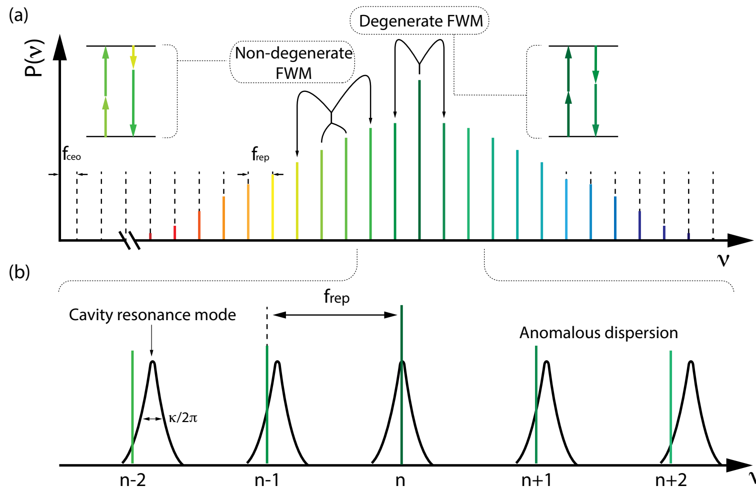

Figure 1.2 – Generation scheme of frequency combs in high-Q microresonators via Kerr nonlinearity. (a) The microresonator is driven by a c.w. pump laser. Degenerate and non-degenerate FMW processes generate frequency sidebands. The final output spectrum constitutes equidistant grid of frequency lines, i.e. a frequency comb. (b) Comparison of the equidistant frequency lines with non-equidistant microresonator resonances (due to anomalous GVD). The spectrum bandwidth of the frequency comb is finally limited by the walk-off between the frequency sideband and the resonance, determined by the microresonator GVD.

comb lines are equidistant, the microresonator GVD causes the variation of FSR with respect to the resonance frequency / wavelength. Therefore, as shown in Fig.1.2(b), at the wings of the frequency combs, the frequency line and the resonance are not commensurate. This walk-off reduces the FWM efficiency and finally limits the comb bandwidth. In reality, more precise description and prediction of the comb bandwidth require also to include the nonlinear phase shift. However, this does not change the fact that the final comb's spectral bandwidth is limited by the microresonator GVD.

The parametric oscillation induced by Kerr nonlinearity in microresonators was first reported in 2004 by T. J. Kippenberg *et al.* [41]. Signal and idler photons are generated symmetrically spaced to the pump, when the Kerr parametric gain exceeds the intrinsic photon loss rate in the cavity. Therefore, low-loss (i.e. high Q factor) microresonators can exhibit high parametric gain or ultralow parametric threshold power, in comparison to the case using fibre loop cavities. In the initial work, an ultrahigh-Q silica microtoroid [46] of an intrinsic Q factor of 50 million was used. The microtoroid was coupled with a taper fibre [47] which was designed to have high coupling ideality [48] (i.e. elimination of any coupling-induced parasitic loss). When the light is coupled into the microtoroid, by controlling the laser detuning to the resonance, the light can experience higher Kerr parametric gain than the Raman scattering gain. It was also found and studied in that work, that the geometry of the microtoroid affects whether Kerr parametric oscillation dominates Raman scattering, or verse versa. Though the microresonator dispersion was not shown in that work, it is nowadays known that the Kerr parametric oscillation requires anomalous GVD, which is affected by the microresonator geometry and optical confinement. In addition, a key information in that work is the analysis of the coupling point of minimum parametric threshold power as a function of the detuning frequency and taper-microtoroid coupling strength. It is found that the minimum threshold power occurs with the laser detuning $\delta\omega = 3\kappa_0$ and $\kappa_\text{ex} = 0.5\kappa_0$ (κ_0 in the intrinsic loss of the microresonator and κ_ex is the taper-microtoroid coupling strength). In short words, **the minimum threshold power is found with small laser detuning in the under-coupling regime** (Indeed, in Chapter 4 of this thesis, most of the soliton spectra with lowest input power have been achieved in the under-coupling regime). T. J. Kippenberg *et al.* experimentally demonstrated 339 μW threshold optical power for parametric oscillator, and 170 μW power in another microtoroid with optimized geometry or Q factor. This value represents a factor of 200 lower than the value found in photonic crystal fibres. This work lays the foundation of later Kerr microcombs. However, interestingly it did not mention frequency combs, and the main motivation was put on ultralow-threshold-power parametric oscillators.

A few years later, in 2007, the first microcomb was reported by P. Del'Haye *et al.* [36]. The threshold power of parametric oscillation was observed with an input c.w. optical power as low as 50 μW, in a silica microtoroid of $Q > 10^8$ and 75 μm diameter (~ 900 GHz FSR). The microcomb spectrum spans more than 300 nm and has a power conversion efficiency exceeding 20%. To verify that the microcomb indeed contains equidistant frequency lines, the microcomb is compared with a reference comb that is based on a fibre laser and has a repetition rate of 100 MHz. The beatnote signal between the microcomb and the reference

comb was photodetected and analyzed in the RF domain. The observed microwave beatnote signal contains also equidistant frequency tones within 5 kHz uncertainty, showing that the microcomb lines are indeed equidistant. Further, three comb lines, f_0, f_1 and f_2, were selected, and their frequency differences were measured. If the microcomb is equidistant, the ratio of frequency difference should correspond to a ration of two integers, i.e. $(f_1 - f_0)/(f_2 - f_0) = M/N$, with M and N being the known relative mode indices relative to the mode of frequency f_0. The fitted standard deviation value of the mean frequency is of several millihertz level, confirming that the microcomb spectrum is indeed equidistant. This value represents a uniformity of the comb spacing to a level of 7.3×10^{-18}.

1.4 Dissipative Kerr solitons

After the first demonstration of microcomb in 2007, many groups have joined this emerging research fields. Since then, efforts have been made on mainly three directions:

- Understanding the comb formation dynamics, and pursuing the approaches to realize phase-coherent microcombs (i.e. formation of coherent ultrashort pulses).
- Exploring new material platforms to build low-loss nonlinear microresonators. Particularly, integrated platforms such as silicon, silicon nitride, aluminium nitride, lithium niobate and aluminium gallium arsenide, have been used for microcomb generation, targeting to realize chip-based microcomb devices fabricated using CMOS technology.
- Using microcombs for applications in which microcombs have advantages over mode-locked-laser-based frequency combs.

In the following, an introduction to each direction will be given. I will first briefly review several key works in understanding the comb formation dynamics, particularly the soliton formation and tuning. The most significant achievement of microcombs in the past decade is the demonstration of the "**dissipative Kerr soliton**"(DKS) formation in optical microresonators, reported by T. Herr *et al.* [44]. These solitons are circulating pulses in the optical microresonators, and are fully coherent. An anomalous GVD is the prerequisite for soliton formation. The integrated microresonator dispersion D_{int}, including GVD and higher-order dispersion terms, can be expressed as:

$$\begin{aligned} D_{\text{int}}(\mu) &= \omega_\mu - \omega_0 - D_1\mu \\ &= D_2\mu^2/2 + D_3\mu^3/6 + \ldots \end{aligned} \tag{1.4}$$

where $\omega_\mu/2\pi$ is the frequency of the μ-th resonance relative to the pump resonance $\omega_0/2\pi$, $D_1/2\pi$ corresponds to the FSR, $D_2/2\pi$ is the GVD and $D_3/2\pi$ is the third-order dispersion. Note that D_2 is related to the GVD parameter β_2 as

$$D_2 = -c \cdot \beta_2 \cdot D_1^2 \cdot n_0^{-1} \tag{1.5}$$

with n_0 being the effective refractive index of the optical mode and c being the speed of light in vacuum. A positive D_2 means anomalous GVD. In addition, in microresonators made from the same material, having the same cross-section but different radii (i.e. FSR), it is important to notice that the D_2 and D_1 are related as $D_2 \propto D_1^2$. The integrated dispersion D_{int} describes the frequency deviation of the resonance grid from an equidistant frequency grid. Its dependence on the frequency or wavelength provides information on the phase matching condition, thus determines the final comb spectral bandwidth.

When the laser is tuned into the resonance from the blue-detuned side to the red-detuned side, the first pair of sidebands emerge around the mode indices $\pm i$ relative to the pump (the pump mode index is 0), i.e.

$$i = \sqrt{\frac{\kappa}{D_2}} \tag{1.6}$$

where $\kappa/2\pi = (\kappa_0 + \kappa_{\mathrm{ex}})/2\pi$ is the loaded resonance linewidth (with $\kappa_0/2\pi$ being the intrinsic loss and $\kappa_{\mathrm{ex}}/2\pi$ being the external coupling rate from the bus waveguide). The first pair of sidebands appear around the mode indices $\pm i$ where the dispersion D_2, nonlinear phase shifts (via SPM and XPM) and pump laser detuning balance each other, such that the parametric gain is maximum [49]. If the closest non-zero integer value to i is 1, the first pair of sidebands emerge in the resonances directly next to the pump mode. Therefore, the subsequent cascade FWM processes preserve a single-frequency spacing, and generate fully coherent frequency lines. This type of comb formation process is called as "**natively spaced comb**" (NMS) [43]. Since $D_2 \propto D_1^2$, this natively spaced comb is the typical formation process in large-FSR (i.e. large D_1 which leads to large D_2), high-Q (i.e. small κ) devices. For example, the first comb generation in ref. [36] in 2007 belongs to this case. Later in this thesis, the combs generated in 1-THz-FSR Si_3N_4 microresonators also belong to this case.

Commonly, in microresonators with relatively lower Q (such as integrated platforms) or weak anomalous GVD (such as low-FSR microresonators), one has $\sqrt{\kappa/D_2} \gg 1$, and the first pair of sidebands appear in the resonance modes of multiple FSR from the pump mode. In this scenario, the comb formation process represents "**multiple mode-spaced**" (MMS) [43]. The first pair of comb lines are generated symmetrically to the pump mode of frequency ω_0 (mode index $i = 0$) by the degenerate FWM process. These two comb lines are generated in the modes of $\pm i = \pm\sqrt{\kappa/D_2} \gg 1$, and the frequency differences are approximately $\pm\Delta = \pm i \cdot D_1/2\pi$. Cascaded FWM to higher-order sidebands preserves this initial frequency spacing Δ as a result of energy conservation. The sidebands generated in this scheme are called "primary comb lines" [43]. Further increase the pump power leads to the "secondary comb lines" generated around the primary comb lines via degenerate or non-degenerate FWM processes, and eventually these secondary lines centred around two adjacent primary lines can merge and form a gap-free continuous spectrum. Generally, the entire comb spectrum does not consist of equidistant lines featuring a single frequency spacing. The complex comb formation process has been studied in detail in ref. [43].

The microcombs formed with NMS and MMS types of processes exhibit strikingly different time-domain behaviours, observed and verified in the previous report on line-by-line pulse shaping of microcomb [50]. For microcombs formed in the NMS process, the output microcomb waveform can be shaped to nearly bandwidth-limited pulses, which indicates that this type of microcombs exhibits high coherence properties over the entire the spectral range. Microcombs formed in the MMS process have only partial coherence revealed from their time-domain waveform characterization.

Despite the complex comb formation process, theory [51] has predicted the generation of "temporal dissipative cavity solitons" [52, 53] in the Kerr-nonlinear, anomalous-GVD microresonators driven by a c.w. laser. This soliton is a travelling pulse with a c.w. background circulating inside the microresonator, and emits a pulse stream via the external coupling to the coupled waveguide. To theoretically describe this damped nonlinear driven system, the "Lugiato–Lefever equation" (LLE) [51] is widely used, which is a nonlinear Schrödinger equation considering the interplay between Kerr nonlinearity, anomalous GVD, the intrinsic optical loss of the microresonator, and the parametric gain from the c.w. pump. The existence of the soliton solution requires the double balances between: 1. the Kerr nonlinearity and anomalous GVD; 2. the intrinsic microresonator loss and the parametric gain from the external c.w. pump. More details of LLE will be given in the later section.

The dissipative cavity soliton, also called "**dissipative Kerr soliton**" (DKS) as the Kerr nonlinearity plays the key role, was first demonstrated in fibre cavities in 2010 by F. Leo *et al.* [52]. In 2014, the demonstration of DKS formation in MgF_2 microresonators was reported by T. Herr *et al.* [44]. As mentioned already, the common microcomb formation via the FWM processes does not yield single line spacing and defined phase relation for each comb line. Therefore, the intracavity waveform is chaotic and does not form an ultrashort pulse stream in the time domain with a well-defined waveform envelope. To form an ultrashort pulse stream, it is required that the comb formation process, not only has a single frequency spacing, but also a defined phase relation such that all the comb lines coherently add up to a pulse waveform. In Herr's work, it has been shown that the coherent soliton state can be accessed by tuning the pump laser from the effectively blue-detuned side of the resonance to the red-detuned side, and the soliton is formed *spontaneously* in the effectively red-detuned regime. During the tuning, the slow thermal-optic effect and the fast Kerr nonlinearity of the microresonator shift the cavity resonance and lock the pump laser to the resonance. In this case, since the nonlinear microresonator is driven strongly by the c.w. pump, the high intracavity power shifts the resonances towards the lower frequency side. This resonance shift results from two effects: the nonlinear phase shift due to the Kerr nonlinearity, and the microresonator thermal-optic effect that increases the refractive index and the mode volume. These two effects occur with different time constants: the Kerr effect is **instantaneous**, while the thermal-optic effect has a time constant of tens of microseconds [54] which corresponds to few kilohertz frequency bandwidth. In sum, these two effects shift the resonance and result in two stable solutions: one solution with higher intracavity power at the effectively blue-detuned side of the "hot" resonance, and the other solution with lower intracavity power at the effectively red-detuned

side of the “cold” resonance. For a given detuning value, in the effective red-detuned side of the “cold” resonance, the entire system is bistable, i.e. both solutions can coexist.

When the c.w. pump (laser linewidth much smaller than the resonance linewidth) scans with decreasing optical frequency from the blue-detuned side of the resonance to the red-detuned side, step-like features are observed in the microresonator transmission spectrum, in addition to the expected thermal triangle shape [55]. A low-noise, narrow RF beatnote is observed at the end of the laser scan, coinciding with the step features in the microresonator transmission spectrum. This narrow RF beatnote signifies the formation of soliton pulses periodically emitted from the microresonator under c.w. driving. The formation of soliton pulses requires particular detuning values, typically around few tens of the resonance linewidth, in the red-detuned side.

A transmission spectrum can exhibit multiple steps, indicating different soliton states. Experimentally, by scanning the laser frequency quickly through the resonance, it is not deterministic which soliton state will be excited. These soliton states, though having different spectral envelopes corresponding to different numbers of solitons circulating inside the microresonator, do have the same narrow beatnote frequency which corresponds to the soliton repetition rate, demonstrating that these spectra are indeed coherent soliton spectra. The most important case is that the soliton spectrum fit is a perfect $sech^2$ function. This is the **single soliton state**. In this case, there is only one soliton circulating in the microresonator. Other soliton spectra are multi-solitons where the interference pattern of the spectral envelope is determined by the relative positions of each soliton in the microresonator. A specific case is that there are N solitons equidistantly spaced in the microresonator, and the soliton spectrum has a comb line spacing increased by a factor of N compared to the case of single soliton, which is equivalent the single soliton spectrum in a microresonator of N-times FSR. This case is referred to as “**soliton crystal**” [56, 57].

Since only the single soliton spectrum exhibits a smooth $sech^2$ envelope, it is often desired in applications. However, tuning the laser into the solitons state is stochastic, thus which soliton state is accessed in the end is not pre-determined. Particularly, experimental observation and simulations show that, the soliton step length decreases with decreasing soliton number N, and N increases with increasing pump power. The transmission trace typically consists of one soliton step corresponding to a high-N multi-soliton state. In sum, these observations indicate that the single soliton state is not readily accessible. Therefore, a scheme allowing to tune the multi-soliton states to the single soliton state *deterministically* is needed.

The first work aiming to achieve deterministic single soliton generation was reported in ref.[58]. H. Guo *et al.* have reported a soliton switching scheme via “**backward tuning**”, which provides a way to reliably access the single-soliton state starting from an arbitrary multi-soliton state. This is in contrast to the previously described method used in ref. [44], where the single soliton is accessed by tuning the c.w. pump laser from the effectively blue-detuned side to the red-detuned side over the resonance via “**forward tuning**”. Once a multi-soliton state is

reached via the forward tuning, the pump frequency is increased slowly (i.e. reducing the pump detuning to the resonance). The backward tuning needs to be adiabatic (i.e. tuning speed slower than the thermal relaxation speed), such that the intracavity thermal equilibrium is maintained during the tuning. This backward tuning allows the number of solitons in the microresonator to be reduced progressively, and thereby to reliably reach the single soliton state.

In the soliton state, the transfer function of the system presents a unique feature that can be experimentally characterized. Once the soliton state is accessed, thermal effect locks the laser frequency at the red-detuned side of the resonance. The detuning value δ_ν is typically around tens of the resonance linewidth κ, i.e. $\delta_\nu \sim 20\kappa$. In this soliton regime, as shown in Fig. 1.3(a), one can use an electro-optic modulator (EOM) and a vector network analyzer (VNA) to study the frequency response of the system, and unambiguously measure the soliton detuning value, as illustrated in ref. [58]. The pump laser is modulated by the EOM and VNA, such that the sidebands are also coupled into the microresonator, and the photodetected signal after the microresonator is sent back to the VNA. The principle is based on measuring the transfer function of a weakly phase-modulated pump to amplitude modulation on the comb power, as shown in Fig.1.3(b). The phase modulation of the pump generates a pair of sidebands of π phase difference. When sweeping the VNA frequency on the EOM, these sidebands move. If one sideband is coupled into the resonator, it is effectively attenuated or rotated, creating an amplitude modulation between the pump and the unbalanced sidebands. In sum, the entire system response presents two resonances on the VNA: the C-resonance corresponds to the resonance and the S-resonance corresponds to the soliton state in the red-detuned side of the resonance. Physically, the double-resonance feature originates from the fundamental cavity bistability in the presence of the Kerr nonlinearity. The Kerr nonlinearity is responsible for the soliton-induced nonlinear phase shift which produces the S-resonance in the system transfer function. Therefore, the double-resonance feature is a unique signature of the soliton state. In addition, the frequency difference between the S- and C-resonance, measured by the VNA, represents the effective soliton detuning.

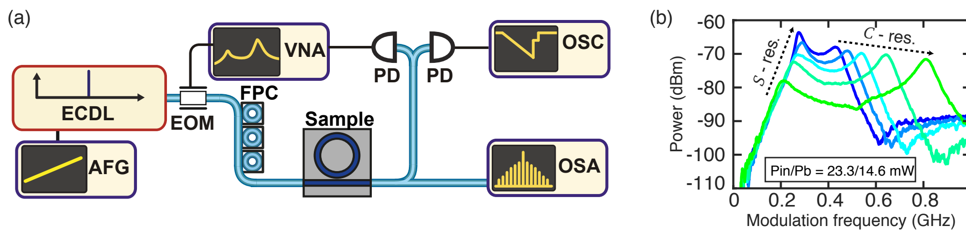

Figure 1.3 – General microcomb formation process. (a) Experimental setup to control the soliton states and characterize the system response. (b) Microresonator frequency response when operated in the soliton regime, which shows the S-resonance and the C-resonance.

1.4.1 Soliton tuning methods

The previously described soliton tuning method using forward and backward tuning represents the *simplest* case. The prerequisite for this method to work is that the soliton step is sufficiently long such that a (multi-)soliton state can be accessed via the forward tuning, which, however is not always the case. Particularly for integrated material platforms such as Si_3N_4, the strong thermal effect due to the inherent thermal absorption and the small mode volume of the microresonator cause short soliton step which can be directly land on. Therefore, forward tuning is likely incapable to access any kind of soliton states. To overcome the strong thermal effect, multiple complex soliton tuning techniques have been demonstrated, listed below:

- **Using a single-sideband modulator** [59]: The c.w. pump laser is sent through a single-sideband suppressed-carrier (SSB-SC) frequency shifter composed of a dual-parallel lithium niobate waveguide Mach-Zehnder intensity modulator driven by a wideband voltage-controlled oscillator (VCO). This allows rapid frequency scan of the sideband across the resonance and the access to the soliton state, with a scanning rate of 100 GHz / μs for 4 GHz frequency excursion. Such frequency scan is so fast that the transition from chaotic combs state to the soliton state, though has drastic intracavity power reduction, does not cause significant temperature change, as the frequency scan time less than 100 ns [60] is much smaller than the characteristic thermal relaxation time ~ 30μs [54]. Further optimizing the frequency scan rate and excursion to better balance the thermal resonance drift enables (single) soliton generation.

- **Using a slowly intensity-modulated pump laser** [61]: A slow modulation of less than 1 GHz rate is applied on the c.w. pump such that a pair of sidebands are generated with an offset optical frequency. In the case without these sidebands, when the pump laser is tuned across the resonance, the transition from chaotic combs state to the soliton state leads to an intracavity power reduction, which results in a thermal shift of the resonance. In the presence of sideband, if the modulation rate is chosen properly based on the loaded resonance linewidth, one sideband is tuned into the same resonance simultaneously to the pump tuning across the resonance. Therefore, the intracavity power drop due to the pump laser during the transition from chaotic combs state to the soliton state can be effectively compensated by the sideband tunned into the same resonance. An optimized combination of the modulation rate and depth could enable arbitrarily slow pump tuning to access the soliton state, with significantly extended soliton step length.

- **Using two pump lasers** [62, 63]: Two lasers coupled to two different resonances are used, the pump laser and the auxiliary laser. First, the auxiliary laser is tuned into a resonance and stopped with small frequency detuning at the effectively blue-detuned side of the resonance. Then the pump laser is tuned into the resonance (can be the same resonance or a different one) from the blue-detuned side. Due to the coupling of the pump laser into the microresonator and the heating, the resonances are pushed

to longer wavelengths, which increase the frequency detuning of auxiliary laser and reduces its intracavity power contribution. In return, the microresonator is cooled, and the resonance thermal shift is reduced. The counteraction between the pump and auxiliary lasers, with optimized power and detuning respectively, allows an equilibrium of the microresonator temperature which is insensitive to the pump laser frequency scan. As such, the soliton step length can be significantly extended. This scheme using two lasers is similar to the previous scheme using a slowly intensity-modulated pump laser.

- **"Power kicking"** [64]: This scheme uses only one laser which is power-modulated using an acousto-optic modulator (AOM) in the pump path. The laser frequency scan and AOM are timed, such that the AOM lowers the pump power before the laser tunes into the resonance and the AOM increases the pump power when the pump laser is accessing the soliton regime. The increase of the pump power counteracts the intracavity power reduction during the transition from the chaotic comb state to the soliton state. By optimizing the scan speed, power modulation level, and the timing sequence, the soliton state can be reliably accessed.

- **Employing photorefractive effect** [65]: This method only applies for materials having photorefractivity, such as lithium niobate ($LiNbO_3$) and lithium tantalate ($LiTaO_3$) etc. The photorefractivity comes from the impurity in the material which causes light absorption and generates electron-hole pairs. The electron diffusion leads to local charge field, and changes the refractive index via electro-optic effect. This effect of refractive index change caused by the light absorption is called "photorefraction". Photorefraction results in a decrease of the refractive index at the order of 10^{-4}. In the WGM microresonator, this leads to the resonance grid shift towards higher optical frequency (shorter wavelength) [66]. The photorefractivity poses the maximum operation power or the lifetime of the device (e.g. $LiNbO_3$ modulator).

  In the work reported by Y. He *et al.*, a self-starting soliton formation was observed in integrated $LiNbO_3$ microresonator of 200 GHz FSR and loaded Q of 2×10^6. Note that the resonance shift caused by thermal effect (towards longer wavelength) is opposite to the shift caused by the $LiNbO_3$ photorefraction (towards shorter wavelength). Therefore, by optimizing the laser frequency scan and pump power, soliton formation is self-starting. Interestingly, the presence of photorefraction also allows soliton state switching to higher-number multi-soliton state, which has not been observed in other platforms such as fluoride crystals, SiO_2, Si_3N_4 and AlN.

  The photorefractivity is also related to the stoichiometry of the material. For $LiNbO_3$, the photorefractivity comes from the fact that the conventional Czochralski method to grow $LiNbO_3$ introduces extra Nb (i.e. the $LiNbO_3$ is Nb-rich). One way to reduce the photorefractivity in Nb-rich $LiNbO_3$ is to increase the operation temperature of the device, such that when electron-hole pairs are generated due to photon absorption, electrons and holes can recombine more quickly with higher temperature. The more

standard method is to add magnesium oxide (MgO) or zinc oxide (ZnO) dopant [67]. Typical dopant concentration is at few mole percent depending on the operation wavelength. With the MgO or ZnO dopant, the refractive index change can be reduced to below 10^{-5} [68]. However the introduced dopant can cause extra optical losses.

- **Turkey soliton generation via injection locking** [69, 70]: This scheme relies on soliton self-injection locking, which has a feedback speed on the laser much faster than the thermal relaxation speed. If the system is optimized with proper parameters for soliton self-injection locking, soliton states are immediately accessed upon turn-on of the laser, without any need of laser frequency tuning. This effect as well as the soliton self-injection locking will be illustrated with more details in the later chapter. Part of the results within this PhD thesis has contributed this work.

Besides the soliton tuning method mentioned above, recently, E. Obrzud *et al.* reported soliton formation driven by optical pulses [71] instead of a c.w. pump used in the conventional case. The microresonator is driven by periodic picosecond optical pulses of a repetition rate matching the microresonator FSR (the expected repetition rate of the generated single soliton). The standard method for electro-optic frequency comb generation [72], which requires the phase and intensity modulation of a c.w. pump, as well as chirp and dispersion management, in order to generate a picosecond pulse stream output via a c.w. input. In the frequency domain, this picosecond pulse stream corresponds to an EO comb spectrum of equidistant frequency grid. By tuning the c.w. carrier and the microwave frequency applied on the modulators, the EO comb spectrum can be frequency-translated and the line spacing can be altered, such that all the EO comb lines can coincide with the microresonator resonance grid which allows the picosecond pulse stream to be coupled into the microresonator. The driving pulse is resonantly enhanced inside the microresonator, and thus can generation solitons co-propagating with the pulse. The synchronization, where the pulse repetition rate f_{ext} equals the soliton repetition rate f_{sol}, is critical such that the soliton keeps tracking the pulse which provides the parametric gain to the soliton. Therefore, changing f_{ext} can alter the generated soliton state. For example, if the microresonator is sub-harmonically driven (i.e. $f_{\text{ext}} = f_{\text{sol}}/N$ with N being an integer), only single soliton is forced to form; if the microresonator is multi-harmonically driven (i.e. $f_{\text{ext}} = N \cdot f_{\text{sol}}$ with N being an integer), a soliton crystal [56, 57] can form.

The pulse-driving soliton formation has several advantages over the conventional c.w.-driving case:

- A single soliton can be generated deterministically.

- The required power for soliton generation scales inversely with the temporal overlap between the soliton pulse and the driving background (c.w. or pulse). Therefore, the pulse-driving scheme offers drastically increased pump-to-soliton power conversion

efficiency which is more than ten-times higher than the value in the case with a c.w. pump.

- Higher power conversion efficiency also enables lower required power for soliton formation in the pulse-driving case. In addition, the lower required power also reduces the thermal effect and allows to generate a soliton state more easily.

- Since the soliton tracks the pulse, the soliton repetition rate is stabilized to the repetition rate of the driving pulses. Meanwhile, the soliton locked to the driving pulses remains stable without requiring any active feedback. This increases the long term stability of the soliton state.

- A certain mismatch between the driving pulse's repetition rate f_{ext} and the soliton repetition rate f_{sol}/N is allowed without losing the soliton state. For example, for resonance linewidth of few megahertz or tens of megahertz, this mismatch $|f_{\mathrm{ext}} - f_{\mathrm{sol}}|$ is less than 100 kHz [71]. Therefore, in combination with the frequency tuning of the pulse carrier and repetition rate, the spectrum of the generated soliton microcomb can be frequency-translated, which manifests as the tuning of the carrier envelope frequency of the frequency comb.

This soliton control via synchronization to external driving has also been demonstrated in soliton synchronization [73] and spectral purification of soliton phase noise [74]. Pulse-driving soliton formation has also been used in demonstration of broadband single soliton of detectable 28 GHz repetition rate in Si_3N_4 microresonators [75] (part of the results within this PhD thesis has contributed this work). This scheme is currently pursued in order to achieve octave-spanning soliton microcomb with electronically detectable repetition rate and tunable carrier envelope frequency.

1.4.2 Theoretical model

The formation of Kerr microcombs in optical microresonators arises from the interaction between the pump laser, the dissipated optical cavity, the inherent cavity chromatic dispersion and Kerr nonlinearity [36]. To describe the formation dynamics of microcombs, the first complete theoretical model was proposed by Y. K. Chembo and N. Yu [76] based on the coupled mode equations (CME) approach. This model treats each frequency comb line as an individual electric field component, and all the comb lines (fields) couple to each other via the FWM under Kerr nonlinearity. The CME model has been employed to well describe the primary comb generation where only few comb lines need to be taken into account [43]. However, for microcomb states in chaos modulation instability or the DKS regime that contain a large number of comb lines, the CME model becomes inefficient and requires huge computation resource. An alternative numerical model based on the *Lugiato-Lefever Equation* (LLE) [51] has been proposed and widely used to simulate the intracavity electric field in the time domain rather than the frequency domain as the case of the CME model[77]. The LLE

model is based on a mean field description and is adopted from the early work in ref. [51] for the spatial dissipative optical system referred to the externally driven damped nonlinear Schrödinger equation (NLSE).

Coupled Mode Equations (CME): The CME model simulates the temporal evaluations of the electrical field for each cavity mode in the same mode family. The optical microresonator is driven by an external c.w. laser with the frequency ω_p. The electrical field of an individual cavity mode is denoted as A_μ and μ is the relative mode number of the cavity mode referred to the pumped mode $\mu = 0$. The rate equation of μ-th cavity mode with frequency ω_μ can be described as [76]:

$$\frac{dA_\mu}{dt} = -\frac{\kappa}{2}A_\mu + \underbrace{ig\sum_{\mu 1,\mu 2,\mu 3} A_{\mu 1}A_{\mu 2}A^*_{\mu 3}e^{-i(\omega_{\mu 1}+\omega_{\mu 2}-\omega_{\mu 3}-\omega_\mu)t}}_{\text{Kerr nonlinearity}} + \underbrace{\delta_{\mu 0}\sqrt{\kappa_{\text{ex}}}s_{\text{in}}e^{i(\omega_p-\omega_0)t}}_{\text{external drive}} \tag{1.7}$$

where μ_0 is the frequency of the pumped mode, κ is the total cavity decay (loss) rate, κ_{ex} is the external coupling rate, and s_{in} is the pump field amplitude. The Kronecker symbol δ indicates that the external drive is only applied on the pump mode $\mu = 0$. The sum term represents the FWM processes resulted from the Kerr nonlinearity. It is only valid when the phase matching condition (momentum conservation) $\mu 1 + \mu 2 = \mu 3 + \mu$ and energy conservation $\omega_{\mu 1} + \omega_{\mu 2} = \omega_{\mu 3} + \omega_\mu$ are simultaneously fulfilled. The normalized Kerr nonlinear coefficient (i.e. Kerr shift per photon) g can be written as

$$g = \frac{\hbar\omega_0^2 c n_2}{n_0^2 V_{\text{eff}}} \tag{1.8}$$

where n_2 is the second-order nonlinear index and V_{eff} is the effective mode volume.

To remove the time-dependences of the Kerr nonlinearity term in Eq. (1.7), the transformation $a_\mu = A_\mu e^{-i(\omega_\mu-\omega_p-\mu D_1)t}$ is applied, where $D_1/2\pi$ is the microresonator FSR. This transformation also regulates the frequency grid with a constant spacing of $D_1/2\pi$. Considering cavity dispersion limited by only the second-order term $D_2/2\pi$, the μ-th mode frequency ω_μ can be expressed as $\omega_\mu = \omega_0 + D_1\mu + \frac{D_2}{2}\mu^2$. As a result, the CME can be rewritten as

$$\frac{da_\mu}{dt} = -i(\omega_0 - \omega_p + \frac{D_2}{2}\mu^2)a_\mu - \frac{\kappa}{2}\mu^2 + ig\sum_{\mu 1,\mu 2} a_{\mu 1}a_{\mu 2}a^*_{\mu 1+\mu 2-\mu} + \delta_{\mu 0}\sqrt{\kappa_{\text{ex}}}s_{\text{in}} \tag{1.9}$$

The CME can be numerically simulated to well reproduce the Kerr microcomb formation that has been observed in experiments. Under a simplified condition, this model can also be analytical solved to derive the parametric oscillation threshold power value. In this case, the CME only consider three comb line: the pumped line ($\mu = 0$) and the first pair of sidebands ($\mu = \pm\sqrt{\kappa/D_2}$). Introducing the parametric gain lobes to the CME model, the parametric

oscillation threshold can be calculated as [43]

$$P_{\text{th}} = \frac{\kappa^2 n^2 V_{\text{eff}}}{4\omega_0 c n_2} \tag{1.10}$$

Lugiato-Lefever Equation (LLE): The above-mentioned CME model is built in the coordinate of propagation time ("slow" time) t and the cavity mode number μ, and describes the Kerr microcomb formation in the frequency domain. Each comb line has an individual equation to simulate its own optical amplitude. To simplify the numerical model and to shorten the simulation time, an alternative approach is to describe the entire system in the spatial or time domain. In optical microresonators, a nature spatial coordinate is the intracavity position in azimuthal angle ϕ. The slowly-varying envelope of the intracavity electric field $A(\phi, t)$ can be expressed as

$$A(\phi, t) = \sum_{\mu} a_\mu(t) e^{-i(\omega_\mu - \omega_p)t + i\mu\phi} \tag{1.11}$$

The azimuthal position ϕ can also be transformed into the time domain as $\phi = 2\pi\tau / T_R = D_1\tau$, where T_R is the round-trip time and τ is the "fast" time coordinate [77]. By substituting Eq. 1.11 into Eq. 1.9, the LLE is derived as:

$$\frac{\partial A(\phi, t)}{\partial t} = \underbrace{-\frac{\kappa}{2} A(\phi, t)}_{\text{loss}} \underbrace{- i(\omega_0 - \omega_p) A(\phi, t)}_{\text{detuning}} + \underbrace{i\frac{D_2}{2}\frac{\partial^2 A(\phi, t)}{\partial \phi^2}}_{\text{cavity dispersion}} + \underbrace{ig|A(\phi, t)|^2 A(\phi, t)}_{\text{Kerr nonlinearity}} + \underbrace{\sqrt{\kappa_{\text{ex}}} s_{\text{in}}}_{\text{external drive}} \tag{1.12}$$

On the right hand side of the equation, there are five terms: loss, detuning, cavity dispersion, Kerr nonlinearity and external drive. This equation together with the boundary condition $A(\phi, t) = A(\phi + 2\pi, t)$ is equivalent to the CME, and can well describe the dynamic of Kerr microcomb formation. Furthermore, Eq .1.12 can be normalized by taking following transformations:

$$\begin{aligned}
\psi &= \sqrt{\frac{2g}{\kappa}} A \\
\tau &= \frac{\kappa}{2} t \\
\theta &= \sqrt{\frac{\kappa}{2D_2}} \phi \qquad \psi = \sqrt{\frac{2g}{\kappa}} A \\
\zeta &= \frac{2(\omega_0 - \omega_p)}{\kappa} \\
f &= \sqrt{\frac{8\kappa_{ex} g}{\kappa^3}} s_{\text{in}}
\end{aligned} \tag{1.13}$$

As a result, the Eq. 1.12 can be rewritten in a dimensionless form as

$$\frac{\partial\psi(\theta,\tau)}{\partial\tau} = -(1+i\zeta)\psi(\theta,\tau) + \frac{i}{2}\frac{\partial^2\psi(\theta,\tau)}{\partial\theta^2} + i|\psi(\theta,\tau)|^2\psi(\theta,\tau) + f \tag{1.14}$$

This is the *standard* LLE [51] and has an approximate steady-state soliton solution for the case of anomalous GVD ($D_2 > 0$):

$$\psi_{\text{soliton}}(\theta) \approx \psi_0 + Be^{i\phi_0} sech(B\theta) \tag{1.15}$$

where ψ_0 is the c.w. background, ϕ_0 is the phase shift of the cavity soliton respect to the external pump, and $B = \sqrt{2\zeta}$ determines the soliton amplitude and bandwidth.

Next, an example is given to show the LLE simulation for the soliton generation in Si_3N_4 microresonators. This example is based on the experimental work of ref. [78]. The simulation parameters obtained from the experiments are: $D_1/2\pi = 19.6$ GHz, $D_2/2\pi = 63.3$ kHz, $\kappa_{\text{ex}}/2\pi =$ 16 MHz, $\kappa_0/2\pi = 11$ MHz, $\omega_0/2\pi = 192.25$ THz, pump power $P_{\text{in}} = s_{\text{in}}^2\hbar\omega_0/2\pi = 100$ mW. Figure 1.4 shows the simulation results. When the pump laser scans from the blue-detuned side to the red-detuned side of a microresonator resonance, the intracavity waveform experiences five different states, including the primary comb, Turing pattern, modulation instability, breather soliton state and multi-soliton state. The corresponding intracavity waveforms and optical spectra are shown in Fig. 1.4(c).

1.5 Integrated materials platforms for microcombs

So far, microcombs have been demonstrated in a wide range of material platforms. In addition to bulk polished ultra-pure crystals such as MaF_2 and CaF_2 [37, 44, 81], and thermal silicon dioxide (SiO_2) grown on silicon wafers [46, 36, 82, 83, 84], integrated platforms, which allow fabrication of waveguide-based microresonators using CMOS foundry processes, have been widely explored for integrated microcomb generation. These integrated platforms include silicon nitride (Si_3N_4) [85, 86, 87, 88, 89, 90, 91, 78, 92, 93, 94, 95, 96, 97, 98, 99, 100, 101], aluminium nitride (AlN) [102, 103, 104], lithium niobate ($LiNbO_3$) [105, 106, 107, 65], aluminium gallium arsenide (AlGaAs) [108, 80], gallium phosphide (GaP) [79], high-refractive index ("Hydex") [109, 110], tantalum pentoxide (Ta_2O_5) [111], silicon (Si) [112], and diamond [113]. Interestingly, single solitons have been achieved in nearly all of these platforms (except diamond and GaP), despite the fact that some materials require complex soliton tuning techniques due to the thermal effects.

Table 1.1 compares these materials in terms of their key optical parameters, such as the refractive index, the Kerr nonlinear index n_2 and the cutoff wavelength for two photon absorption (TPA) (equivalent to the bandgap of the material). Meanwhile, the optical loss (i.e. microresonator Q factor) is also critical to microcomb generation. The optical loss not only depends on the material property such as the intrinsic photon absorption loss, but also depends on the

fabrication technology.

Despite the fact that currently, the Q of all integrated platforms remains several orders of magnitude lower than the values obtained in bulk fluoride crystals and suspended SiO_2 microdisks / microtoroids, main technological effort has been paid on these integrated platforms in order to reduce the optical losses and increase the microresonator Q factors. In addition, new material platforms are still emerging. The key advantages of integrated platforms over the fluoride crystals and SiO_2 microdisks are:

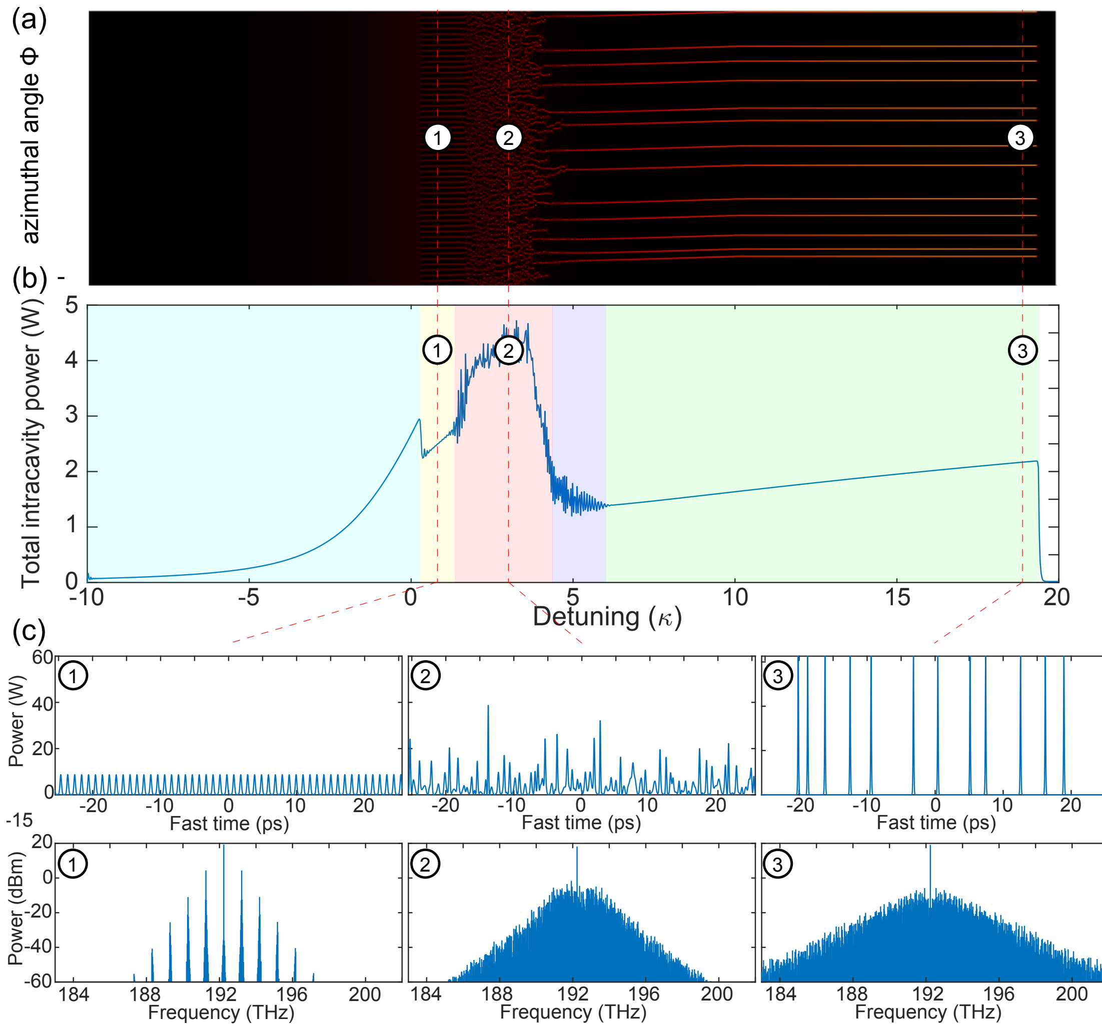

Figure 1.4 – LLE simulation for the Kerr microcomb generation in Si_3N_4 microresonator. (a) The intracavity waveform evolution. (b) The total intracavity power evolution versus the pump laser detuning. The frequency generation shows five different regimes: primary comb (blue), Turing pattern (yellow), modulation instability comb (red), breathers (purple), soliton comb (green). (C) The intracavity waveforms (top row) and optical spectra (bottom row) of three typical frequency comb states: 1. Turing pattern, 2. modulation instability comb, and 3. multi-soliton state.

- Fabrication of microresonators can employ the CMOS technology to fabricate electronic circuits. The CMOS fabrication allow scalable manufacturing of integrated devices, while for fluoride crystals requires manual polishing in a one-by-one basis.

- Both the microresonator and the bus waveguide can be directly fabricated together on the same chip, thus the coupling between them is much more robust as compared to the tapered fibre coupling used for fluoride crystalline microresonators and suspended SiO_2 microdisks, which is sensitive to mechanical vibrations. In addition, the coupling strength between the microresonator and the bus waveguide is lithographically controllable, i.e. the precise gap distance between them is well defined in the lithography process with typical precision better than 20 nm.

- The integrated microresonator does not need to be perfect circular shapes, as long as the waveguide is close. For example, for microresonators of small FSRs, they can be designed in racetracks [114] or finger shapes [98]. This design freedom allows to significantly reduce the device's footprint and densely pack multiple devices on a single chip.

- These integrated materials all have high refractive indices ($n > 2$). The microresonator of large FSR (small diameter) can be fabricated thanks to the lithography technology. This capability allows the access to terahertz FSR for high-repetition-rate, octave-spanning soliton microcomb generation [89, 99, 60]. This is very challenging for fluoride crystalline microresonators and SiO_2 microdisks, as their low refractive indices can cause significant bending loss due to the small radii. In addition, manual polishing small

Table 1.1 – Key optical parameters of materials studied for microcomb generation. n_2 is the Kerr nonlinear index. λ_{TPA} is the TPA cutoff wavelength. The table combines the tables shown in ref. [79] and [80].

Material	RI	n_2 (10^{-19} m^{2}W^{-1})	λ_{TPA} (nm)	highest Q (10^6)
SiO_2	1.45	0.22	280	270
Hydex	1.7	1.2	280	1.7
Si_3N_4	2.0	2.5	460	37
AlN	2.1	2.3	440	0.9
$LiNbO_3$	2.2	1.8	–	2.2
AlGaAs	3.3	260	1520	1.5
GaP	3.1	110	1100	0.2
Ta_2O_5	2.05	6.2	–	3.2
Si	3.5	50	2250	0.6
Diamond	2.4	0.82	450	1

fluoride crystalline microresonators is challenging.

- The fully cladded, planar waveguides allow other functions to be integrated on the microresonators, such as thermal heaters [54, 97] and piezoelectric actuators [115, 116].
- The waveguide geometry can be fully controlled. The waveguide width is lithographically controlled, and the waveguide height is controlled by film growth. This full freedom of geometry control allows geometry dispersion engineering and tailor the anomalous GVD [49, 117]. This capability is critical for microcomb generation. For example, different from fluoride crystals and SiO_2 which have anomalous GVD in the telecommunication wavelength range around 1550 nm, Si_3N_4 and other integrated platforms have normal GVD in this wavelength range. In addition, all these materials have strong normal GVD close to the visible wavelength range due to the light absorption at ultraviolet. Therefore, achieving anomalous geometry dispersion to compensate the normal material dispersion is key to achieve a net, anomalous GVD.

All these features and advantages highlight the potential of integrated platforms, and outline the trend to microcomb chip devices with the mature CMOS technology in scalable manufacturing at foundry levels.

1.5.1 Dispersion engineering

Among all the key features of integrated platforms, dispersion engineering endows unprecedented capability to engineer the frequency comb spectrum and bandwidth, leading to the direct access to octave comb bandwidth without external spectrum broadening. Here a more detailed discussion on dispersion engineering is given.

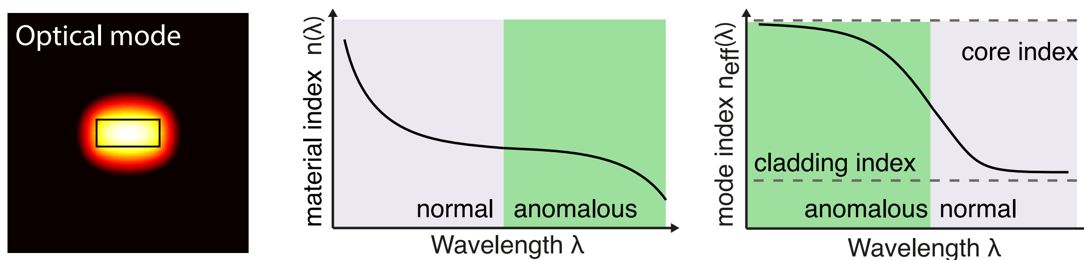

Figure 1.5 – Integrated materials can exhibit different GVD at different wavelength range, depending on the wavelengths of their absorption features. For FWM process and microcomb generation, anomalous GVD is required. In order to compensate the normal material dispersion, geometry dispersion engineering is used to achieve a net anomalous GVD. This is realized by controlling the mode field distribution in the waveguide core and cladding, as the waveguide core size is comparable to the optical wavelength. Typically, to reach anomalous GVD, the optical confinement needs to be strong, i.e. the main of the optical field is confined in the waveguide core. This figure is adapted from ref. [88].

The effective refractive index $n(\omega)$ of the waveguide and the linear susceptibility $\chi^{(1)}(\omega)$ are both frequency-dependent. They are related by $n(\omega) = \sqrt{1+\chi^{(1)}(\omega)}$ ($\omega/2\pi$ is the optical frequency). This relation is called " chromatic dispersion" [42]. In materials exhibiting chromatic dispersion, light has two characteristic velocities, the phase velocity v_p and the group velocity v_g, defined as:

$$\begin{aligned} v_p &= \frac{\omega}{k} = \frac{c}{n(\omega)} \\ v_g &= \frac{d\omega}{d\beta} \end{aligned} \tag{1.16}$$

where β is the propagation constant. For optical pulses such as travelling solitons, the phase velocity v_p is the speed of the carrier frequency and the group velocity v_g is the speed of the carrier envelope, as

$$E(x,t) \approx A(t - z/v_g)\exp[i\omega(t - z/v_p)] \tag{1.17}$$

It is evident that the phase velocity depends on the frequency through the effective refractive index $n(\omega)$. This dependence is known as "phase velocity dispersion" (PVD), described by the parameter $dn(\omega)/d\omega$. If $dn(\omega)/d\omega > 0$, it means that the frequency component of higher optical frequency travels slower than the component of lower frequency. This case is referred as "normal PVD". The opposite case is $dn(\omega)/d\omega < 0$ which is called "anomalous PVD".

The group velocity also depends on the frequency, known as "group velocity dispersion (GVD)" [118]. The propagation constant $\beta(\omega)$ can be express in a Taylor series around ω_0, as

$$\beta(\omega) = n(\omega)\frac{\omega}{c} = \beta_0 + \beta_1(\omega-\omega_0) + \frac{1}{2}\beta_2(\omega-\omega_0)^2 + \frac{1}{6}\beta_3(\omega-\omega_0)^3 + ... \tag{1.18}$$

where $\beta_m = (d^m\beta/d\omega^m)_{\omega=\omega_0}$ is m^{th}-order term. The 1st-order term β_1 is related to the group velocity v_g via

$$\beta_1 = \frac{1}{v_g} = \frac{n_g}{c} = \frac{1}{c}(n(\omega) + \omega\frac{dn(\omega)}{d\omega}) \tag{1.19}$$

The 2nd-order term β_2 is related with the dispersion parameter D_λ as

$$\begin{aligned} \beta_2 &= \frac{1}{c}(2\frac{dn(\omega)}{d\omega} + \omega\frac{d^2n(\omega)}{d\omega} = -\frac{D_\lambda\lambda^2}{2\pi c} \\ D_\lambda &= \frac{d\beta_1}{d\lambda} = -\frac{2\pi c}{\lambda^2}\beta_2 = -\frac{\lambda}{c}\frac{d^2n(\lambda)}{d\lambda^2} \end{aligned} \tag{1.20}$$

The dimension of D_λ is [ps][nm]$^{-1}$[km]$^{-1}$. If $\beta_2 > 0$ ($D_\lambda < 0$), it is called "positive GVD" and the optical pulse has frequency up-chirp. If $\beta_2 < 0$ ($D_\lambda > 0$), it is called "negative GVD" and the

pulse has frequency down-chirp. In the community of integrated photonics and microcombs, people often speak of "normal GVD" and "anomalous GVD" instead of positive GVD and negative GVD. It might be confusing here because replacing "positive" and "negative" by "normal" and "anomalous" could encourage the erroneous belief that PVD nearly parallels to GVD [42], while in fact there is no necessary connection between them. Nevertheless, in this thesis, it is stipulated that positive GVD and normal GVD are equivalent, and negative GVD and anomalous GVD are equivalent.

In the context of microresonators, dispersion describes the variation of the FSR over frequency. It can be expressed in a Taylor series in analogue to Eq. 1.18 as

$$\omega_\mu = \omega_0 + D_1\mu + \frac{1}{2}D_2\mu^2 + \frac{1}{6}D_3\mu^3 + \frac{1}{24}D_4\mu^4 + ... \tag{1.21}$$

Here μ is the mode index relative to the reference resonance ω_0 (the pump mode in the case of microcomb). $D_1/2\pi$ corresponds to the FSR. $D_2/2\pi$ is the microresonator GVD, and D_3 and D_4 are higher-order dispersion term. Specifically, D_2 and D_3 are related to the GVD parameters β_2 and β_3 via

$$\begin{aligned} D_2 &= -\frac{c}{n}D_1^2\beta_2 \\ D_3 &= -\frac{c}{n}D_1^3\beta_3 + 3\frac{c^2}{n^2}D_1^3\beta_2^2 \approx -\frac{c}{n}D_1^3\beta_3 \end{aligned} \tag{1.22}$$

A non-zero D_2 leads to a parabolic deviation from an equidistant D_1-spaced resonance grid. The positive D_2 corresponds to the anomalous GVD, while the negative D_2 corresponds to the normal GVD. However, such parabolic deviation due to D_2 can be modified by the higher-order dispersion such as D_3 and D_4. To include the total deviation given by D_2 and all higher-order dispersion terms, the integrated dispersion D_{int} is defined as

$$\begin{aligned} D_{\text{int}} &= \omega_\mu - \omega_0 - D_1\mu \\ &= \frac{1}{2}D_2\mu^2 + \frac{1}{6}D_3\mu^3 + \frac{1}{24}D_4\mu^4 + ... \end{aligned} \tag{1.23}$$

The microresonator dispersion can be simulated numerically with finite-element method (FEM) using COMSOL Multiphysics, by considering both the material dispersion and geometrical dispersion. For example, for Si_3N_4 waveguide fully cladded in SiO_2, the Si_3N_4 material has normal GVD in the wavelength range of telecommunication bands. if the waveguide core size is comparable to the wavelength, a part of the optical mode leaks into the SiO_2 cladding in the form of evanescent field. This part of the mode sees the SiO_2 cladding index rather than the Si_3N_4 core index. Therefore the effective refractive index n_{eff} is between the Si_3N_4 index and SiO_2 index, as shown in Fig.1.5. The actual value of n_{eff} is determined by the waveguide shape and the optical wavelength, thus can be controlled during waveguide fabrication process. Engineering the effective index n_{eff} of the optical mode and subsequently tailoring the GVD via waveguide geometry control is called "geometry dispersion engineering". Fig.1.7 shows an

example for a Si_3N_4 microresonator with 1 THz FSR and a fixed waveguide height of 870 nm. As not only the D_2 but also the D_3 and D_4 terms change with the varying waveguide width, the broadband D_{int} profile can be lithographically controlled.

In the presence of higher-order dispersion, the spectrum and the pulse shape of the soliton can change, leading to the dispersive wave emission in the normal dispersion window [120, 121, 86]. The coherence is fully maintained with the dispersive wave. Figure 1.6, cited from ref. [86], shows that the dispersive wave generation enables the extension of the soliton spectrum bandwidth to 2/3 octave and power enhancement at the dispersive wave mode, both of which facilitate the 2f-3f self-referencing [122]. Figure 1.6(c) shows the measured microresonator dispersion using the frequency-comb-assisted spectroscopy using cascaded diode laser [119], a method developed in this thesis and will be illustrated later. Based on the frequency measurement of each microresonator resonance, the fitted dispersion parameters

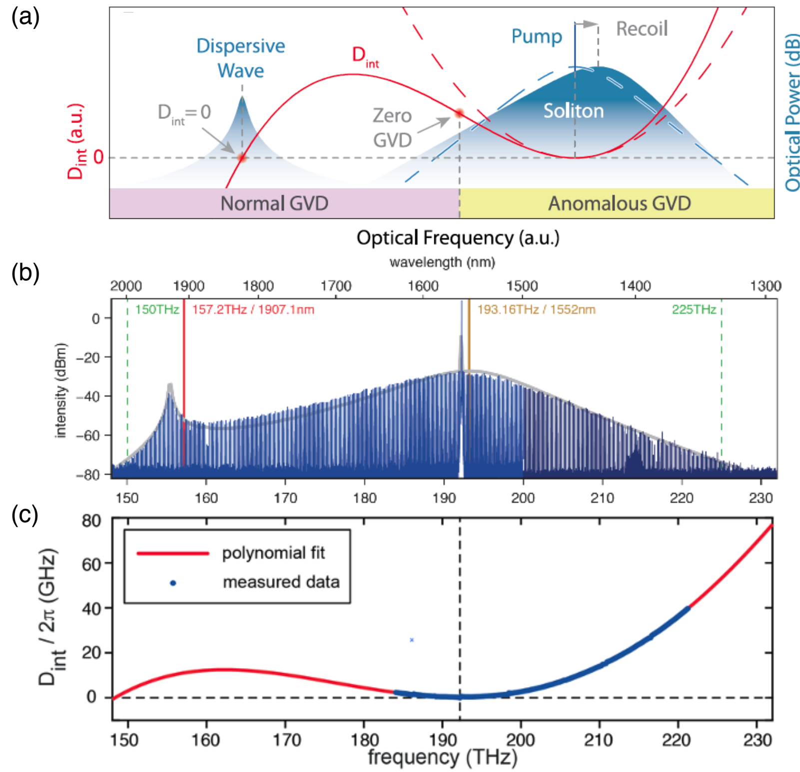

Figure 1.6 – Spectrum of the single soliton state featuring a dispersive wave generated in a dispersion-engineered, integrated Si_3N_4 microresonator of 200 GHz FSR. (a) Schematic showing the dispersive wave generation in the spectral position where the integrated dispersion $D_{\text{int}}(\mu_{\text{DW}}) = 0$. The main soliton envelope may experience a frequency shift (soliton recoil) due to the dispersive wave generation. (b) Single soliton spectrum featuring a dispersive wave and 2/3-octave spectral bandwidth, in an integrated Si_3N_4 microresonator of 200 GHz FSR. (c) Measured microresonator dispersion using the frequency-comb-assisted spectroscopy using cascaded diode laser, illustrated in ref. [119]. Panel (a, b) are taken from ref. [86].

are $D_2/2\pi = 2.55$ MHz, $D_3/2\pi = 22.6$ kHz, and $D_4/2\pi = -173$ Hz. Via extending the dispersion profile using the fitted dispersion parameter, a spectrum position where $D_{\text{int}} = 0$ is found, in agreement with the soliton spectrum. Via engineering the higher-order dispersion of integrated microresonators, it is possible to generate two zero dispersion points on the D_{int} profiles (with a negative D_4), thus a soliton spectrum featuring two dispersive waves. The generation of dispersive waves can efficiently extend the soliton spectrum bandwidth to an octave [99, 89, 60, 123], which could allow the implementation of self-referencing to fully stabilize the soliton microcomb [124, 125, 126, 122].

In a broad sense, dispersion engineering can also be realized by combining different cladding materials [85, 127]. In addition, in microresonator of large FSR (i.e. small radii), ring shape is often used, which form the standard WGM microresonator. The strong waveguide bending not only causes bending loss, but also builds a WGM potential which introduces normal GVD. This normal GVD comes from the fact that the mode of higher optical frequency is pushed more towards to the outer boundary of the microresonator. This leads to the result that the higher-frequency mode propagates slower than low-frequencies, manifesting an effective normal GVD. The smaller the WGM radius is, the stronger the normal GVD is.

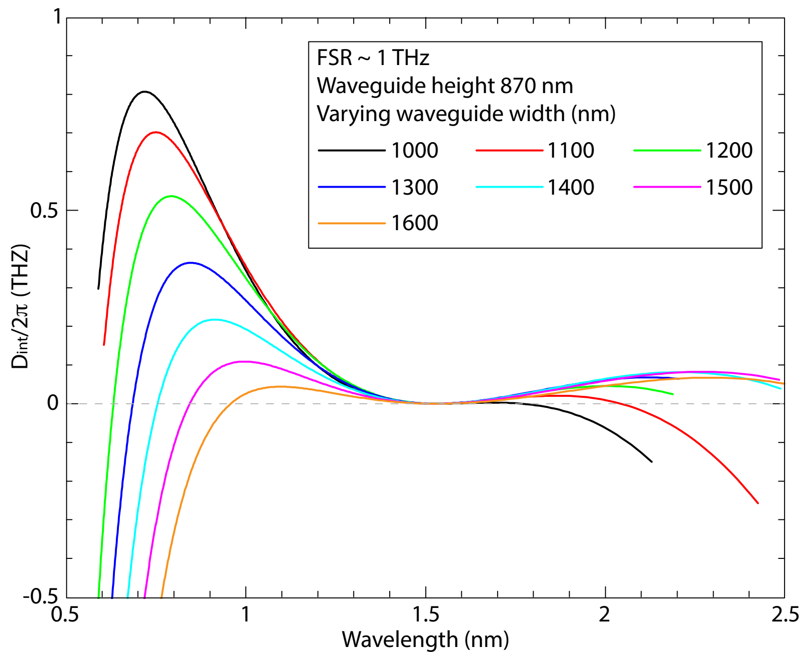

Figure 1.7 – An example showing that the engineering of the dispersion D_{int} profile by varying the waveguide width.

1.6 Application of soliton microcombs

So far, soliton microcombs have already been used in several system-level demonstrations, such as coherent telecommunications [128], ultrafast ranging [129, 130], astronomical spectrograph calibration [131, 132], photonic microwave synthesis [81, 78], dual-comb spectroscopy [133, 134, 135, 136], coherent LiDAR [137], optical frequency synthesizers [138], miniaturized atomic clocks [139, 140], pulse shaping [50] and optical coherent tomography [141, 142]. Some results achieved within this PhD thesis have contributed directly or indirectly to several applications, as shown in Fig.1.8. In the following, a brief introduction on few selected applications is given. The photonic microwave synthesis using soliton microcomb will be illustrated in more details in Chapter 6.

Coherent telecommunication [144, 128, 145]: Typical telecommunication channels are spaced by more than 10 GHz. For high capacity telecommunication, these repetition rates are ideally multiplies of 12.5 GHz, such as 25, 50 and 100 GHz. Therefore, due to the inherent large repeti-

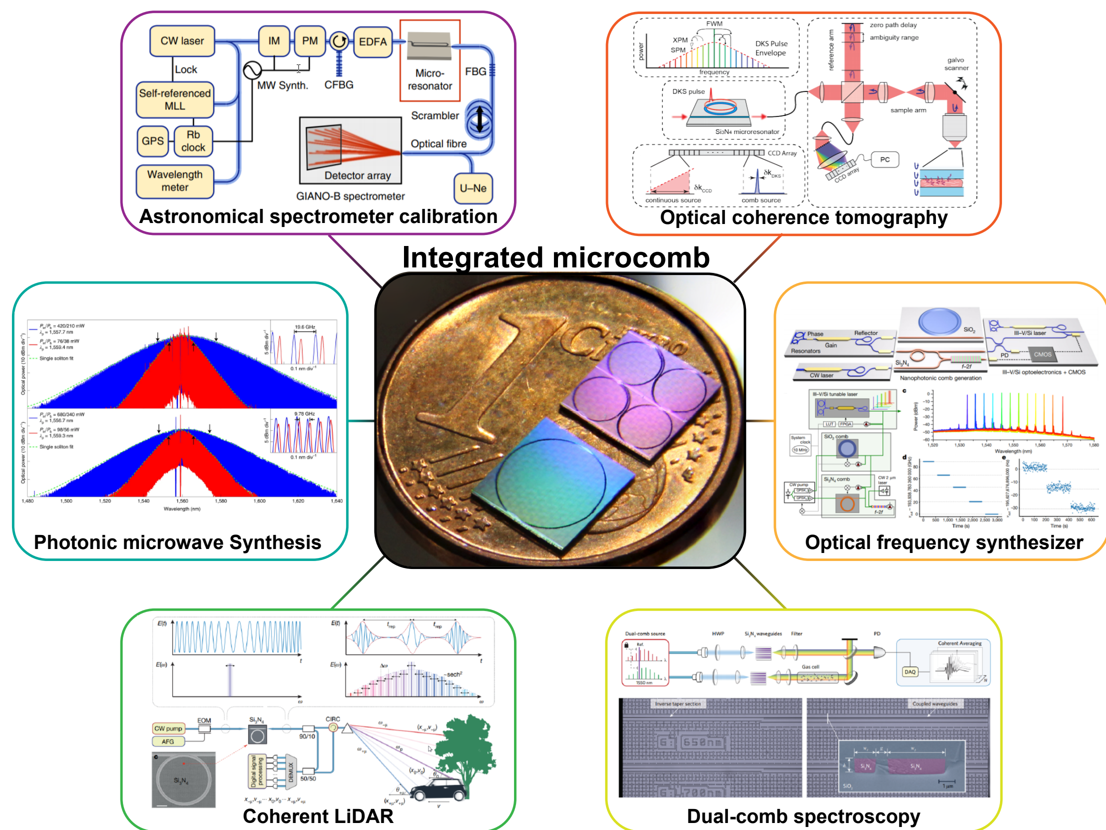

Figure 1.8 – Selected system-level demonstrations using soliton microcombs, which some results within this PhD thesis have contributed directly or indirectly to. Panel images are taken from: ref. [78] (photonic microwave synthesis), ref. [131] (astronomical spectrograph calibration), ref. [142] (optical coherence tomography), ref. [137] (coherent LiDAR), ref. [143] (dual-comb spectroscopy), ref. [138] (optical frequency synthesizers).

tion rates, soliton microcombs could be a useful element of massively parallel wavelength-division multiplexing (WDM). The soliton scheme only employs a single c.w. pump laser to generate simultaneously hundreds of well-defined narrowband optical channels for massively parallel WDM, while in the conventional scheme this requires equal number of individual lasers. Thus the soliton scheme overcomes the scalability limitations, and can be employed at both the transmitter and the receiver ends. Compared with the chaotic microcombs [144], higher transmission rates can be achieved with coherent soliton combs due to the lower carrier noise levels and the more uniform comb powers over a broadband spectral range. In the work reported by P. Marin-Palomo *et al.* [128], ninety-four carriers spanning over the entire telecommunication C and L bands from a Si_3N_4 soliton microcomb of 100 GHz line spacing were used to transmit data. Using 16-state quadrature amplitude modulation (16QAM) to encode data on each line at a symbol rate of 40 GBaud, an aggregate line rate of 30.1 Tbit per second was achieved. By interleaving two soliton microcombs from two different devices, the number of usable carriers was further doubled, and enabled the data transmission with a total of 179 carriers and an aggregate line rate of 55.0 Tbit per second over a 75 km span of fibres. Moreover, the soliton comb also allows coherent detection as a multi-wavelength local oscillator (LO) at the receiver end. The LO comb is coarsely synchronized to the transmitter comb, and digital signal processing is used to account for remaining frequency differences. These works show the potential of solitons microcombs that might replace the arrays of c.w. lasers currently used in high-speed telecommunication systems.

For telecommunication systems, the *spectral efficiency* is a key figure of merit. As the amplifier bandwidths of EDFA is finite, making full use of this limited bandwidth to maximize the spectral efficiency becomes a key concern. In the work by P. Marin-Palomo *et al.*, the transmission capacity is restricted by the large comb line spacing (100 GHz), leading to exploited bands between neighbouring channels and thus a low spectral efficiency (2.8 bit s^{-1} Hz^{-1}). The interleaving of two (nearly) identical soliton microcombs is to reduce the comb line spacing by a factor of 2, thus to increase the spectral efficiency. A simpler scheme is to use a soliton microcomb with a smaller line spacing. In the work reported by M. Mazur *et al.* [145], a soliton microcomb of 22.1 GHz line spacing based on a fully packaged SiO_2 microdisk

Astronomical spectrograph calibration [131, 132]: The universe is expanding and planets are moving. This movement causes Doppler frequency shifts in the light emitted from the studied planet to our earth. Therefore, analyzing the Doppler shifts in stellar spectra enables the discovery of planets, and possibly the elements of their atmosphere. To calibrate the astronomical spectrograph, a frequency combs of line spacing much larger than the frequency resolution of the spectrograph is needed. The typical comb line spacing ideal for this purpose lies in 10–30 GHz range, such that these comb lines are resolvable by the astronomical spectrometer. While generating frequency combs with such large spacing using mode-locked lasers is possible but challenging (by filtering some comb lines to increase the line spacing) [146, 147], microcomb has the unique advantage due to the inherent large microresonator FSR. In addition, the comb generation can be achieved with only one c.w. laser and the comb spectrum shape can be engineered by carefully designing the microresonator. Thus the entire

scheme using a microcomb is much simpler than using a mode-locked laser.

In the work reported by E. Obrzud *et al.* [131], a Si_3N_4 soliton microcomb of 23.7 GHz repetition rate was used to calibrate the GIANO-B high-resolution near-infrared spectrometer at the Telecopio Nazionale Galileo (TNG) on La Palma, Spain. GIANO-B is a cross dispersing echelle-type spectrometer which projects the near-infrared spectrum from 0.9–2.4 μm onto a 2D detector array of 2048×2048 pixels. The Si_3N_4 microresonator was driven by a picosecond coherent optical pulse [71] with the repetition rate (11.85 GHz) as the half of the generated soliton's (23.7 GHz). This sub-harmonic synchronization driving forces the deterministic generation of the single soliton state. The soliton is stabilized as the repetition rate of the driving pulse is stabilized to a microwave reference, and the c.w. pump is stabilized to an optical frequency standard. The wavelength calibration is to provide an accurate and precise pixel-to-wavelength mapping of the GIANO-B spectrometer. The calibration of the echelle spectrum reveals a global spectrometer drift of 3.24 ± 0.23 MHz, corresponding to a radial velocity equivalent precision of 25 cm s^{-1}, significantly exceeding the precision and accuracy of using conventional calibration using hollow cathode lamps such as uranium-neon (U-Ne). (Note: part of the results within this PhD thesis has contributed to this work.)

In a parallel work, M.-G. Suh *et al.* [132] reported in situ astronomical spectrometer calibration using a SiO_2 soliton microcomb of 22.1 GHz repetition rate, in order to measure the periodic Doppler shift induced by the radial velocity shift of orbiting planet.

Dual-comb spectroscopy [133, 134, 135, 136]: Soliton microcombs can also be used for dual-comb spectroscopy built on two solitons microcombs of slightly different repetition rates which are generated in two different microresonators by two different lasers which are mutually phase-locked to each other. Upon photodetection of the periodically time-varying interferogram created by these two soliton streams, the slight difference in repetition rates maps the comb line grid in the optical domain to the RF line grid in microwave domain, facilitating the acquisition and processing the optical absorption features electronically. In the work reported by M.-G. Suh *et al.* [133], two SiO_2 soliton microcombs with 2.6 MHz difference in their repetition rates (22 GHz) were used. By combining the two soliton pulse streams and separating the signal into two branches, one can use the measurement branch to detect the molecular absorption features and the reference branch to calibrate the measurement branch, to extract the spectroscopy information from the RF spectrum. Such microresonator-based dual comb spectroscopy can also be applied in the mid-infrared regime, provided by the silicon microresonators used, as reported in ref. [134, 135]. In addition, the scheme of microresonator-based dual comb spectroscopy can also be simplified to use only one microresonator, which allows the coexistence and mutual locking of counter-propagation solitons [148, 149, 136]. This scheme has a unique advantage that, as the two combs are generated in the same microresonator and experience the same system drift and fluctuation, the mutual coherence between the two combs are significantly extended, enabling higher spectrum resolution. Moreover, by exploiting the multi-mode nature of optical microresonators, solitons in several spatial modes can be co-generated using the spatial multiplexing scheme [150].

Optical frequency synthesizer [138]: As mentioned early, for a frequency comb, once the two comb parameters f_{rep} and f_{ceo} are locked to microwave standards, the optical frequency of each comb line is unambiguously known. This microwave-to-optical link, i.e. translate the known frequency and frequency stability of microwave standards into the optical domain, is optical frequency synthesis. Though optical frequency synthesizers based on mode-locked laser have been demonstrated [151], microcomb-based frequency synthesizers have not been demonstrated. The key challenging here is to fully stabilize the microcomb to microwave standards, which requires: (1) detectable soliton repetition rate f_{rep}, e.g. below 30 GHz, and (2) octave spanning bandwidth to allow the detection of f_{ceo} (f_{ceo} should be also detectable). In the work reported by D. T. Spencer *et al.*, an optical synthesizer was demonstrated using a III-V/Si laser and two soliton microcombs. One is a SiO_2 microcomb of a detectable 22 GHz repetition rate, the other is a Si_3N_4 microcomb of 1 THz repetition rate which is beneficial to achieve an octave-spanning bandwidth. Two constrained must be considered in the design of the Si_3N_4 microresonator dispersion [99, 89]: (1) Via engineering the higher-order dispersion terms D_3 and D_4, two dispersive waves need to be generated around 1 μm and 2 μm wavelengths, which mark the octave-spanning bandwidth. The higher power of the dispersive wave modes than other normal comb lines are beneficial to implement frequency doubling and self-referencing. (2) The expected detected f_{ceo} via self-referencing must below 20 GHz such that it is electronically detectable with fast photodiode. Once these two design constraints are fulfilled, the Si_3N_4 microcomb still cannot be stabilized as its repetition rate of 1 THz cannot be electronically detected. Therefore, a SiO_2 microcomb of a detectable 22 GHz repetition rate [83] was used to stabilize the repetition rate of the Si_3N_4 microcomb, through an interlocking scheme [60]. The 22 GHz repetition rate of the SiO_2 microcomb was detected and stabilized to the microwave standard (clock). Then, two adjacent comb lines of the Si_3N_4 microcomb were selected, and their beating signals with two SiO_2 comb lines closest to them were measured and stabilized. These two SiO_2 comb lines spanned over 46 repetition rate frequency, as 22 GHz $\times 46 = 1.012$ THz, i.e. the repetition rate of the Si_3N_4 microcomb was stabilized to 46 multiplies of the SiO_2 microcomb. In this way, the 1 THz repetition rate of the Si_3N_4 microcomb was stabilized. As long as the Si_3N_4 microcomb was fully stabilized, the SiO_2 microcomb was also stabilized through the microcomb interlocking.

A tunable, narrow linewidth ring-resonator laser consisting of InGaAsP multiple-quantum-well epitaxial material wafer-bonded onto a lithographically patterned silicon-on-insulator wafer was locked to the stabilized SiO_2 microcomb. Via controlling and stabilizing the beat frequency between the tunable laser and the nearby comb line of the SiO_2 microcomb, the laser output frequency was unambiguously determined. An out-of-loop characterization using a self-referenced, fully stabilized erbium-fibre laser frequency comb was implemented to explore the coherence and stability of the optical frequency synthesizer. The measured frequency synthesis uncertainty is 7.7×10^{-15}.

The current work of D. T. Spencer *et al.* has used other non-integrated components such as multiple fibre lasers, fibre amplifiers and bulk modulators. For further full integration on a single chip, targeted improvements should be made to increase microresonator Q for

lower-power operation, to improve the intensity of dispersive waves in the Si_3N_4 microcomb for self-referencing, and to improve the efficiency of chip-based second-harmonic generation.

Miniaturized atomic clock [139, 152, 140]: In a similar concept to the optical frequency synthesizer, the combination of integrated laser and interlocking soliton microcombs has also been employed to demonstrate an architecture of integrated optical atomic clocks. Previous report by S. Papp *et al.* [139] demonstrated a soliton-microcomb-based frequency division linking an optical frequency reference to a microwave output. A SiO_2 microcomb of 33 GHz line spacing centred in the 1550 nm telecommunication band was generated, amplified and spectrally broadened. Two selected comb lines spanning over 108 modes were locked to rubidium (Rb) frequency references (780 nm and 795 nm) separated by 3.5 THz, via two-photon atomic transition. The output optical clock is a 33 GHz microwave signal which inherits the optical frequency uncertainty of the Rb transitions but by a reduction factor of 108. Self-referencing and fully stabilizing the microcomb can further enhance the frequency stability.

When witnessing the fast development of chip-scale frequency combs, one should not overlook the rising of chip-scale atomic devices [153] as the other half of an optical clock. Combining both, building atomic references for timing and metrology on chip becomes feasible. Nowadays, the most widely used, portable frequency reference is the temperature-compensated quartz-crystal oscillators, which consume tens of milliwatts of power and have a fractional frequency uncertainty of 10^{-9} to 10^{-7} at 1 s integration time. Their long-term instability and performance degradation make them inadequate for applications such as global positioning systems (GPS), where atomic clocks with much better stability play the key role (for example, hydrogen maser has a fractional frequency uncertainty of $1\times10^{-12}/\sqrt{\tau}$, where $\sqrt{\tau}$ is the integration time). A main goal is to vastly reduce the size and power consumption of an atomic clock such that portable, battery-driven atomic clocks become possible. In the early work reported by S. Knappe *et al.* [154], a chip-scale atomic frequency standard based on the microwave transitions between the hyperfine ground-states of Cs atoms was demonstrated using MEMS microfabrication techniques (silicon micromachining) that may allow large-scale manufacturing at foundry levels. The Cs vapour cell [155] was fabricated using **anodic bonding** of borosilicate glass and silicon. With heating and electric field, oxide atoms diffuse into silicon and form Si/SiO_2 interface. Metallic Cs and buffer gases were sealed in the cell by reacting a mixture of BaN_6 and CsCl. Heating the cell can increase the Cs vapour density. Conventional microwave excitation of these alkaline atoms poses a size limitation to few centimetre scale due to the fact that the microwave cavity cannot be smaller than the microwave wavelength used. To further reduce the size of alkaline vapour cell down to millimetre scale, optical excitation is preferred. A vertical-cavity surface emitting laser (VCSEL) was used and its current was modulated with 4.6 GHz RF signal. Therefore the two generated sidebands have 9.2 GHz frequency difference, equal to the Cs hyperfine ground-state splitting. These two sidebands were used to implement **coherent population trapping** [156] with the two hyperfine ground-states and the excited state for Cs D_2 transition at 852 nm. When the modulation frequency was tuned to the value precisely corresponding to the ground-state's

hyperfine splitting, a dark line resonance (i.e. the "dark state") was observed due to CPT as the Cs vapour became transparent to the laser light. This dark resonance can be used to lock the laser to the CPT optical transition and the modulation frequency to ground-state's hyperfine splitting. Also, the VCSEL laser only consumed 5 mW power to implement CPT.

Integrating this vapour cell on photonic integrated waveguides allows to directly stabilize chip-scale lasers to the atomic reference via optical transition. In the work reported by M. T. Hummon *et al.* [152], a photonic chip device interfacing fibre input / output, fully cladded single-mode Si_3N_4 waveguides and atomic vapour cell was demonstrated, and an external laser locked to the Rb atomic optical transition via precision spectroscopy was implemented. The chip device containing the Si_3N_4 waveguides and atomic vapour cell was only 27 mm^3 in volume. A distributed Bragg reflector (DBR) laser with the emission wavelength of 780 nm and a fibre output was used. Light coupled into the Si_3N_4 waveguides on chip was expanded and coupled to a free space mode of 120 μm mode diameter using an extreme mode-converting apodized grating structure [157]. Optical heating of the Rb dispenser generated Rb vapour in the cell chamber. When the DBR laser was stabilized to the vapour cell, the laser fluctuation is reduced to less than 10 kHz at an integration time longer than 1 s. The fractional frequency uncertainty at 780 nm was measured as 10^{-11} with the integration time from 10 to 10^4 s.

In a similar manner of using photonic chip devices and microfabricated atomic vapour cell, in the parallel work reported by Z. L. Newman *et al.* [140], the interlocking, fully referenced microcombs were used to synthesize microwave signals via optical frequency division. When the interlocking microcomb system is self-referenced, it lacks the frequency tunability. Therefore the key here is to link the interlocking microcomb system to the Rb optical transition. This was realized by using a helping c.w. laser of 778 nm output, which was locked to a two-photon Rb transition ($5S_{1/2}(F=2)$ to $5D_{5/2}(F=4)$) of a microfabricated Rb vapour cell [154]. The pumps and selected modes of the interlocking microcomb systems, after amplification and frequency doubling, were further locked to this helping laser. Via this helping laser, the interlocking microcombs were phase-stabilized to the Rb two-photon atomic transition. In the end, the 22 GHz microwave output via optical frequency division shows a fractional frequency uncertainty of 10^{-13}.

Massively Parallel coherent LiDAR [137]: Coherent ranging, also known as "frequency-modulated continuous-wave (FMCW) laser-based light detection and ranging (LiDAR)", has seen advances particularly in the development of autonomous driving. Different from the time-of-flight LiDAR which measures the relative distance based on the time delay of the light reflected from the object, FMCW LiDAR employing linearly chirped c.w. laser allows simultaneous measurement of the relative distance and velocity from the reflected light via the delayed homodyne detection. The beatnote signal between the output light and reflected light provides the distance information of the moving object via the signal delay, and the velocity information based on the Doppler frequency shift. To increase the data acquisition speed and ranging precision, using multiple c.w. lasers to enable parallel FMCW LiDAR is a feasible scheme. In this case, frequency comb can be useful to realize massively parallel FMCW LiDAR, with

each comb line serving as a c.w. channel. Large mode line spacing (e.g. more than 50 GHz) is desired as: (1) Each comb line can be separated by WDM and spatially dispersed. (2) Several gigahertz frequency excursion of each comb line can be implemented without introducing intra-channel cross-talk. (3) The RF spectrum generated by WDM and dispersed over the delayed homodyne detection shows only the beatnote signal in the same channel. Parallel FMCW LiDAR has been reported by N. Kuse *et al.* [158] using electro-optic (EO) frequency combs. In this work, coherently stitched of all comb channel was implemented to create an equivalent large frequency scan range which is proportional to the number of the stitched comb modes (three in that work). In a parallel work, J. Riemensberger *et al.* [137] reported a massively parallel FMCW LiDAR using a Si_3N_4 soliton microcomb. By chirping the pump laser's frequency within the soliton existence range, all the comb lines inherit the frequency chirping synchronously. The frequency excursion range of few gigahertz is determined by the soliton existence range, within which the modulating of the pump frequency does not annihilate the soliton state. However, the frequency chirping transduced from the pump mode to other comb lines has compromised chirp linearity due to change in the soliton repetition rate. This change is caused by the Raman self-frequency shift [87, 159] which is detuning-dependent. Nevertheless, with the soliton microcomb, 30 distinct channels with nearly 2 GHz frequency excursion range have been used to successfully demonstrate both parallel distance and velocity measurements. (Note: part of the results within this PhD thesis has contributed this work.)

Pulse shaping [50, 160, 161]: The objective of pulse shaping, or "optical arbitrary waveform generation" (OWAG) [160], is to modulate multiple comb lines of a frequency comb in parallel. Each comb line is applied with a specific phase and amplitude, in order to generate a particular optical waveform with both controllable ultrafast time structure and long-term coherence. Frequency combs based on mode-locked lasers typically have comb line spacing less than 1 GHz, which poses challenges to spectrally resolve these comb lines by the programmable pulse shaper based on spatial light modulators [162]. Therefore, for line-by-line shaping, a comb repetition rate of several gigahertz or higher is required.

In the work reported by Z. Jiang *et al.* [160], programmable line-by-line shaping of more than 100 spectral lines was demonstrated with an EO comb in order to achieve 5 GHz line spacing. Microcombs with inherently large line spacing are intrinsically beneficial for this purpose. In addition, dispersion-engineered microcombs can have broad bandwidth, thus are highly desirable as more comb lines provide more degrees of freedom for OWAG. In the work reported later by F. Ferdous *et al.* [50], line-by-line pulse shaping was demonstrated using a Si_3N_4 microcomb of ~ 600 GHz FSR. The line-by-line pulse shaping and the time-domain characterization of the microcomb optical waveform revealed distinct coherence properties resulted from the comb formation dynamics [43]. This technique allows to generate particular pulse shapes other than $sech^2$ shape for bright solitons, for example, "odd pulse" that is asymmetric in time [163].

2 Fabrication of Ultralow-Loss Si_3N_4 Integrated Waveguides

This chapter focuses on the technological advancements of Si_3N_4 photonic integrated circuits featuring ultralow optical loss, tight optical confinement, and anomalous GVD, with the main focus on the fabrication process. High-Q microring resonators using this Si_3N_4 waveguides are the central element for integrated soliton microcomb generation. The ultralow waveguide losses and high microresonator Q factors greatly facilitate the soliton formation, with an ultralow power level that can be met by state-of-art integrated III-V/Si lasers.

This chapter starts with a brief review of the past and current key works on integrated soliton microcombs built with Si_3N_4 integrated waveguides. Then, a brief introduction of Si_3N_4 photonic integrated circuits will be given, highlighting the optical properties of Si_3N_4 and its applications in integrated photonics other than nonlinear optics. Afterwards, the readers can find a detailed description of our nano-fabrication process of Si_3N_4 photonic integrated circuits featuring ultralow optical loss, tight optical confinement, and anomalous GVD. This fabrication process, the "photonic Damascene process", has been developed at EPFL since 2015 and yielded a number of results in terms of soliton generation and applications. However only very recently, within the framework of this PhD thesis, the Damascene process has achieved ultralow propagation loss near 1 dB/m, enabling soliton microcomb generation with a power level affordable by III-V/Si lasers, which offers the prospect to build fully integrated soliton microcomb devices with all-integrated components and technology. In fact, the main achievements of this PhD thesis are based on the development and optimization of the photonic Damascene process. Several person have contributed to this process development, including Rui Ning Wang, Michael Zervas, Tiago Morais and Bahareh Ghadiani. Many Si_3N_4 samples used in this thesis were fabricated with the assistance from Rui Ning Wang.

While silicon is the leading material for integrated photonics, Si_3N_4, with a wide transparency window from visible to mid-infrared, has drawn increasing attention as a promising platform for low-loss integrated photonics. Silicon nitride has a large bandgap of 5 eV, which makes it free from two-photon absorption in the telecommunication wavelength band (~ 1550 nm). It has a refractive index of $n = 2$ at 1550 nm, thus allows to build photonic waveguides of strong optical confinement using SiO_2 as cladding material. Silicon nitride is also space-compatible

[164], thus is suitable for space applications on satellites. Meanwhile, amorphous Si_3N_4 has a nonlinear refractive index of $n_2 = 2.5 \times 10^{-19}$ m^2W^{-1}, nearly an order of magnitude higher than value of SiO_2. Though Pockels nonlinearity is largely absent in Si_3N_4 due to the symmetry, the waveguide interface exhibiting symmetry breaking and non-isotropic distribution of the dipoles inside the amorphous matrix endows small Pockels nonlinearity to Si_3N_4, which allows second-order nonlinear effects such as second-harmonic generation (SHG). The presence of coherent photogalvanic effect [165, 166] can further enhance the SHG generation efficiency in all-optical control manner. Recently, the stimulated Brillouin scattering (SBS) gain of Si_3N_4 has been measured, which is almost 1000 times smaller than the gain value in standard single-mode fibre [167]. As SBS usually limits the maximum optical power in waveguides, the ultralow SBS gain of Si_3N_4 endows excellent handling capability of high optical power and intensity. All these features outline that Si_3N_4 is an excellent waveguide material not only for linear optics, but more importantly for nonlinear optics.

A Si_3N_4 photonic integrated circuit has been used for on-chip nonlinear parametric oscillation since its first report on 2009 by J. S Levy *et al* [93]. Parametric FWM processes were demonstrated, and a microcomb spectrum was observed. These demonstrations were not possible prior to this work for two main reasons: (1) Silicon nitride film of 725 nm thickness was successfully grown such offers the freedom to tailor the dispersion property in the anomalous GVD regime. Such a thick Si_3N_4 film can not be grown previously due to the intrinsic high tensile stress introduced during the film growing process using low-temperature chemical vapour deposition (LPCVD). This issue was overcome by A. Gondarenko *et al* using a thermal cycling treatment during the film growth [94]. (2) Via improving the fabrication process, the microresonator Q reached a value of 0.5×10^6 which enables the threshold power of parametric oscillation below 100 mW in the microresonator of 403 GHz FSR.

In a parallel work at the same time, L. Razzari *et al* reported on-chip nonlinear parametric oscillation in a different integrated material – "**Hydex**^{TM}". Hydex is high-index doped silica-glass, which can be grown via standard chemical vapour deposition process of SiO_2. It is to me not clear what the dopant is, but similar process has been demonstrated to grow silicon oxynitride(SiON) [168] in which nitrogen atom serves as the dopant to increase the material refractive index. Hydex has a refractive index of $n = 1.7$, therefore waveguides made of Hydex can also use SiO_2 as the cladding. In fact, the relatively lower refractive index contrast compared to the case of Si_3N_4 reduces the light scattering losses caused by the roughness at the waveguide surface. Meanwhile, the nonlinear refractive index of Hydex is $n_2 = 1.15 \times 10^{-19}$ m^2W^{-1}, about five times larger than that of SiO_2. As a result, a microresonator Q of 1.2×10^6 has been achieved by L. Razzari *et al*, a remarkable value at that time. A microcomb spectrum of 200 GHz line spacing was demonstrated, with a threshold as low as 54 mW.

These two works have made integrated materials, particularly Si_3N_4, as promising platforms for miniaturized optical frequency combs. Since then, many research groups have joined to study microcomb generation using integrated materials and technology, which have resulted in a number of reports and demonstrations on the microcomb formation process and appli-

cations [85, 86, 88, 89, 90, 91, 78, 78, 93, 94, 95, 96, 98, 99, 100, 101]. In the meantime, parallel work were still ongoing in bulk fluoride crystals and silica microdisks. Nevertheless, Si_3N_4 is the *most mature* integrated platform for microcomb generation. Particularly, it is the first platform on which single soliton state has been demonstrated, as reported in V. Brasch *et al* [86]. In this work, a c.w.-driven, dispersion-engineered, integrated Si_3N_4 microresonator of $Q \sim 1 \times 10^6$ and 200 GHz FSR was used to generated dissipative Kerr solitons. The "power kicking" technique [64] was used to access to the single soliton state. In addition, as the microresonator has an engineered dispersion which exhibits a strong third-order dispersion term D_3, a dispersive wave [121, 120] was generated in the longer wavelength side via the soliton-induced Cherenkov radiation, significantly extending the entire soliton spectrum bandwidth. In the presence of a strong D_3 and a weak D_2, the dispersive wave is generated in the spectral position where the linear phase matching condition is satisfied, corresponding to the integrated dispersion $D_{\text{int}}(\mu_{\text{DW}}) = 0$. Due to the dispersive wave generation, the main soliton envelope may experience a frequency shift [87], also called as "soliton recoil", due to the dispersive wave generation. In the presence of a negative D_4, two dispersive waves can be generated at both sides of the soliton spectrum, demonstrated recently in [60, 123]. The coherence is fully maintained with the dispersive wave. The power enhancement at the dispersive wave modes facilitates the f-2f [60] or 2f-3f self-referencing [122].

As integrated waveguides typically have cross-sections comparable to the optical wavelength, the effective mode volume V_{eff} is inherently small, enabling tight optical confinement and enhanced optical intensity. As outlined in the previous chapter, the threshold power P_{th} for soliton formation scales with the microresonator Q factor as $P_{\text{th}} \propto V_{\text{eff}}/Q^2$. Therefore, the microresonator Q factor is absolutely critical for achieving lower P_{th}. Great efforts have been invested into the optimization of the fabrication processes including lithography, etching, and film growth. Nowadays, integrated Si_3N_4 microresonators with Q factor near 10×10^6 have been routinely achieved. In small Si_3N_4 microresonators (FSR exceeding 100 GHz), the soliton formation threshold power has now been reduced to only few milliwatts or even lower. In a recent work reported by B. Stern *et al* [101], a single soliton state was achieved in a fully integrated III-V/Si_3N_4 chip device. A III-V gain chip based on reflective semiconductor optical amplifier (RSOA) [169] was directly butt-coupled to the Si_3N_4 chip containing a microresonator of $Q \sim 8 \times 10^6$ and 194 GHz FSR. With two microring Vernier filters built on the Si_3N_4 chip as the laser cavity, lasing in the III-V gain chip was observed, and the laser wavelength was actively controlled via thermal tuning the Vernier filters. An electric power of 98 mW was used to drive the III-V chip laser. Remarkably, B. Stern *et al* demonstrated the operation of this compact III-V/Si_3N_4 chip device in the single soliton regime powered by AAA batteries. Later, multi-mode laser diodes and DFB lasers have also been used to demonstrate compact soliton microcomb modules via hybrid integration [170, 69, 70].

In the future, the trend might shift towards the fabrication of ultralow-loss Si_3N_4 photonic circuits directly with III-V/Si laser [171, 172, 173, 174], using the mature heterogeneous integration [175, 176] and wafer-bonding technologies [177]. In fact, exploring the possibility to integrated Si_3N_4 photonic circuits with other materials platforms is also a main topic of this

PhD thesis. Via photonic integration, it is possible to build ultracompact microcomb modules, or to realize integrated modulation of microcombs. Figure 2.1 shows several selected works on photonic integration with Si_3N_4 which have been achieved or are still ongoing within the scope of this PhD thesis. The hybrid integration with III-V lasers will be described in Chapter 5. The monolithic integration with aluminium nitride for integrated piezoelectric modulation of soliton microcombs will be illustrated in details in Chapter 7.

2.1 Silicon nitride photonic integrated circuits

Date back to 1980s, silicon-on-insulator (SOI) wafers which had been used to fabricate electronic circuits were proposed to be also used for integrated photonic circuits. Shortly afterwards, silicon ridge waveguides of single mode, low loss and absence of birefringence were demonstrated, together with a series of demonstrations of integrated optical components built on SOI wafers, which made the start of commercializing silicon photonics in the early 1990s [180]. The prospect created by silicon photonics, as the optical analogue of silicon microelectronics, is inspiring [181] – it is a technology combining integration and photonics, offering the capability to process high-data-rate optical signals on small chips that can be manufactured in high volume with low cost.

Since then, with almost three decade effort from both the academic units and industrial players, silicon photonics has evolved into a mature technology with mature solutions for lasers, modulators, photodetectors, wavelength multiplexers and demultiplexers, and filters. Nowadays, silicon photonics has a broader meaning – new materials, which can be grown on

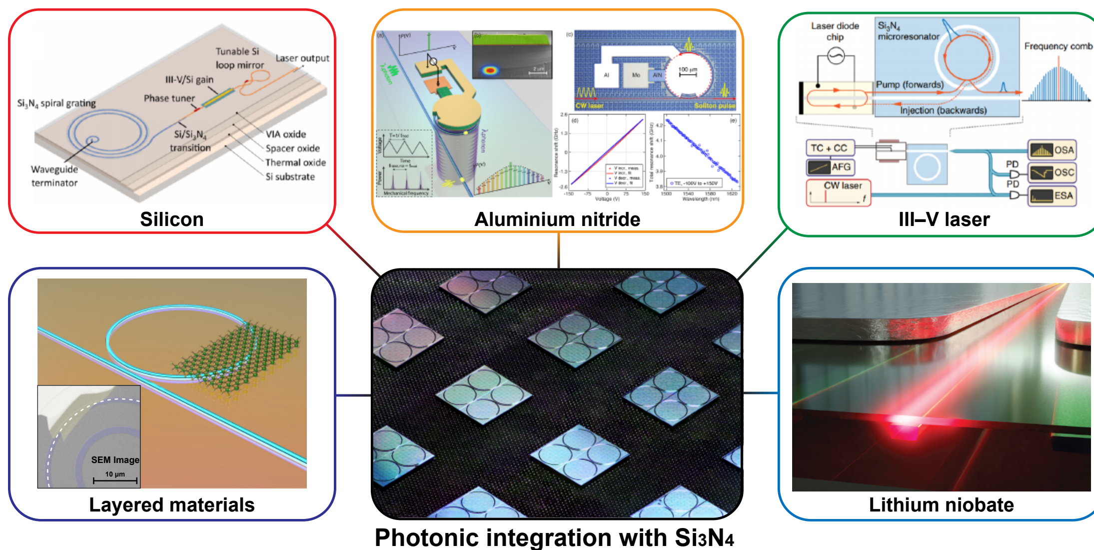

Figure 2.1 – Selected works on photonic integration with Si_3N_4 that have been achieved or are still ongoing within the scope of this PhD thesis. Panel images are taken from: ref. [178] (aluminium nitride), ref. [170] (III-V laser), ref. [179] (lithium niobate), ref. [174] (silicon).

silicon wafers and processed with the techniques to process silicon (more broadly, compatible with CMOS production), are emerging and evolving together. It is however not surprising – note that the Pockels nonlinearity required for high-speed modulators is absent in silicon, and the indirect bandgap of silicon limits the capability to create light source. New materials have been already added into silicon photonics technology, for example, germanium (Ge) is widely used to make Si-Ge photodetector [182], and III-V materials such as indium phosphide (InP) is used to make III-V/Si laser [171]. Therefore, “combining integration and photonics" is no longer the unique feature owned by silicon. **Integrated photonics**, almost the synonym for silicon photonics today, is advancing and creating new possibilities that were not possible before with silicon.

Today, integrated photonics has evolved into a mature technology enabling the synthesis, processing and detection of optical signals on-chip. Currently developed PIC has enabled nearly all needed functionalities via heterogeneous or hybrid integration of different material platforms [183, 184, 185, 176], and is now utilized at a commercial level for telecommunications and datacentres. A second wave is currently under way in which the nonlinearity of PICs becomes relevant for applications, i.e. *integrated nonlinear photonics*. The Kerr, Pockels and Brillouin nonlinearities inherent in these waveguides enable new capability for nonlinear optical signal generation and processing [185, 186, 187, 188].

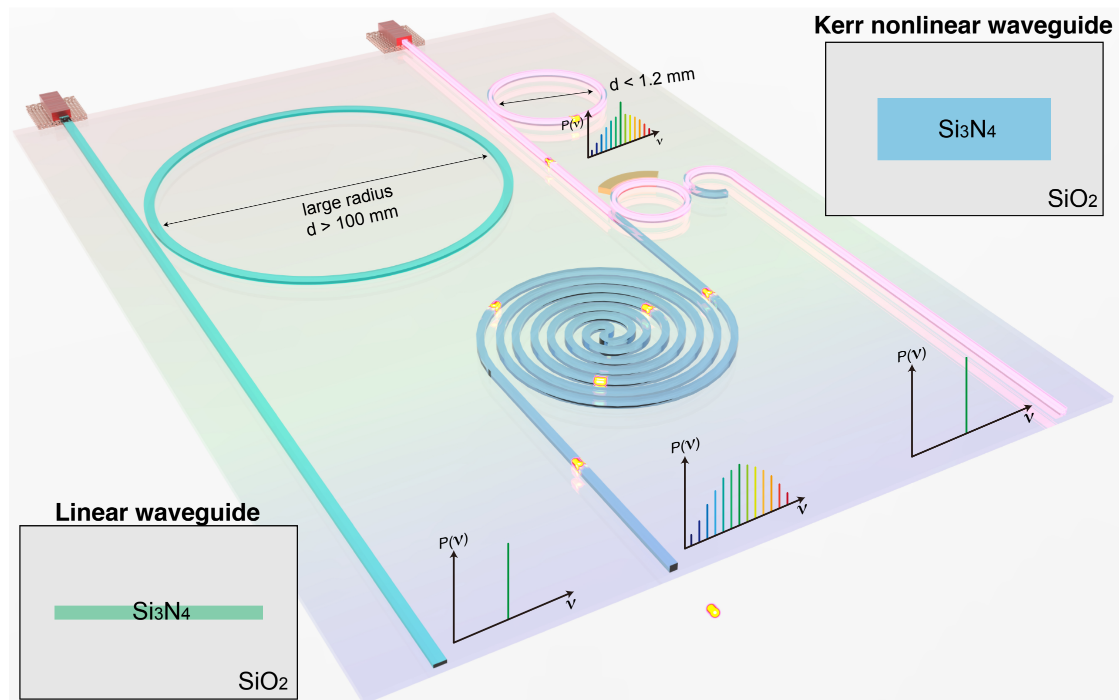

Figure 2.2 – A conceptual chip design of the low-loss Si_3N_4 platform for on-chip tunable filters, true-time optical delay lines, and high-Q nonlinear micro-ring microresonators. Depending on the Si_3N_4 waveguide geometry, the nonlinear processes (mainly Kerr, Pockels and Brillouin nonlinearity) can be harnessed.

Among all materials studied and employed in integrated photonics today, silicon, InP and Si_3N_4 are the three leading platforms. Compared with silicon and InP which are widely used to build active components such as lasers, photodetectors and modulators, Si_3N_4 has limited capability due to its insulator nature. Nevertheless, Si_3N_4 is (most) excellent in optical losses – it has a low linear optical loss due the high film quality grown via chemical vapor deposition (CVD), and a low nonlinear loss as Si_3N_4 has 5 eV bandgap which makes it immune from two-photon absorption (TPA) in the widely used telecommunication wavelength around 1550 nm. The exceptional low losses in Si_3N_4 are currently not achievable in any other materials including silicon and InP. In addition, the refractive index of Si_3N_4 ($n(Si_3N_4) = 2.0$) is lower than the refractive indices of silicon and InP ($n(Si) = 3.5$, $n(InP) = 3.1$). The lower refractive index exhibits lower optical confinement as a con, but it meanwhile reduces the mode mismatch to an optical fibre mode and can facilitate the fibre-chip interface coupling. Yet, Si_3N_4 is all passive, however few active function can still be realized on Si_3N_4 in combination of other materials, thanks to the maturity and versatility of integrated photonics. For example, modulators can be realized on Si_3N_4 with integrated 2D-materials (such as graphene) [189, 190, 191], ferroelectric lead-zirconate-titanate (PZT)[192, 193, 194] and piezoelectric aluminium nitride [115, 116, 178]. Multiple Interface and coupling schemes have been proposed and demonstrated to connect Si_3N_4 photonic circuits with III-V/Si laser [171, 172, 173, 174, 195]

Today, Si_3N_4 has emerged as a leading material for integrated linear [196] and nonlinear [197] photonics due to its low loss and superior power handling capability [167]. Figure 2.2 shows several examples of integrated photonic elements relying on low waveguides losses, including tunable filters, true-time optical delay lines, and high-Q nonlinear micro-ring microresonators. To date, among all integrated platforms [198], optical losses below 1 dB/m have only been demonstrated in two categories of Si_3N_4 waveguides of different height (h): the thin-core ($h < 100$ nm) [199, 200, 201], and the thick-core ($h > 700$ nm) [98, 100, 91, 202, 203]. While at first glance, this distinction seems minor, the waveguide height essentially determines the technical area of applications. The thin-core waveguides feature low optical confinement and low Kerr nonlinearity, ideal for linear photonics, while the thick-core waveguides feature high optical confinement and anomalous group velocity dispersion (GVD), targeted for nonlinear photonics. Figure 2.3(a) highlights the lowest-loss nonlinear (ref. [98, 100] and this work) and linear [199, 200] Si_3N_4 waveguides in terms of their optical losses and effective area of the fundamental optical mode, in comparison with the state-of-the-art, lowest-loss silicon [204, 184], InP [205, 183] and AlGaAs [80] waveguides. The optical losses below 1 dB/m has been achieved in linear and nonlinear Si_3N_4 waveguides respectively, however is still more than three orders of magnitude higher than the loss in optical fibres (~ 0.2 dB/m). Meanwhile, the difference in optical confinement leads to dramatic difference in device sizes, as outlined in Fig. 2.3(b). The bending loss determined by the optical confinement poses a constraint on the minimum device size, as key parameter when considering photonic integration. As shown by the simulated dispersion parameter D_λ and bending loss in Fig. 2.3(c, d), increasing the waveguide height reduces the bending loss and enables the access to the anomalous GVD region ($h > 700$ nm), thus transforming linear Si_3N_4 waveguides to nonlinear waveguides that

require low loss, high optical confinement and anomalous GVD. The nonlinear waveguides featuring low loss, high optical confinement and anomalous GVD are the foundation of microcomb generation in integrated chip devices.

2.1.1 Refractive index of Si_3N_4

As mentioned earlier, engineering the refractive index of Si_3N_4 is key for nonlinear four-wave mixing and microcomb formation. To precisely tailor the dispersion property of Si_3N_4, it requires the precise knowledge of the material refractive index, and the precise control of

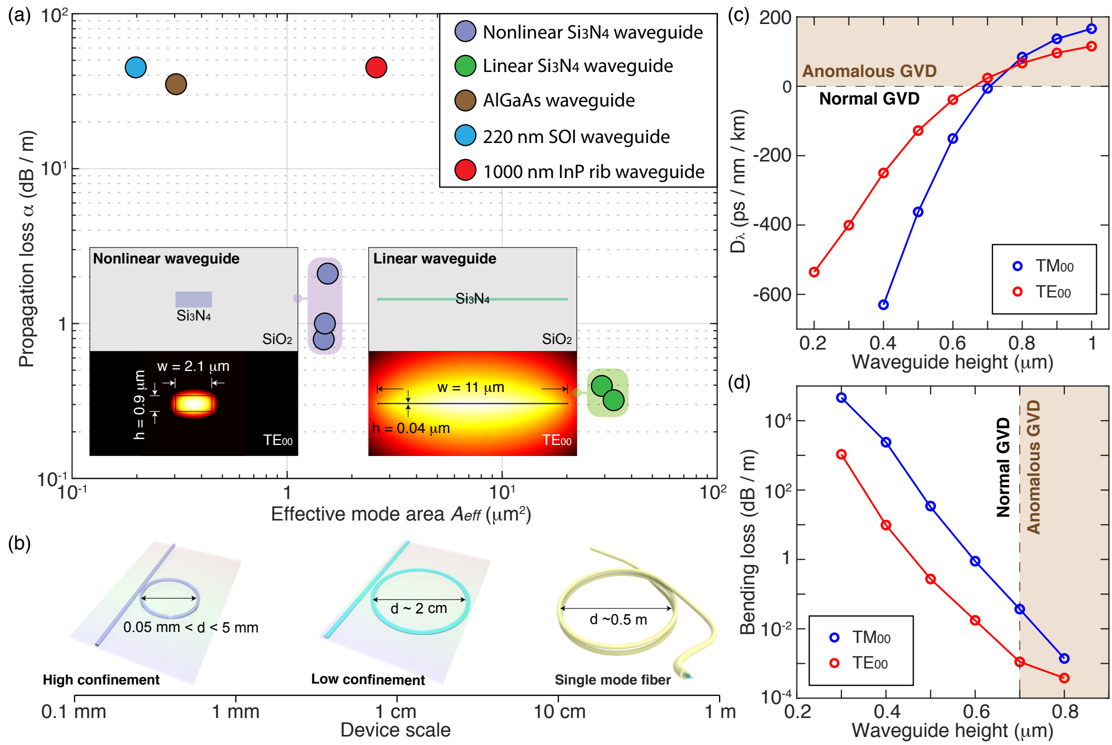

Figure 2.3 – Comparison of ultralow-loss linear and nonlinear Si_3N_4 platforms with single-mode fibres and state-of-the-art silicon, InP and AlGaAs platforms. (a) Comparison of optical losses and effective mode areas (in the telecommunication band of 1550 nm) in state-of-the-art, low-loss waveguides, including nonlinear (ref. [98, 100] and this work) and linear (ref. [199, 200]) Si_3N_4 waveguides, 220 nm silicon-on-insulator (SOI) waveguides [204], 1000 nm InP rib waveguides [205], nonlinear AlGaAs waveguides [80]. The insets show the waveguide geometry and optical mode profile of the Si_3N_4 waveguides. (b) Comparison in device size for linear and nonlinear Si_3N_4 waveguides and single-mode fibres. (c) Simulated GVD parameter D_λ as a function of the waveguide height, with a fixed waveguide width of $w = 2.1$ μm. Anomalous GVD region is brown-shaded, which is accessed with heigh $h > 700$ nm. (c) Simulated bending loss as a function of the waveguide height, with a fixed bending radius of $d/2 = 25$ μm and waveguide width of $w = 2.1$ μm. The brown-shaded region indicates the anomalous GVD region. The wavelength studied here is 1550 nm.

waveguide geometry for geometry dispersion. Here, a brief description on the method to characterize the refractive index of Si_3N_4 is given, as well as the actual refractive index profile of our Si_3N_4 grown at EPFL. The geometry control is mostly related to waveguide fabrication process which will be illustrated later in this chapter.

The refractive index of a thin film can be measured by an **ellipsometry**, which illuminates the wafer with thin films with a broadband, linearly polarized light, and simultaneously measures the reflected light from the thin film which contains the optical response. In comparison to the incident light, the reflected light contains the information of the dielectric properties of the thin films which changes the polarization and phase of the incident light. To extract this information, the material stack in case of multiple films of different materials must be provided. If the refractive indices of each film is known, fitting the measured optical response to the theoretical model containing the material stack allows extraction of the thickness of each film with an accuracy down to sub-nanometre. Vice versa, if the film thickness is known (in the case of only one film), fitting the measured optical response allows extraction of the refractive index of the thin film.

The complex refractive index $\tilde{n}$ of a material consists of the real part n and the imaginary part k, as

$$\tilde{n} = n + ik \tag{2.1}$$

The real part n describes the reduction of the speed of light in the medium compared to the value in vacuum, due to the induced polarization of medium caused by the light field. The imaginary part k describes the attenuation of light in the medium, caused by the material absorption, e.g. molecular rotational or rovibrational transitions in the near-IR or mid-IR, and electronic state excitation in UV. The real and imaginary optical constants are not independent

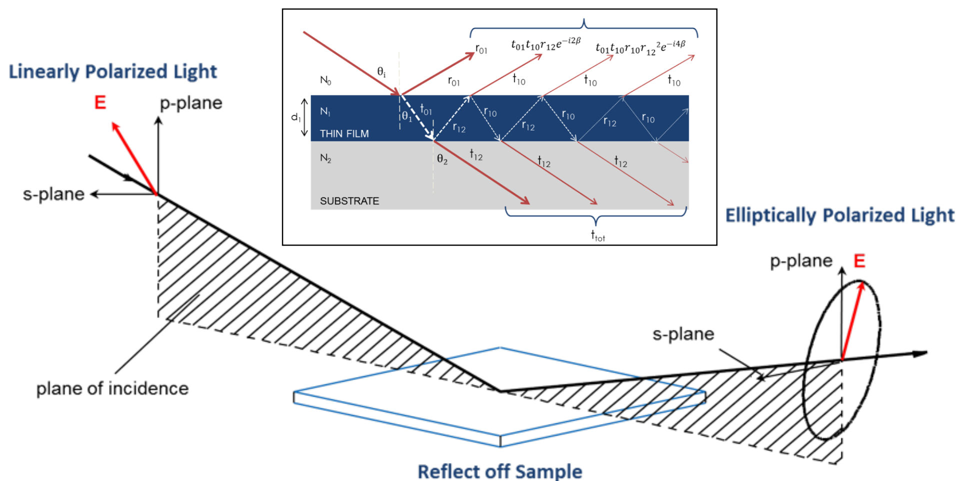

Figure 2.4 – Schematic and principle of the ellipsometry to measure the optical properties and thickness of a thin film. **Figure source**: https://www.jawoollam.com.

– they are mathematically coupled through the **Kramers-Kronig relation**.

When the light is incident to a thin film with an incident angle, the reflected and refracted light follows the Snell's law at the film boundaries (in the case of only one film on silicon substrate, there are only air-film and film-silicon boundaries). In fact, light can experience multiple reflection and refraction between the film boundaries, as illustrated in Fig. 2.4. The total reflected light power is thus determined by multiple beam interference which depends on the refractive indices of the thin film and silicon, wavelength, the thickness of the thin films, and the light incident angle. Therefore, when a broadband or wavelength-sweeping light source is used, a pattern of interference fringes is detected in the reflected light. It is important that the thin film is transparent within the wavelength range. By fitting the interference fringes, the film thickness with a precision to nanometre can be obtained. In addition, as thicker film causes denser interference fringes, there is a maximum measurable film thickness determined by the spectral resolution of the detector, which is typically up to few micrometer.

If the incident light is linearly polarized, i.e. the polarization can be decomposed into s- and p-polarizations in the directions normal to the light incident direction, the reflected light will be polarized differently from the incident linear polarization. An ellipsometry measures primarily the amplitude and phase change of s- and p-polarization components of the reflected light from the thin film. Normally, the light interaction with the medium results in an elliptical polarization of the reflected light, in comparison to the linear polarization of the incident light. This is why ellipsometry gets its name.

As a broadband light source is used, the optical response of the thin film is wavelength-dependent. If a good knowledge of the film thickness is provided (unnecessary to be very accurate) and the optical spectrum of the light source is well calibrated, the complex refractive index at each measured wavelength point can be extrapolated. Figure 2.5 shows the complex refractive index of Si_3N_4 from UV (250 nm) to the mid-IR (30 μm), measured via a commercial service provided by **J. A. Woollam Co.**. In fact, such a measurement over a broad spectrum range requires to use multiple ellipsometries operating at different wavelength ranges. In

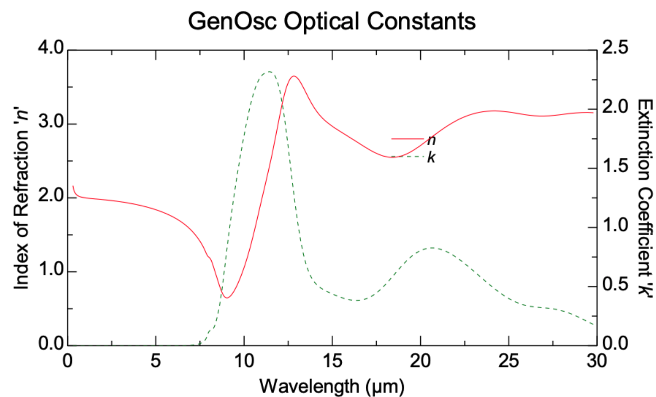

Figure 2.5 – The complex refractive index of Si_3N_4 from UV (250 nm) to the mid-IR (30 μm).

addition, to get the highest precision and accuracy, multiple measurements at the same wavelength are performed, and post-processing of the measurement data and statistical analysis are implemented. This also requires to calibrate the substrate (usually Si) response with the employed ellipsometries for background reference.

With all the measured refractive indices, it is possible to fit the discrete data to obtain a continuous **Sellmeier equation** of the refractive index $\tilde{n}(\lambda) = n(\lambda) + ik(\lambda)$ of the thin film as a function of the wavelength λ. This Sellmeier equation typically has the form as:

$$n^2(\lambda) = 1 + \sum \frac{B_i \lambda^2}{\lambda^2 - C_i} \tag{2.2}$$

The Sellmeier equation distinguishes itself from the **Cauchy equation** by conforming to the Kramers-Kronig relation with the presence of optical absorption peak. For our Si_3N_4 measured by J. A. Woollam Co., the fitted Sellmeier equation within the spectral range from 250 nm to 6 μm is shown in Fig. 2.6, expressed as

$$\begin{aligned} n^2(\lambda) = 1 &+ 1.750893106708352 \frac{\lambda^2}{(\lambda^2 - 0.159333426051559^2)} \\ &+ 1.222742709909494 \frac{\lambda^2}{(\lambda^2 - 0.054765813233156^2)} \\ &+ 2.584602943737831 \frac{\lambda^2}{(\lambda^2 - 11.600661120564506^2)} \end{aligned} \tag{2.3}$$

2.2 Fabrication process overview

The ability to achieve ultralow optical losses in photonic waveguides is the foundation of modern telecommunication networks. The most representative example is the success

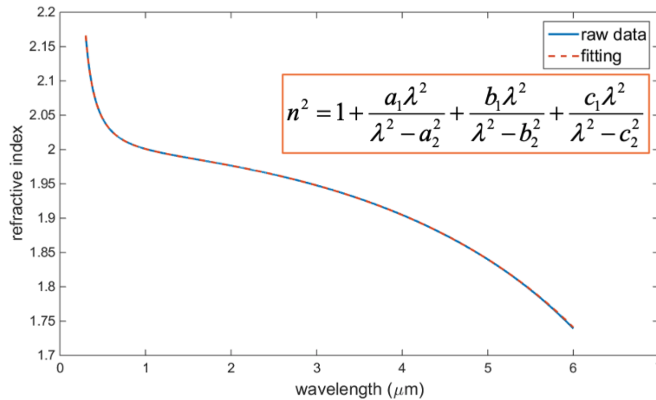

Figure 2.6 – Fitted Sellmeier equation of our Si_3N_4 with respect to the measured data within the spectral range from 250 nm to 6 μm.

of optical fibres used in global communications, which has so-far the lowest optical loss of only 0.2 dB/km. With the rise of photonic integrated circuits, effort has been made to achieve ultralow loss on-chip. It is needed indeed, as ultralow-loss integrated resonant microstructures have already enabled new applications, ranging from narrow-linewidth lasers [206, 174], microwave photonics [185, 186] and nonlinear optics [187, 45] to quantum optics [207, 208]. To date, ultralow-loss optical microresonators are primarily fabricated from silica [82, 209] and crystalline fluoride materials [210, 81]. To translate this technology into applications [211], the capability to achieve similar loss performance with established wafer-scale foundry manufacturing processes [196, 212] is critical. For this purpose, Si_3N_4 is the most mature platform to achieve low loss. Figure 2.7 plots the development of high-Q (low-loss) Si_3N_4 microresonators since 2009, with the continuous efforts from multiple research groups [85, 86, 88, 89, 91, 78, 93, 94, 95, 98, 100, 101, 202]. Today, Si_3N_4 microresonators of Q factors exceeding 10×10^6 has been routinely achieved, and soliton microcombs and Brillouin lasers have been demonstrated at ultralow initiation power [101, 91, 200] with these high-Q microresonators, showing the maturity of Si_3N_4 platforms compared with other integrated platforms.

2.2.1 Fabrication challenges

Currently, the main technological focus is to develop a high-yield, highly reproducible fabrication process of Si_3N_4 photonic integrated circuits. To achieve ultralow optical loss, while simultaneously accessing the anomalous GVD by using thick Si_3N_4 waveguides (height more than 600 nm), there are three outstanding fabrication challenges:

Crack prevention: For nonlinear photonics such as microcomb and supercontinuum generation, anomalous GVD is required. However, Si_3N_4 has as-material normal GVD. Therefore, geometry dispersion engineering to achieve a net anomalous GVD is needed, which typically requires Si_3N_4 waveguide thickness exceeding 600 nm [95, 117]. However, the widely used Si_3N_4 of superior film quality is deposited from low-pressure chemical vapour deposition (LPCVD) based on SiH_2Cl_2 and NH_3. The LPCVD Si_3N_4 film shows high tensile stress, typically between 1.0 GPa to 1.3 GPa, therefore often generates crack when depositing the film over 500 nm thickness, resulting in low fabrication yield. This tensile stress of LPCVD Si_3N_4 film comes from two processes. The first process is the thermal-chemical kinetics of SiH_2Cl_2 and NH_3 reaction on the substrate surface. The Si-N bonds are generated by combining Si-H and N-H bonds and eliminating H_2, and are much stronger than Si-H and N-H bonds, resulting in strained Si-N bond and a tensile Si_3N_4 film globally. This process creates an as-grown internal stress. The second process is the cooling process from the deposition temperature ($> 750°C$) to the room temperature, while the difference in thermal expansion coefficients between the Si_3N_4 film and SiO_2 substrate / cladding creates the thermal-expansion-induced stress.

Reducing the light propagation loss in Si_3N_4 waveguides: Integrated optical microresonators built on Si_3N_4 waveguides can significantly benefit from their low losses, in order to achieve

high optical Q factor for nonlinear parametric processes. The optical losses in Si_3N_4 waveguides come from two main parts: The waveguide sidewall roughness causing Rayleigh scattering losses [213, 214], and the hydrogen absorption losses due to the residual Si-H and N-H bonds in Si_3N_4 [215, 216, 217, 201]. The hydrogen absorption losses can be efficiently eliminated via multiple cycles Si_3N_4 deposition and thermal annealing [218], which has been experimentally verified in ref. [91]. Therefore, extensive study have been focus on describing waveguide sidewall roughness [219, 220, 221], and reducing roughness via optimized dry etching [100, 222, 223, 224], wet etching [225], waveguide preform reflow [226], and etchless process [227, 228]. Note that, TPA is not considered here as it is absent in stoichiometric Si_3N_4. However, local stoichiometry variation can still generate silicon nano-crystals after thermal annealing [229, 230, 231]. Though not reported so far in stoichiometric Si_3N_4, this effect may be revealed in the future in ultrahigh-Q Si_3N_4 microresonators.

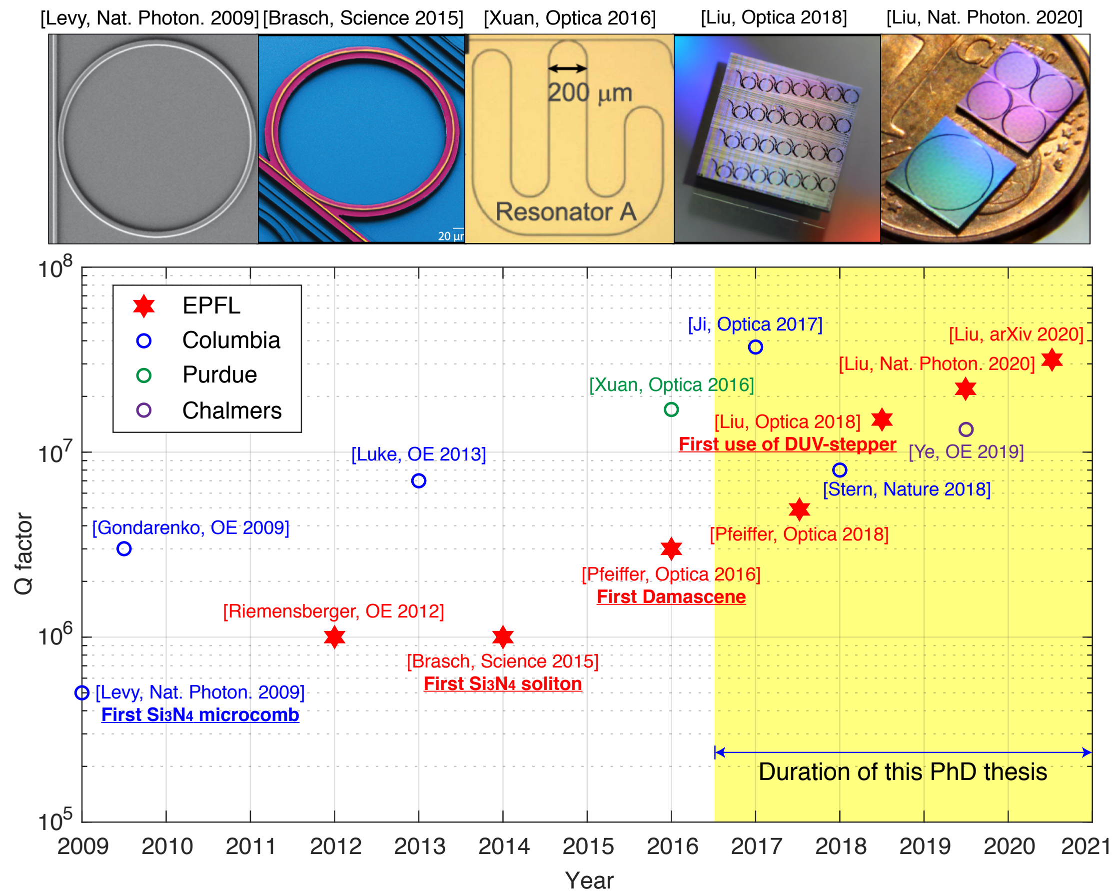

Figure 2.7 – The development of high-Q (low-loss) Si_3N_4 microresonators with the continuous efforts from the entire Si_3N_4 community. Here, for the limited space, I only select several works reported by Columbia University (groups of M. Lipson and A. L. Gaeta) [93, 94, 95, 100, 101], Purdue University (groups of M. Qi and A. M. Weiner) [98], Chalmers University of Technology (group of V. Torres-Company) [202], and EPFL (group of T. J. Kippenberg) [85, 86, 88, 89, 91, 78].

Precise waveguide geometry control for dispersion engineering over octave bandwidth: Integrated waveguides are the ideal platform to generate broadband optical sources, such as octave-spanning soliton microcombs and supercontinuum. The octave-spanning bandwidth allows full stabilization of these optical sources [13, 2] for metrology, spectroscopy and microwave frequency synthesis. In the case of soliton microcombs, the octave-spanning spectral bandwidth can be enabled by soliton-induced Cherenkov radiation, commonly referred as "**dispersive waves**" [232, 121, 120, 77, 86]. Dispersive waves are generated near the spectral positions where the integrated dispersion is zero, which can be designed and controlled with precise engineering of higher-order dispersion profile [89, 99]. For integrated waveguides in the simple rectangular or trapezoidal shapes, such a dispersion engineering requires controlling waveguide geometry, i.e. width and height, with a precision typically better than 20 nm. While the waveguide width can be precisely controlled via lithography with a resolution better than 10 nm, controlling the waveguide height is challenging, as the Si_3N_4 film deposited using CVD typically has a non-uniformity of $\pm3\%$. This film thickness non-uniformity is presented on a single wafer, wafer-to-wafer in a single run, and run-to-run in a batch, and can give a thickness variation of ±24 nm for 800 nm film thickness. Nevertheless, for those proof-of-concept experiments, yield is so far not the key concern.

Currently there are two main processes to fabricate Si_3N_4 waveguides: the standard **subtractive process** [94, 98, 100, 202, 203] and the recently developed **photonic Damascene process** [88, 226]. In the following I will briefly describe the subtractive process, and then focus mainly on the Damascene process.

2.2.2 The subtractive process

The subtractive process is widely used to fabricate photonic integrated circuits based on a wide range of material platforms. The process flow is shown in Fig. 2.8(a). Silicon nitride thin

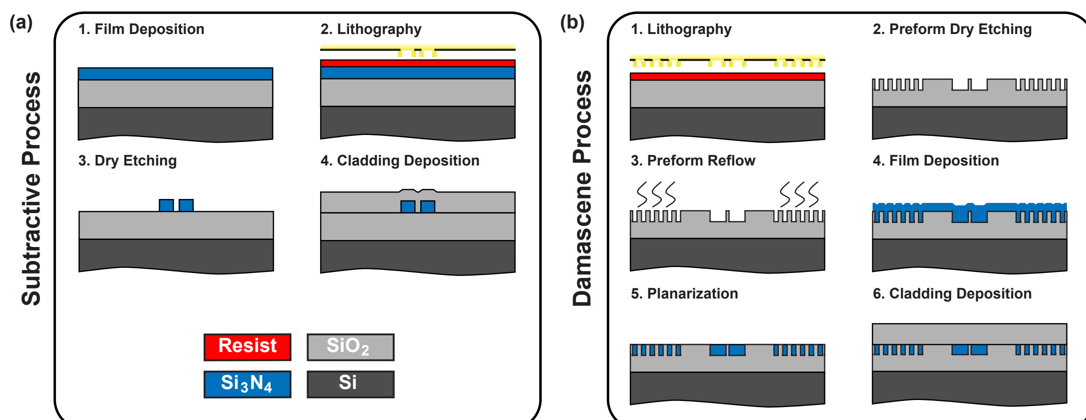

Figure 2.8 – Comparison of the process flows of the subtractive process (a) and the photonic Damascene process (b).

film is deposited on a clean silicon substrate with a thick SiO_2 bottom cladding. The waveguide pattern is written via electron beam lithography (EBL) or photolithography, which one to use depends on the required minimum critical dimension. The waveguide pattern is dry-etched into Si_3N_4 to form waveguides using CHF_3. The EBL resist or photoresist (PR) work as the etch mask, while the required resist thickness depends on the etching selectivity, non-uniformity, and etching sidewall angle. Hardmask may be required if the available resist thickness or the etch selectivity is insufficient. For superior etch quality and smooth waveguide sidewall, oxygen is usually added, in order to remove CF polymers as etch by-product [100]. Then top SiO_2 cladding is deposited on the wafer, which usually require high-temperature annealing to drive out the residual hydrogen content.

The advantages of subtractive process is the simplicity. The flat wafer top surface allows any CVD and physical vapour deposition (PVD) film deposition, as well as wafer bonding if the substrate is selected properly. However, the disadvantages of subtractive process are equally outstanding: 1. Depending on the waveguide material, the dry etching process needs to be specifically developed, including the selection of the etchant gases and the etch mask, which affects the waveguide sidewall verticality and roughness through the effects of mask damage, erosion, tapering and sidewall passivation. All these effects, in combination, determine the light propagation loss in the waveguide due to surface Rayleigh scattering, which is currently a central problem preventing waveguide loss reduction. For example, chloride-based etchants are used to etch e.g. AlN and GaP, and the serious mask damage introduces extra roughness in addition to the lithography-related roughness, which significantly increases the optical losses. 2. For waveguides of large height and made of film with tensile stress, cracks can occur which reduces the fabrication yield. For example, fabricating waveguides of LPCVD Si_3N_4 with height exceeding 500 nm remains challenging, regardless of the use of multi-step deposition / thermal treatment [218, 100]. 3. The wafer top surface with waveguides, with and without top cladding deposition, is not flat, which poses challenges for bonding and integration with other materials.

2.2.3 The photonic Damascene process

The recently developed photonic Damascene process [88, 226] is an additive process. The Damascene process was firstly used for copper interconnects, but recently also for Si_3N_4 integrated waveguides. The Damascene process flow is shown in Fig. 2.8(b). The lithography directly patterns the waveguides on the SiO_2 substrate. The pattern is then dry-etched to the SiO_2 substrate to make the waveguide preform. A preform reflow step [226] follows, in which the substrate is annealed at 1250°C, and can further reduce the sidewall roughness of waveguide preform to nanometre level, leading to reduce Rayleigh scattering losses [90]. Thick LPCVD Si_3N_4 film is then deposited on the pattered preform, filling the trenches and forming the waveguides. Chemical-mechanical polishing (CMP) [233, 234] is used to remove the excess Si_3N_4 and planarize the wafer top surface. Finally, top SiO_2 cladding is deposited on the wafer followed by high-temperature annealing.

The Damascene process has several unique advantages over the subtractive process: 1. The stress-release filler pattern [90] can be written simultaneously with the waveguide pattern during the lithography step. These filler pattern can significantly release the high tensile stress of thick LPCVD Si_3N_4 film [235, 95, 88], resulting in crack-free as-deposited film. 2. It allows the waveguide height of several micrometers, utilizing the deposition conformality of LPCVD Si_3N_4 process based on $SiCl_2H_2$ and NH_3 [236]. Large cross-section Si_3N_4 waveguides is required for dispersion engineering at Mid-IR wavelength range, e.g. for supercontinuum generation. 3. The flat, smooth wafer top surface after CMP facilitates hybrid or heterogeneous integration of Si_3N_4 with other materials, via wafer bonding [237] or transfer technique. 4. The dry etching process to define waveguide patterns only needs to be optimized for SiO_2, regardless of the material forming the waveguide core. In addition, the preform reflow can further reduce the waveguide roughness. Therefore, Damascene process is ideal for low-loss waveguides made of materials requiring aggressive echants such as Cl-based gases that simultaneously create serious etch profile roughness. 5. The preform etch, showing inherent aspect-ratio dependent etch (ARDE) [238], provides extra freedom to engineer the waveguide geometry, particularly the formation of two-dimensional structure variation, which is useful for e.g. double inverse nanotapers for fibre-chip coupling [239].

Recently, the photonic Damascene process has achieved several advancements, including: 1. Thick Si_3N_4 waveguides of ultralow optical losses ~ 1 dB/m, which have enabled high-Q Si_3N_4 microresonators for reliable soliton microcomb generation with milliwatt power [91], and repetition rate below 10 GHz [78]. 2. Precise waveguide geometry control which allows the engineering of GVD, critical for e.g. octave-spanning soliton microcomb generation featuring two dispersive waves [89], and broadband supercontinuum generation [240]. More details on several key fabrication steps will be given in the following sections.

2.3 Deep-UV stepper lithography

It is well known that the waveguide roughness can significantly affect the light propagation loss. To reduce optical losses, the lithography and dry etching need to be optimized. Concerning the lithography process, both electron beam lithography (EBL) and deep-ultraviolet (DUV) photolithography have been used to pattern waveguides. Which one is more suitable depends mainly on the minimum critical dimension (CD), e.g. the inverse nanotapers [241, 239] used for light input coupling from fibres or free-space to the integrated waveguides. In both lithography processes, line edge roughness (LER) is usually associated with beam size, beam stability, pattern fracture, aliasing, stitching errors, resist used and approach of resist development etc. While the combination of different parameters can perform significantly differently, in general, minimum LER can be achieved with large beam size and multipass writing [242]. For high-optical-confinement, nonlinear Si_3N_4 waveguides, the typical waveguide width ranges from 1 μm to 2.5 μm, comparable to the operation optical wavelength that dispersion engineering can perform effectively. This waveguide width CD is fully compatible with DUV stepper lithography. In addition, the minimum CD resolution of DUV stepper lithography (e.g. 193 nm or 248 nm) is below 180 nm, sufficiently small for efficient fibre coupling of light at telecommunication wavelength bands into the Si_3N_4 waveguides using inverse tapers. Therefore, though EBL is widely used to pattern PIC, in this thesis, a main research topic is on the development of DUV stepper lithography technique to fabricate ultralow-loss Si_3N_4 waveguides.

Deep-UV stepper is a photolithography equipment used to manufacture integrated circuits (ICs). It uses a DUV light source to expose DUV-sensitive photoresists through a mask, generally referred as the "**reticle**". The typical wavelengths employed are 248 nm using krypton fluoride (KrF) lasers and 193 nm using argon fluoride (ArF) lasers. The ArF 193 nm is much more widely used for industrial manufacture, as smaller wavelength can enable higher lithography resolution. The lithography resolution is described by Abbe criterion:

$$\mathrm{CD} = k_1 \frac{\lambda}{\mathrm{NA}} \tag{2.4}$$

where CD is the minimum critical dimension to be resolved, λ is the wavelength of the light source used, and NA is the numerical aperture. k_1 is the technical factor and depends on the features to be imaged, illumination geometry, photoresist, processing conditions and other details. This equation represents the first Rayleigh criterion of optical projection lithography.

Stepper lithography tools use projection systems consisting of mirrors and lenses to create a de-magnified image of the mask on the photoresist. The de-magnification factor is usually ×4 or ×5 reduction. This is in opposition to contact lithography, where the reticle is placed in contact or in close proximity to the wafer and the pattern is printed on the wafer in 1:1 ratio. One exposure shot through the reticle will expose only one small part of the wafer, called a "**field**". Consequently, to pattern the entire wafer, the stage will accurately move step by step such that different positions on the wafer is placed under the exposure area. The stepping

continues until the entire wafer is exposed.

While an ASML PAS 5500/350C was recently installed at EPFL CMi, the DUV stepper used in this work is a refurbished **Canon FPA-3000 EX4** installed at DTU Danchip.. This tool was first produced in 1998. Figure 2.9(a) shows a typical DUV stepper (source: DTU Danchip). Table 2.1 lists the key specifications of the tool. As time passed, more cutting-edge technologies have been introduced (scanners, immersion lithography, EUV lithography) to further push the resolution towards the nm range. DUV steppers are slowly being replaced in fabs, and are being refurbished by the original manufacturers for companies of the "More than Moore" market as well as microfabrication centers!

Besides DUV stepper lithography, electron-beam lithography (EBL) is also widely used to pattern photonic integrated waveguides. The advantages of DUV stepper lithography over EBL, besides the higher yield and lower cost, are: 1. The stitching errors on the wafer are 4 or 5 times smaller than the ones on the reticle used in the industrial standard 4 or 5 demagnification lens systems; 2. The reticle writing using standard photolithography (~ 1 hour) is much faster than the wafer writing using EBL (> 10 hours), thus the field-to-field (or stripe-to-stripe) time delay is significantly shorter with DUV than with EBL, leading to smaller stitching errors caused by the beam drift; 3. The field (or stripe) size of photolithography for reticle writing is much larger than the field size of EBL for wafer writing, leading to fewer stitching errors; 4. Multipass for reticle writing can be easily adapted with reasonable cost increases. Consequently, DUV stepper lithography can provide superior lithography quality, and has been used in recently demonstrated integrated Brillouin laser[200] based on low-confinement Si_3N_4 waveguides of optical propagation loss below 1 dB/m[201, 199].

To complete the DUV exposure job, key steps include: 1. Reticle fabrication; 2. Wafer cleaning and photoresist coating; 3. Exposure; 4. Photoresist development. Each step will be illustrated in more details in the following.

Table 2.1 – Specification of Canon FPA-3000 EX4

De-magnification	×5 ±0.5 ppm
Resolution	180 nm
Wavelength	248 nm
Numerical aperture	0.4 - 0.6
Maximum field size	22 mm × 26 mm
Reticle Size	6-inch square, 0.25-inch thickness
Maximum wafer size	6-inch
Stage Repeatability	< 35 nm
Alignment precision	< 50 nm
Throughput (6-inch wafer)	100 wafers per hour

2.3.1 Reticle

Lithographic photomasks are typically transparent fused silica or quartz blanks covered with a pattern defined with a chrome metal-absorbing film. In photolithography for the mass production of integrated circuit devices, the more correct term is usually "photoreticle" or simply "reticle". In this sense, when discussing photolithography, "photomask" and "reticle" are synonyms.

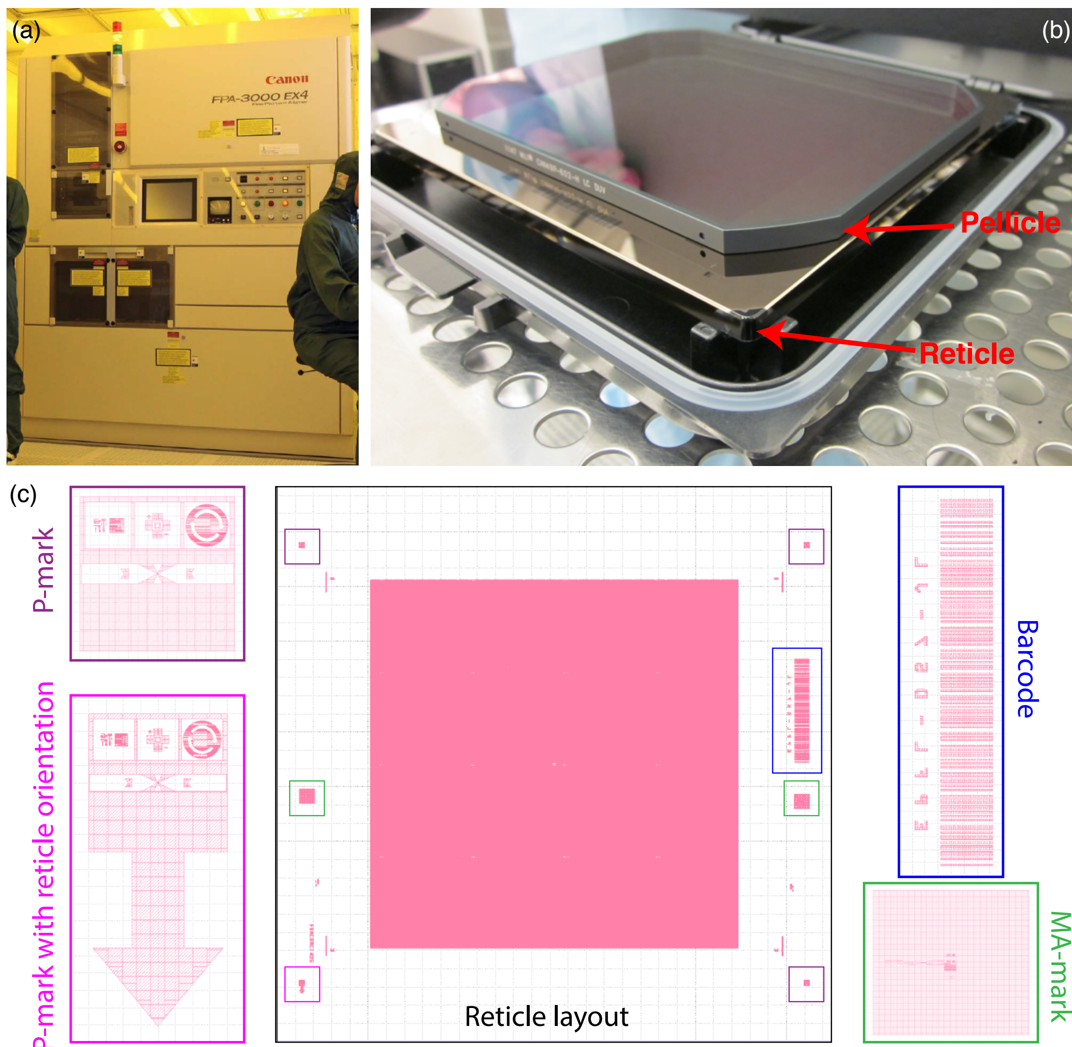

Figure 2.9 – Images of a DUV stepper lithography tool, a reticle and a reticle layout. (a) The Canon DUV stepper installed in DTU Danchip. **Image source**: DTU-Danchip, https://www.nanolab.dtu.dk/english. (b) A quartz reticle with a pellicle used in standard DUV stepper. (c) All alignment markers used in the lithography with alignment. The chip release maker is used to align the chip release layout in CMi. The TVPA and AGA alignment markers are used for stepper lithography alignment in Danchip stepper tool. All the alignment markers must be included in the design of field layout (on reticle).

On the reticle, there is a proportional ratio between the reticle pattern and the wafer pattern. In conventional contact photolithography, this ratio is 1:1. In modern stepper lithography (as the tool used in this thesis), the ratio is 5:1, i.e. the pattern on the reticle is 5-times smaller than the pattern on the wafer. Therefore, to write the pattern covering the entire wafer area, the wafer is repeatedly "stepped" from one position to to another under the optical column until full exposure is achieved.

Figure 2.9(b) shows the photo of a reticle manufactured by **Compugraphics**. The reticle contains mainly two parts: the quartz blank which contains the patterns to be written on the wafer, and the pellicle. The pellicle is a thin transparent film stretched over a frame that is glued over one side of the reticle, to prevent dust and particles falling on the reticle. The pellicle is far enough away from the mask patterns so that moderate-to-small sized particles that land on the pellicle will be too far out of focus to print. Although they are designed to keep particles away, pellicles become a part of the imaging system and their optical properties need to be taken into account. Pellicles material are Nitrocellulose and made for various transmission wavelengths.

The reticle is typically manufactured in the following way: Direct laser writing or electron-beam lithography are used to write the design pattern on the reticle blank covered by chrome and coated with resist. After the exposure, the resist is developed and the pattern is revealed. This resist acts as a mask for etching the pattern into the chrome layer. The etching process can be performed via either wet etching or dry etching. Afterwards, the resist layer is removed. The finished reticle is further examined by the manufacturer, in order to ensure the quality. The pattern is inspected for any defects that may affect device functionality, which are repaired if necessary. Once the reticle meets the quality level, the reticle is cleaned, and a protective pellicle is installed.

Figure 2.9(c) shows the pattern layout on the reticle. The part covering the large central area in the reticle is the waveguide pattern that needs to be written on the wafer. Our current DUV stepper lithography tool can resolve features with sizes down to 180 nm (i.e. 900 nm size on the reticle, if with x5 demagnification factor). Smaller features will require phase-shifting to enhance the image quality to acceptable values, and can be achieve in modern high-performance stepper tool, not the one used here.

There are also other features. Key features include: P-marks and MA-marks are used for precise alignment of the reticle in the stepper tool, i.e. the reticle should be positioned properly under the optical field without rotation and tilting. Orientation mark, barcode and human readable code (HRC) are for identification of the reticle orientation and IDs and can be clearly seen with human eyes.

Figure 2.10(a) shows the amplified design layout on the reticle, with zoom-in details of the waveguide and ring patterns. My design rule is to place 4×4 chip designs on the reticle, which form the **field layout**. Each shot of exposure writes the field layout on the certain position on a wafer. For 4-inch wafers, 21 exposure shots are needed in order to uniformly write the field

layout on the entire wafer. Each chip on the wafer is 4960×4960 mm^2 in size, with 100 μm distance between adjacent chips (i.e. the periodicity is 5060 μm). On the **chip layout**, multiple rings are densely packed. The rings are coupled by straight or meander bus waveguides.

One reticle only contains one layer of design. Therefore to write multiple layers, same number of reticles are needed, and exposure between each of them requires optical alignment of layers. For this purpose, In addition to the main waveguide structure, alignment markers are also needed if a second exposure is needed on top of the first exposure. Therefore, the alignment for the second exposure needs to be written during the first exposure. Currently, four alignment markers are used in one each reticle: TVPA markers are used to roughly overlay the second exposure on top of the first exposure. AGA x- and y-axis markers are for fine alignment and to remove the error due to slight rotation TVPA and AGA markers are needed for DUV stepper lithography tool for alignment. The chip release marker is for separating the wafer into chips, and is only needed for other photolithography tool used in the end of the process.

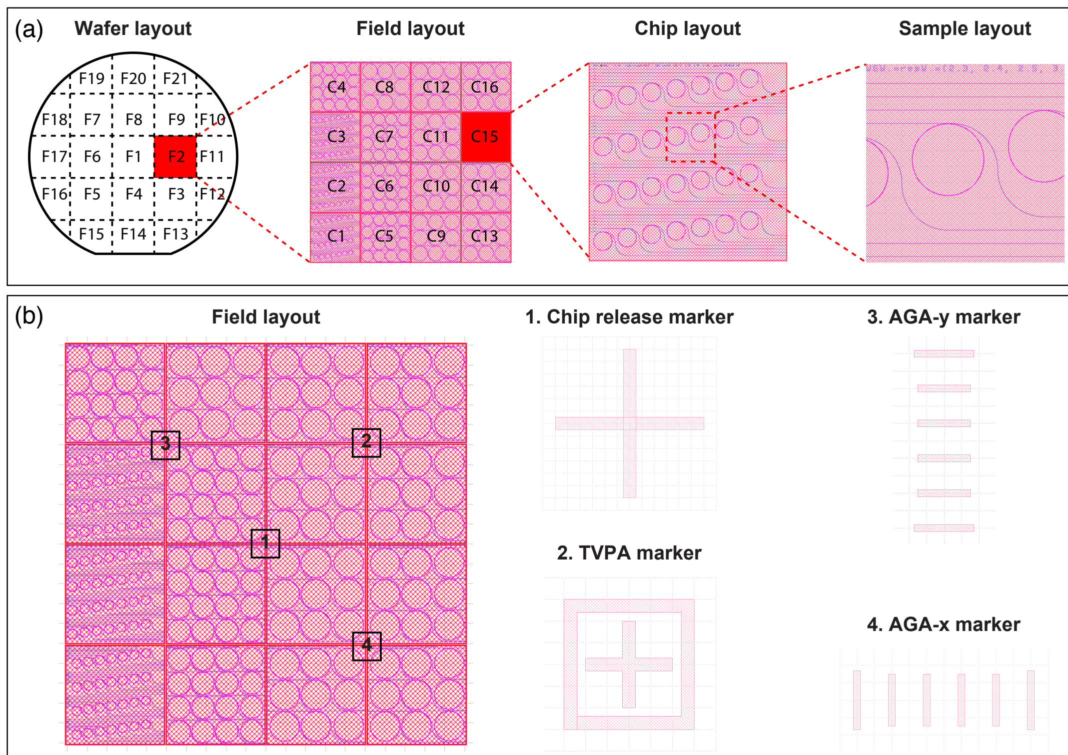

Figure 2.10 – Wafer and reticle layout. (a) Schematic of design layouts. (b) All alignment markers used in the lithography with alignment. The chip release maker is used to align the chip release layout in CMi. The TVPA and AGA alignment markers are used for stepper lithography alignment in Danchip stepper tool. All the alignment markers must be included in the design of field layout (on reticle)

2.3.2 BARC and photoresist coating

Once the reticle is finished, the wafer are ready for exposure. Before the exposure, the wafer needs to be coated with DUV-sensitive photoresist. In my process, the wafer is coated with 65 nm BARC and 350 nm M230Y.

Bottom anti-reflective coatings (BARC) is spin-coated on the wafer, before the DUV photoresist is coated. The BARC used in the current process is from **Brewer Science**. It used at the interface between the wafer substrate and the photoresist to reduce the bottom reflectivity, and to provide better linewidth control with minimal loss of resist performance. The reflected light can cause processing problems due to the formation of standing waves. Figure 2.11 shows the SEM image of photoresist after exposure and development, without proper control of back reflection. In this case, standing waves are formed and cause roughness of the resist edge. When using BARC with a proper thickness, the reflectivity is reduced by either attenuating light that passes through the BARC, or by matching the refractive indices of BARC to the resist and the substrate. However, the application of BARCs increases the complexity of the process. The etch performance of the BARC and its compatibility with the resist and the substrate have to be considered in the process design.

After the spin-coating of BARC, DUV photoresist of 350 nm **JSR M230Y** is spin-coated on top of the BARC. M230Y is based on positive-tone chemically amplified resist (CAR), which works at exposure wavelength below 300 nm. The the wafer is ready to be exposed with DUV stepper tool.

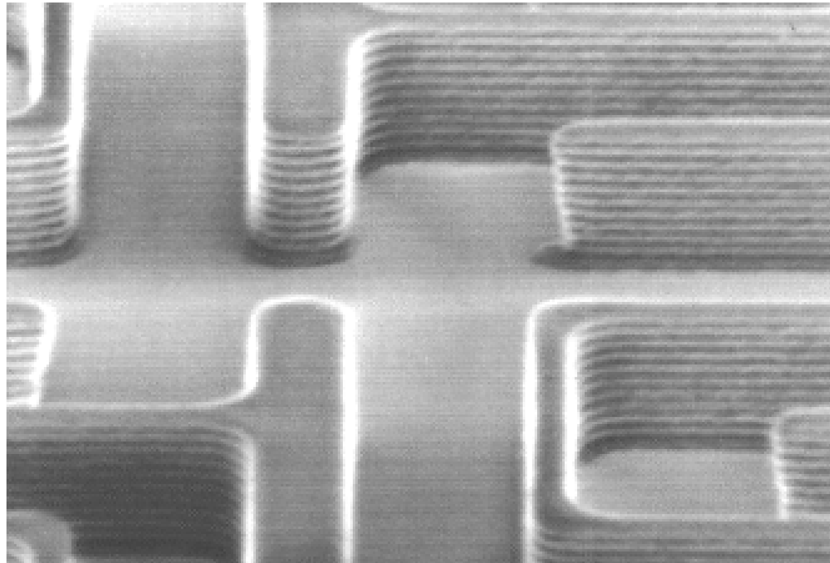

Figure 2.11 – The SEM image of photoresist after exposure and development, without proper control of back reflection. **Figuer source**: http://www.lithoguru.com

2.3.3 Exposure

To exposure the pattern from the reticle to the wafer properly, the parameters for DUV exposure need to be input to the tool. The two key parameters are dose and focus. **Dose** is the light intensity illuminated on wafer. Sufficient dose is needed in order to trigger photo-chemical reaction in the photoresist. **Focus** is where the light spot is within the photoresist. Since the light wavelength is smaller than the photoresist thickness, the focus can significantly impact the resist profile after development, as well as the feature's critical dimension (CD).

Though the optimal parameters of dose and focus can be found via a series of experimental tests, these values can be predetermined via photolithography simulation, such as using the software **ProLith**. For given input of the wafer and resist information, **Bossung curves**, i.e. curves showing CD values versus dose and focus, is plotted by **Prolith**, as shown in Fig. 2.12. Flat Bossung curves indicate a low sensitivity of the process to the focus. The distance between the individual curves in dose direction is a measure of the dose sensitivity of the resist.

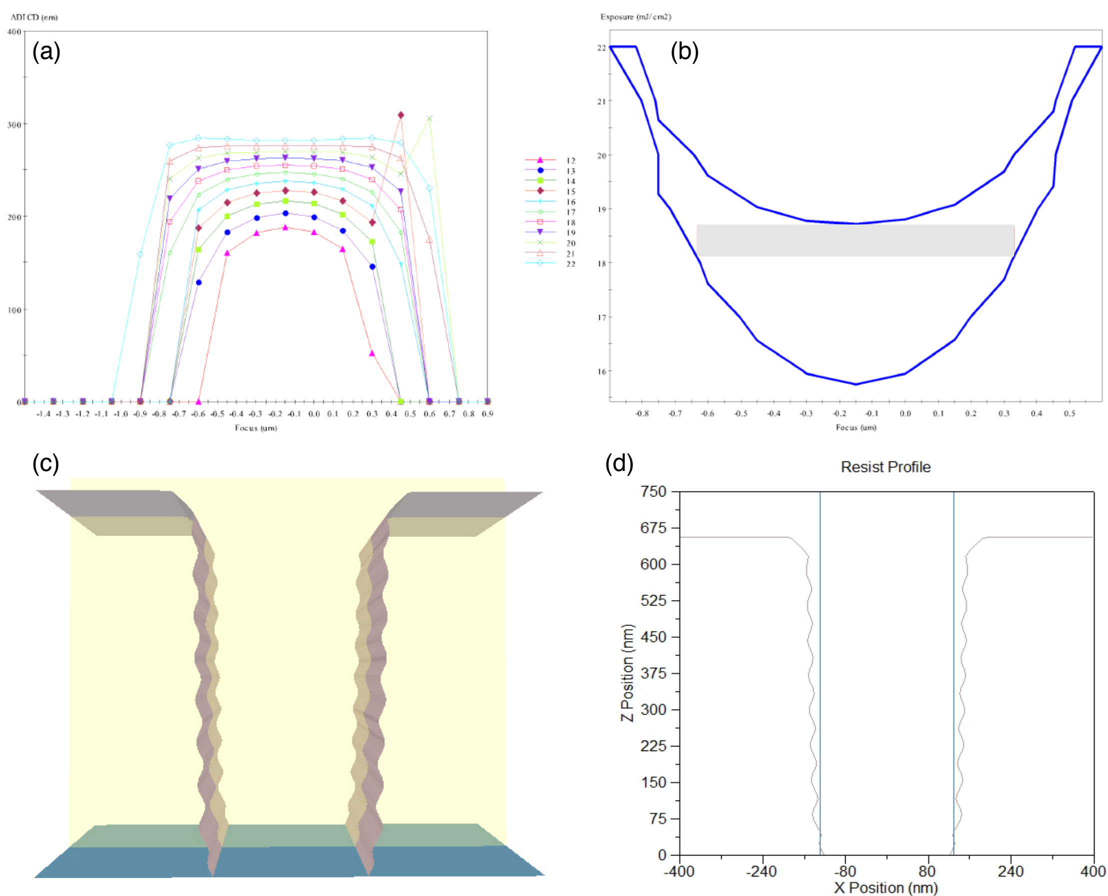

Figure 2.12 – Simulation of photolithography exposure using Prolith. (a) Simulated Bossung curves. (b) Simulated process window in the gray area. (c, d) Simulated resist cross-section profiles.

The dependency of CD versus dose and focus can be also plotted in an alternative way. Figure 2.12(b) represents the **process window** (the gray area) The two blue curves are the dose values are required to generate features with 90% of the target CD (upper curve), and 110% of the target CD (lower curve). All combinations of dose and defocus between the upper and lower curve produce the target with an accuracy of ±10%. The rectangular gray area is the process window. According to Fig. 2.12(a), for target CD of 220 nm, the required dose is 14 mJ/cm^2, and the focus is 0. Figure 2.12(c, d) shows the simulated resist cross-section profiles. Standing waves are observed due to the reflection, as explained earlier.

The wafer is then exposed with given dose and focus from the simulation. After post-exposure bake (PEB) which causes diffusion of chemical species inside the resist and can modify the solubility of the exposed photoresist, the photoresist is developed and the waveguide pattern is revealed on the wafer. In fact, the experimental results agree well with the simulation. After the final SRD cleaning of the wafer, the entire lithography job is finished.

2.4 Dry etching

After the DUV lithography and resist development, the waveguide pattern is created on the DUV photoresist mask. The next step is to transfer the pattern into the SiO_2 substrate and to create waveguide preforms. This pattern transfer is realized via etching, typically with anisotropic dry etching using reactive ions, to maintain the critical dimension (CD) of the waveguide pattern. Wet etching using liquid etchants has been used to make microdisks with device undercut, however is not suitable for fabrication of PIC due to the incapability to maintain the CD and create sub-micrometre structures.

Dry etching is performed by using gas-phase etchants ("dry", as opposed to "wet" etching using liquid etchants) at low pressure (typically 0.1 - 100 mbar) and plasma environment. On the substrate, a mask is needed which opens the area where patterns need to be created, and covers the rest area. The etchants become reactive only when plasma dissociates neutral molecules into radicals and ions. A RF current of 13.56 MHz frequency is used to drive the RF coils and to induces the plasma concentrated on top of the substrate within a skin depth of few centimetre. The RF drive induces macroscopic oscillation, such that the initially generated electrons and ions causes more collisions with neutral molecules under the RF oscillation, which finally ignite plasma.

Carbon fluorides C_xF_y are often used to etch dielectric materials such as silicon, Si_3N_4 and SiO_2. These C_xF_y (CF_4, C_4F_8 etc) molecules are stable, and only the fluorine radicals F generated by dissociating C_xF_y under plasma etch the dielectric materials chemically and *isotropically*. The by-products C_xF_{y-1} can be adsorbed by the substrate and form fluorocarbon polymer as passivation masks (i.e. protect the substrate from etch). In short words, when choosing the carbon fluorides C_xF_y, the ratio x/y needs to be considered as it determines the strength between passivation and etch (more passivation with more carbon C, and more etch with more fluoride F). Therefore, by choose a proper value of x/y, the etch anisotropy can be controlled, and an anisotropic etch can be achieved (i.e. etching the substrate only happens in the vertical direction, but not in the horizontal direction which increase the CD), which is a result of sidewall passivation. Normally, this case corresponds to $x/y \approx 0.4$, and its precise value can vary depending on other gases such as O_2 (consume C and form CO_2) or H_2 (consume F and form HF). Adding O_2 and H_2 also changes the etch rates due to that each gases change the passivation or etch (note, do not add O_2 and H_2 simultaneously as this mixture is highly explosive).

It should be noted that, not only the substrate is etched, but also the mask. Depending on the material of the mask, the **etch selectivity**, defined as the ratio of etch rates between the substrate material and mask, can be different. For example, if the mask is photoresist and the substrate is SiO_2, adding O_2 into C_4F_8 increases both the etch rates for SiO_2 (as C is consumed by O_2, and less fluorocarbon polymer passivation layer is formed) and mask (the photoresist is organic and can react with O_2). Overall the selectivity is lower with higher concentration of O_2.

One phenomenon which presents universally and can be prominently observed during dry

etching is the “**aspect ratio dependent etching (ARDE)**” effect [238]. The ARDE describes a phenomenon that the etch rate varies depending on the pattern CD value. The trench of smaller CD is etched more slowly than the trench of larger CD. Above a certain CD value, the etch rate is constant. Figure 2.13(a) shows an SEM revealing the CD-dependent etch rate variation for multiple etched trenches on a SiO_2 substrate with amorphous silicon as the etch mask (green shaded). Figure 2.13(b) shows the measurement data and fit of the etch rate as a function of the CD value of the trench pattern. When CD reaches the threshold value of ~1 μm, the ER reaches a stable value of ~0.29 μm/min and becomes nearly independent of CD. From 0 to 0.5 μm CD, ER increases nearly linearly. The ARDE curve can be fitted with $\mathrm{ER} = a \cdot \exp(-\mathrm{CD}/b) + c$, with $a = -0.444$ μm/min, $b = 0.195$ μm, $c = 0.286$ μm/min.

The ARDE effect has been given other names such as “RIE lag” and ”microloading”. It should be noted that these effects can be very different things from each other. For example, ARDE is also observed in inductively coupled plasma (ICP) etcher and electron cyclotron resonance (ECR) etcher, not only reactive ion etcher (RIE); also, ARDE is a global effect on the wafers and can be independent on the local pattern density, opposite to microloading which is affected

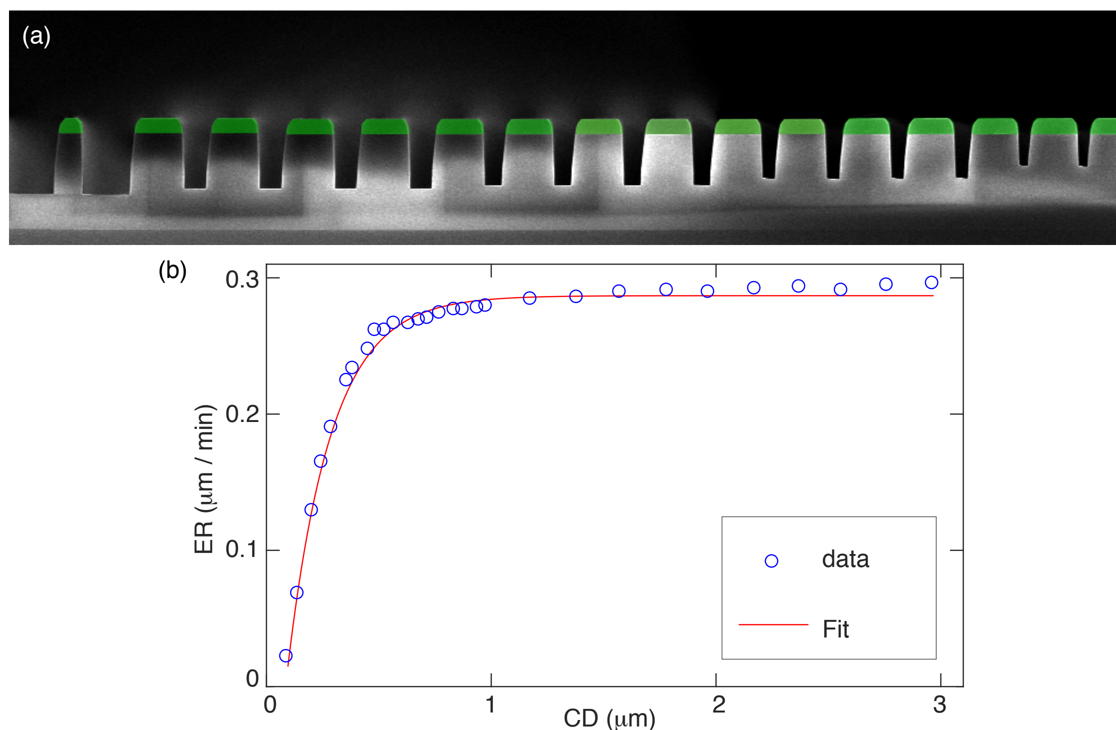

Figure 2.13 – Characterization of the ARDE effect. (a) Scanning electron micrography showing the ARDE effect on a SiO_2 substrate with amorphous silicon as the etch mask (green shaded). The trench width values by design, from left to right, are 300 nm (×2), 400 nm (×4), 500 nm (×4), 600 nm (×4), and 1000 nm (×1), respectively. (b) Measurement and fit of the etch rate as a function of the CD value of the trench pattern. The fitted ARDE curve is $\mathrm{ER} = a \cdot \exp(-\mathrm{CD}/b) + c$, with $a = -0.444$ μm/min, $b = 0.195$ μm, $c = 0.286$ μm/min.

largely due to the local environment. The only proper synonym for ARDE is the "**aperture effect**", which is self-explained. Note that the etchant radicals impinging the substrate are not directed perfectly vertically – these radicals have a diverging angle. The pattern with small CD works as a spatial aperture that limits the incident etchant radicals to reach the bottom of the trench and prevent the extraction of etch by-products from the trench. In combination, less etchant radicals are allowed to etch the trench, thus the etch rate is reduced. In this sense, the aperture effect, or ARDE, essentially limits the aspect ratio of the trench (i.e. ratio of width to depth). This effect needs to be considered in design, and may also be utilized to created tapered structures (for example, see "double inverse tapers" in Chapter 3).

The waveguide pattern transfer from the DUV photoresist mask to the SiO_2 substrate via dry etching often causes extra LER and reduces the surface quality. This etch-induced roughness

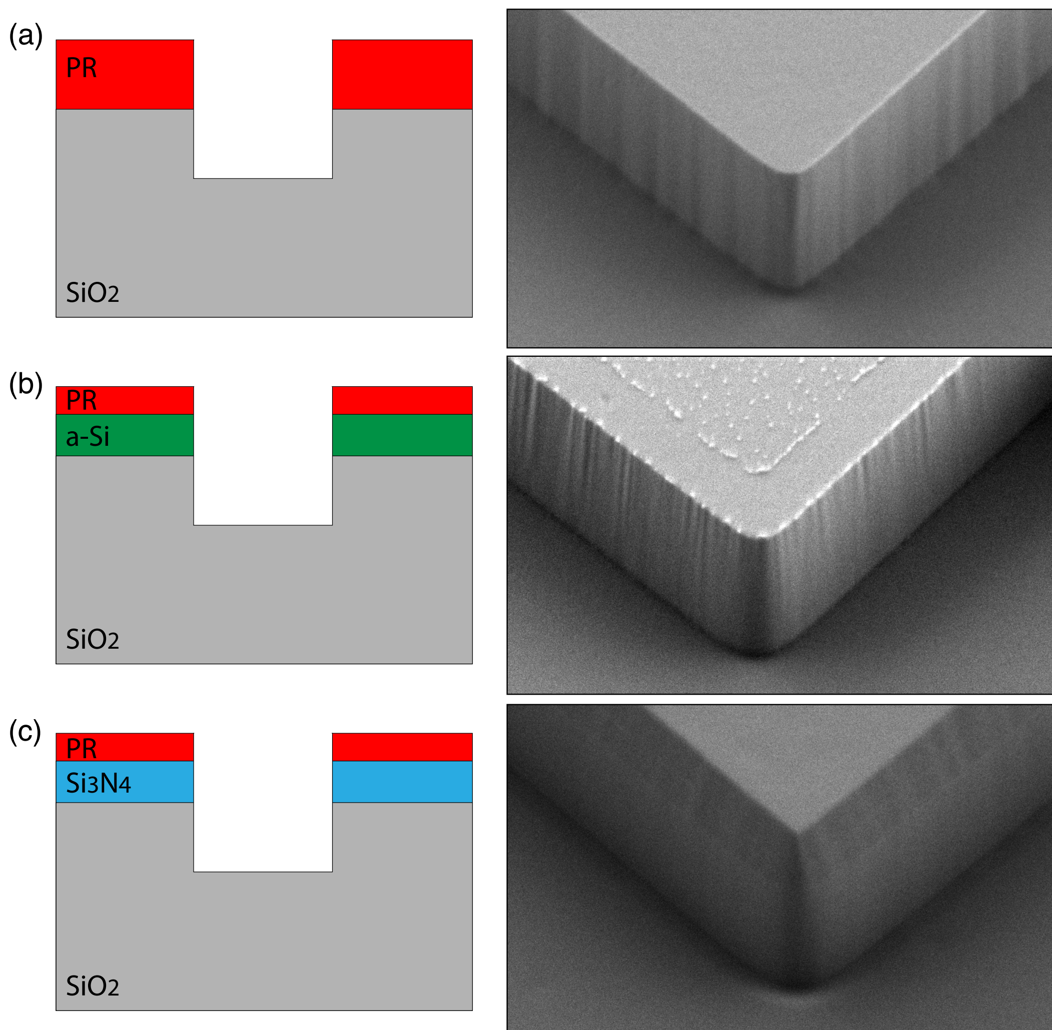

Figure 2.14 – Comparison and SEM showing the difference in sidewall roughness using three kind of etch masks, DUV-photoresist (a), amorphous silicon (b), and Si_3N_4 (c).

is affected by the selection and combination of etchant gases, reactor configuration such as temperature, RF power, and can be mitigated. However, it should be noted that, the selection of etchant gases depends also on the etch mask. In the current Damascene process in which SiO_2 is etched, C_4H_8 and O_2 are used. The main etchant is C_4H_8, and the addition of O_2 is to eliminate the fluorocarbon monomer and polymer deposition during the etch [100]. Figure 2.14 shows the SEMs of the etch sidewall roughness on the SiO_2 substrate, using the similar dry etching recipe but with different etch masks (photo resist, amorphous silicon, and Si_3N_4). For the case using the photoresist mask, O_2 is removed as it reduces the etch selectivity significantly (photoresist reacts with O_2). The striation and roughness are found small on the top, and large in the bottom, due to the fluorocarbon polymer deposition which aggregate during etch. For the cases using the amorphous silicon and Si_3N_4 masks, where the pattern is transferred from the photoresist mask, the etch recipes are the same. The striation and roughness are still observed in the case of the amorphous silicon mask, but are found large on the top and small in the bottom, which is due to the the corrosion of the amorphous silicon mask (the conner of the mask attracts radicals due to the silicon charging effect). The best etch quality is observed in the case using the Si_3N_4 mask, which is used in the current Damascene process .

2.5 Preform reflow

After the dry etching, the sidewall bottom angle α is $90° < \alpha < 92°$, as shown in Fig. 2.15 (left). As mentioned, the SiO_2 dry etching process has been continuously developed, which currently reaches a balanced trade between the etch verticality and surface roughness. Before the Si_3N_4 deposition on the patterned substrate, a novel "**preform reflow**" step is performed to further reduce the waveguide sidewall roughness (root mean square) to sub-nanometre level [90]. The entire substrate is annealed at 1250°C such that the substrate is heated slightly above the melting temperature of thermal wet SiO_2, which is ~ 1200°C [243]. It should be noted that, pure SiO_2 has a melting temperature above ~ 1700°C. The much lower melting temperature of ~ 1200°C in thermal wet SiO_2 is due to the extra dopants of phosphide (P) and boron (B). Similarly, heavily doped SiO_2 such as borophosphosilicate glass (BPSG) can have a melting temperature even below 900°C (however, the P and B dopants significantly reduce the SiO_2 quality in terms of the density and porosity). It should be also noted that, standard LPCVD tubes or atmosphere-pressure CVD (APCVD) tubes use quartz as the tube wall which has a melting temperature below 1200°C. Therefore, quartz tube cannot be used for the reflow process. For the reflow process, silicon carbide (SiC) is used to build the tube and wafer table.

When heating the substrate above the melting temperature of thermal wet SiO_2, the surface tension can remove short-range (high spatial frequency) roughness introduced during etching as well as lithography. The preform reflow was firstly came up by M. H. P. Pfeiffer, and initially performed in O_2 atmosphere for 24 hours. The long reflow in O_2 atmosphere leads to the growth of extra SiO_2 due to the oxygen diffusion and dry oxidation of the silicon substrate. Later, during this PhD thesis, the preform reflow has been optimized. The O_2 atmosphere

has been changed to N_2 atmosphere, in order to avoid the extra growth of SiO_2. The reflow time was also reduced to 12 hours, as the new dry etching process already offers superior waveguide sidewall roughness quality which does not require long reflow healing. Importantly, after these major changes, the new reflow process does not lead to prominent deformation of the waveguide preform which is a serious issue in the old precess, shown in ref. [90]. The measured sidewall bottom angle after the current reflow is $\alpha \approx 93°$, as shown in Fig. 2.15 (right).

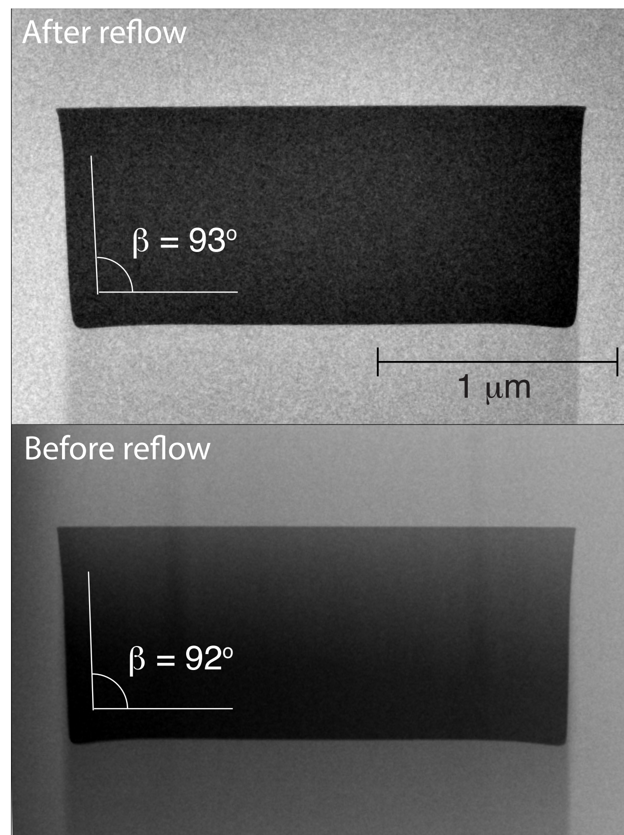

Figure 2.15 – Transmission electron micrographs (TEM) image of the waveguide cross-section, before (left) and after (right) the preform reflow. The waveguide sidewall bottom angle is $\alpha = 92°$ before reflow, and is $\alpha = 93°$ after reflow.

2.6 Chemical vapour deposition

Chemical vapour deposition (CVD) is a deposition technique used to produce high-quality, high-purity solid materials in controlled environment. As its name, the material deposition is based on chemical reaction of reactant gases, activated and driven by energy from chemical, thermal or plasma. The process is widely used in the semiconductor industry to produce thin films, as well as optical fibre industry to produce pure SiO_2.

In a CVD tool, the wafer is placed in a vacuum chamber filled with several kind of flowing gases, including volatile precursors whose reaction with each other produces solid thin film deposited on the substrate, and buffer gas such as N_2 to maintain the environment with constant pressure, temperature and flow rate. The mixing gases are activated and dissociated by heat or plasma. The reactive radicals or ions are adsorbed on the substrate surface, where chemical reaction takes place and a solid film is formed. The gases are flowing constantly in the chamber, as reaction by-products are often generated and need to be exhausted in time. The reaction by-products must be also volatile, key issue to be considered when choosing the chemical reaction, as only one high-purity solid product is wanted at a time. It must be noticed that, the thin film is deposited not only on the wafer but also on the CVD reactor walls (if hot). Therefore, the reactor needs to be constantly cleaned, otherwise flakes falling on the substrate from the reactor wall can happen (causing particle contamination), and the equilibrium of the chamber condition can be affected. In addition, most of the precursors used in CVD are extremely toxic, thus safety issue is of paramount importance.

The CVD technique is excellent in producing thin film of dielectric and metallic materials, with nanometre or even sub-nanometre thickness precision, high conformality, Today, for CVD of thin films for semiconductor manufacturing of electronic and photonics circuits, there are several widely used CVD techniques and tools, including:

- **Low-pressure chemical vapour deposition (LPCVD)** works in quarts tube reactor at a low atmospheric pressures (0.1 to 1 mbar) and high temperature (to thermally drive the chemical reaction). LPCVD allows processing of a batch of wafers at a time, and therefore has high throughput despite that the entire process is slow (due to the low deposition rate and the time needed for temperature raise and descent). System design and construction to achieve good balance between the temperature gradient and the depletion of reactant gases are needed to achieve deposition uniformity on each wafer and wafer to wafer in the same batch.

  The LPCVD process is often used for reactions which are fast and could be explosive, such as the mixture of SiH_4 and O_2. The reduced pressure reduces the reaction rates (thus to avoid gas-phase reactions), and promotes the gas diffusion (to improve film uniformity across the wafer). In order to dissociate the precursors, in the absence of plasma, high temperature is needed. For example, Si_3N_4 and SiO_2 deposition processes using SiH_2Cl_2 are usually operated at a temperature above 700°C. Compared with other CVD processes, the thin films produced by LPCVD process are typically of the highest

quality in terms of uniform, density, number of defects, and step coverage. The key disadvantage of LPCVD is the use of high temperature, making this process incompatible for substrates having metallic structures or layers.

- **Plasma-enhanced chemical vapour deposition (PECVD)** utilizes plasma to enhance chemical reaction rates of the precursors, allowing CVD process operated at low temperatures (below 350°) compatible with electronic circuits. An RF power at 400 kHz or 13.56 MHz is used to dissociate the neutral precursors, and to generate plasma (i.e. a partially ionized gas mixture) containing ions, electrons and radicals. The presence of plasma effectively reduces the activation energy to allow chemical reactions to happen at a much lower temperature compared with the temperature used in the LPCVD process for the same material (however, higher temperature is still advantageous to further enhance film quality). The deposition rate can thus be increased or controlled by changing the driving RF power and controlling the plasma conditions.

  The amorphous films such deposited via PECVD are typically more porous, rougher and less dense, which are affected by the gas-phase reaction. Applying a high bias voltage on the substrate can induce ion bombardment on the substrate, which may cause plasma damage to the device such as film delamination and crater formation. In addition, the interface poisoning can happen as the results of implantation of deposition by-products in the film, and the embedded impurities such as H, Cl, and F are extremely harmful for microelectronic devices (to cause current leakage and low threshold breakdown voltage threshold). However, if configured and controlled well, the ion bombardment can effectively treat the film as *physical etch* and can increase the film quality. Higher RF power results in higher film density and more compressive stress. The physical etch caused by higher-energy ion bombardment is further exemplified in **High-density-plasma chemical vapour deposition (HDPCVD)** The HDP-CVD is an upgraded form of PECVD with an inductively coupled plasma (ICP) source to significantly increase the generated plasma density, comparing to the normal parallel-plate PECVD configuration. In this sense, the HDP-CVD configuration is very similar to an ICP dry etcher, where system works in the reverse regime. The higher plasma density can further reduces the deposition temperature, increase the film quality and significantly improve the deposition uniformity and step coverage (prevent void formation). The step coverage, or gap filling, is a result of the ion bombardment, when the HDP-CVD physically etched the deposited film in situ. The sharp edge has higher etch rate due to the edge charging effect in dielectric materials. As a result, the non-uniform etch rate results in a deposited film surface much flatter than the pre-patterned structure. The difference between PECVD and HDP-CVD is highlighted in Fig. 8.1. This gap filling capability is critical for SiO_2 and Si_3N_4 films, which are normally used as cladding and encapsulation for electronic circuits as well as photonic waveguides. Figure 2.17 shows examples of void formation in SiO_2 in the case that the SiO_2 lacks sufficient deposition conformality.

  Atomic layer deposition (ALD) is based on the sequential use of two precursors A and B to form thin composite layers. The two precursors react with the surface of the substrate

individually, such that one precursor is applied on the substrate at a time, and form atomically thin coating. The mixture of two precursors on the substrates triggers the chemical reaction, and form the composite film. The application of the precursors is sequential (i.e. one molecular monolayer deposition at a time), and the chemical reaction is self-limited (i.e. the process stops once all reactive sites on the surface of the wafer are occupied). Through the repeated step to expose the substrate to each precursor, a highly conformal, atomically specified, very thin film is slowly formed. An example is the formation of Al_2O_3 dielectric films using $Al(CH_3)_3$ and H_2O precursors.

- **Metal-organic chemical vapour deposition (MOCVD)** is based on metal-organic precursors. The molecules of these precursors are heavy, thus the precursors at room temperature are often liquid but have high vapor pressure. **Bubbler** systems are used for MOCVD processes, which transport the volatile precursor molecules by a carrier gas (often N_2) into the reactor chamber. Surface reaction of metal-organic compounds (liquid precursors) and hydrides (gaseous precursors) allows deposition of compound semiconductors, e.g. GaAs or InP, at a temperature ranging from 300°C to 500°C. The MOCVD process is not used in our current process illustrated in this PhD thesis.

Besides CVD, there are alternative methods to grow thin film:

Thermal oxidation is widely used to grow the highest-quality SiO_2 on the silicon substrates. As a batch process, thermal oxidation can process large number of wafers (>100) at a time, thus has a high throughput. In thermal oxidation, O_2 is the main reactant that transforms silicon into SiO_2, at a high temperature above 900° which facilitates the diffusion of oxide atoms into the silicon substrate. Depending on whether O_2 or H_2O (formed by H_2 and O_2) is used, the thermal oxidation is classified as **dry oxidation** or **wet oxidation**. Their chemical reactions, respectively, are $Si + O_2 \longrightarrow SiO_2$ and $Si + 2H_2O \longrightarrow SiO_2{}^{+}{}_2H_2$. Both thermal oxidation

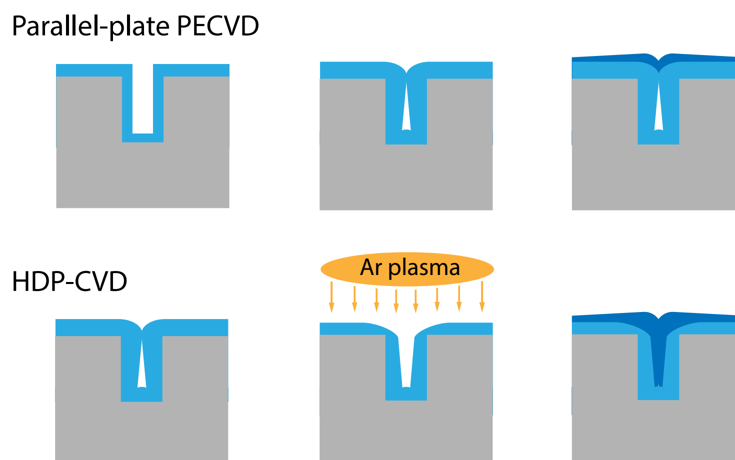

Figure 2.16 – Difference in the topography of deposited films using PECVD and HDP-CVD. The gap filling capability of the HDP-CVD is highlighted.

processes are slow compared with the SiO_2 CVD processes. The SiO_2 thermal-growth rate is described by the Deal–Grove diffusion model. Initially, the SiO_2 thickness d is proportional to the time t as $d \propto t$. Later, due to the increased diffusion length, $d \propto \sqrt{t}$, thus thick SiO_2 layer ($d > 2$ μm) as the substrate cladding typically requires more than a day. Dry oxidation is much slower than wet oxidation and is only used for thin SiO_2 ($d < 0.5$ μm).

Physical vapour deposition (PVD) is used for depositing conductor and metallic thin films that cannot be achieved by CVD. PVD can also deposit dielectric thin films, however the film quality is much worse than that from CVD processes. The most common PVD processes are **sputtering** and **evaporation**.

The stoichiometric silicon nitride Si_3N_4 is a transparent, hard, chemically inert, solid insulator and has high-melting temperature. Its importance to modern semiconductor technologies lies in its impermeability to most impurities, which qualifies its primary use as a passivation layer, especially as a diffusion barrier to moisture and sodium, or as a selective oxidation mask to prevent oxygen from penetration into the silicon beneath. Silicon nitride is a good candidate for the capacitor dielectric as well as gate dielectric to reduce device geometry, due to its high dielectric constant. In addition, silicon nitride is also used as etch hardmasks or etch stop layers.

Stoichiometric Si_3N_4 films for electronic and structural applications in semiconductor manufacture are formed typically using chemical CVD, including:

- LPCVD process works at high temperature of 750 - 850 °C and pressure of 150 - 250 mbar in tube furnaces. The chemical reaction is $3\,SiCl_2H_2 + 4\,NH_3 \longrightarrow Si_3N_4 + 6\,HCl + 6\,H_2$.

- PECVD process which works at relatively low temperature of ~ 350°C in vacuum chambers. The chemical reaction is
  $3\,SiH_4 + 2\,N_2 \longrightarrow Si_3N_4 + 6\,H_2$, or $3\,SiH_4 + 4\,NH_3 \longrightarrow Si_3N_4 + 12\,H_2$. The latter one is more common.

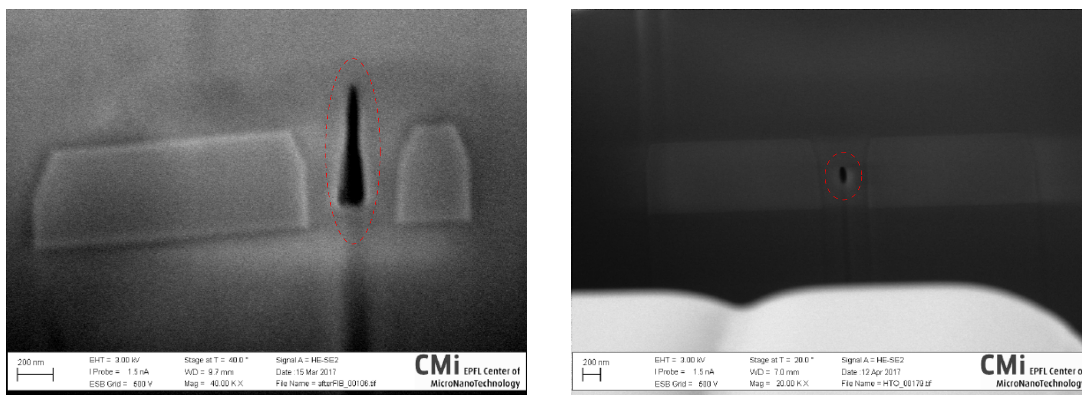

Figure 2.17 – Examples of void formation in SiO_2 cladding. The red circles mark the void.

The Si_3N_4 formed using CVD is amorphous not crystalline. The key advantages of PECVD Si_3N_4 are:

- The process temperature ~ 350°C is compatible with most of the metal process, thus PECVD Si_3N_4 is widely used with integrated electronic circuits, and can be applied after the electronics process.
- The film stress, compressive or tensile, can be controlled and engineered by varying the process parameters such as temperature, RF power, chamber pressure, and gas ratio.

The disadvantages of PECVD Si_3N_4 are:

- The film quality such as density and uniformity is worse compared with LPCVD Si_3N_4.
- The film contains a high content of hydrogen, due the SiH_4 and NH_3 used in the process and the insufficient chemical dissociation under plasma.

As the material density and uniformity affect the light scattering in Si_3N_4, and hydrogen content affects the light absorption, LPCVD Si_3N_4 is generally preferred to make low-loss photonic integrated circuits, unless the process temperature poses issues. In this thesis, only LPCVD Si_3N_4 is used to build ultralow-loss waveguides and high-Q microresonators.

2.6.1 LPCVD Si_3N_4 film stress and crack prevention

The LPCVD Si_3N_4 process based on $SiCl_2H_2$ and NH_3 yields high-quality film with stoichiometric Si:N ratio, minimal hydrogen impurities, and low etch rate e.g. for buffer hydrofluoric acid (BHF). In addition, due to the fact that the SiH_2Cl_2 and NH_3 reaction is driven by surface chemical thermodynamics, the deposition process shows excellent step coverage, i.e. the deposition is *conformal*, as shown in Fig. 2.18. The deposition conformality is critical in the cases of using Si_3N_4 as passivation or capping layer, or in our photonic Damascene process, filling the patterned trenches with Si_3N_4.

Symbol	Description	Value
n_M	Refractive index	2.0
n_2	Kerr nonlinear index	2.5×10^{-19} m^2/W
E_g	Bandgap	5 eV
ρ	Density	3100 kg/m^3
E	Young's modulus	280 GPa
ν	Poisson's Ratio	0.23 – 0.27

Table 2.2 – Main parameters of optical and mechanical properties of Si_3N_4.

However, the surface thermodynamics also results in low deposition rate (1 - 2 nm/min), and more importantly, highly tensile stress of 1.1 - 1.3 GPa which can cause significant film cracks. The Si-N bonds are generated by combining Si-H and N-H bonds and eliminating H_2, and are much stronger than Si-H and N-H bonds, resulting in strained Si-N bond and a tensile Si_3N_4 film globally. This process creates an as-grown internal stress. In addition, the cooling process from the deposition temperature (> 750°C) to the room temperature, while the difference in thermal expansion coefficients between the Si_3N_4 film and SiO_2 or silicon substrate creates the thermal-expansion-induced stress. Generally, it is suggested to use deposit LPCVD Si_3N_4 film with thickness below 300 nm. Film with thickness exceeding 500 nm can show significant cracking.

For nonlinear integrated photonics, such as soliton microcomb and supercontinuum generation that are studied in this thesis, Si_3N_4 film with thickness exceeding 600 nm is needed. As will be illustrated later, parametric process based on Kerr nonlinearity requires anomalous group velocity dispersion (GVD), while the bulk Si_3N_4 shows as-material normal GVD at telecommunication wavelength of 1550 nm. Therefore, the only way to achieve anomalous GVD is to tailoring the waveguide geometry [49], such that the **geometry dispersion** can compensate the material dispersion. In this wave, waveguides with proper geometry can exhibit anomalous GVD. The geometry dispersion comes from the fact that, when the waveguide cross-section size is smaller than the light wavelength, the refractive index of the optical mode is wavelength-dependent not only due to the chromatic dispersion of the material but also (mainly) due to the spatial confinement of the optical mode in the waveguide. Part of the optical mode is in the waveguide core, while a significant portion is in the cladding. The effective refractive index of the optical mode is an integral result of the mode distribution in the waveguide core and cladding.

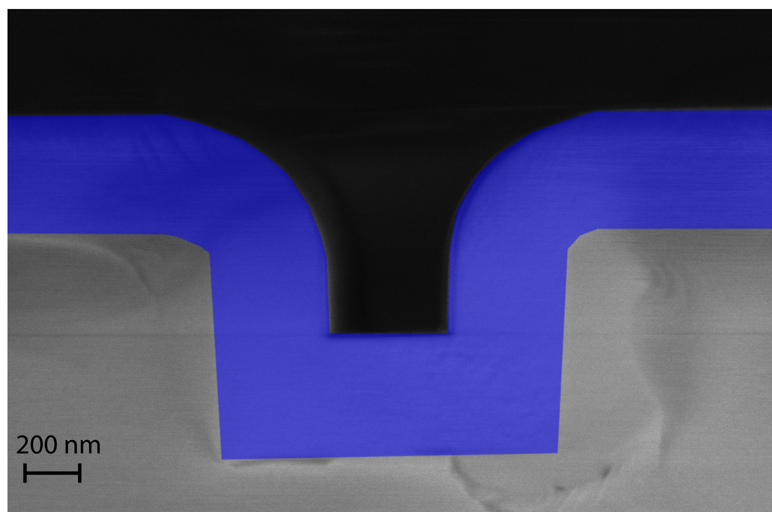

Figure 2.18 – SEM image showing the deposition conformality of LPCVD Si_3N_4 in patterned trenches on a SiO_2 substrate. The Si_3N_4 is blue-shaded.

While the geometry dispersion depends on the waveguide width and height, it is typically required to have waveguide height (i.e. Si_3N_4 film thickness) exceeding 600 nm [95, 117], such that anomalous GVD is accessible. Therefore, film cracking issue when depositing LPCVD Si_3N_4 more than 600 nm needs particular caution and approach to avoid.

Several fabrication techniques can be used to relax the film stress and to avoid LPCVD Si_3N_4 film cracks. The first method, employed in our Damascene process, is to pre-structure the substrate surface [95, 235, 226] with filler patterns, such that the film stress is not accumulated in the wafer plane. Tensile stress accumulates in continuous thin film, and can yield a strong force which ultimately causes cracks. The key idea here is to avoid stress and breaking force accumulation via periodically interrupting the film continuity, realized by adding filler patterns which define boundaries and enclose individual local areas with manageable stress. Figure

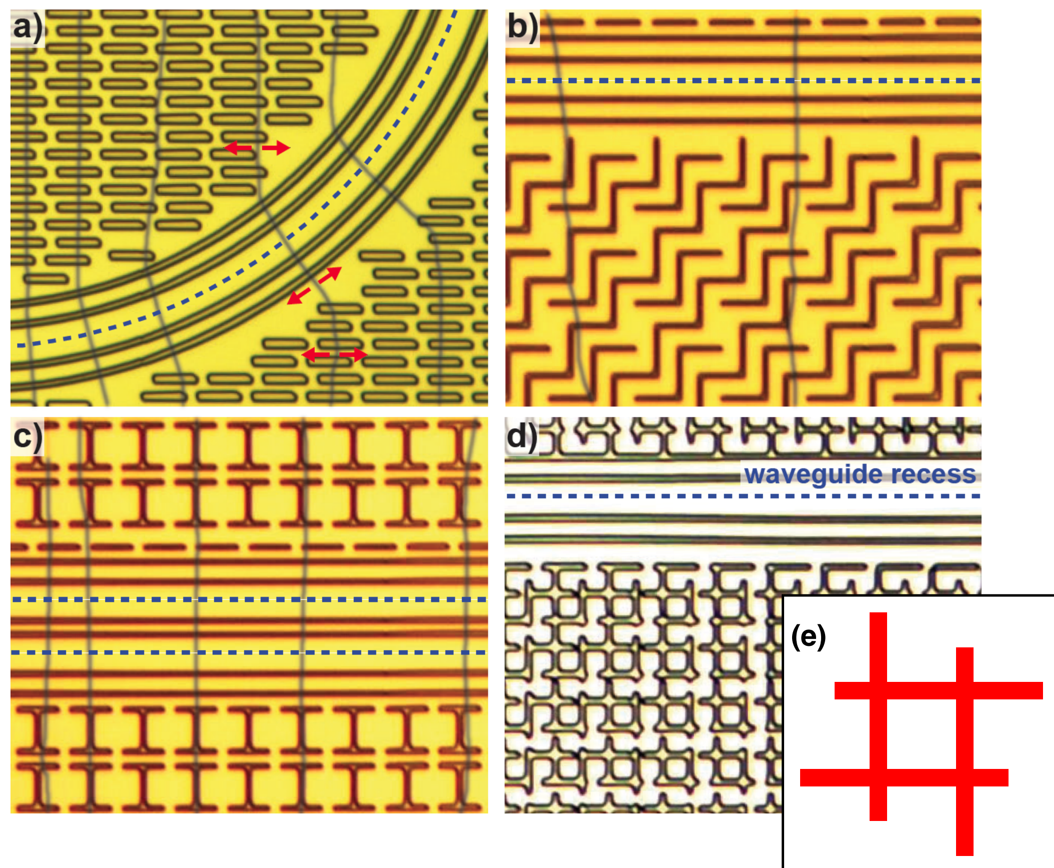

Figure 2.19 – Crack formation and propagation in tensile LPCVD Si_3N_4 film with different filler patterns. (a, b, c) Crack formation dominant in the vertical direction as a result of accumulated stress in the horizontal direction. The densely patterned horizontal bars, which break the film continuity in the vertical direction, relax the stress in the vertical direction and prevent crack formation in this direction. (c, d) The currently employed "#" filler patterns, which equal bar density in the horizontal and vertical direction, to prevent crack formation for high yield. This figure is adapted from ref. [226].

2.19 shows different filler pattern around the main waveguide structures, and crack formation and propagation in with these filler patterns. It is observed that, for example, the horizontal bars, which break the film continuity in the vertical direction, relax the stress in the vertical direction. Therefore, only vertical cracks are formed as a result of accumulate stress in the horizontal direction. It is thus optimal to place equal density of horizontal and vertical bars, which form a unit cell of "#" as shown in Fig. 2.19(d, e), to relax the stress in both directions and prevent crack formations. In addition, the filler patterns are uniformly distributed on the entire substrate, not only for crack formation but also needed for etching and planarization (will be explained later) uniformity.

The second method is to deposit Si_3N_4 in multiple cycles. In each cycle, thin Si_3N_4 film is deposited, followed by wafer cooling to room temperature to relax the stress [94, 244, 245]. However this method still has difficulty to achieve Si_3N_4 film thickness exceeding 800 nm, and is time-consuming.

Engineering Si_3N_4 film properties can also change the film stress. Silicon nitride from PECVD [246, 247, 248, 249, 250] can be used for this purpose, and the film stress can be altered from tensile to compressive stress by controlling the ion bombardment intensity via plasma RF power. Alternatively, "low-stress nitride" [251, 202, 252, 253], can be used from both the LPCVD and PECVD processes, which is silicon-rich nitride (not stoichiometric Si:N ratio of 3:4) by changing SiH_2Cl_2 to NH_3 gas flow ratio and process parameters. Besides much lower stress, silicon-rich nitride also has larger refractive index (~ 2.07) and higher Kerr nonlinearity ($n_2 = (9 \pm 3) \times 10^{-15}$ cm^2/W), while is still free from TPA. However, both nitrides have not shown so far ultralow waveguide loss below 5 dB/m, likely caused by the compromised film quality such as impurity and density.

Finally, anomalous GVD can also be achieved with thin Si_3N_4 film using coupled waveguide structures [240, 254, 255, 256], in which optical modes are highly hybridized.

The detailed process flow and parameters for reflow and LPCVD Si_3N_4 deposition are shown in Table 2.3.

Table 2.3 – **Reflow and LPCVD Si_3N_4 process**

Operation	Machine	Recipe	Parameters
RCA cleaning	RCA wet bench		300 sec SC1, 10 sec DHF, 300 sec SC2
Reflow	Diffusion tube	JLIU	1250°C, N_2 atmosphere
DHF cleaning	RCA wet bench		10 sec DHF
Si_3N_4 deposition	Nitride tube	N-Nit-NX	In two steps, e.g. 500×2=1000 nm

2.7 Planarization

Integrated waveguides are ideal for nonlinear photonics due to the high flexibility to engineer the waveguide dispersion properties via geometry variation. Such dispersion engineering is critical for generating broadband optical sources, such as octave-spanning soliton microcombs and supercontinuum. However, stringent waveguide dimension control, usually at a precision better than 20 nm, is required in order to obtain wide bandwidth via high-order dispersion engineering [89, 99]. While the waveguide width can be lithographically controlled at nanometre precision, the waveguide height is difficult to control in the Damascene process due to the planarization process.

So far the Damascene process still has non-ideal fabrication yield, mainly limited by the CMP step which remove the excess Si_3N_4 and planarize the wafer top surface. Previous works using only chemical-mechanical planarization (CMP) have achieved microcombs of octave spanning bandwidth [89, 257]. However, challenges remains in controlling the polishing rate and uniformity, which are: 1. Despite the fact that the stress-release patterns can result in thick, crack-free as-deposited Si_3N_4 film, the wafer is highly bowed when the backside LPCVD Si_3N_4 film is removed. CMP for highly bowed wafer requires high back pressure to overcome the wafer bow, thus to achieve an ideal polishing uniformity. However, the high back pressure, and the friction during the CMP, can lead to film crack, particularly common for thick Si_3N_4 film. Thus the cracks due to CMP reduces the fabrication yield. 2. CMP to remove thick Si_3N_4 film of ~ 1 μm thickness presents large polishing non-uniformity, typically exceeding 10%, particularly in the exclusion zoom. In addition, due to the fact that the film

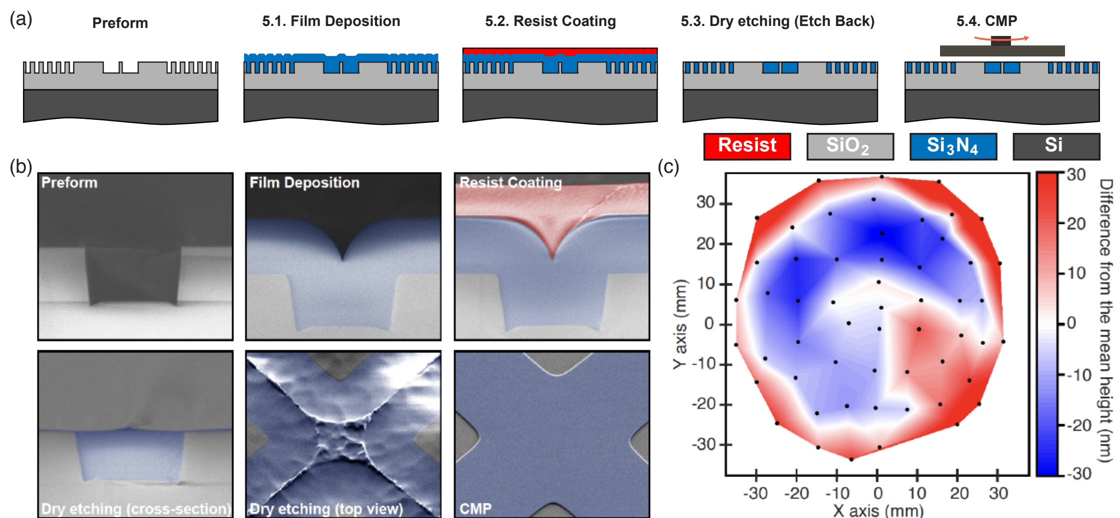

Figure 2.20 – The process flow of etch-back planarization, and the final Si_3N_4 waveguide height map. (a) Etchback process flow. (b) SEM images of the wafer cross-section / tilted top view at different step. (c) The final Si_3N_4 waveguide height measured at different positions on a 4-inch wafer. The height map is plotted in such a way that the height difference from the mean height is shown.

stress is released during CMP, the wafer bow changes accordingly, making the uniformity control very challenging. 3. Common CMP tool does not allow end point detection (EPD) for Si_3N_4 / SiO_2, which is realized based on slurry temperature / friction monitor. Over-polishing can happen, which leads to entire wafer failure. Consequently, the planarization using CMP requires frequent calibration of polishing rate and uniformity, thus is time consuming, and can lead to complete wafer failure in the case of over polishing.

To overcome the aforementioned CMP operation challenges, in this section I will present a novel planarization technique which allows crack-free, risk-free, highly uniform, fast and cheap wafer polishing with reliable EPD and sub-10-nm waveguide height control precision.

2.7.1 Etchback

The etch-back planarization process combines dry etching and CMP, as the process flow is shown in Fig. 2.20(a), and the SEM images of each step is shown in Fig. 2.20(b). After LPCVD Si_3N_4 deposition, the wafer is coated with common photoresist (PR). Depending on PR viscosity, spin-coating speed and waveguide pattern feature size, a proper PR thickness is needed for sufficient coating conformality. In our case, 600 nm PR is coated on the wafer, followed by PR reflow, to achieve a flat wafer top surface. Then an dry etching process with etch selectivity of Si_3N_4 : PR : SiO_2 =1 : 1 : 1 is used, to uniformly removing the excess Si_3N_4 together with the PR. Note that, adding O_2 increases the PR etch rate, while Si_3N_4 etch rate is largely unaffected. Figure 2.21(a) shows the etch rates of Si_3N_4 and PR as a function of the O_2 flow. Therefore by changing the O_2-to-CHF_3 ratio, independent etch rate control for PR and Si_3N_4 can be achieved. Different from the common CMP process where the end point detection (EPD) is difficult to implement, prominent EDPs can be observed on the dry etcher,

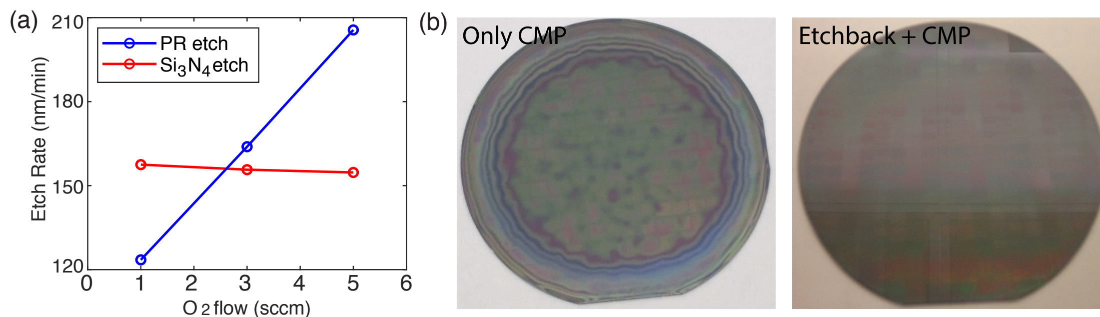

Figure 2.21 – Etchback etch rate control, and comparison of wafer images using different planarization processes. (a) When increasing the O_2 flow, the etch rate (ER) is nearly unchanged for Si_3N_4 etch, while the ER increases linearly for PR etch. It is found that, when the O_2 flow is ~ 2.5 SCCM (Standard Cubic Centimetres per Minute), the ERs for Si_3N_4 and PR etch are nearly equal (~157 nm/min). (b) Comparison of the wafer images using only CMP and CMP combined with etchback. The visible color patterns are due to nature light interference, caused by the SiO_2 thickness variation on the wafer.

Table 2.4 – **Etchback process.**

Operation	Machine	Recipe	Parameters
PR coating & reflow	ACS	No. 2114	
Dry etching	SPTS	JL-EB-1:1	Etch rate ~160 nm/min
PR removal	Tepla	High-Strip-10min	
Backside Si_3N_4 removal	SPTS	ZZ-backside-Nit	

during the transitions from PR to Si_3N_4, and from Si_3N_4 to SiO_2. Therefore the etch-back can be critically stop when all recess Si_3N_4 is removed.

After etchback, the wafer top surface, though flat, is not sufficiently smooth. A short CMP step less than 30 second, is used to reduce the roughness of the wafer top surface (sub-nm RMS roughness after CMP, measured using AFM as demonstrated in Ref. [90]), together removing a thin layer of Si_3N_4 less than 50 nm. While dry etcher is usually stable, CMP tool can drift significantly due to the usage by multi-user for multi-materials. For example, > 20% CMP removal rate drift is frequently observed. However, since the CMP process here is only to remove < 50 nm film, thus the removal rate drift does not significantly over-polish the wafer in the worst case, e.g. 10 nm over-polishing for targeted 50 nm removed film. Meanwhile, as the wafer does not suffer from Si_3N_4 stress and the wafer bow is small, the CMP polishing rate and uniformity can be easily calibrated and represent run-to-run stability. In addition, the final CMP step can serve as a fine control to reach precisely the target waveguide height, which finally allows precise waveguide height control over the full wafer scale. Figure 2.20(c) shows the measured Si_3N_4 waveguide height at different place over a full 4-inch wafer, using Nanospec reflectometer. The measured waveguide height map shows $\pm$ 30 nm variation, corresponding to $\pm$3.1% of 950 nm waveguide height, a value comparable to typical LPCVD Si_3N_4 deposition uniformity.

Figure 2.21(b) compares the wafer images using only CMP and CMP combined with etchback. The visible color patterns are due to nature light interference, caused by the SiO_2 thickness variation on the wafer. It is clear that, using CMP with etchback, the final wafer is much flatter than the case of using only CMP, leading to a better SiO_2 thickness uniformity. Table 2.4 lists the tools and recipes used for etchback process.

2.7.2 Chemical-mechanical polishing

To implement chemical-mechanical polishing, the CMP tool **STEAG MECAPOL 460** is used. The operation flow is below.

- **Slurry preparation**: Water / 30H50 = 2/1 for SiO_2 and Si_3N_4 polishing. Water / 30N50 = 2/1 for AlN polishing. Dilution with wafer is to change not only the particle density (for mechanical polishing), but also the PH value (for chemical polishing).

Table 2.5 – **CMP parameters.**

Step	Head speed	Pad speed	Pressure	Back pressure	Time
#1	50	30	0.67	-	10 s
#2	-	-	-	-	-
#3	55	67	0.7	0.43	3 min + x
#4	95	100	0.2	-	20 s

- **Parameter setup**: For the CMP parameters of each step, see Table 2.5. Check if all the following function are enabled: head and pad rotation in the clockwise direction, slurry speed at level 2, Step #1 and #3 use turbo No. 2, step #2 is skipped, back pressure in step #3 is enabled, wafer rinse is enabled in step #4.

- **Priming**: 39 s conditioning → 3 min polishing with a blank oxide wafer → 19 s conditioning → 3 min polishing with the blank oxide wafer → 19 s conditioning → 3 min polishing with the blank oxide wafer → 19 s conditioning.

- **Polishing of project wafers**: Using the parameters listed in Tab. 2.5. The polishing rate is 70 nm per 40 second.

- **Post-CMP cleaning**: full rinse in deionized water → 30 s in BHF, shaking → full SRD rinse. The post-CMP cleaning is critical to remove the contamination of CMP slurry particles from the Si_3N_4 waveguides. A comparison with and without post-CMP cleaning is outlined in Fig. 2.22.

See detailed process flow and process parameters of CMP step in Table 2.5.

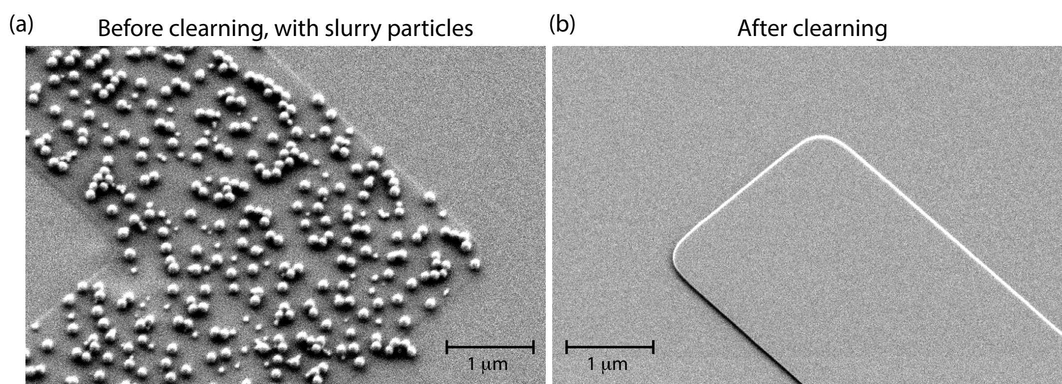

Figure 2.22 – SEM images showing the CMP slurry particles attached on the Si_3N_4 waveguides. (a) After CMP, before BHF cleaning, significant amount of CMP slurry particles are observed which only attach to the Si_3N_4 waveguides. (b) These slurry particles can be removed by BHF clean.

2.7.3 CMP dishing effect

It should be note that the dishing effect, outlined in Fig. 2.23, is commonly presented if the CMP polishing rates for the waveguide material and cladding are different. In our case, it is observed that, using the CMP slurry containing SiO_2 nano-particles, the polishing rate of Si_3N_4 is lower than that of thermal wet SiO_2, which facilitated dishing effect to occur. Therefore, the current process is only optimized for waveguide width (i.e. critical dimension) below 3 μm. Above this value, the dishing effect leads to significant roughness on the waveguide top surface which compromises the waveguide loss. A further optimization to reduce the dishing effect requires to use a different CMP slurry providing higher polish rate for SiO_2 than that of Si_3N_4, or an optimized etchback process.

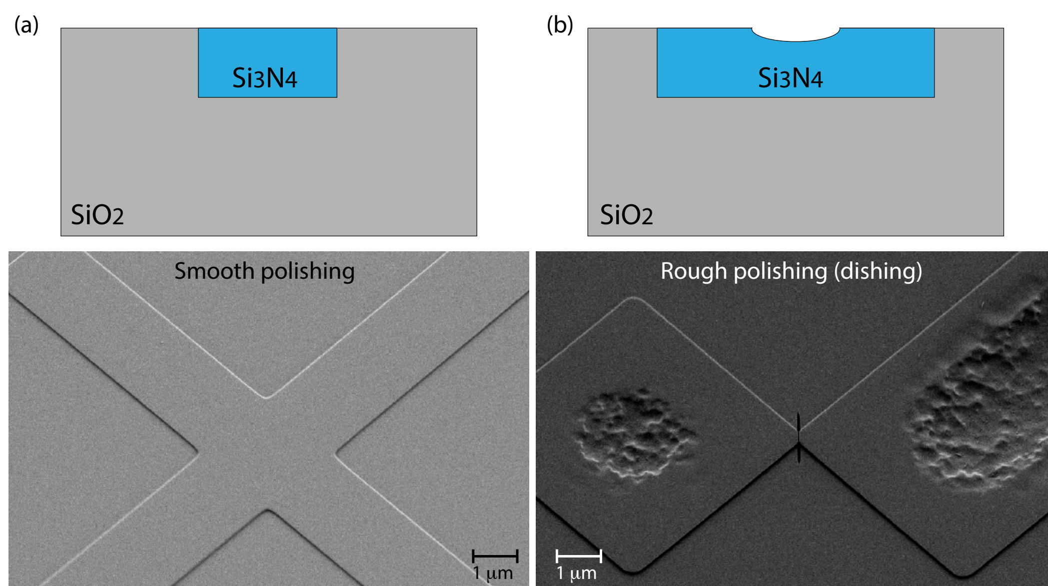

Figure 2.23 – SEM images showing the CMP dishing effects observed. (a) Smooth surface is achieved with CMP for waveguides with smaller critical dimension (below 3 μm). (b) Rough surface is resulted due to the CMP dishing effect for waveguides with larger critical dimension (above 3 μm).

2.8 Thermal annealing and SiO_2 cladding deposition

After the CMP, the wafer is thermal-annealed to drive out the residual hydrogen impurities in Si_3N_4, which are introduced during LPCVD Si_3N_4 deposition using $SiCl_2H_2$ and NH_3 as precursors. There are two kinds of hydrogen contents, Si-H and N-H bonds. At telecommunication wavelength, the absorption peaks of Si-H bonds lies around 1540 nm and the peaks of N-H bonds around 1520 nm [201, 216, 217]. The N-H bonds have higher bonding energy than the Si-H bonds, as well as the absorption cross-section. To thermally drive out the residual hydrogen contents, and to break Si-H and N-H bonds, the thermal annealing temperature needs to exceed 1100° [229]. In addition, the diffusion distance L_{diff} is typically proportional to the square root of the diffusion time t_{diff}, i.e. $L_{\text{diff}} \propto \sqrt{t_{\text{diff}}}$. Therefore, depending on the thickness of the Si_3N_4 film, the thermal annealing time needs to be varied accordingly. Usually the duration is more than 3 hours. In addition, Si_3N_4 deposition - Si_3N_4 annealing - Si_3N_4 deposition - Si_3N_4 annealing cycles [218] can efficiently reduce the required annealing time for thick Si_3N_4 film.

Figure 2.24 shows the linewidth (loss) characterization data of a partially annealed Si_3N_4 sample [91]. The intrinsic loss (blue circle) data show larger loss in the wavelength range from 1500 - 1560 nm, which corresponds to Si-H and N-H absorption bands. Samples with longer annealing time do not show this phenomena.

After the Si_3N_4 thermal annealing, top SiO_2 cladding is deposited on the wafer, to prevent direct contact of Si_3N_4 waveguide to the dust and moisture in the air. The thick SiO_2 top cladding composed of TEOS and LTO, both of which uses LPCVD processes.

- The **TEOS** process is based on tetraethyl orthosilicate $Si(OC_2H_5)_4$, a colorless liquid at

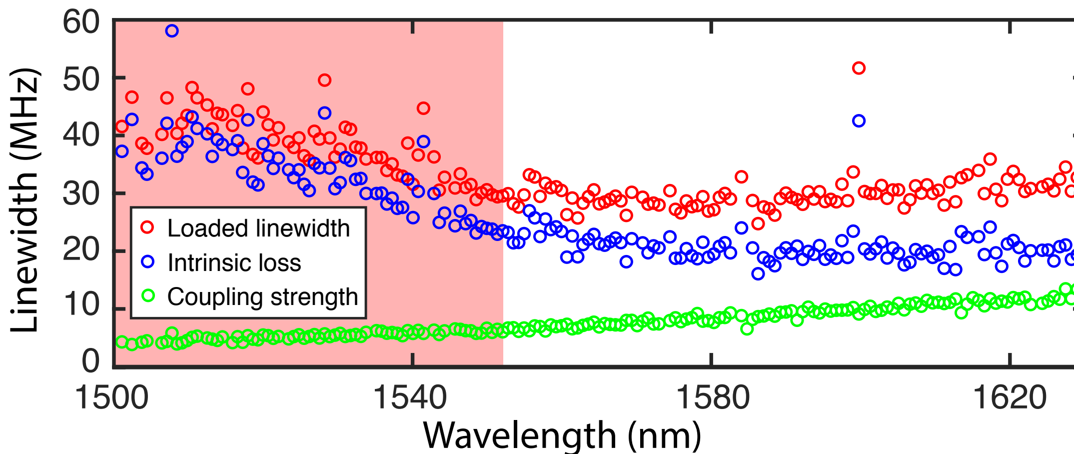

Figure 2.24 – Hydrogen absorption loss characterization of a partially annealed Si_3N_4 sample. The intrinsic loss (blue circle) data show larger loss in the wavelength range from 1500 to 1560 nm, which corresponds to Si-H and N-H absorption bands.

room temperature. The LPCVD TEOS process is based on the dissociation of TEOS at temperature exceeding 600°C:

$Si(OC_2H_5)_4 \longrightarrow SiO_2 + 2\,C_2H_4 + H_2O$

This process is known to show great step coverage and uniformity of SiO_2 deposition, as the chemical reaction is driven by surface thermodynamics, similar to the LPCVD Si_3N_4 process. While the process temperature above 600°C is not compatible with electronic circuits, the TEOS process temperature can be dramatically reduced by adding ozone (O_3) in a PECVD tool.

- The **low temperature oxide (LTO)** based on SiH_4 and O_2 is the most commonly used SiO_2 process both from LPCVD and PECVD:

  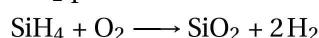

  $SiH_4 + O_2 \longrightarrow SiO_2 + 2\,H_2$

  The LTO process can be conducted at temperature of 350°, thus it is compatible with electronic circuits. However, LTO SiO_2 film is low-quality and has rich hydrogen content introduced with SiH_4. The deposition uniformity is also poor as the process is driven by gas-phase thermodynamics and the reaction rate is critically depending on the temperature. Thus the deposition uniformity is a result of the temperature gradient in the tube furnace.

- Though not used in this thesis, **high temperature oxide (HTO)** based on $SiCl_2H_2$ and N_2O is also a good choice for high-quality, low-hydrogen-impurity SiO_2. The chemical process is conducted at elevated temperature of 850 - 950° in a tube furnace

  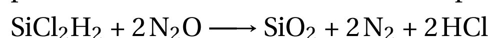

  $SiCl_2H_2 + 2\,N_2O \longrightarrow SiO_2 + 2\,N_2 + 2\,HCl$

  The SiO_2 film deposited using LPCVD HTO process is very similar to the LPCVD Si_3N_4 film, and the film stress is also high tensile.

After TEOS and LTO deposition, the entire SiO_2 cladding is thermally annealed to drive out the residual hydrogen contents. The detailed process flow and process parameters of thermal annealing and top cladding deposition are shown in Table 2.6.

Table 2.6 – **Annealing and top SiO_2 cladding deposition**

Operation	Machine	Recipe	Parameters
RCA cleaning	RCA wet bench		300 sec SC1, 10 sec DHF, 300 sec SC2
Si_3N_4 annealing	Diffusion tube	diff-CMi	1200°C, N_2 atmosphere, 3h
TEOS deposition	TEOS tube	TEOS-CMi	1000 nm
LTO deposition	LTO tube	LTO-CMi	2000 nm
LTO annealing	Diffusion tube	diff-CMi	1200°C, N_2 atmosphere, 3h
Si_3N_4 deposition	Nitride tube	N-Nit	50 nm

2.9 Heaters module

After the top SiO_2 cladding deposition and annealing, the wafer is ready to be separated into chips. At this moment, it is also possible to fabricate integrated heaters [97, 54] on top of the Si_3N_4 waveguides, in order to thermally tune the microresonators in the future. Note that, heaters based on metallic thin film are absorptive at telecommunication wavelength, therefore thick SiO_2 cladding needs to be placed between the Si_3N_4 waveguides and the metallic heaters, such that the optical mode in the Si_3N_4 waveguides does not extend to the heaters. In our case, the SiO_2 top cladding thickness is more than 2.5 μm.

The metallic materials for heaters can be aluminium (Al), gold (Au), titanium (Ti) or chromium (Cr) etc. All of these materials can be patterned via a lift-off process. In addition, Al can also be patterned via a dry etching process based on BCl_3 and Cl_2. Compared with lift-off process, dry etching of Al can provide better lithography resolution, useful to make thinner metallic wires. However, lift-off is the *only* approach in cases where direct dry etching of metals is not possible. For example, there is no dry etching process to etch Au, as Au is chemically inert to most of the aggressive etchants. In this section, only the Au lift-off process used in the current fabrication process is presented.

Before the lift-off process, the wafer needs to be shortly polished using CMP, in order to achieve smooth wafer top surface. Then the wafer is thoroughly cleaned using RCA cleaning process. Afterwards, 50 nm LPCVD Si_3N_4 and 70 nm TiN (via sputter) are deposited on the wafer. The LPCVD Si_3N_4 layer is to prevent Au diffusion into the substrate. The TiN layer also serves as a diffusion barrier to prevent Au diffusion, but more importantly it is the adhesion layer for the Au layer to grow on the wafer.

The **lift-off** process is a method to pattern structures on the wafer using a sacrificial material such as photoresist. It is an additive method as opposed to etching which is subtractive. The

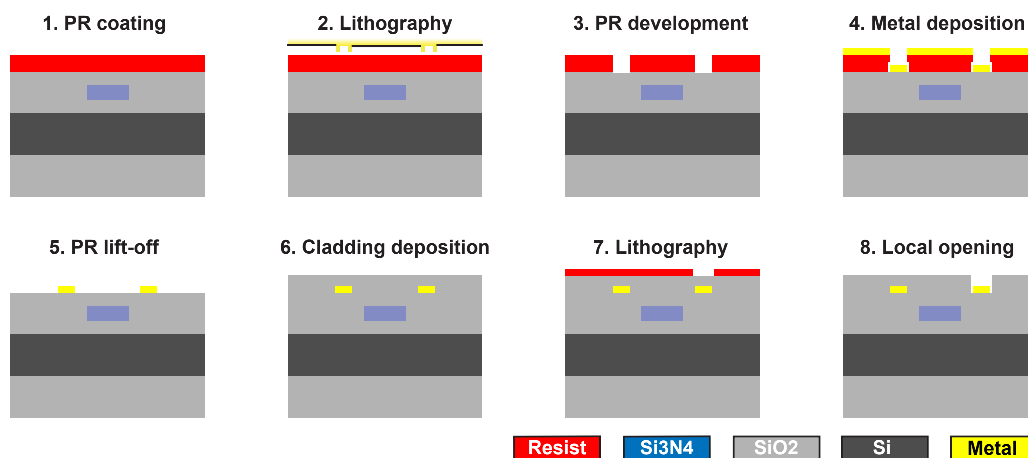

Figure 2.25 – Simplified process flow of heater deposition and patterning using lift-off process.

process flow is shown in Fig. 2.25. First, the pattern is written on the sacrificial photoresist mask coated on the wafer. The photoresist in the area where the metal wires should sit is locally removed via photolithography and resist development. A cleaning step with O_2 plasma is applied to further clean the locally opened area where photoresist is removed but residual may stay. The metal thin film is deposited over the entire wafer via sputter or evaporator. The deposited metal only reaches the wafer surface in the open area, while other part of metal sits on top of the photoresist mask. Then the sacrificial photoresist mask is removed in a photoresist solvent. Therefore, only the metal sitting directly on the wafer in the open area stays, while other part is lift-off.

In order to protect the heaters, SiO_2 capping layer can be deposited on the wafer and to cover the Au heater pattern. However, in order to preserve the Au pattern, only PECVD SiO_2 operated at the deposition temperature of 350°C is employed. No SiO_2 thermal annealing can be applied. A second lithography is implemented to locally open the SiO_2 cladding, such that the Au contact pads are accessible. Electric probes can directly contact these open pads with Au, to deliver current for heating. Figure 2.7 shows the microscope image of a fabricated sample with Au heaters and wires (the bright parts which are reflective), as well as the open pad for electric contact. The detailed process flow and parameters for the deposition and patterning of heaters are shown in Table 2.7.

Table 2.7 – **Metalic heater deposition and patterning**

Operation	Machine	Recipe	Parameters
Polishing	CMP		30 s
RCA cleaning	RCA wet bench		
Si_3N_4 deposition	Nitride tube	N-Nit-NX	50 nm
TiN deposition	SPIDER 600	TIN	70 nm
Lift-off PR coating	EVG	No EBR	700 nm LOR+1600 nm AZ1512
Pattern exposure	MLA		dose 105 mJ/cm^2, focus 0
PR development	ACS	AZ1512onLOR.0um82	
Descum	Tepla	Strip high	30 s
Au deposition	LABH600	Au	100 nm
Lift-off	Lift-off bench		overnight
IPA rinse			
SiO_2 cladding	PECVD		1000 nm
Pad opening			

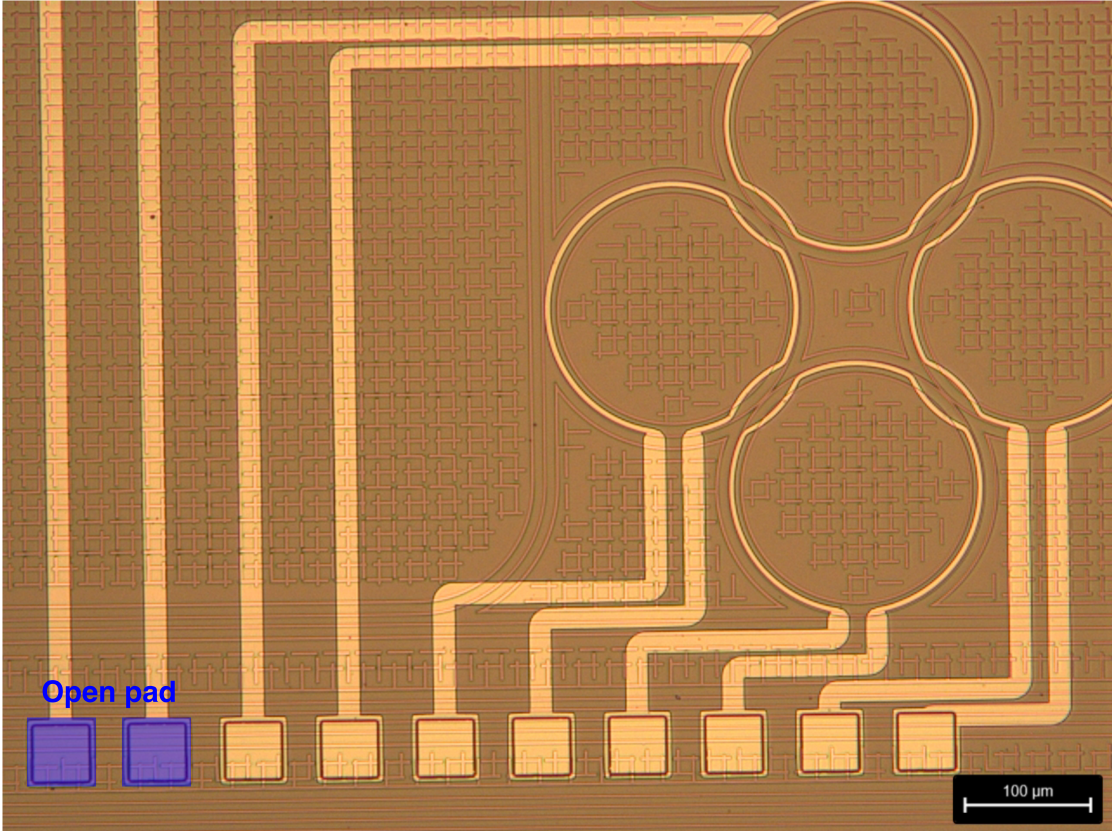

Figure 2.26 – The microscope image of a fabricated sample with Au heaters and wires (the bright parts which are reflective), as well as the open pad for electric contact.

2.10 Chip release

After the top cladding deposition and thermal annealing, the full wafer needs to be separated and released into chips in 5 × 5 mm^2 for experiments. The schematic of simplified process flow for chip release is shown in Fig. 2.27. Key idea here is to use deep RIE to etch the wafer frontside, which defines the chip facet, and then use backside grinding to separate the chips. Note that, dicing can also be used for chip release and separation. The advantage of deep RIE used here is to achieve much smoother chip facet compared with the facts achieved by dicing. In addition, the deep RIE can work with chip separation distance less than 10 μm, while dicing requires the distance larger than 100 μm. Thus chips can be placed more tightly on the wafer.

Figure 2.28 shows the SEM image of the chip facet with superior quality, using deep RIE to define the facet. Such high-quality, smooth facet is critical for laser self-injection locking [170, 69, 70], where the Si_3N_4 chip is directly butt-coupled to a laser diode. In this case, the smooth facet of the Si_3N_4 chips enables seamless contact with the laser diode, thus high optical power coupling efficiency from the laser to the Si_3N_4 chip. More details on laser self-injection locking will be illustrated in the following chapter.

In the following in this section, detailed illustration of the process steps and parameters are provided.

2.10.1 Photolithography

The lithography step is to define the chip boundaries and facets. The lithography can be implemented using either direct laser writer (**Heidelberg MLA 150 Maskless Aligner**), or contact mask aligner (**Süss MA3Gen3 Mask Aligner**). Both lithography tools use UV light source e.g. from mercury i-line, and require alignment as the chip release layer needs to be superimposed on the waveguide pattern with reasonable overlap precision. Both processes

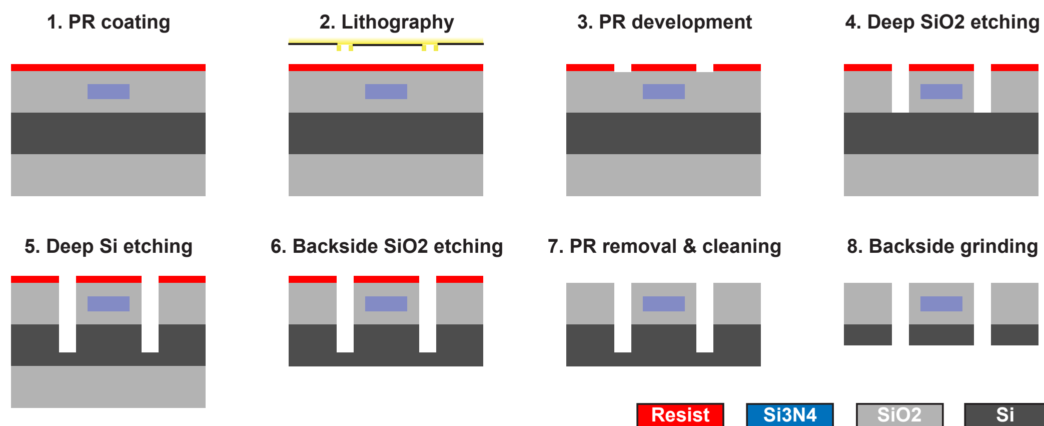

Figure 2.27 – Simplified process flow of chip separation steps.

can reach minimum feature size of 1 μm (determined by the UV wavelength, photoresist thickness, and exposure parameters). To reach the optimal lithography quality, optimal parameter sets of dose and focus are needed, and can be found via a series of test. Both methods require alignment markers for lithography alignment.

The advantages of using direct laser writer include:

- Quick writing a test or unqualified design, without the need to prepare a separate mask.
- Modification of the same design from run to run is easy and quick.
- Alignment accuracy better than 500 nm.

The main disadvantage is that, each exposure job takes ~ 30 min. Thus if the same design needs to be written on many wafers, directly laser writing is not economical.

The advantages of using contact mask aligner include:

- Each exposure is less than 1 min, thus if the same design needs to be written on many wafers, this method is economical.
- Flood exposure can be easily implemented.

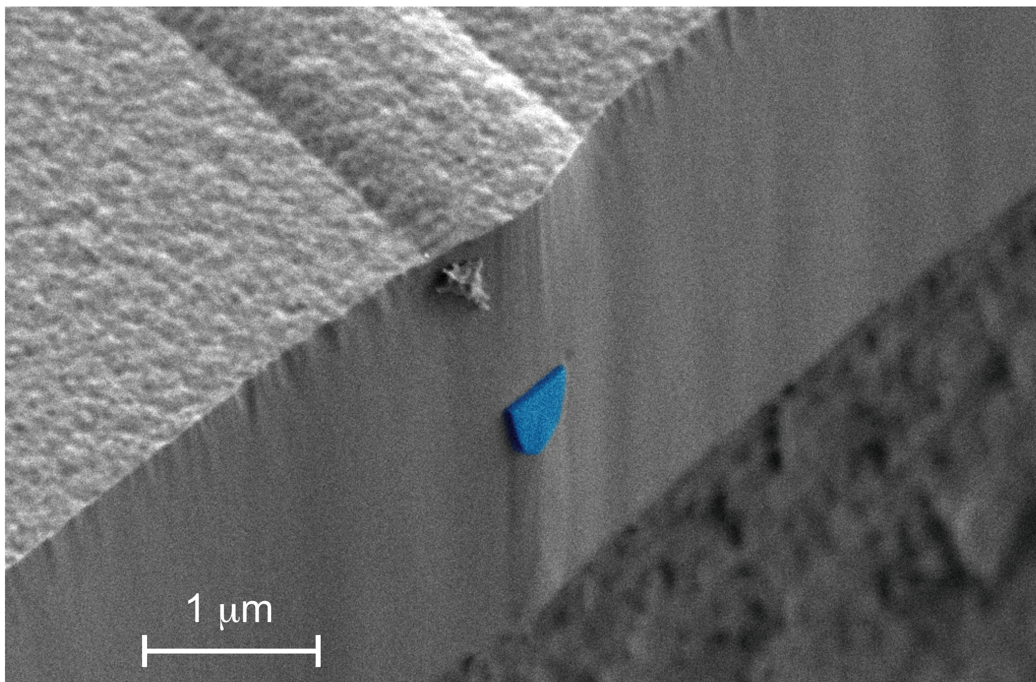

Figure 2.28 – SEM image showing the chip facet with superior quality, using deep RIE to define the facet.

The main disadvantages are:

- A separate chrome mask needs to be prepared separately. The chrome mask can be written by direct laser writer, e.g. **Heidelberg VPG 200 Laser Writer**. However, every new design requires a different chrome mask, so this method is not economical for quick prototype,
- The edge bead removal (EBR) after photoresist coating on the wafer is absolutely critical and can significantly impact the lithography quality.

Figure 2.29 shows the design layout to separate a 4-inch wafer into chips, with four alignment markers (cross) used to align the chip release layer to the waveguide pattern.

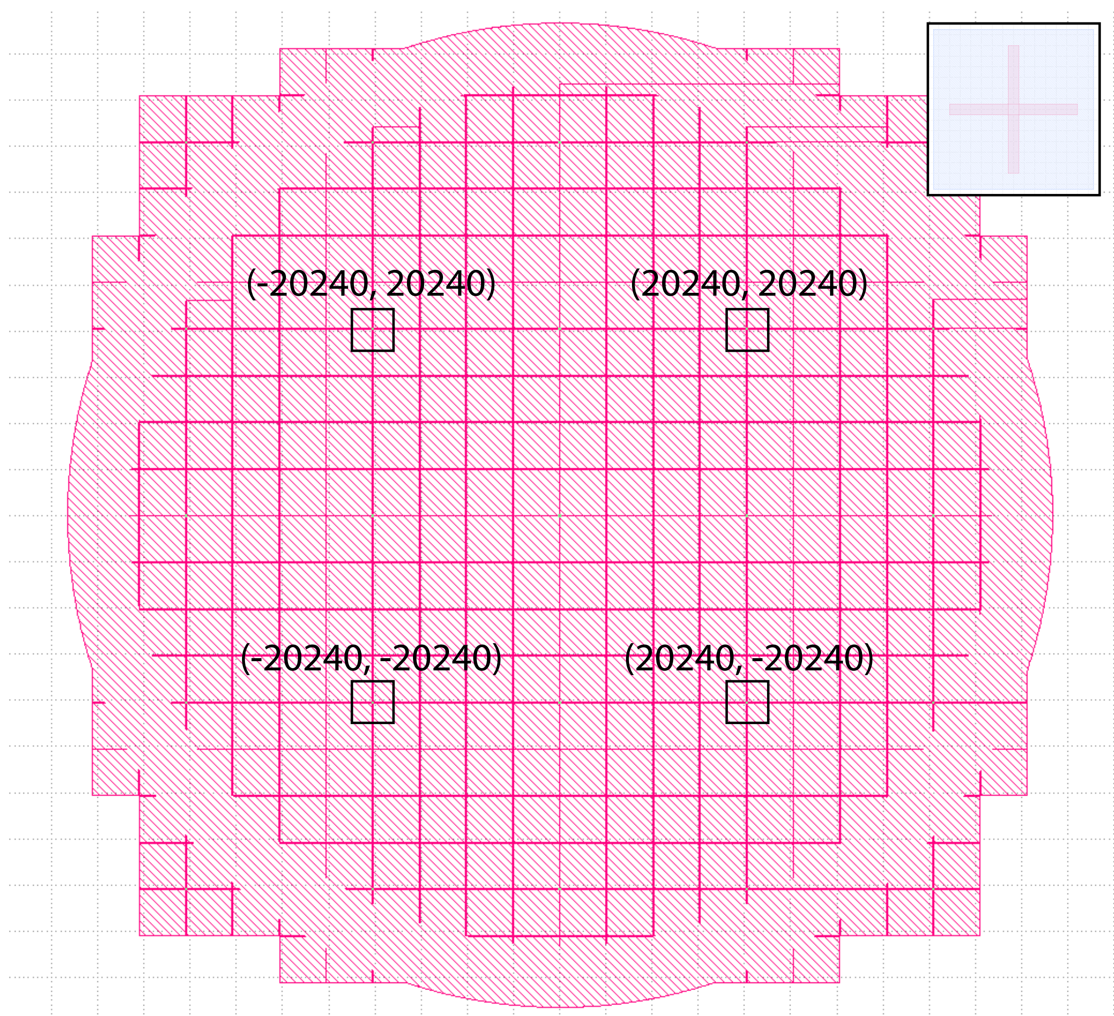

Figure 2.29 – Design layout to separate a 4-inch wafer into chips. Four alignment markers (cross) are used to align the chip release layer to the waveguide pattern.

2.10.2 Photoresist

As deep RIE follows, the photoresist needs to be thick enough, and the deep RIE needs to have a modestly high SiO_2-to-resist and Si-to-resist selectivity. In addition, deep RIE requires long etch time, thus the wafer backside needs to be thoroughly clean such that resist burning must not happen. With several concerns and limitations, currently there are two photoresists used in the chip release lithography: AZ9260 and AZ15nXT.

AZ9260 is a *positive* photoresist with high viscosity, thus it can form thick resist layer from 5 μm to 20 μm. Making thinner resist layer requires dilution of AZ9260. It is UV-sensitive to, thus can be exposed by, mercury i-line and h-line from 310 to 410 nm wavelength.

In the chip release process, 8 μm thick AZ9260 is coated on the wafer, after an HMDS layer is applied in the gas phase as an adhesion promoter for AZ9260 on the heated wafer substrate. Both HMDS and AZ9260 are applied in **Süss ACS200 Coater**.

After the resist coating, the wafer is placed in humid environment for 20 min, in order to rehydrate AZ9260. As AZ9260 is based on DNQ, and the photo-chemical reaction of DNQ consumes water and release nitrogen, the resist rehydration, particularly for thick resist like 8 μm AZ9260, is required in order to achieve complete photo-chemical reaction, and removal of exposed resist after resist development.

After the resist rehydration, the wafer is exposed with UV lithography described above. After the exposure, the resist is developed with **Süss ACS200 Developer**. An examination of exposure / development results with an optical microscope is needed. Figure 2.30 compares the microscope images of chip boundaries after photoresist development. The bad lithography quality can result from insufficient exposure (usually due to insufficient dose), insufficient development, or EBR issues.

Before the deep RIE, two steps need to be performed: 1. As mentioned earlier, the photochemical reaction of DNQ consumes water and release nitrogen. RIE generates plasma and can emit UV light, which will expose the unexposed AZ9260 resist. The release of nitrogen

Table 2.8 – **AZ9260 lithography process**

Operation	Machine	Recipe	Parameters
PR coating	ACS	No. 350	HMDS, 8 μm AZ9260, EBR
PR rehydrate			20 min in moisture environment
Exposure	MA3Gen3	JL.tsa.ma	i-line, 1200 mJ/cm^2, alignment
PR development	ACS	No. 950	
Flood exposure	MA3Gen3	JL.ma.flood.line	3000 mJ/cm^2
Cleaning	SRD	program 1	full cleaning

can swell the resist, leading to CD drift and rough resist surface. Thus, to prevent the resist exposure by the UV light during deep RIE, a flood exposure with sufficient dose, e.g. 3000 mJ/cm^2, is needed. 2. The wafer needs a thorough SRD cleaning, in order to remove backside contamination during resist development, which frequently happens due to the dirty chuck of the photoresist developer. Once the chip release pattern is well defined on the resist, the wafer can proceed with the deep RIE.

The detailed process flow and parameters of lithography with 15NXT are shown in Table 2.8.

During the process development, it is found regularly that, AZ9260 can easily get burned in the deep RIE of SiO_2 etch, especially when the wafer backside is contaminated due to the

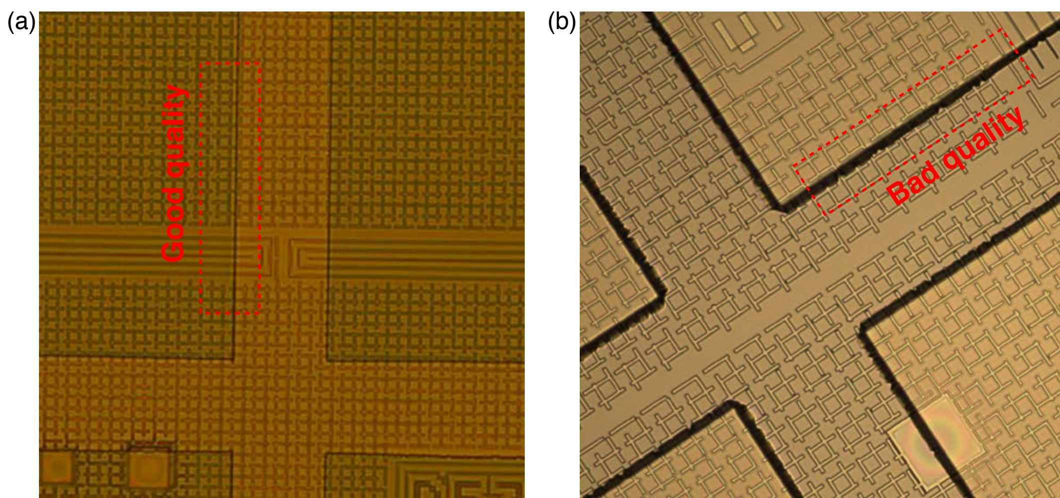

Figure 2.30 – Microscope images of chip boundaries after photoresist development, comparing good (a) and bad (b) lithography quality.

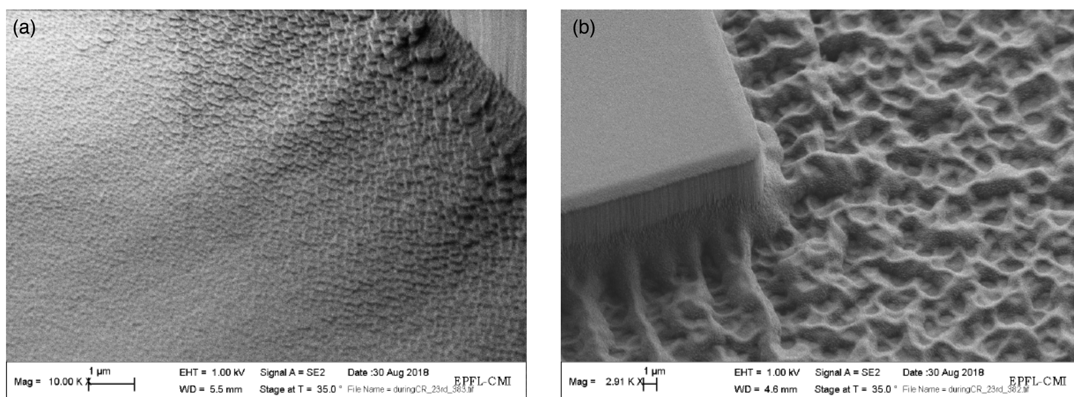

Figure 2.31 – (a) AZ15NXT photoresist staying in the zoom where it should be clear. The fish-scale shape is the typical topography of photoresist. (b) If the etch zoom is covered with resist, and dry etching process will lead to extremely rough etch.

photoresist development, or other reasons. Therefore, when using AZ9260, particular caution needs to be paid on the wafer backside, and the helium leakage pressure in SPTS during SiO_2 RIE (helium leakage pressure exceeding 200 mTorr will surely burn AZ9260). If the AZ9260 gets burned during dry etching, the chip facet will be extremely rough, leading to very low edge coupling efficiency, typically $< 5\%$.

To solve this issue, **AZ15nXT** process has been developed and used. AZ15nXT is a cross-linking *negative* photoresist based on chemical amplified resist (CAR), and can form thick resist layer of 10 μm. It is UV-sensitive to mercury i-line. More importantly, it has much better thermal resistance and thus less chance of resist burning than AZ9260. As the photo-chemical reaction is based on CAR, resist rehydration and flood exposure are not needed for AZ15nXT.

The exposure of AZ15nXT is usually done with MA3Gen3 mask aligner, with contact lithography. As AZ15nXT is negative tone, and the contact lithography is used, the EBR is particularly important. Bad contact of the coated wafer with the chrome mask, due to the problematic EBR during coating, will ruin the lithography, leaving considerable amount of photoresist in the place where it should be clear, after the photoresist development. For example, the trench between the chips should be clear, thus it is the zoom where dry etching targets. However due to the EBR issue, this zoom can be slightly exposed during contact lithography, thus resist development still leaves some resist in the trench, as shown in Fig. 2.31. Without removing the residual resist, the dry etching only makes the topography worse.

The detailed process flow and parameters of lithography with 15NXT are shown in Table 2.9.

2.10.3 Deep RIE

For the deep RIE of SiO_2, the ideal process needs to be: 1. Fast, i. e. high etch rate; 2. High selectivity of SiO_2 to photoresist; 3. Vertical; 4. Smooth. Including all factors together and their balance, the chosen process recipe for SiO_2 etch is "SiO_2 PR3:1" on **SPTS APS**. The etch rate is around 340 nm/min, and the SiO_2-to-resist selectivity is around 4. Typically, for 7 μm SiO_2, 25 min etch is needed; for 9 μm SiO_2, 30 min etch is needed. These times ensure the complete removal of SiO_2.

Afterwards, deep RIE of Si follows. The chosen process recipe for Si etch is "SOI_Accu_++++"

Table 2.9 – **AZ15NXT lithography process**

Operation	Machine	Recipe	Parameters
PR coating	ACS	No. 2021	15 μm 15NXT, EBR
Exposure	MA3Gen3	JL.tsa.ma	i-line, 350 mJ/cm^2, alignment
PR development	ACS	No. 2014	
Cleaning	SRD	program 1	full cleaning

on **Alcatel AMS200**. This process is based on the **Bosch process**, and has an etch rate of Si around 5 μm/min, and the Si-to-resist selectivity exceeding 75. Typically 45 min process time removes >250 μm Si depth using the Bosch process.

The detailed process flow and parameters of deep RIE and wafer cleaning are shown in Table 2.10.

2.10.4 Grinding

The last step is grinding of the wafer backside. The wafer backside is Si, so the grinder should be configured for Si grinding. The process is for Si grinding (recipe number 25, with P2 cut = 10 μm and P3 cut = 50 μm). The finial sample thickness is 250 μm (chip thickness) + 140 μm (tape thickness) = 390 μm. The thickness control needs to be reasonable precise, so the polishing rate needs to be calibrated in the first run (e.g. to a thickness value around 500 μm).

The wafer needs to be taped 24 hours before the grinding, for good adhesion with the tape during grinding, in order to avoid wafer detaching from the tape. To tape the wafer, first, install wheel frame which should be magnetically attached to the tape setup. Second, place the wafer on the stage for 4-inch wafer, and activate the vacuum. Third, use the roll stick to check if the wafer is slightly higher than the wheel frame, and lift up the stage if not. Fourth, cover the wafer and wheel frame with the tape, and facilitate the tape attach with the roll stick, such that no bubble is presented. Last, cut the tape, deactivate the vacuum for the wafer, and remove the wheel frame together with the wafer. If the wafer attaching to the tape is not good, do not detach it by force. Use the UV lamp to cure the tape with three full passes, and afterwards the wafer can be easily detached from the tape.

To start the grinding, first of all, make sure that the adequate wheel is installed on the tool (check empty storage box). Run a first grinding with a target thickness of 500 μm (360 μm wafer thickness +140 μm tape thickness). Check the final thickness and adjust it with the offset parameter on the tool. Also, confirm that the spindle current does not exceed 6.7 A. If the spindle current exceeds this value at any moment during the process, check the roughness of

Table 2.10 – **Deep RIE process**

Operation	Machine	Recipe	Parameters
SiO_2 etch	SPTS	SiO2-PR-3:1	Etch time 30 min
Si etch	AMS	SOI-accu-++++	Etch time 45 min
backside SiO_2 etch	SPTS	zz-oxide-etch	Etch time 30 min
PR removal	Tepla	High-Strip-15min	
DHF clean	Plade Oxide		DHF 30 sec
Dry	Plade Oxide		Manual N_2 gun blow

the work piece and dress the wheel for at least 50 μm.

All subsequent wafers can be ground in one step to the final thickness of 390 μm (250 μm wafer thickness +140 μm tape thickness). The final steps should be run at a lower in-feed (P2 cut = 10 μm at 0.5 μm/sec removal rate, and P3 cut = 50 μm at 0.3 μm/sec removal rate). After the grinding is complete, the tape needs to be fully cured (two or three passes under the UV lamp), before being cut and stored in a box for collection.

3 Design and simulation of Integrated Photonic Circuits

This chapter will describe the design and simulation of photonic circuits. The main waveguide structures, consisting of polygons with any number of vertices are created using the Python programming language with the package **Gdspy**. The generated photonic circuit layout can be directly imported into simulation software of light propagation in integrated circuits. In this chapter, the simulation of chip input coupling (i.e. from an input fibre to the bus waveguide on the chip) and the bus-waveguide-to-microresonator will be presented in details. Experimental characterization data will be shown, which agree with and validate the simulations.

3.1 Photonic circuit design using Python's Gdspy package

The photonic circuit design file is usually in the **GDSII format**. The GDS format is widely used as industry standard format for data exchange of integrated circuit layout. It shows the planar geometry of integrated circuit layout in a hierarchical order. Shapes belong to the same group are placed in the layer (level). The data in each layer or combined layer are used to create photomask for lithography fabrication, or input in software to simulate the device behaviour. Figure 3.1 shows the design layout of our Si_3N_4 photonic circuits. Since our design is quite simple, and only contains Si_3N_4 photonic circuit in one plane, therefore all the data structures, including ring resonators, waveguides, tapers, text labels, stress-release filler pattern, and lithography alignment markers, are in the same layer.

The Python package **Gdspy** used for photonic integrated circuit design is an open source to create GDSII stream files. The module provides a scripting environment for adding geometries on each layer and eventually exporting them into GDSII format. Here, the code structure for circuit design and the core methods involved in the coding are shown. The design scripts can be separated into two parts: defining a class for the chip based on target geometries, and a main function that generates GDSII file using this specific class. The entire code flow chart is shown in Fig. 3.2. Each of these steps implemented in coding is illustrated in the following.

- A class for the chip design should create an object including all the tunable parameters

defining this design, and a method to draw the geometries or polygons using these parameters. Notably all geometries / polygons must be added in a **cell** object, which is created in the main function. To define the cell, the code should have the structure as:

$$def\ __init__(self, cell):$$
$$\quad self.parameter1 = DefaultValue1$$
$$\quad \ldots$$
$$def\ draw(self, cell):$$
$$\quad \ldots$$

Inside the *draw* method, each of the geometries / polygons is added to designate the positions and layers of each components. The generated geometry is then placed in the cell with:

$$cell.add(Geometry)$$

Three types of geometries can be created: polygons, paths and texts.

– As an example for polygons, the following code draws a box:

$$gdspy.Rectangle(lowerleftCorner,$$
$$upperrightCorner, layer = layerNumber)$$

And for the rings:

$$gdspy.Round(center, OuterRadius, InnerRadius,$$
$$number_of_points = 3000, max_points = 1000,$$
$$layer = layerNumber)$$

Note that, the curvatures and holes are approximated by polygons with a large number of vertices. Therefore, it is important to estimate how many vertices are needed in order to create a smooth ring or circle. In the *Round* method, the

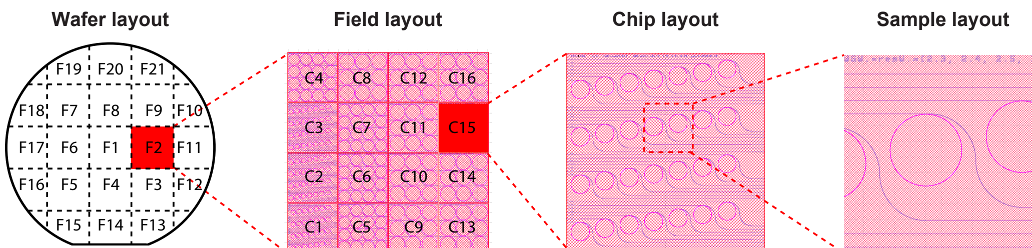

Figure 3.1 – Schematic of the wafer and reticle layout showing in the GDS format.

number_of_points determines the vertices in the polygon. When this number is larger than *max_points*, the ring is constructed using multiple polygons satisfying the vertices limitation. It is also possible to transform the polygons with Gdspy methods.

– Besides polygons, Gdspy can also create paths, which are also stored as polygons or combination of multiple polygons. This is usually how waveguides are drawn. A

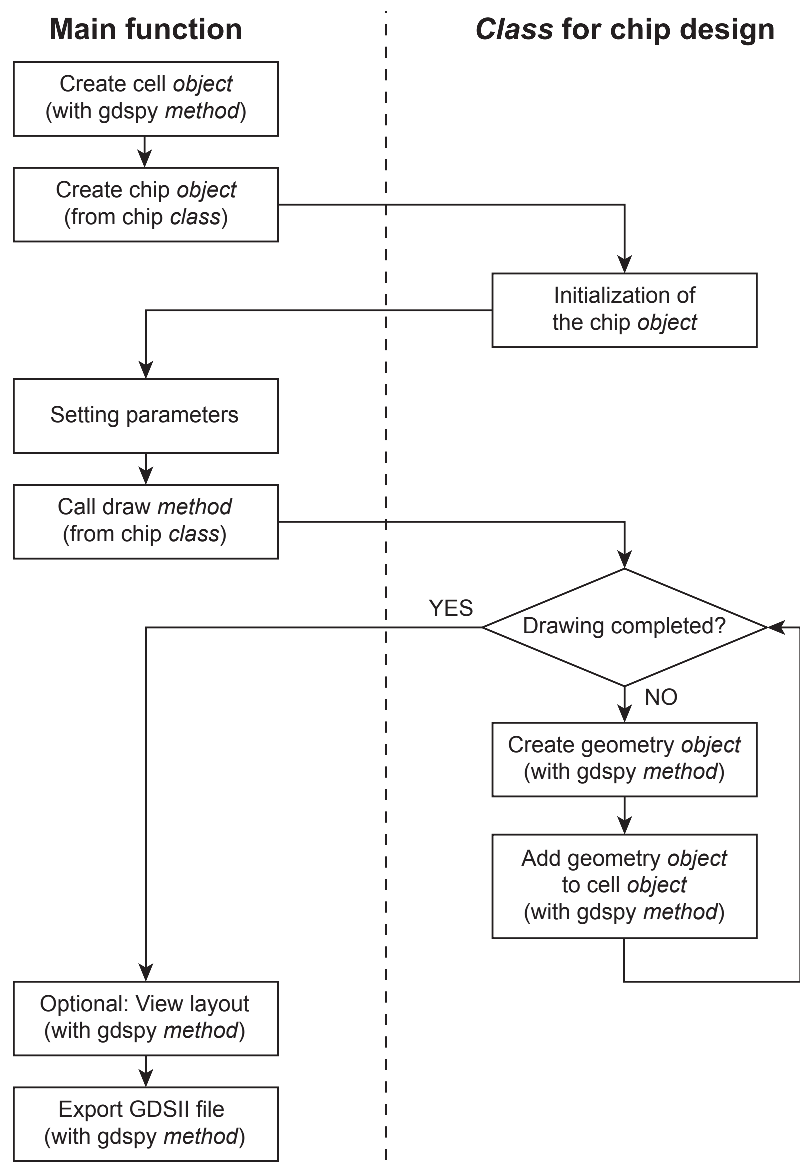

Figure 3.2 – Chart showing the code flow to generate integrated circuits in the GDSII format, using Python's Gdspy package.

path is created with:

$$waveguidePath = Path(width = Initial_width, \\ initial_point = (x, y))$$

After setting the start point, the path is extended with:

$$waveguidePath.segment(Length, final_width = Finalwidth, \\ layer = layerNumber)$$

– In addition, ASCII annotations can be generated with:

$$gdspy.Text(text =' Text', size = TextSize, \\ position = (x, y), layer = layerNumber)$$

- In the main function, the script calls the method in the chip class and generates the GDSII file. First, a cell object needs to be created as the input:

$$cell = gdspy.Cell(cellname) chip = ChipClass(cell)$$

The parameters can be changed using the returned chip object:

$$chip.parameter1 = NewValue1$$

After initialization, use the defined draw method and create the layout:

$$chip.draw(cell)$$
$$gdspy.LayoutViewer()$$
$$gdspy.write_gds('FileName.gds')$$

Table 3.1 shows the key components that need to be defined in the circuit design using Gdspy.

3.2 Finite-difference time-domain method

The **finite-difference time-domain (FDTD)** [258, 259] method is a numerical analysis technique used for modelling computational electrodynamics. It solves Maxwell's equations in the time domain using finite-difference approximations. Being a time-domain method, FDTD can cover a wide frequency range with a single simulation run and treat nonlinear material properties in a natural way. It works by creating a "movie" of the fields flowing through a device, thus is more intuitive than other finite-element techniques.

The FDTD method belongs to the general class of grid-based differential numerical modelling

methods (finite difference methods). The time-dependent Maxwell's equations in the partial differential form, i.e. Ampere's and Faraday's laws, are discretized using central-difference approximations to the spatial and temporal derivatives. As firstly proposed by Kane Yee in 1966, the FDTD algorithm employs the second-order central differences, and it can be summarized as follows:

- 1. All the derivatives in Ampere's and Faraday's laws are replaced with finite differences. The space and the time are discretized such that the electric and magnetic fields are staggered in both the space and the time domains.
- 2. The resulting difference equations are solved to obtain the "update equation" that express the (unknown) future fields in terms of the (known) past fields.
- 3. The magnetic fields one time-step into the future is evaluated so they are now known (effectively they become past fields). Such evaluation relies on the electric field one time-step before.
- 4. The electric fields one time-step into the future is evaluated so they are now known (effectively they become past fields). Such evaluation relies on the magnetic field one time-step before.
- 5. The previous two steps are repeated until the desired transient or steady-state electromagnetic field behaviour is fully evolved.

As shown in the step 3 and 4, the magnetic field is advanced in time, and then the electric field is advanced. A method in which one field is advanced and then the other, and then the process is repeated, is known as a **leap-frog method**.

Table 3.1 – Key components defined in the photonic integrated circuit design.

Layer	Function
1	Lithography alignment markers
2	Straight waveguide only in the perfect horizontal or vertical directions
3	Straight waveguides which does not belong to Layer 2, and curved waveguides
4	Label and text
5	**Exclusion zoom** covering all the main structures
6	Chip size frame, typically 5×5 mm^2
7	Chip release frame, typically 4.96×4.96 mm^2
8	Ring resonators
9	Pulley coupler waveguides
11	Dummy waveguide next to the main waveguide structures
21	Stress release filler pattern which uniformly covers the entire design area except the exclusion zoom (Layer 5)
51	Frame defining the unit cell of filler pattern

In FDTD simulations there are restrictions on how large a temporal step Δ_t can be. If it is too large, the algorithm produces unstable results quickly extending to the infinity. To prevent the numerical divergence, it must be satisfied that $c\Delta t \leq \Delta x$, where Δx is the minimum meshed space cell and c is the speed of light. This is because in the FDTD algorithm each node only affects its nearest neighbours and the effect should not extend further than the light propagation distance. It turns out that the optimum ratio, defined as **Courant number** S_c, is the maximum ratio as

$$S_c = \frac{c\Delta_t}{\Delta_x} \tag{3.1}$$

Treating time as an additional dimension adds more complication. Therefore in most situations, it is more convenient to treat only space grid while time grid only makes the electric and magnetic fields a half spatial step offset from each other.

Defining the boundary of the the simulation zone is also important. Contrary to the metal boundary condition which reflects all incident waves, the **perfectly matched layer** (PML) [260] is generally considered to eliminate the boundary reflection. Involving with time, the most used PML formulation today is the convolutional-PML (CPML).

FDTD has several computational advantages, as it is intuitive for learning, excellent for large-scale simulations, excellent for broadband and transient simulations, and it naturally handles linear and nonlinear behaviour with dielectric and magnetic materials. FDTD also have several drawbacks. Since FDTD requires meshing the entire computational domain with the grid spatial discretization sufficiently fine to resolve both the smallest electromagnetic wavelength and the smallest geometrical feature in the model, it generates very large computational domains and requires a very long simulation time. Employing the symmetries of the certain structures to be simulated, artificial boundary conditions inside the simulation zone such as "symmetric" or "anti-symmetric" depending on the field polarization across it can be employed such that simulation volume and time are reduced by 1/2, 1/4 or 1/8. Other drawbacks include tedious to incorporate dispersion, curved surface not efficiently represented by structured grids, slow for small devices, difficult to models with long and thin features such as wires as well as far-field extensions, very inefficient for highly resonant devices etc.

In this PhD thesis, **Lumerical FDTD Solutions** is used to model the FDTD simulation. Lumerical FDTD is a high-performance 3D FDTD Maxwell solver for the design, analysis and optimization of nanophotonic devices, processes and materials. It is widely used for photonic integrated circuits design by industry.

3.3 Inverse taper coupler: simulations

Central to nonlinear photonic applications is the ability to couple light to photonic chip devices with low loss over a broad optical bandwidth. Widely employed grating couplers [261] are not well suited for this purpose due to their restricted bandwidth. In contrast, inverse nanotapers [241], possessing simultaneously high coupling efficiency, broad operation bandwidth and the use of standard CMOS-compatible fabrication process, are widely used in integrated photonic devices and particularly well suited for nonlinear integrated photonics. An inverse taper works as a mode transformer which adiabatically transforms an incident fibre or free-space optical mode (of several micron mode diameter) to a waveguide mode (of sub-micron mode diameter). The taper mode at the device facet matches the incident fibre or free-space mode, due to the small taper waveguide size and thus the strong evanescent field.

Here, only the case of coupling light from a lens fibre to a Si_3N_4 waveguide via an inverse taper is considered, as shown in Fig. 3.3. The lens fibre and the inverse taper together form a mode transformer which transforms the fibre mode to the waveguide mode.

A **lens fibre** is a fibre whose one side is a common optical fibre and the other side is a micro-lens, connected by a tapered fibre. There are two types of lens fibres [262]. The **tapered-cladding** lens fibre has a uniform core with a tapered cladding, fabricated by etching, fire polishing and melting [263]. The **tapered-core** lens fibre has a tapered core and a tapered

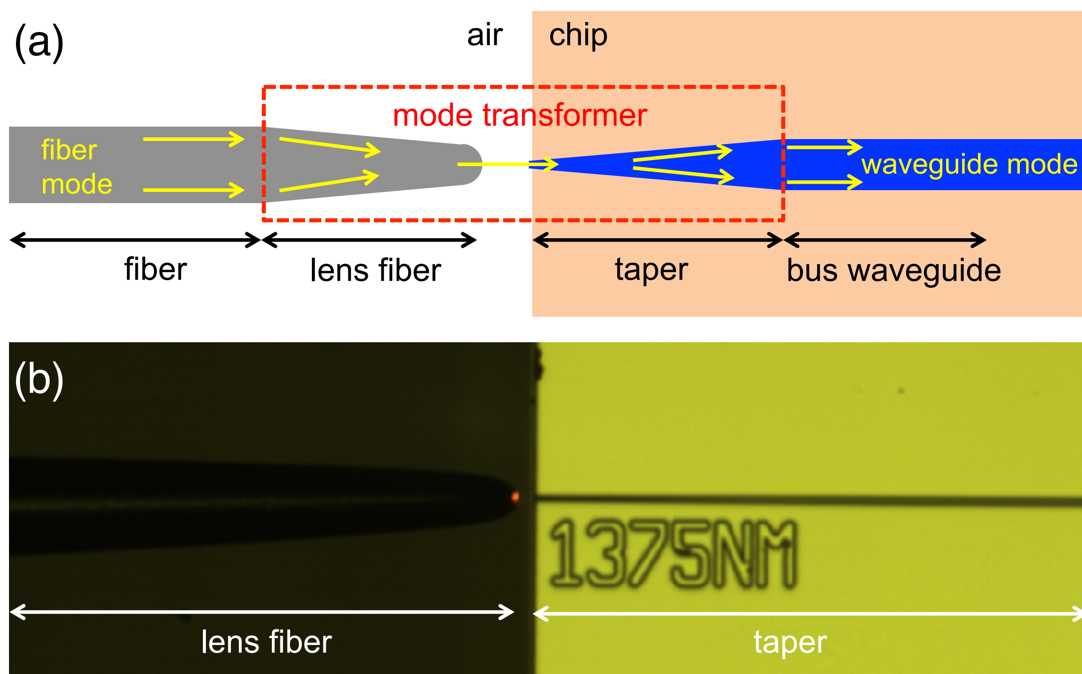

Figure 3.3 – (a) Schematic of the mode transformer composed of a lens fibre and a taper coupler to transform the fibre mode to the waveguide mode. (b) A photo showing the lens fibre and the taper coupler under the microscope.

cladding, fabricated by fibre pulling and melting. The lens fibre can transform the fibre mode into a tightly focused Gaussian beam spot in free space. Depending on the fabrication and the geometry of the lens fibre, the Gaussian mode diameter varies and can be reduced to below 2 μm. A simple way to measure the Gaussian mode diameter is to measure the Gaussian beam divergence, and the diameter is calculated by the Gaussian beam formula $\theta = \lambda/(\pi w_0)$ [264]. Note that the mode radius is a near-field property and the divergence is far-field property. Measuring the Gaussian mode radius at near-field is inevitably introduced averaging, thus the measurement is not precise. Measuring the beam divergence at far-field suffers less from the averaging issue, thus should be more precise. As the lens fibre transforms the fibre mode into a free-space Gaussian beam mode, the coupling model is reduced to the case of **coupling light from a free-space Gaussian mode to the waveguide mode**. For the lens fibre used in this thesis, the calculated Gaussian mode radius varies from 2 μm to 3 μm.

A **taper coupler** is a tapered waveguide that transforms the Gaussian mode in free space into the bus waveguide mode. There are two types of taper couplers. The **funnel-type** taper coupler [262, 265] has a large input cross-section size and the waveguide is gradually tapered down to the normal bus waveguide size. The **inverse-type** taper coupler [241, 266] has a small input cross-section size and the waveguide is gradually expanded up to the normal bus waveguide size. Both types of taper couplers are shown in Fig. 3.4.

Each type of the taper couplers are used in different situations. In this thesis, the inverse taper is often used, thus this type of tapers is the main focus. The funnel-type can be used to couple light of 780 nm wavelength where the photolithography resolution is insufficient to pattern small inverse taper with sub-100-nm critical dimension.

The coupling efficiency between the free-space Gaussian mode and the inverse taper mode is determined by the mode mismatch, including:

- **Effective index mismatch** is due to the reflection at the interface of air to the waveguide,

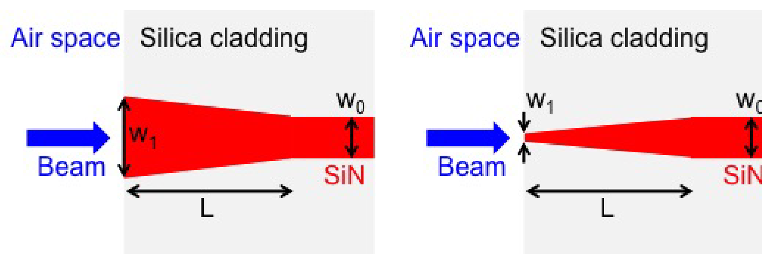

Figure 3.4 – (a) The funnel-type taper coupler which has a large input cross-section size w_1 and the waveguide is gradually tapered down to the normal bus waveguide size w_0. (b) The inverse-type taper coupler which has a small input cross-section size w_1 and the waveguide is gradually expanded up to the normal bus waveguide size w_0. L is the length of the taper.

described by the Snell's law as

$$T = \frac{4n_1 n_2}{(n_1 + n_2)^2} \tag{3.2}$$

where T is the transmission coefficient at the interface and n_1, n_2 are the respective (effective) refractive indices at both sides of the interface. For example for the light of 1550 nm wavelength, at the air-silica interface, $n_1 = 1$, $n_2 = 1.44$, and $T = 0.9674$ (4% loss per interface); for the air-Si_3N_4 interface, $n_1 = 1$, $n_2 = 1.98$, and $T = 0.8904$ (11% loss per interface, indicating a strong intra-chip Fabry-Pérot interference, will be shown later).

- **Mode size mismatch** is described by how different the waveguide mode is from the fibre / free-space mode. Frequently it is the primary mismatch factor that limits the high coupling efficiency. The coupling efficiency between two modes is determined by the modal overlap integral [267] as:

$$\eta = \frac{|\int_{-\infty}^{+\infty}\int_{-\infty}^{+\infty} \overrightarrow{E_1(x,y)} \cdot \overrightarrow{E_2^*(x,y)} dxdy|^2}{\int_{-\infty}^{+\infty}\int_{-\infty}^{+\infty} \overrightarrow{E_1(x,y)} \cdot \overrightarrow{E_1^*(x,y)} dxdy \cdot \int_{-\infty}^{+\infty}\int_{-\infty}^{+\infty} \overrightarrow{E_2(x,y)} \cdot \overrightarrow{E_2^*(x,y)} dxdy} \tag{3.3}$$

  $\eta \leq 1$ can be proved via Couchy-Schwarz inequity. Equation 3.3 indicates that: 1. $\eta = 1$ for two identical modes with precise overlap and $\eta < 1$ for two different modes; 2. By making both modes more identical to each other, η can be increased. Therefore, reducing the mode size mismatch by accommodating one mode to the other is critical.

- **Optical misalignment** is described by how well the optical fibre is aligned with the waveguide as shown in Fig. 3.5. The misalignment can lead to the deviation of the propagation path of the input mode from the waveguide path, or reduce the mode overlap integral Eq.3.3 by separating the modes. Usually the misalignment is not a severe limitation, as human eyes can easily distinguish misaligned angle below 2° and the high-precision position stages allows to finely tune the relative position between the lens fibre and the chip.

The coupling also shows mode selectivity, as for the same input Gaussian mode, different waveguides modes have different coupling efficiencies. In most of the cases, coupling to the fundamental mode of the waveguide is of interest.

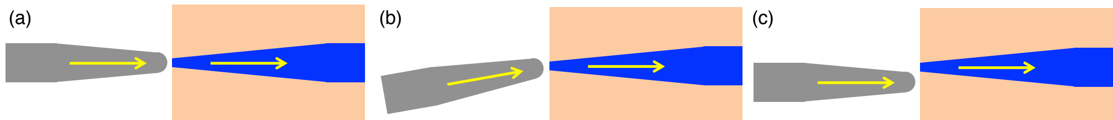

Figure 3.5 – Schematic to show the alignment issues. **A.** An example of the perfect alignment. **B** & **C.** Examples of the bad alignment.

For example, for a Si_3N_4 bus waveguide of $2 \times 0.82\ \mu m^2$ cross-section, its fundamental mode has a mode radius of approximately 1 μm, smaller than the input Gaussian mode radius ≈1.3 μm. Thus to reduce the mode size mismatch, the waveguide mode should be expanded. This can be achieved by using the taper couplers. It is straightforward to understand that the funnel-type taper coupler can expand the mode size, as the larger waveguide has larger fundamental mode. However, to understand why the inverse-type taper coupler can also expand the mode size, examining the the fundamental mode size of different taper geometries is necessary.

The fundamental waveguide mode as well as other higher-order eigenmodes can be simulated using **finite-element method** (FEM). The wavelength in the simulation is 1550 nm. Consider an example of the inverse-type taper. The tip has a $0.4 \times 0.82\ \mu m^2$ cross-section and its eigenmodes are shown in Fig. 3.6. The bus waveguide side has a $2 \times 0.82\ \mu m^2$ cross-section and its eigenmodes at 1550 nm are shown in Fig. 3.7. (Quasi-) **TE mode** is defined as the mode polarizing parallel to the width direction. (Quasi-) **TM mode** is defined as the mode polarizing perpendicular to the width direction (parallel to the height direction). These modes are designated as TE_{mn}/TM_{mn} with m and n being the horizontal and vertical orders of the pattern. TE_{00}/TM_{00} is the TE/TM fundamental mode of the waveguide.

Figure 3.8 plots the TE_{00} modes of the both sides of the taper in comparison with the input Gaussian mode. It shows: 1. The TE_{00} modes of both sides are smaller than the Gaussian mode, thus larger TE_{00} mode is desired for higher coupling efficiency; 2. The TE_{00} mode of the tip side shows a larger mode size than the TE_{00} mode of the bus waveguide side, especially prominent in the logarithmic scale. This is because, when the waveguide size is smaller than the wavelength, the mode (e.g. the TE_{00} mode) is no longer confined well inside the waveguide. The mode becomes delocalized and leaks into the cladding, leading to a strong evanescent field. Smaller waveguide has a weaker mode confinement and lower effective refractive index,

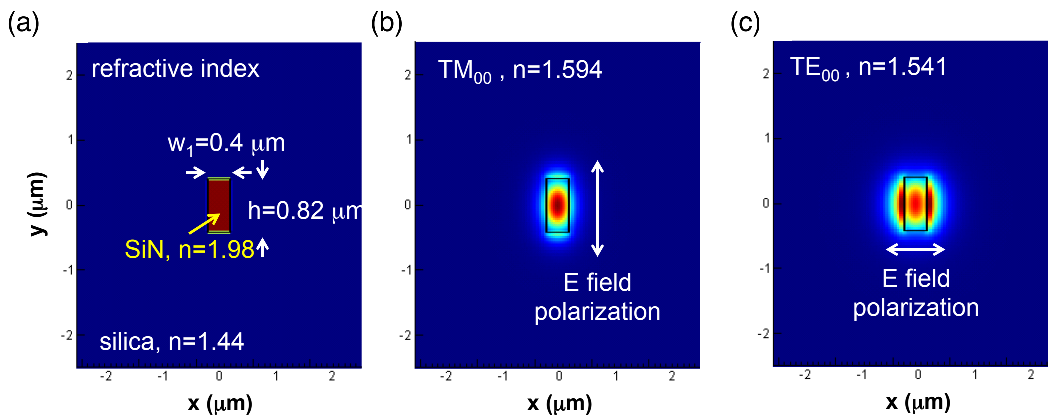

Figure 3.6 – **A.** The refractive index map of the tip side. **B** & **C.** The eigenmodes (only the fundamental modes TE_{00} and TM_{00}) of the tip side. Color bar is the field intensity $|E|^2$ in the linear scale.

thus leading to an effectively larger mode.

As seen from the above eigenmode simulations, the inverse taper can expand the size of the waveguide mode to accommodate the Gaussian mode from the lens fibre. As a result, the mode size mismatch is reduced and the coupling efficiency is improved. So far, this discussion is still *qualitative*. Next, Si_3N_4 samples with different taper geometries are experimentally characterized and benchmarked to FDTD simulations.

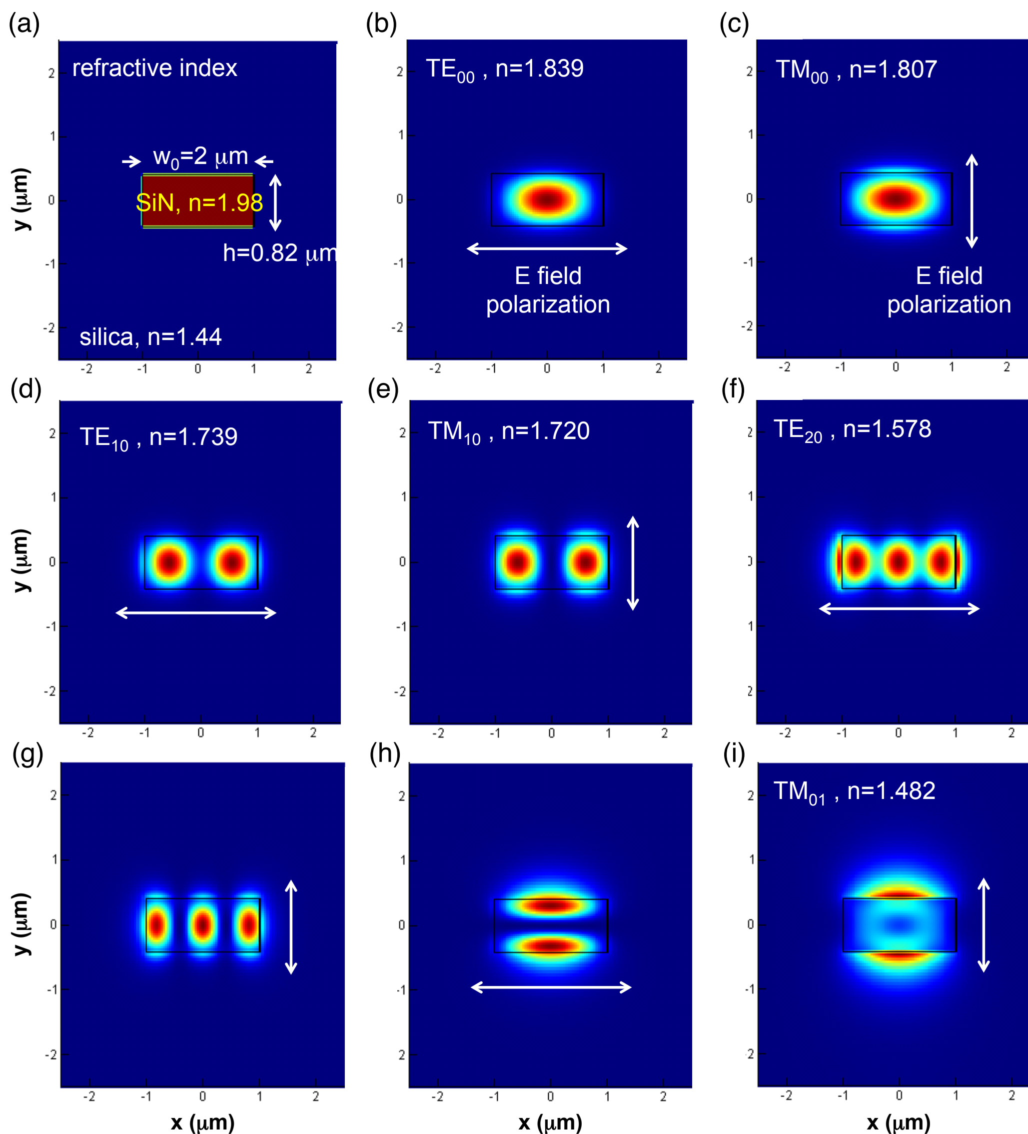

Figure 3.7 – **A.** The refractive index map of the bus waveguide side. **B, C, D, E, F, G, H** & **I.** The eigenmodes of the bus waveguide side. Color bar is the field intensity $|E|^2$ in the linear scale.

3.3.1 FDTD model to simulate inverse taper coupling

Here, the coupling of the Gaussian mode in free space to the waveguide through the inverse taper is simulated with Lumerical FDTD software. At first the waveguide with a rectangular cross-section is considered. In fact due to fabrications, the real waveguide has a non-90 degree base angle, thus appearing as a trapezoid rather than a rectangle. However, as the rectangle has two symmetrical axes, a FDTD simulation of the 1/4 volume is able to give the result of the full volume, but only needs 1/4 of the full simulation time; while the trapezoid has one symmetrical axis, a FDTD simulation of 1/2 volume is able to give the result of the full volume with 1/2 of the full simulation time, as shown in Fig. 3.9. At the first step I am interested to examine whether the taper with a smaller tip side has a higher coupling efficiency, simulations of the rectangular cross-section is more economical and faster.

To reduce the simulation volume, the symmetrical axes are treated as artificial boundaries in the model. The axes (boundary condition) are set correspondingly as **symmetrical** when the polarization is parallel to the axes or **anti-symmetrical** when the polarization is perpendicular

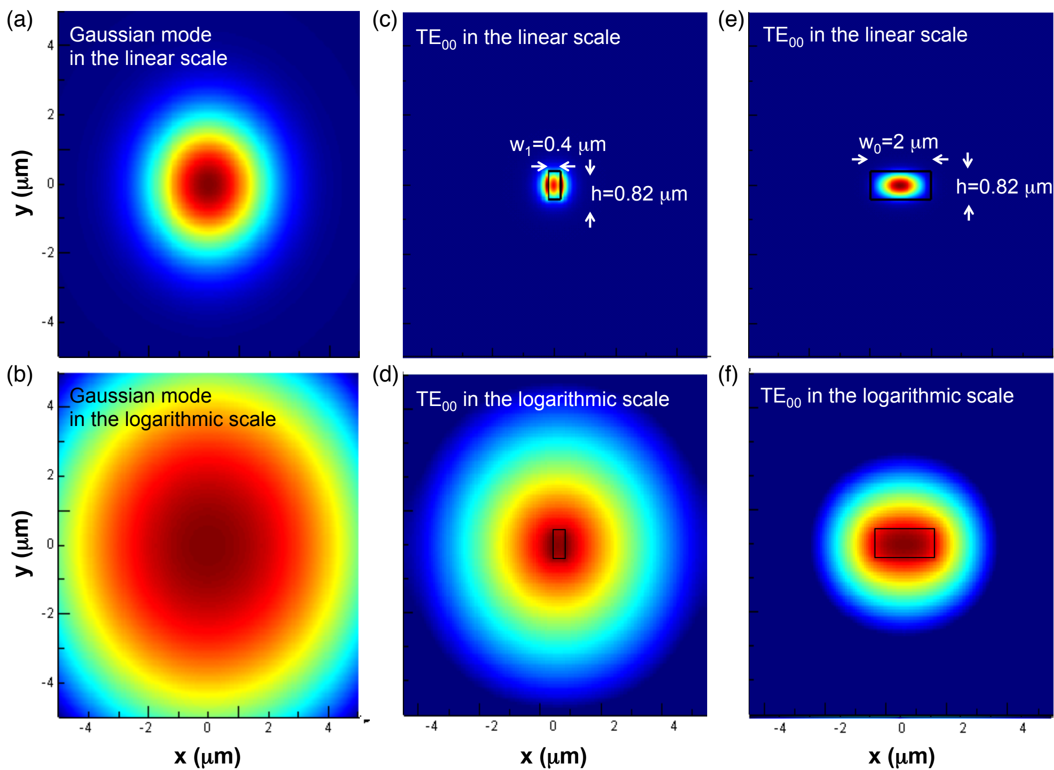

Figure 3.8 – Comparison of the mode sizes of the Gaussian mode and the TE_{00} modes of the both sides of the taper. **A** & **B.** The Gaussian mode in the linear and the logarithmic scales. **C** & **D.** The TE_{00} mode of the tip side of the taper in the linear (C) and the logarithmic (D) scale. **E** & **F.** The TE_{00} mode of the bus waveguide side of the taper in the linear (E) and the logarithmic (F) scale. The fact that the tip side has a lager TE_{00} mode size than the bus waveguide side is observed. Color bar is the field intensity $|E|^2$.

to the axes. The real boundary is set as a PML boundary.

The FDTD simulation model to simulate the coupling of the Gaussian mode in free space to the waveguide through the inverse taper is shown in Fig. 3.10. A Gaussian mode with the radius of 2.85 μm and the normalized power $P_{\text{in}} = 1$ is launched from the air side to the waveguide. A monitor is set at $L_0 = 500$ μm distance from the Gaussian mode and it records the transmitted power P_{out}. The normalized transmission is defined as $P_{\text{out}}/P_{\text{in}} = P_{\text{out}}$ (as $P_{\text{in}} = 1$), which is the coupling efficiency of interest. The taper's tip width w_1 and the taper length L_1 are continuously varied in each simulation, in order to examine the transmission's dependence on w_1 and L_1. In addition, linear and exponential taper shapes are taken into account.

The power coupled to the TE_{00} mode can be calculated from the total coupled power P_{out}. Mathematically, the waveguide supports a set of eigenmodes $\psi_m = (\overrightarrow{E_m}, \overrightarrow{H_m})$, and any mixed

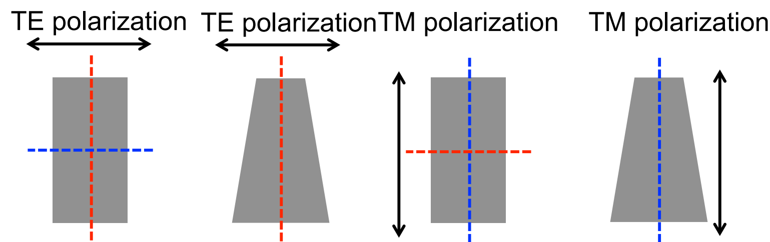

Figure 3.9 – Schematic to show how to reduce the simulation volumes by treating the symmetrical axes of the simulation models as artificial boundary conditions, for the investigated mode with different polarizations. Blue dotted line is the "symmetrical boundary condition", and red dotted line is the "anti-symmetrical boundary condition".

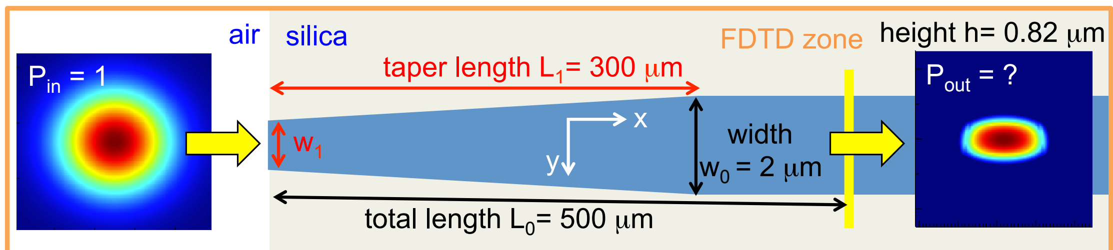

Figure 3.10 – The FDTD simulation model to simulate the coupling of the Gaussian mode in free space to the waveguide through the inverse taper. The Gaussian mode with the radius of 2.85 μm and the normalized power $P_{\text{in}} = 1$ is launched at the air side. Its beam waist coincides with the air-silica interface. The waveguide has a refractive index of 1.98 corresponding to the SiN's refractive index. A monitor is set at $L_0 = 500$ μm distance from the Gaussian mode and it records the transmitted power P_{out}.

waveguide mode $\Phi_{in} = (\overrightarrow{E_{\text{in}}}, \overrightarrow{H_{\text{in}}})$ can be expanded using these eigenmodes as basis, as

$$\Phi_{in} = \Sigma(a_m \psi_m^{\text{forward}} + b_m \psi_m^{\text{backward}}) \tag{3.4}$$

where a_m and b_m are the complex coefficients of the forward and backward propagating waves respectively. Since the eigenmodes are orthogonal as basis, the coefficients can be determined from the overlap integrals, as:

$$\begin{aligned}
a_m &= 0.25\left(\frac{\int d\overrightarrow{S} \cdot \overrightarrow{E_{\text{in}}} \times \overrightarrow{H_m}^*}{N_m} + \frac{\int d\overrightarrow{S} \cdot \overrightarrow{E_m}^* \times \overrightarrow{H_{\text{in}}}}{N_m}\right) \\
b_m &= 0.25\left(\frac{\int d\overrightarrow{S} \cdot \overrightarrow{E_{\text{in}}} \times \overrightarrow{H_m}^*}{N_m} - \frac{\int d\overrightarrow{S} \cdot \overrightarrow{E_m}^* \times \overrightarrow{H_{\text{in}}}}{N_m}\right) \\
N_m &= 0.5 \int d\overrightarrow{S} \cdot \overrightarrow{E_m} \times \overrightarrow{H_m}^* \\
P_{\text{in}} &= 0.5 \int d\overrightarrow{S} \cdot \overrightarrow{E_{\text{in}}} \times \overrightarrow{H_{\text{in}}}^*
\end{aligned} \tag{3.5}$$

where N_m is the power of the m-th eigenmode propagating in the waveguide, and P_{in} is the total power summing all the waveguide modes.

The **Mode Expansion** function of the Lumerical FDTD software can realize the above mathematics. If the mode conversion is sufficiently adiabatic, the power in the TE_{00} mode is approximately equal to the total coupled power.

3.4 Inverse taper coupler: experiments

In this section, Si_3N_4 samples with different taper geometries are experimentally characterized and benchmarked to their FDTD simulations. Particularly, a novel, double inverse tapers ("2D-tapers") for efficient light coupling from lensed fibres to Si_3N_4 waveguides is presented. In comparison with the regular inverse tapers ("1D-tapers") which have only the reduced waveguide width to match the incident mode (as shown in Fig. 3.11(a)), 2D-tapers have both the reduced waveguide height as well as the width (as shown in Fig. 3.12(b)). First, the simulation of light coupling from a lensed fibre to Si_3N_4 bus waveguides via 1D-tapers using 3D FDTD simulation is presented. The 1D-tapers of 820 nm height but different widths are fabricated, and their coupling efficiencies at 1550 nm wavelength is experimentally characterized. It is demonstrated that >45% coupling efficiency for the transverse electric (TE) polarization can only be achieved in a taper of 80 nm width. Such small feature can only be achieved with electron beam lithography (EBL). It is also revealed that the coupling efficiency for the transverse magnetic (TM) polarization is lower than the TE polarization due to the taper's large height-to-width aspect ratio (HWAR). To relax the stringent lithography requirement to

fabricate tapers of 80 nm width and to further improve the coupling for the TM polarization, the 2D-tapers are fabricated using the novel photonic Damascene process. Due to the inherent aspect-ratio-dependent etch (ARDE), the 2D-tapers have increasing height over taper length, therefore enabling further reduction of the taper size. Coupling efficiency more than 45% at 1550 nm wavelength is achieved for both the TE and TM polarizations in 2D-tapers of >300 nm width, which can be easily achieved with DUV lithography, significantly relaxing the lithography requirement. Furthermore, by comparing the coupling performance of several groups of 2D-tapers, the flexibility to engineer the 2D-taper's shape is demonstrated, enabling >45% coupling efficiency with ~500 nm taper width. Therefore these 2D-tapers are promising for light coupling at short wavelength range e.g. 1064 nm or 780 nm, which is usually challenging as EBL is required to pattern very small taper size for optimized coupling.

The main result of this section has been published in ref. [239], J. Liu et al, "**Double inverse nanotapers for efficient light coupling to integrated photonic devices**", *Opt. Lett.* 43, 3200 (2018). I developed the FDTD simulation method, performed the FDTD simulations, fabricated the Si_3N_4 devices, and led the experimental characterization of samples. Arslan S. Raja has contributed to sample testing. Michael Zervas has contributed to sample fabrication.

3.4.1 Standard inverse tapers

Silicon nitride waveguides fully buried in SiO_2 cladding, as shown in Fig. 3.11(a), are experimentally studied. The 1D-tapers are fabricated using a subtractive process [94, 98], a standard CMOS-compatible fabrication process widely used for integrated photonic devices. In this process, patterns e.g. tapers and bus waveguides, are defined by EBL and transferred to Si_3N_4 film via dry etching (CHF_3/O_2). All the patterns, including tapers and bus waveguides, have the uniform height as the Si_3N_4 film thickness. As shown in Fig. 3.11(a), tapers fabricated using this process have increasing width but constant height over the taper length.

The light coupling from a lensed fibre to Si_3N_4 bus waveguides via 1D-tapers of different taper widths at a chip facet is simulated using FDTD method. Due to the Si_3N_4 dry etching process, the 1D-tapers as well as the bus waveguides have a sidewall bottom angle of $\sim 80^o$. Here, the "taper width" is defined as the top side width of the taper's trapezoidal cross-section (see Fig. 3.11(a) inset), which is defined by EBL. Other taper parameters used in the simulation are shown in Fig. 3.11(c), (d). A free-space Gaussian mode of 2.5 μm waist diameter is used to represent the incident mode from the lensed fibre, according to the lensed fibre's specification. The normalized transmitted power through the bus waveguide, i.e. coupling efficiency per chip facet T_1, can be calculated in the simulation. Thus the full device coupling efficiency including two facets is defined as $T_2 = T_1^2$.

The parameter T_2 at the wavelength 1550 nm is calculated based on the simulations, for both the TE and TM polarizations of the incident Gaussian mode. The simulated T_2 as function of taper width from 50 to 300 nm is shown in Fig. 3.11(b), together with the experimentally measured data which, will be discussed later.

The simulation results present two prominent trends: First, a smaller taper has better coupling, due to the weaker light confinement (lower effective refractive index) which improves the mode match to the incident Gaussian mode. Second, the TE mode has better coupling than the TM mode. As shown in Fig. 3.11(c), due to the taper's high height-to-width aspect ratio (HWAR), the TE mode has a larger size than the TM mode, leading to a better match to the incident Gaussian mode. Figure 3.11(d) show the simulated mode propagation profile of the case of ~80% coupling efficiency, illustrating that a small taper providing improved mode match can well guide the incident Gaussian mode to the bus waveguide.

A large number of 1D-taper chips of ~820 nm bus waveguide height (as the Si_3N_4 film thickness) are fabricated, and their coupling efficiencies at 1550 nm wavelength are experimentally characterized using a setup similar to the one described in Ref. [89]. The measured coupling efficiency of each sample, plotted in Fig. 3.11(b), agrees well with the simulated results, supporting the two aforementioned claims: A smaller taper has better coupling, and the TE mode has better coupling than the TM mode. The deviation between the measured data

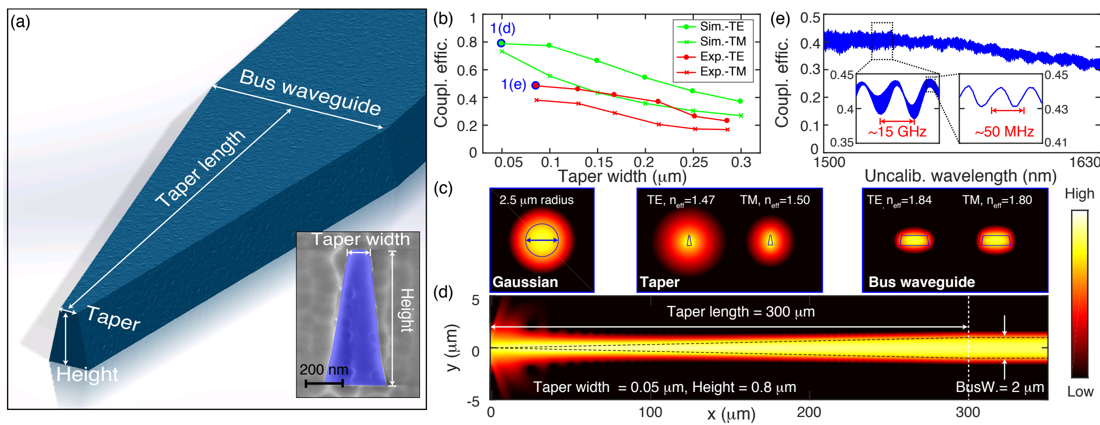

Figure 3.11 – Schematic, simulation and characterization of the regular 1D inverse tapers. (a) Schematic of a 1D inverse taper of increasing width and constant height over the taper length. Inset: SEM image of the taper cross-section (Si_3N_4 is blue shaded), 80 nm in width and 820 nm in height, at the chip facet, buried in SiO_2 cladding. The taper width is defined as the trapezoid's top side width. (b) Simulated coupling efficiency (including two chip facets) versus different taper widths for both the TE and TM polarizations (green), in comparison with the experimentally measured data (red). Blue shaded data points are studied with more details in (d), (e). (c) Simulated mode profiles of the incident Gaussian mode, 0.1-μm-width taper's TE and TM modes, and 2-μm-width bus waveguide's TE and TM fundamental modes, to illustrate the taper's working mechanism as a mode transformer, to bridge the incident Gaussian mode and the bus waveguide mode. n_{eff}: effective refractive index. (d) Simulated mode coupling profile in the case of ~80% coupling efficiency marked in (b). (e) Characterized coupling efficiency from 1500 to 1630 nm, of the taper marked in (b). Two Fabry-Pérot interference patterns are observed. The ~15 GHz one is due to the reflection between two chip facets (5 mm cavity length), and the ~50 MHz one is likely due to the reflection between the input chip facet and the laser (2 m cavity length).

and the simulated results is likely due to the fact that the lensed fibre we use has non-unity transmission, due to the fact that the lensed fibre does not have anti-reflection coating. Higher coupling efficiency can be achieved by replacing the lensed fibre by a free-space objective of high numerical aperture, as demonstrated in several references e.g. Ref. [248].

The coupling from 1500 to 1630 nm bandwidth is also characterized using a tunable laser. A weak trend of decreasing coupling efficiency with increasing wavelength is observed, as shown in Fig. 3.11(e). However this trend is more likely caused by the broadband response of e.g. the 50-50 fibre couplers used in the setup rather than the taper itself, as the opposite trend, increasing coupling efficiency with increasing wavelength, is observed when the 50-50 fibre coupler's two output branches are interchanged. Nevertheless, the coupling efficiency remains >30% over the 130 nm range. In addition, ~15 GHz and ~50 MHz Fabry-Pérot interference patterns are observed. The stronger ~15 GHz interference corresponds to the reflection between two chip facets (5 mm cavity length) and the weaker ~50 MHz interference is likely due to the reflection between the input chip facet and the laser (2 m cavity length), which might be removed by using a light isolator.

3.4.2 Double inverse tapers

As mentioned above, 1D-tapers show polarization-dependent coupling, i.e. the TM polarization has lower coupling efficiency than the TE polarization, due to the 1D-taper's large HWAR. However, many photonic devices are specifically operated with TM mode, to couple vertically between different components, such as the coupling between photonic dielectric and plasmonic waveguides [268, 269]. Therefore for these devices, efficient TM coupling is important and needs to be optimized.

Further improving the TM coupling requires reducing the taper size. However reducing the taper width further is challenging due to the lithography resolution and quality. In addition, thin but tall tapers of high HWAR tend to collapse which reduces fabrication yield. Therefore, reducing the taper height is a feasible solution, however simultaneously the height of other components, e.g. bus waveguides, should remain unchanged in order to operate the device in the same situation. As a result, tapers of both increasing width and height, manifesting as "double inverse tapers" or "2D-tapers", are desired.

In the subtractive process all the patterns have the uniform height determined by the Si_3N_4 film thickness, thus achieving 2D-tapers, particularly tapering the waveguide height, is challenging. Multi-stage spot-size mode converters [270, 271] have been proposed and fabricated, which however requires complex fabrication process including multi-steps of lithography with precise alignment and dry etching. Alternatively, fabrication using gray-scale mask lithography has achieved tapering waveguide height efficiently [272], however this process requires using high-energy beam-sensitive glass which need to be specifically designed, engineered and patterned by EBL.

The photonic Damascene process allows to fabrication 2D-tapers. In this process, the patterns are defined by lithography and transferred to a SiO_2 substrate via dry etching. The Si_3N_4 film is then deposited on the SiO_2 substrate and fill the defined pattern trenches, followed by a chemical mechanical planarization (CMP) which removes the excess Si_3N_4 and planarizes the wafer top surface. As the dry etching process has inherently aspect-ratio-dependent etch (ARDE) rate [238], the pattern trench depth increases with increasing pattern size. For pattern sizes exceeding a certain threshold value, the ARDE effect becomes negligible, thus the trench depths can be considered as uniform. As a consequence, a taper of increasing width has increasing height, manifesting a 2D-taper. Other components, e.g. bus waveguides, have uniform height on the wafer.

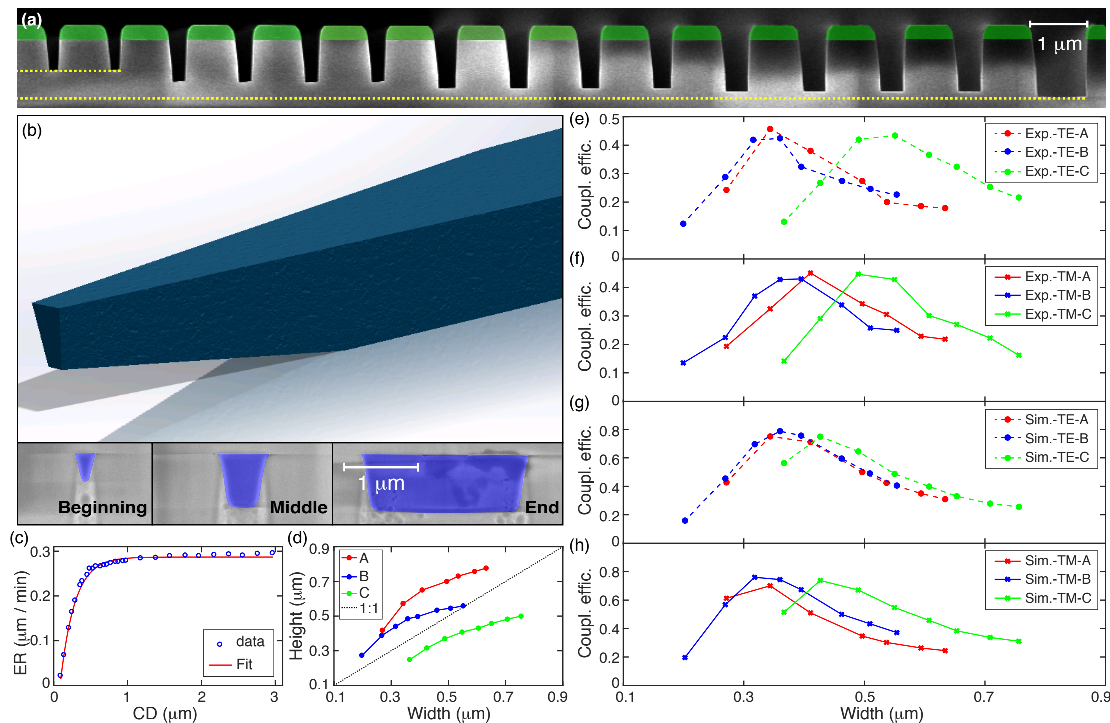

Figure 3.12 – Schematic and the characterization of the novel 2D double inverse tapers. (a) SEM image of the ARDE effect on a SiO_2 substrate with Si etch mask (green shaded). (b) Schematic of the 2D-taper. SEM images of the taper cross-sections (Si_3N_4 is blue shaded) at the taper beginning (chip facet side), middle, and end (bus waveguide side) are shown. (c) Characterized ARDE effect. SiO_2 is etched for 3 mins with a 400 nm Si etch mask. The blue circles are measured data via SEM and the red curve is the ARDE fit curve. CD: critical dimension of the trench width. ER: etch rate. (d) Measured height-to-width aspect ratios (HWAR) of 2D-tapers. A, B, C stand for 2D-taper chips 2D-A (red), 2D-B (blue) and 2D-C (green). (e) Measured coupling efficiency at 1550 nm wavelength (through two chip facets) of 2D-taper Chips A (red), B (blue), C (green), for both the TE (dash) and TM (solid) polarizations. By controlling the ARDE effect, the taper width at the optimum coupling can be shifted. Optimum coupling with >500 nm taper width can be achieved, enabling the use of normal UV lithography for the taper fabrication.

Figure 3.12(a) shows the ARDE effect on a SiO_2 substrate, after SiO_2 dry etching (C_4F_8/He) with a 400 nm thick amorphous Si etch mask. The ARDE effect creates non-uniform, pattern-dependent trench depths, and is characterized by measuring the mean etch rate (ER) as function of trench width (critical dimension, CD), as shown in Fig. 3.12(c). When CD reaches the threshold value of ~1 μm, the ER reaches a stable value of ~0.29 μm/min and becomes nearly independent of CD. From 0 to 0.5 μm CD, ER increases nearly linearly. The ARDE curve can be fitted with $\text{ER} = a \cdot \exp(-\text{CD}/b) + c$, with $a = -0.444$ μm/min, $b = 0.195$ μm, $c = 0.286$ μm/min. Figure 3.12(b) shows the SEM images of taper cross-sections at taper beginning (chip facet side), middle, and end (bus waveguide side), revealing the double inverse shape with increasing width and height.

Three groups of 2D-taper chips (2D-A, B, C) were fabricated. The bus waveguides' heights are measured with SEM (±2% tool measurement uncertainty), and are listed in Tab. 3.2, in comparison with the 1D-taper chip. These tapers' HWARs and coupling efficiencies for both the TE and TM polarizations are experimentally characterized, as shown in Fig. 3.12(d), (e) and (f). Again, the taper width is defined as the taper's top side width. Compared with the 1D-taper chip shown in Fig. 3.11(b), Chip 2D-A achieves >45% TM coupling, while >45% TE coupling is maintained. Different from the 1D-tapers in which the smaller taper width shows better coupling, in Chip 2D-A, there is an optimum coupling point which is achieved with >300 nm taper width, due to the ARDE and the reverse trapezoidal shape (bottom angle 96°). This optimum coupling requires weak waveguide confinement for large taper mode of improved mode match, but simultaneously the waveguide confinement needs to be sufficient to overcome the Gaussian beam's divergence. Such >300 nm taper width for optimum coupling can be easily achieved with deep-UV photolithography instead of EBL, significantly relaxing the stringent requirement of lithography resolution. Moreover, optimized coupling for shorter wavelengths, e.g. 1064 nm and 780 nm, requires very small tapers, which is challenging to fabricate with 1D-tapers due to the waveguide height. Therefore 2D-tapers are more useful to work in these wavelengths.

The ARDE and the taper shape can be engineered simply by changing the etch mask thickness. A thicker etch mask gives a stronger ARDE effect. To demonstrate this scheme, Chips 2D-B and 2D-C were fabricated. Chip 2D-C was fabricated with a 750 nm thick deep-UV photoresist mask with a stronger ARDE. Chip 2D-B was fabricated using the same process as Chip 2D-A but the bus waveguide height was made to 650 nm via more CMP time, in order to directly compare to Chip 2D-C. Both chips have the similar bus waveguide height, but their taper HWARs are significantly different due to their different ARDEs, as shown in Fig. 3.12(d). As shown in Fig. 3.12(e) and (f), compared with Chip 2D-A, the coupling of Chip 2D-B is not

Table 3.2 – **2D-taper chips' specifications.**

Chips	1D	2D-A	2D-B	2D-C
Mask thickness (nm)		~400	~400	~750
Bus waveguide height (nm)	~820	~820	~650	~670

prominently different, because, as long as the taper's HWAR exceeds unity (>1), the mode size is more constrained by the taper width rather than the taper height. However, the stronger ARDE (HWAR <1) of Chip 2D-C shifts the optimum coupling to >500 nm taper width. In this case the required lithography precision is further reduced, enabling the use of common UV photolithography.

The coupling for all 2D-taper chips is further simulated using the measured waveguide geometries. The simulated coupling efficiencies are shown in Fig. 3.12(g) and (h), which agree well with the measured data, supporting the two claims: 2D-tapers show polarization-independent coupling, and the optimum coupling is shifted to larger taper width via engineering the ARDE.

In summary, a comprehensive study of inverse (1D-) and double inverse (2D-) tapers for efficient light coupling from a lensed fibre to Si_3N_4 waveguides is presented. The coupling performances of 1D- and 2D-tapers are experimentally compared, illustrating the main mechanisms in the fabrication processes which lead to the performance difference. The advantages of 2D-tapers include: First, better coupling of the TM polarization. Second, larger taper width at optimum coupling, enabling the use photolithography instead of EBL. Third, flexibility to change the taper shapes via engineering the ARDE effect. The data presented in this study is from several chip devices, but is highly reproducible in many other chips that we have experimentally characterized. Our results demonstrate the advantages of 2D-tapers over 1D-tapers, particularly promising for light coupling at near-IR or visible wavelengths.

3.5 Bus-waveguide-to-microresonator coupling

Microresonator devices are ubiquitously used in integrated photonic circuits. While most microresonator devices in integrated photonics are formed by single-mode waveguides [273, 274], many recent photonic integrated circuits rely on multi-mode waveguides due to their lower losses [275, 201], higher data capacity [276], and tailored dispersion properties e.g. to attain anomalous group velocity dispersion required for parametric frequency conversion [41, 49, 277]. In contrast to the well-established approach of the input-output formalism of a damped quantum system [278] which considers a well-defined, single input and output channel, the presence of higher-order modes as output channels requires extra consideration.

Early research on bulk ultrahigh-Q microresonators led to the development of several adjustable evanescent coupling techniques based on prisms and tapered optical fibres [279, 280, 281, 47, 48]. To quantitatively describe the performance of these couplers with multiple output channels, "**coupling ideality**" was defined for tapered fibre coupling to microspheres, as the ratio of the power coupled from the resonator to the fundamental fibre mode divided by the total power coupled to all guided and non-guided fibre modes [48]. A high coupling ideality enables to operate the resonator in the strongly overcoupled regime, where the output losses are dominated by the coupling to the single, targeted output channel. This regime is in particular relevant for quantum optics e.g. to preserve quantum correlations of generated intracavity photon pairs [282] and squeezed states of light [283]. It is thus important to avoid degradation of coupling ideality in the presence of multiple output channels.

In the context of integrated planar microresonator devices, design rules [284, 285] and optimized coupler geometries [199, 286] have been reported. However, comparatively little attention has been paid to their coupler performance, especially with regard to the multi-mode nature of the waveguides used. Only few reports of coupler-induced excess losses [287, 288] have been published. Most integrated microresonator devices, single- or multi-mode, still rely on the coupler design consisting of a simple side-coupled straight bus waveguide with a cross-section identical to the resonator waveguide.

In this section, a comprehensive study of integrated planar high-Q Si_3N_4 microresonator devices with several different coupler designs is presented. Experimental resonance characterization with sufficiently large statistics and full 3D FDTD simulations allow to unambiguously reveal the detrimental effect of non-ideal coupler designs, even in the presence of statistical fluctuations of resonator properties due to fabrication variations. The commonly employed coupler design using the bus waveguide of the same cross-section as the resonator is found to exhibit parasitic losses due to the modal coupling to higher-order bus waveguide modes, which can severely limit the device performance. In contrast, in the design of the multi-mode resonator coupled to a single-mode bus waveguide, nearly ideal coupler performance is observed. Finally, the simulations show that coupling between different resonator modes can originate from the coupler. This provides a novel insight into the origin of modal coupling in microresonators observed in the previous work [86, 289], which leads to distortion of resonator

dispersion properties.

The main result of this section has been published in ref. [290], M. H. Pfeiffer, J. Liu et al, "**Coupling ideality of integrated planar high-Q microresonators**", *Phys. Rev. Applied* 7, 024026 (2017). I developed the theoretical model and FDTD simulation method, performed the FDTD simulations and participated in the experimental characterization. Martin H. P. Pfeiffer fabricated all the Si_3N_4 samples used in this work and led the experimental data collection.

3.5.1 Input-output formalism and coupling ideality

The simplest mode to describe the bus waveguide to a ring resonator coupling is the classical input-output formalism (IOF) [48, 291, 292, 207]. The schematic of the coupling is shown in Fig. 3.13. A waveguide mode (assuming the fundamental mode) with the field amplitude s and the frequency ω_L close to a resonance frequency ω_C of the resonator excites the resonator mode (assume the fundamental mode) through the the evanescent field coupling. The coupling strength is κ_{ex}. The excited resonator mode has the field amplitude a and experiences an intrinsic loss κ_0. Both the κ_{ex} and the κ_0 are normalized to the light circulating time (1/FSR) and have the unit of Hz. Therefore the external power coupling strength and the intrinsic loss per round trip are κ_{ex}/FSR and κ_0/FSR. The equation of motion describing the coupling is written as:

$$\frac{da}{dt} = i\omega_C a - \frac{1}{2}(\kappa_0 + \kappa_{\mathrm{ex}})a + \sqrt{\kappa_{\mathrm{ex}}} s e^{-i\omega_L t} \tag{3.6}$$

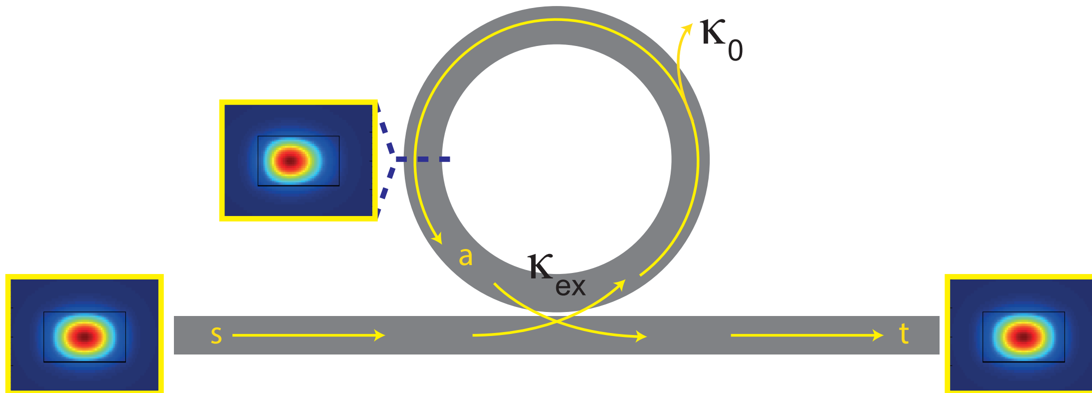

Figure 3.13 – The schematic of the ideal waveguide-ring resonator coupling described by the IOF. The input waveguide mode (fundamental mode) with the field amplitude s is coupled to the resonator mode (fundamental mode) with the coupling strength κ_{ex}. The resonator mode has the field amplitude a and experiences the intrinsic loss κ_0 during the circulation. It then out-couples to the waveguide. The transmitted waveguide mode has the field amplitude t_0.

Transform into a rotating frame with the driving laser frequency ω_L and use the approximation of slowly varying amplitude, Eq. 3.6 becomes

$$\frac{da}{dt} = i\Delta a - \frac{1}{2}(\kappa_0 + \kappa_{ex})a + \sqrt{\kappa_{ex}}s \tag{3.7}$$

where $\Delta = \omega_L - \omega_C$ is the detuning of the driving laser frequency from the resonance frequency.

In the steady state $da/dt(a = a_0) = 0$, Eq. 3.7 becomes

$$a_0 = \frac{\sqrt{\kappa_{ex}}s}{\frac{1}{2}(\kappa_0 + \kappa_{ex}) - i\Delta} \tag{3.8}$$

The field power of the resonator mode is $P_0 = |a_0|^2$, as

$$P_0 = \frac{\kappa_{ex}s^2}{\frac{1}{4}(\kappa_0 + \kappa_{ex})^2 + \Delta^2} \tag{3.9}$$

The transmitted field through the waveguide consists of the partially transmitted input field and the out-coupled field from the resonator, as

$$t_0 = s - \sqrt{\kappa_{ex}}a_0 \tag{3.10}$$

The "**extinction (T)**", defined as the waveguide transmitted power normalized to the waveguide input power, is

$$\begin{aligned} T &= |t_0/s|^2 \\ &= |1 - \sqrt{\kappa_{ex}}a_0/s|^2 \\ &= |1 - \frac{\kappa_{ex}}{\frac{1}{2}(\kappa_0 + \kappa_{ex}) - i\Delta}|^2 \\ &= |\frac{\frac{1}{2}(\kappa_{ex} - \kappa_0) - i\Delta}{\frac{1}{2}(\kappa_{ex} + \kappa_0) - i\Delta}|^2 \end{aligned} \tag{3.11}$$

Note: There are few versions of equation of motion as Eq. 3.6, different by the phase of the last term (driving term) $\sqrt{\kappa_{ex}}s$. Note that the transmitted field Eq. 3.10 will change correspondingly as shown in Table 3.3. it should be noted that, Eq. 3.6 and Eq. 3.10 are used together and lead to the same final expression of Eq. 3.11.)

In the resonant case where $\Delta = 0$, Eq. 3.11 is simplified to

$$T = |\frac{\kappa_{ex} - \kappa_0}{\kappa_{ex} + \kappa_0}|^2 \tag{3.12}$$

Equation 3.12 defines three coupling regimes:

- If $\kappa_0 = \kappa_{ex}$, $T = 0$. This is the condition for **critical coupling**. In this case, the intrinsic loss and the external coupling with the bus waveguide (driving) are balanced to each other.
- If $\kappa_0 << \kappa_{ex}$, $T \approx 1$. This is the condition for **overcoupling**. In this case, the external coupling dominates the intrinsic loss.
- If $\kappa_0 >> \kappa_{ex}$, $T \approx 1$. This is the condition for **undercoupling**. In this case, the intrinsic loss dominates the external coupling.

Figure 3.14 plots Eq. 3.12 of the extinction T as a function of the linewidth $(\kappa_{ex}+\kappa_0)/2\pi$, assuming an intrinsic loss of $\kappa_0/2\pi$ = 100 MHz. This curve has been experimentally characterized in ref. [47]. It should be noted that, the IOF derived above accounts only two loss factors, i.e. the intrinsic loss κ_0 and the external coupling κ_{ex}. If other loss factors such as any parasitic loss κ_p are presented, Eq. 3.12 will have a different form thus the extinction-linewidth dependence is different from the one shown in Fig.3.14. One possible parasitic loss is introduced if the resonator mode out-couples to a higher-order mode of the bus waveguide other than the initial input fundamental mode of the bus waveguide.

Figure 3.15 shows the situation where parasitic losses are presented. For example, the funda-

driving term	transmitted field
$\sqrt{\kappa_{ex}}s$	$t = s - \sqrt{\kappa_{ex}}a_0$ [292, 207]
$-\sqrt{\kappa_{ex}}s$	$t = s + \sqrt{\kappa_{ex}}a_0$
$i\sqrt{\kappa_{ex}}s$	$t = s + i\sqrt{\kappa_{ex}}a_0$ [293, 48]
$-i\sqrt{\kappa_{ex}}s$	$t = s - i\sqrt{\kappa_{ex}}a_0$

Table 3.3 – Different versions of the driving term and the transmitted field.

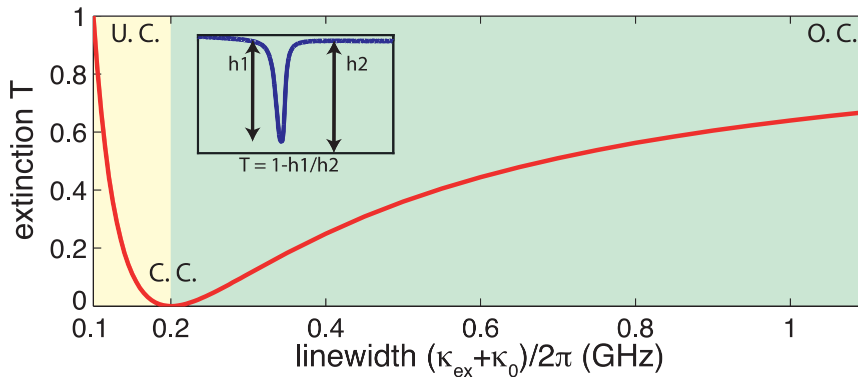

Figure 3.14 – Plot of the extinction T as a function of the linewidth $(\kappa_{ex}+\kappa_0)/2\pi$ with an assumed intrinsic loss $\kappa_0/2\pi = 0.1$ GHz. Under-coupling and over-coupling regimes are color shaded. O.C. : over-coupling; C.C. : critical-coupling; U.C. : under-coupling. Inset: The extinction T is defined as the power extinction ratio of the resonance.

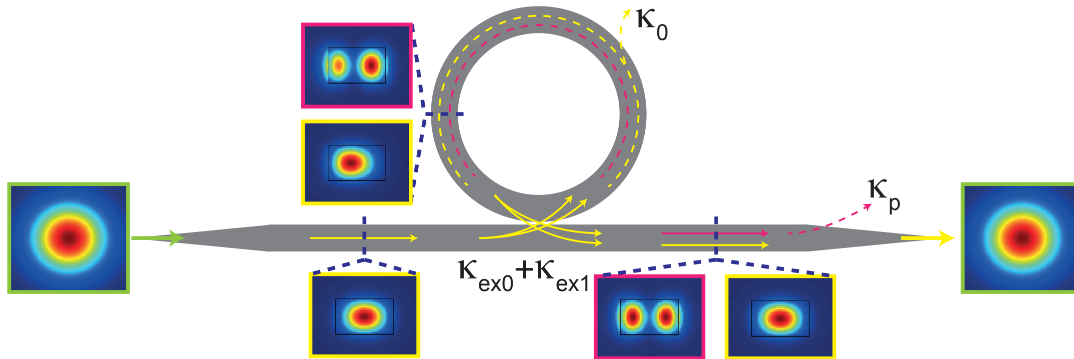

Figure 3.15 – Schematic of the non-ideal waveguide-ring resonator coupling. The input waveguide fundamental mode excites the resonator fundamental mode as well as other higher order resonator modes. Only the resonator fundamental mode is of interest. Such a fundamental mode circulates inside the resonator and experiences the intrinsic loss κ_0. It then out-couples to several waveguide modes with individual external coupling strength $\kappa_{\mathrm{ex},i}$. The taper in the waveguide-fibre out-coupling port filters out the waveguide higher order modes, creating a parasitic loss κ_p.

mental mode of the bus waveguide can in principle excite several resonator modes. However, one must note that, the current coupling situation is different from a co-directional coupler, as a close ring resonator is used here. Therefore, which resonator mode is actually excited depends on which mode is resonant at this optical frequency. Often only the fundamental mode of the resonator is of interest. Once excited, this mode circulates and out-couples to the bus waveguide after a round trip. Due to the fact that the bus waveguide is multi-mode, the fundamental mode of the resonator can couple to higher-order modes of the bus waveguide, as well as the fundamental mode. Note that, this coupling situation is same as a co-directional coupler. The inverse taper placed at the chip's out-coupling facet only allows the fundamental waveguide mode to pass and to be collected by the lensed fibre. Equivalently, this leads to the filtering of all the high-order modes of the bus waveguide. Consequently, a parasitic loss due to the loss of all the higher-order modes is introduced. This is an example how parasitic losses can present due to the design.

The IOF derived in Eq. 3.12 is only valid for ideal couplers working in the single-mode to single-mode coupling regime. Only two loss factors are included, i.e. the intrinsic loss κ_0 and the loss due to the external coupling κ_{ex}. If the bus waveguide is multi-mode, the IOF needs to be revised in order to capture this effect, with the introduction of "coupling ideality".

The concept of the **coupling ideality** was first introduced in ref. [48]. It is defined as the ratio of the power coupled to the bus waveguide's fundamental mode to the total out-coupled power from the resonator. In the ideal case of single-mode to single-mode coupling regime, the coupling ideality is always unity. If the bus waveguide is multi-mode, several waveguide modes as well as the radiation mode are coupled to the resonator mode, thus the coupling ideality is likely non-unity.

Consider the resonance case $\Delta = 0$, the modified equation of motion [48] based on the Eq. 3.7 is

$$\frac{da}{dt} = -\frac{1}{2}\left(\sum_{i=0}^{n} \kappa_{ex,i} + \kappa_{\mathrm{rad}} + \kappa_0\right) a + \sqrt{\kappa_{ex,0}}\, s \tag{3.13}$$

where the $\kappa_{ex,0}$, $\kappa_{ex,i}$ and κ_{rad} are the coupling strengths to the waveguide fundamental mode, the i-th waveguide mode and the radiation mode. In the steady state $da/dt(a = a_0) = 0$, Eq. 3.13 becomes

$$a_0 = \frac{2\sqrt{\kappa_{ex,0}}\, s}{\sum_{i=0}^{n} \kappa_{ex,i} + \kappa_{\mathrm{rad}} + \kappa_0} \tag{3.14}$$

The **coupling ideality** I is defined as

$$I = \frac{\kappa_{ex,0}}{\sum_{i=0}^{n} \kappa_{ex,i} + \kappa_{\mathrm{rad}}} \tag{3.15}$$

The total loss thus includes the intrinsic loss κ_0, the external coupling to the waveguide

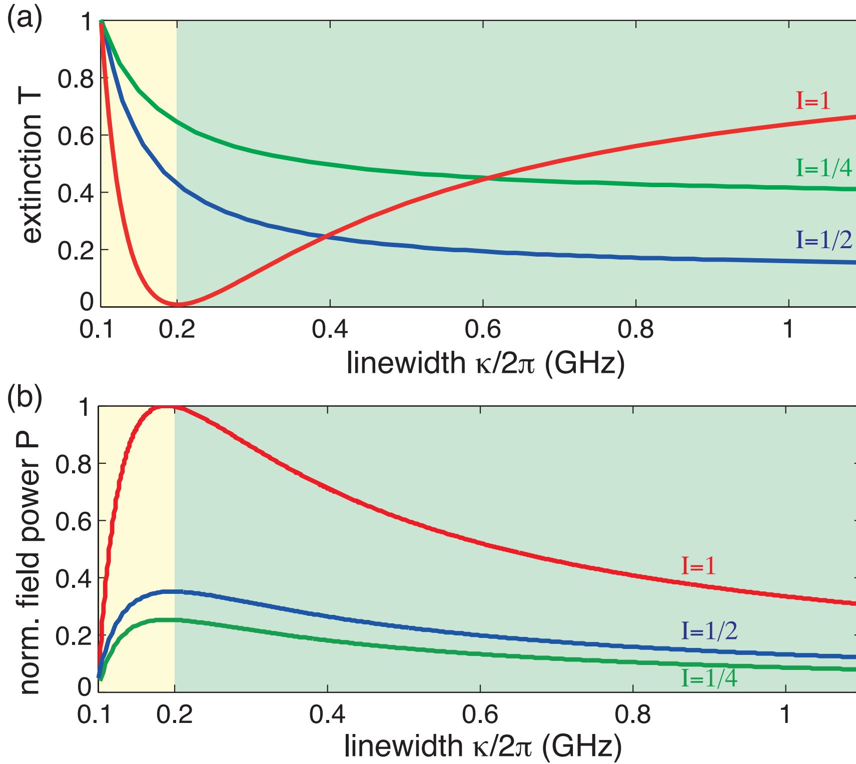

Figure 3.16 – Plot of the the extinction T and the normalized intra-resonator field power P as a function of the linewidth κ for different coupling ideality values I. $\kappa_0/2\pi = 0.1$ GHz is assumed. The higher coupling ideality shows the higher maximum intra-resonator field power.

fundamental mode $\kappa_{ex,0}$ and the parasitic loss κ_P as

$$\begin{aligned}\kappa &= \kappa_0 + \kappa_{ex,0} + \kappa_P \\ \kappa_P &= \sum_{i=1}^{n} \kappa_{ex,i} + \kappa_{\text{rad}}\end{aligned} \tag{3.16}$$

The intracavity power is expressed as

$$P_0 = |a_0|^2 = \frac{4\kappa_{ex,0}s^2}{(\sum_{i=0}^{n}\kappa_{ex,i} + \kappa_{\text{rad}} + \kappa_0)^2} = \frac{4\kappa_{ex,0}s^2}{(\kappa_0 + \kappa_{ex,0}/I)^2} \tag{3.17}$$

The extinction T is

$$\begin{aligned}T &= |1 - \sqrt{\kappa_{ex,0}}a/s|^2 \\ &= |\frac{\kappa_{\text{ex},0} - \kappa_0 - \sum_{i=1}^{n}\kappa_{ex,i} - \kappa_{\text{rad}}}{\sum_{i=0}^{n}\kappa_{ex,i} + \kappa_{\text{rad}} + \kappa_0}|^2 \\ &= |\frac{(2 - I^{-1})\kappa_{ex,0} - \kappa_0}{\kappa_{ex,0}/I + \kappa_0}|^2\end{aligned} \tag{3.18}$$

For $I = 1$, Eq. 3.18 becomes Eq. 3.9.

Figure 3.16 plots the extinctions T and the normalized intra-resonator field powers P as functions of the linewidth $\kappa/2\pi$ for different ideality values. It shows: 1. The coupling ideality for a certain coupling geometry can be characterized by measuring the extinction as a function of the linewidth; 2. With the same intrinsic loss $\kappa_0/2\pi$, the larger ideality value has the higher maximum intra-resonator field power. Therefore, the coupling ideality is an important parameter directly showing the intra-resonator power enhancement, in analogue to the Q factor. For the investigation of nonlinear processes, e.g. the FWM process, the intra-resonator field power as high as possible is desired, therefore achieving a good coupling ideality is necessary.

3.5.2 Analytical description of a multi-mode coupling section

Typically the evanescent coupling of light to a microresonator is described using coupled-mode theory as a power transfer to a resonator mode at the rate $\kappa_{\text{ex},0}$ [281, 47, 292]. Treating the resonator in a lumped model [294, 295], the coupling rate $\kappa_{\text{ex},0}$ is typically estimated using the model of coupling between two co-propagating modes in adjacent waveguides [296]. In contrast to the power coupling ratios of conventional directional couplers, the high-Q microresonator's low internal loss rate κ_0 requires only minute power transfer to achieve critical coupling (i.e. $\kappa_{\text{ex},0} = \kappa_0$) for which the intracavity power build-up is maximal. Thus the coupled modes in both the resonator and the bus waveguides can be essentially treated as independent, and $\kappa_{\text{ex},0}$ depends on the mutual modal overlap and propagation constant

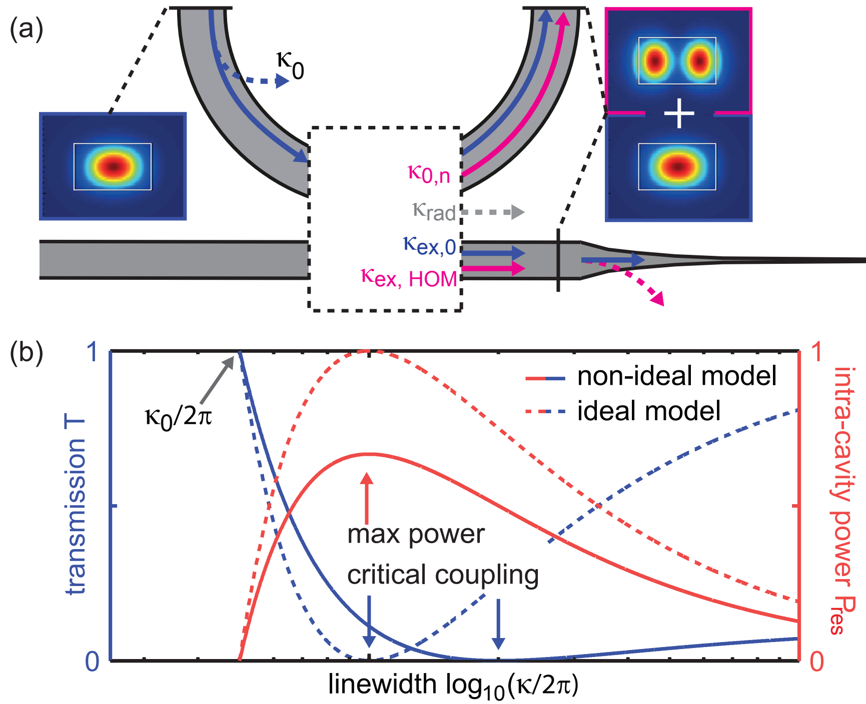

Figure 3.17 – (a) Schematic representation of the coupling rates in an integrated microresonator with multi-mode waveguides. The parasitic coupling processes of a fundamental resonator mode to higher-order bus waveguide modes are illustrated. κ_0 represents the resonator's internal loss rate and $\kappa_{ex,0}$ represents the coupling rate to the fundamental bus waveguide mode. $\kappa_{ex,HOM}$ represents the coupling rate to the higher-order bus waveguide modes, which are later filtered out by the inverse taper mode converter. $\kappa_{0,n}$ represents the coupling rate to other resonator modes, while κ_{rad} represents the coupling rate to free-space modes. (b) Plot of the transmission T (blue) and the intra-cavity power P_{res} (red) as function of the total linewidth $\kappa/2\pi$ for the ideal ($I = 1$, dashed lines) and non-ideal ($I = 0.67$, solid lines) case.

mismatch $\Delta\beta$ (i.e. phase mismatch) [281, 296, 297]. This model is widely applied as it provides a qualitative insight for most cases where coupling between only two modes is considered, neglecting the coupling to other modes.

In practice for high-Q microresonators, a commonly employed coupler design consists of a side-coupled, straight bus waveguide whose cross-section is identical to that of the resonator waveguide. The cross-section is chosen in order to match the propagation constants of e.g. the fundamental resonator and bus waveguide modes. However in the case of multi-mode waveguides, as found for tapered fibre coupled to high-Q microspheres [48], coupling between different modes has to be considered as depicted in Fig. 3.17(a). Moreover, the coupler can scatter light into free-space modes and recently was also identified to couple the counter-propagating, clockwise (CW) and counter-clockwise (CCW), waveguide modes [288]. As a result, the corresponding equations of motion for the resonator modal amplitude a_0 of

frequency ω_0 in the rotating frame of the driving laser ω_L is extended to

$$\frac{d}{dt}a_0 = i\Delta_0 a_0 - \left(\frac{\kappa_0 + \kappa_{\mathrm{ex},0} + \kappa_{\mathrm{p}}}{2}\right)a_0 + \sqrt{\kappa_{\mathrm{ex},0}}s_{\mathrm{in}} + \frac{i}{2}\sum_{n\neq 0}\kappa_{0,n}a_n e^{i\Delta_n t} \tag{3.19}$$

Here $\Delta_0 = \omega_L - \omega_0$ and $\Delta_n = \omega_L - \omega_n$ are the frequency detunings between the driving laser with amplitude s_{in} and the resonator modes a_0 and a_n. The intracavity field decays due to the internal loss rate κ_0 and the external coupling rate $\kappa_{\mathrm{ex},0}$ to the fundamental bus waveguide mode. The radiation into free-space modes with the rate κ_{rad} and to higher-order bus waveguide modes with the rate $\kappa_{\mathrm{ex,HOM}} = \sum_{q\neq 0}\kappa_{\mathrm{ex},q}$ are considered as parasitic coupling losses, and thus form the parasitic coupling rate $\kappa_{\mathrm{p}} = \kappa_{\mathrm{rad}} + \kappa_{\mathrm{ex,HOM}}$, which accelerates the intra-cavity field decay.

In addition, the modal coupling term $\frac{i}{2}\sum_{n\neq 0}\kappa_{0,n}a_n e^{i\Delta_n t}$ is introduced to account for the fact that the resonator mode a_0 can couple to other modes with the rate $\kappa_{0,n}$. Such modal coupling is usually considered to arise from surface roughness and bulk defect, but is later found to originate also from the coupler. This term is only relevant if the coupled modes are simultaneously resonant. Such modal coupling causes deviations of the resonance frequencies, so called "**avoided modal crossings**", that locally distort the resonator dispersion. At such modal crossing points the coupling to another resonator mode a_n (with total loss κ_n) effectively adds an extra contribution to the parasitic loss κ_p. However, away from the modal crossing point where only the resonator mode a_0 is resonant, the added parasitic loss is negligible. The coupling ideality I of the resonator mode a_0, describing the relative strength of parasitic coupling rates, is defined according to Ref. [48] as:

$$I = \frac{\kappa_{\mathrm{ex},0}}{\kappa_{\mathrm{ex},0} + \kappa_{\mathrm{p}}} \tag{3.20}$$

In the following the effects of coupling ideality on device performance are considered. While the light scattering into free-space modes directly represents a power loss, power coupled to higher-order modes of the bus waveguide is not necessarily lost. In most cases however, the higher-order bus waveguide modes are filtered out e.g. by inverse tapers placed at the chip facets [241, 239] (as described in the previous section of this chapter). Thus the measured power at the device facets only consists of the power of the bus waveguide's fundamental mode, and therefore the input-output relation $s_{\mathrm{out}} = s_{\mathrm{in}} - \sqrt{\kappa_{\mathrm{ex},0}}a_0$ holds and $\kappa_{\mathrm{ex,HOM}}$ represents a parasitic loss which increases the resonance linewidth. On resonance ($\Delta_0 = 0$), the device power transmission T and intra-cavity power P_{res} as function of the coupling ideality I and

coupling parameter $K = \kappa_{\mathrm{ex},0}/\kappa_0$ are expressed as:

$$T = |1 - \frac{2}{K^{-1} + I^{-1}}|^2 \tag{3.21}$$

$$P_{\mathrm{res}} = \frac{D_1}{2\pi} \cdot \frac{4}{\kappa_{\mathrm{ex},0}(K^{-1} + I^{-1})^2} P_{\mathrm{in}} \tag{3.22}$$

Assuming an input power $P_{\mathrm{in}} = |s_{\mathrm{in}}|^2 = 1$ and a constant D_1, Fig. 3.17(b) plots both the transmission T and intra-cavity power P_{res} as function of the total linewidth $\kappa/2\pi = (\kappa_0 + \kappa_{\mathrm{ex},0}/I)/2\pi$ for the ideal ($I = 1$) and non-ideal ($I < 1$) case, with a constant κ_0 and varying $\kappa_{\mathrm{ex},0}$. The effects of the non-ideal coupling become apparent: In the case of the ideal coupling (dashed lines), the point of the full power extinction (i.e. $T = 0$, the critical coupling point) coincides with the point of the maximum intracavity power. This is different for the non-ideal case (solid lines), in which the parasitic losses increase linearly with the coupling rate $\kappa_{\mathrm{p}} = 0.5\kappa_{\mathrm{ex},0}$ in a first order approximation. More importantly, the value of the maximum intra-cavity power is reduced compared to the ideal case. Due to the parasitic losses, critical coupling and over-coupling are only achieved at larger total resonance linewidth, or can not be achieved at all if $\kappa_{\mathrm{p}} > \kappa_{\mathrm{ex},0}$. It is therefore evident that in applications exploiting the resonator's intracavity power enhancement, e.g. for nonlinear photonics, device performance will improve with higher coupling ideality. Likewise, the analysis shows that linewidth measurements carried out at the critical coupling point include possible parasitic loss channels, preventing faithful measurements of the intrinsic microresonator quality factor.

3.5.3 Experimental study of coupling ideality

We experimentally study the coupling ideality for integrated Si_3N_4 microresonators. For microresonator platforms with adjustable couplers e.g. tapered fibres and prism couplers, changing the evanescent coupling rates allows to measure the transmission-linewidth dependence of a single resonance and to retrieve the coupling ideality via Eq. 3.21. In contrast, here we study photonic chips with several microresonator devices that consist of resonators and bus waveguides, as well as inverse tapers placed at the chip facets [241, 239]. The microresonator devices on each chip are identical but have varying gap distances between the resonator and the bus waveguide, providing varying external coupling rates. In this case, coupling ideality is evaluated by analyzing the transmission-linewidth dependence of many resonances acquired for each microresonator device. By measuring several resonators with varying gap distances, the variations in quality factor Q inherent to the fabrication process itself can be revealed.

All measured SI_3N_4 samples were fabricated on the same wafer using the photonic Damascene process [226]. Light is coupled efficiently (loss< 3dB per facet) into a single fundamental mode

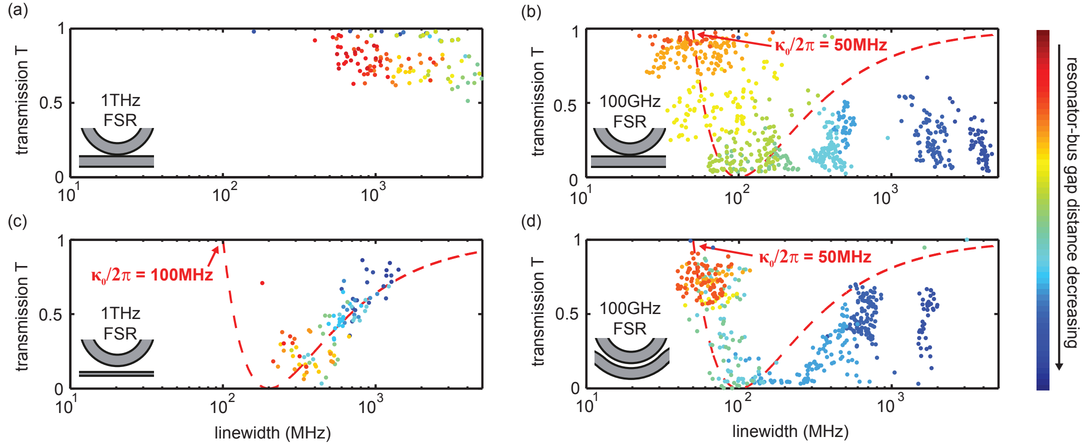

Figure 3.18 – Characterization of coupling ideality for the fundamental $TM_{R,00}$ mode family of 1 THz FSR (Panels a, c) and 100 GHz FSR (Panels b, d) microresonator devices. Dots of the same color correspond to resonances of the same resonator with the color bar indicating their mutual resonator-bus distance trend. The red dashed lines indicate the trend expected for ideal coupling to resonators with the internal loss rates of $\kappa_0/2\pi = 100$ MHz (c) and $\kappa_0/2\pi = 50$ MHz (b, d). For (a), (b) and (d) the bus waveguide has the same cross section as the resonator waveguide. Panels (b) and (d) show improved ideality and achieved overcoupling through the use of a single-mode bus waveguide (b) and a pulley-style coupler (d).

of the bus waveguide via lensed fibres and inverse tapers. Calibrated transmission traces are acquired for all devices on the chip from 1500 nm to 1630 nm using frequency-comb-assisted diode laser spectroscopy [298, 119]. A polarization controller is used to select and maintain a stable input polarization over the full measurement bandwidth. Resonances in each recorded device transmission trace are automatically identified and fitted using a model of a split Lorentzian lineshape [214].

Figure 3.18 compares the measured transmission-linewidth dependence of the resonator's transverse magnetic fundamental mode families ($TM_{R,00}$) for two 1 THz FSR (Panels a, c) and two 100 GHz FSR (Panels b, d) microresonator device chips. Each chip consists of multiple, identical microresonator coupled to bus waveguides but with vary gap distance, thus allowing to plot the transmission-linewidth dependence. The cross-section of the resonator waveguide is 0.87 μm height, and 2 μm (100 GHz FSR) and 1.5 μm (1 THz FSR) width, respectively. Each point represents a measured resonance, and the points with the same color are from the same microresonator device. Different colors denote microresonator devices with different resonator-bus distances on the same chip. The red dashed line traces out the transmission-linewidth dependence for the ideal coupling of unity ideality with a fixed internal loss κ_0.

Figure 3.18(a) shows an example of low coupling ideality. A small radius ($r \approx 23$ μm), 1 THz FSR resonator coupled to a multi-mode bus waveguide of the same cross section. The measured resonances of the fundamental $TM_{R,00}$ mode family have GHz linewidth and low extinction (i.e. high transmission), and their measured transmission-linewidth dependence does not

follow the expected trend of high coupling ideality as shown in Fig. 3.17(b). Due to the identical cross-sections of the resonator and the bus waveguides, this coupler design was naively assumed to provide good propagation constant match between the resonator and bus waveguide TM fundamental modes, i.e. $TM_{R,00}$ and $TM_{B,00}$. However due to the small ring radius $r \approx 23$ μm, the propagation constants of the $TM_{R,00}$ and $TM_{B,00}$ modes are strongly mismatched, despite the identical waveguide cross sections. Therefore, the coupling ideality is compromised due to the mode mismatch between the two coupled modes.

As shown in Fig. 3.18(b), also a 100 GHz FSR resonator, with a ten times larger radius ($r \approx 230\mu$m), can have limited coupling ideality when interfaced with a straight waveguide of the same cross section. Although featuring resonance linewidths below $\kappa_0/2\pi = 30$ MHz and an average linewidth of $\kappa_0/2\pi \approx 50$ MHz, the microresonator can not be strongly overcoupled, indicating the presence of parasitic losses.

Figure 3.18(c) and (d) present two possible coupler designs that improve coupling ideality. First, as shown in Fig. 3.18(c), almost unity ideality and strong overcoupling are achieved for a 1 THz FSR microresonator coupled to a single-mode bus waveguide. The bus waveguide has a cross section of 0.6 μm height and 0.4 μm width due to the aspect-ratio-dependent etch rate during the preform etch [238, 239]. It can thus be concluded that the main source of parasitic losses leading to the low ideality in Fig. 3.18(a) originates from the coupling to higher-order bus waveguide modes. Therefore using a single-mode bus waveguide can essentially avoid this kind of parasitic losses and significantly improve coupling ideality to near unity. As a result, strong overcoupling can be achieved with an external coupling rate $\kappa_{ex,0}$ almost a magnitude larger than the internal losses, with a coupling parameter K=$\kappa_{ex,0}/\kappa_0 = \kappa/\kappa_0 - 1 > 9$.

However in most cases when using a single-mode bus waveguide, though coupling ideality is improved, the propagation constants of bus and resonator fundamental modes (e.g. $TM_{B,00}$ and $TM_{R,00}$) are strongly mismatched, which limits the maximum value of the coupling rate $\kappa_{ex,0}$. Thus a narrow gap is needed to achieve sufficient modal overlap to increase the coupling rate $\kappa_{ex,0}$ and to achieve overcoupling. For the 1 THz FSR resonator, a coupling rate $\kappa_{ex,0}$ sufficient for overcoupling is achieved due to its small mode volume and low internal loss per round-trip ($\propto \kappa_0/D_1$). However for smaller FSR resonators with larger mode volumes e.g. 100 GHz FSR, overcoupling might not be achieved in the case of strong propagation constant mismatch, as fabrication processes pose limitations on the smallest resonator-bus gap distance. One alternative solution for smaller FSR, larger radius resonators to achieve efficient overcoupling is to use a pulley-style coupler [285]. Figure 3.18(d) shows the measurement results for a 100 GHz FSR microresonators coupled with a multi-mode bus waveguide of the same cross-section as the resonator but in a pulley-style configuration. The comparison between the two 100 GHz FSR resonators in Fig. 3.18(b) and Fig. 3.18(d) reveals an improved coupling ideality for the pulley-style coupler. The improved coupling ideality of the pulley-style coupler is not as high as in the case of the 1 THz FSR resonator coupled to a single-mode bus waveguide in Fig 3.18(c). However such a comparison neglects the large difference in resonator mode volume. In fact the fundamental $TM_{R,00}$ mode of the present 100

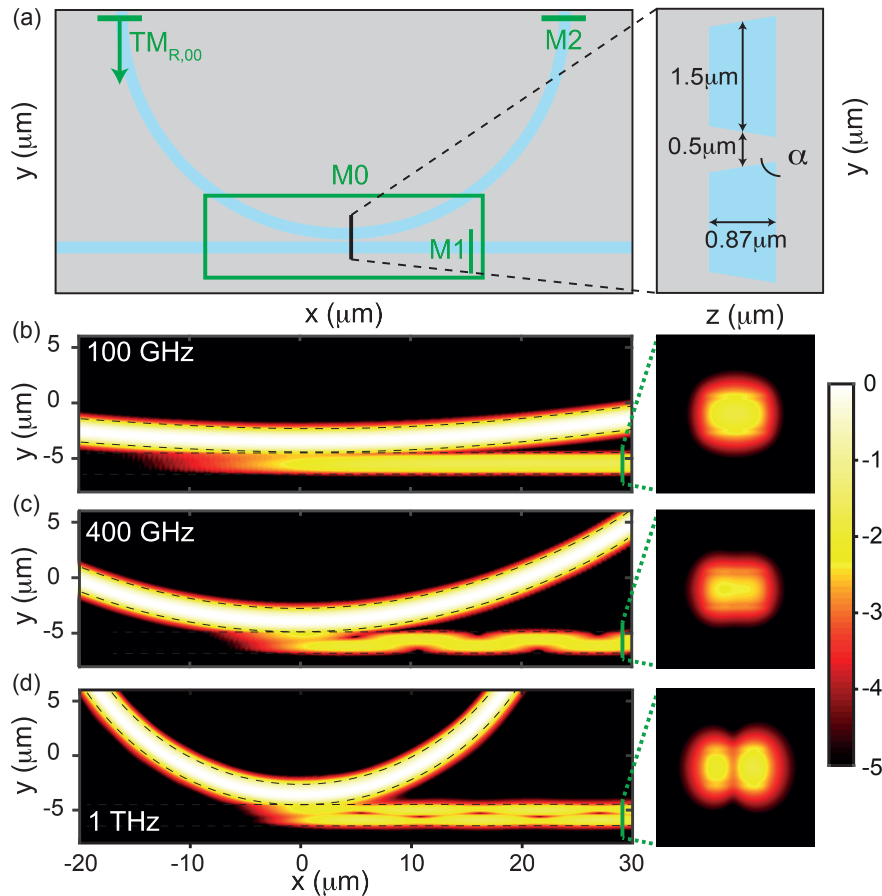

Figure 3.19 – FDTD simulations of waveguide coupling for 100 GHz, 400 GHz and 1 THz FSR resonators. (a) Schematic representation of the simulation model. The boundary condition (thick black lines) enclosing the simulation region is set as PML. The resonator fundamental $TM_{R,00}$ mode is launched into the resonator waveguide and the monitors M0, M1 and M2 record the field distributions in their individual planes. (b, c, d) The field distributions recorded by M0 and M1 for the 100 GHz, 400 GHz and 1 THz FSR resonators. The $TM_{R,00}$ mode is coupled not only to the bus waveguide's fundamental $TM_{B,00}$ mode but also to its higher-order $TM_{B,10}$ mode. The propagation constant difference of both bus waveguide modes causes the interference pattern visible along their propagation direction. This indicates degraded coupling ideality, which is more prominent in the case of 1 THz FSR. The color bar denotes the field intensity in logarithmic scale.

GHz FSR resonator can not be overcoupled using a single-mode bus waveguide, as the strong propagation constant mismatch limits the maximum achievable coupling rates.

3.5.4 Simulations of coupling ideality

In order to verify the dominant origin of parasitic losses and the observed strong design-dependence of coupling ideality, a full 3D finite-difference time-domain (FDTD) simulations

[299] (*Lumerical FDTD Solutions*) is implemented. This allows to study numerically the light propagation through the coupler by solving Maxwell's equations in the time domain. The simulation model is shown in Fig. 3.19(a). Considering the designs of the microresonator devices experimentally characterized in the previous section, the resonator and the bus waveguide have the same cross sections, which is $1.5 \times 0.87\ \mu\text{m}^2$ (width×height) for the 1 THz FSR resonator and $2.0 \times 0.87\ \mu\text{m}^2$ for the 100 GHz FSR resonator. The sidewall angle is $\alpha = 90°$ and the resonator-bus gap distance is set as 0.5 μm. A graded mesh of rectangular cells with the maximum cell volume of $(22\ \text{nm})^3$ is applied to the simulation region. The boundary condition enclosing the full simulation region is set as perfectly matched layer (PML) [260], to absorb the incident light to the boundary and thus to prevent back-reflection.

The resonator fundamental $\text{TM}_{\text{R},00}$ mode at the center wavelength of 1550 nm is launched with unity power and the light field propagates until the field distribution reaches the stationary state in the full simulation region. Monitors M0, M1 and M2 record the field distributions in their individual monitor planes. Figure 3.19(b) and (c) show the field distributions recorded by M0 and M1 for the resonators of 100 GHz, 400 GHz and 1 THz FSR, respectively. An interference pattern in the field distribution along the bus waveguide is observed in all cases, and is more prominent in the case of 1 THz FSR. The field distributions recorded by M1 show that: In the case of 100 GHz FSR, the field propagates predominantly in the bus waveguide fundamental $\text{TM}_{\text{B},00}$ mode, which indicates a limited, non-unity coupling ideality; While in the case of 1 THz FSR, a significant portion of power is coupled to the higher-order $\text{TM}_{\text{B},10}$ mode that beats with the $\text{TM}_{\text{B},00}$ mode along the propagation in the bus waveguide, which indicates a lower coupling ideality. The case of 400 GHz lies in the middle of the 100 GHz and 1 THz FSR cases. These qualitative conclusions from Fig. 3.19 agree well with the experimental observation that the 1 THz FSR resonator in Fig. 3.18(a) shows higher parasitic losses thus a lower coupling ideality compared to the 100 GHz FSR resonator in Fig. 3.18(b).

Further analysis to quantify the degradation of coupling ideality in the 1 THz FSR resonators is performed. The total power $P(\text{total})$ coupled into the bus waveguide can be obtained by calculating the Poynting vector normal to the monitor plane of M1. In addition, using the "**Mode Expansion Function**" (MEF) of *Lumerical FDTD Solutions*, the field distribution recorded by M1 can be projected on each waveguide eigenmode and their individual power ($> 10^{-12}$) can be calculated. All powers are normalized as they derive from the resonator fundamental $\text{TM}_{\text{R},00}$ mode that is launched with unity power. The respective coupling rates $\kappa_{\text{ex},i}$ follow by relating the coupled power to the resonator FSR ($D_1/2\pi$) by $\kappa_{\text{ex},i} = D_1 \times P(i)$. The fundamental bus waveguide mode's power $P(\text{TM}_{\text{B},00})$ can be obtained and the coupling ideality can thus be approximately estimated as $I = P(\text{TM}_{\text{B},00})/P(\text{total})$, assuming that the coupling to the higher-order bus waveguide modes ($\kappa_{\text{ex,HOM}}$) is the dominant origin of parasitic losses. In addition, in order to investigate how the resonator mode is affected by the coupler, also the field distribution recorded by M2 in the resonator waveguide after the coupling section is decomposed into individual modes.

Table 3.20 compiles the simulation results of different coupler designs (No. 1-7) with varying

geometrical parameters, including the resonator FSR, the cross-sections of the resonator and the bus waveguides, the gap distance, and the waveguide sidewall angle α. This angle α takes into account the fact that the fabricated waveguides have slanted sidewalls ($\alpha \approx 80°$). For each design we calculate the individual power of the selected eigenmodes in the resonator ($TM_{R,10}$ and transverse electric fundamental resonator mode $TE_{R,00}$) and the bus waveguide ($TM_{B,00}$, $TM_{B,10}$ and $TE_{B,00}$), and numerically compute the coupling ideality I.

First, Table 3.20 shows that the commonly employed coupler design of a straight bus waveguide coupling to a resonator waveguide of the same cross-section, has a higher coupling ideality for the 100 GHz FSR resonators (No. 7, $I \approx 0.968$) than for the 1 THz FSR resonators (No. 2, $I \approx 0.163$). This agrees well with the previously discussed observations in Fig. 3.18 and Fig. 3.19. The degraded ideality in the case of 1 THz FSR resonators illustrates the limited applicability of this coupler design. The fact that the resonator radius strongly affects coupling ideality is more directly seen by comparing the cases No. 2 and 6, as both cases have exactly the same geometrical parameters except for the resonator FSR.

In addition, the coupling ideality of 100 GHz FSR resonators (No. 6 and No. 7) depends also on the waveguide width when coupled to a bus waveguide of the same cross section. The degradation of coupling ideality in the case No. 7 is due to more power coupled to the higher-order bus waveguide mode ($TM_{B,10}$) which can be explained with the smaller propagation constant mismatch between the fundamental resonator mode ($TM_{R,00}$) and the higher-order bus waveguide mode ($TM_{B,10}$). Additionally the wider waveguide cross-section reduces the mutual modal overlap between the fundamental $TM_{R,00}$ and $TM_{B,00}$ modes and thus their mutual power transfer $P(TM_{B,00})$. Furthermore, our simulations verify the experimentally observed improvement of coupling ideality for the 1 THz FSR resonator coupled to a single-mode bus waveguide (No. 5, $I \approx 1.00$). However this is achieved at the expense of reducing power transfer to the bus waveguide $P(TM_{B,00})$ by nearly one order of magnitude, which is due to the propagation constant mismatch between the $TM_{B,00}$ and $TM_{R,00}$ modes.

Second, though only the fundamental $TM_{R,00}$ mode is launched in the resonator, a non-zero power in a higher-order mode ($P(TM_{R,10})$) is recorded by M2. In addition, it is observed by comparing the uncoupled (No. 1) and coupled cases (No. 2, 3) that this power in the higher-order resonator mode power $P(TM_{R,10})$ increases with decreasing gap distance. In the case of the uncoupled resonator (No. 1), the appearance of $P(TM_{R,10}) = 1.28 \times 10^{-4}$ is mainly attributed to the mesh which acts as a $(22\text{ nm})^3$ surface roughness at the material interface. Such surface roughness is well known to lead to modal coupling e.g. the coupling between the resonator modes $TM_{R,00}$ and $TM_{R,10}$. In addition, compared with the 100 GHz FSR resonator (No. 6, 7), this effect is more prominent in the 1 THz FSR resonator (No. 1). Nevertheless for the coupled resonators (No. 2, 3), the enhancement of $P(TM_{R,10})$ with decreasing gap distance unambiguously reveals the existence of a coupler-induced modal coupling. This is an important finding revealing a novel origin of modal coupling [289] in microresonators, which causes distortion of microresonator dispersion properties.

Third, the coupling of the launched $TM_{R,00}$ mode to the modes with the orthogonal polarization, i.e. $TE_{R,00}$ in the resonator and $TE_{B,00}$ in the bus waveguide, is observed in the case of slanted waveguide sidewalls (No. 4). Such a cross-polarization coupling occurs if the modal field distribution is asymmetric with respect to its center [300, 301] and its strength depends on the degree of this asymmetry. In the simulated case, the asymmetry is introduced by the ring bending and the $\alpha = 80°$ sidewall angle. However by comparing the cases No. 2 and 4, the sidewall angle $\alpha = 80°$ only enhances significantly the power $P(TE_{R,00})$, while the powers of other modes as well as the coupling ideality remain almost the same.

In summary, coupling ideality of monolithically integrated high-Q Si_3N_4 microresonator devices is presented in this section. For the commonly employed coupler design where both the resonator and the bus waveguides have the same cross-sections, the presence of parasitic losses due to the coupling to higher-order bus waveguide modes is revealed. This degrades coupling ideality which is shown both through systematic experimental characterization of resonances and full 3D FDTD simulations. Consequently, an optimized coupler design using a single-mode bus waveguide with efficiently mitigated parasitic losses (ideality $I \approx 1$) and achieved strong overcoupling ($K > 9$) was demonstrated. Moreover, it is discovered that the coupler waveguide can induce modal coupling between different resonator modes which is frequently observed in high-Q microresonators. For microresonator devices based on multi-mode waveguides, coupling ideality is non-trivial to analyze and strongly depends on coupler designs and target mode families. State-of-the-art microresonator devices for applications typically operate around the critical coupling point or the overcoupled regime, thus high device performance requires optimized coupler designs with low parasitic losses and high coupling ideality. This study of coupling ideality in integrated photonic circuits demonstrates the importance of anticipating coupling ideality in device design and the significant improvements it can unlock. The ability to strongly overcouple planar integrated photonic resonators will in particular benefit quantum optical and nonlinear photonic experiments.

No.	1	2	3	4	5	6	7
FSR	1 THz	1 THz	1 THz	1 THz	1 THz	100 GHz	100 GHz
$w_{res} \times h_{res}$ (μm^2)	1.5×0.87	1.5×0.87	1.5×0.87	1.5×0.87	1.5×0.87	1.5×0.87	2.0×0.87
$w_{bus} \times h_{bus}$ (μm^2)	$(\cdots)$	1.5×0.87	1.5×0.87	1.5×0.87	0.40×0.60 (SM)	1.5×0.87	2.0×0.87
Gap (μm)	$(\cdots)$	0.5	0.2	0.5	0.5	0.5	0.5
α	90°	90°	90°	80°	90°	90°	90°
$P(\mathrm{TM}_{R,10})$	1.28×10^{-4}	7.87×10^{-4}	0.0116	7.6×10^{-4}	3.9×10^{-4}	1.82×10^{-6}	1.72×10^{-5}
$P(\mathrm{TE}_{R,00})$	$<10^{-12}$	$<10^{-12}$	$<10^{-12}$	1.08×10^{-6}	$<10^{-12}$	$<10^{-12}$	$<10^{-12}$
$P(\mathrm{TM}_{B,00})$	$\cdots$	3.36×10^{-3}	0.0344	3.31×10^{-3}	3.92×10^{-4}	0.0237	5.73×10^{-3}
$P(\mathrm{TM}_{B,10})$	$(\cdots)$	0.0176	0.0974	0.0173	$(\cdots)$	3.4×10^{-6}	1.81×10^{-4}
$P(\mathrm{TE}_{B,00})$	$\cdots$	$<10^{-12}$	$<10^{-12}$	4.89×10^{-6}	$<10^{-12}$	$<10^{-12}$	$<10^{-12}$
P(total)	$(\cdots)$	0.0209	0.133	0.0203	3.92×10^{-4}	0.0237	5.92×10^{-3}
I	$(\cdots)$	0.161	0.259	0.161	1.00	1.00	0.968

Figure 3.20 – Table of simulated coupled powers for different coupler designs. The resonator fundamental $\mathrm{TM}_{R,00}$ mode is launched with unity power. The individual modal powers in the resonator and the bus waveguides after the coupling section are listed. P(total) is the total power recorded in the bus waveguide after the coupling section and I is the coupling ideality calculated as $I = P(\mathrm{TM}_{B,00})\,/\,P(\mathrm{total})$. The bus waveguide is single-mode (SM) in the case No. 5, while all the other bus waveguides are multi-mode. Modes which do not exist are marked with hyphen " - ".

4 Chip Characterization and Waveguide Loss Analysis

In this chapter, I will present the method to characterize the microresonator dispersion and resonance linewidths (i.e. to extract microresonator Q). A large number of microresonators are measured, and all the measured resonances can be statistically analyzed to find the most probable value, which is representative for microresonator Q. In the end of this chapter, a linear microresonator response measurement is performed to quantitatively measure the thermal absorption losses, which in our high-Q devices, are only 0.2 MHz.

4.1 Characterization of microresonator dispersion and Q

There are several methods to measure the microresonator GVD parameter D_2. Among these methods, **frequency-comb-assisted diode laser spectroscopy** [298], enabling broadband spectral characterization with fast measurement speed (> 1 THz/s) and simple implementation, has been successfully applied for distance measurement [302, 303], dynamic waveform detection [304], plasma diagnostics [305] and molecular spectroscopy [306, 307]. One application benefiting from the advantages is the dispersion characterization of high-Q optical microresonators [85, 44, 308, 309, 88], while alternative methods using direct frequency comb [310, 311], white light source [37] or sideband spectroscopy [312] have several limitations including system complexity, low data acquisition speed, narrow bandwidth and inability to measure microresonators with large free spectral ranges exceeding 100 GHz. In this section, the dispersion characterization of microresonators using frequency-comb-assisted diode laser spectroscopy is presented. The main result has been published in ref. [119], J. Liu et al, "**Frequency-comb-assisted broadband precision spectroscopy with cascaded diode lasers**", *Opt. Lett.* 41, 3134 (2016).

4.1.1 Dispersion Characterization with One Diode Laser

Figure4.1 shows the schematic of the experimental setup for characterization of microresonator dispersion and resonance linewidth, using frequency-comb-assisted diode laser spec-

troscopy. The laser from a widely tunable, mode-hop-free, external cavity diode laser (ECDL) working in the wavelength range of 1500 – 1630 nm (Santec TSL-510) is split into three branches. The polarization of the input light is tuned by a polarization controller (PC). A fully-stabilized, spectrally-broadened, erbium-fiber-laser-based frequency comb (MenloSystems FC1500) extending from 1050 nm to 2100 nm is used, whose repetition rate $f_{\text{rep}} \approx 250.14424$ MHz and carrier-envelope offset frequency $f_{\text{ceo}} \approx 20$ MHz are both locked to a reference microwave clock. The first branch from the ECDL's output is sent to beat with the fiber frequency comb.

When ECDL scans, the ECDL beats with the frequency comb and "running" beat notes were generated in the frequency domain. The beat notes between the ECDL and its two nearest comb lines at frequencies f_{beat} and $f_{\text{rep}} - f_{\text{beat}}$ are of particular interest. The optical beat signal is detected by a photodiode (PD 1) which outputs the electrical beat signal. The electrical beat signal is split by a 50/50 RF splitter, followed by two band-pass filters (BP 1 and BP 2, bandwidth $\Gamma/2\pi \approx 2$ MHz). BP 1 has the center frequency of $f_{\text{BP}\,1} = 35.13$ MHz and BP 2 has the center frequency $f_{\text{BP}\,2} = 69.80$ MHz. Due to the presence of BP 1 and BP 2, when the running beat notes fall in the band-pass ranges, a "**calibration marker**" is generated. Therefore, the ECDL scan generates four calibration markers per f_{rep} interval when the frequency distance to its nearest comb line is $\pm f_{\text{BP}\,1}$ or $\pm f_{\text{BP}\,2}$. Two markers center symmetrically to the comb line which generates them with distance of $35.13\text{MHz} \times 2 = 70.26$ MHz ("inner marker"), and two markers center symmetrically to the comb line with distance of $69.80\text{MHz} \times 2 = 139.60$ MHz ("outer marker"). The calibration markers are recorded by the oscilloscope in the "peak-detect" sampling mode, as shown in Fig.4.2. The polarization of the frequency comb is controlled by a PC to improve the calibration markers' signal-to-noise ratio (SNR).

The second branch from the ECDL's output is sent to the Si_3N_4 chip. The transmission spectrum through the Si_3N_4 microresonator is detected by PD 2 and also recorded by the oscillo-

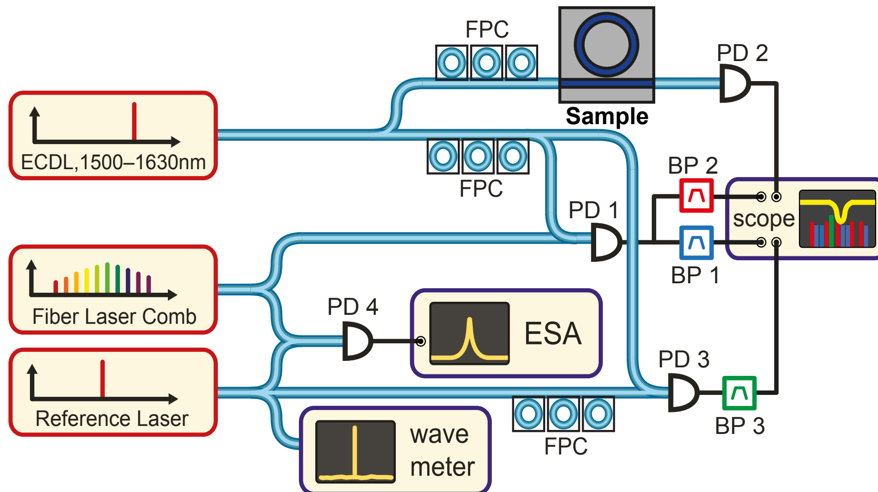

Figure 4.1 – Schematic of the setup for the dispersion characterization using frequency comb assisted diode laser spectroscopy. BP: band-pass filter. OSA: optical spectrum analyzer.

scope. A PC is used to change the polarization of the input light such that both TE and TM mode resonance can be recorded individually.

The third branch from the ECDL's output is sent to beat with a stable reference laser (Koheras BASIK) whose wavelength is 1548.7 nm. With a low-pass filter (BP 3), a "**reference marker**" is generated when the ECDL scans through the reference laser. Such reference marker is used for the absolute frequency calibration. Also, a PC is used to change the polarization of the reference laser to improve the reference marker's SNR.

During the ECDL scan, the transmission spectrum through the Si_3N_4 microresonator is recorded by the oscilloscope in the time domain. To project the time domain to the frequency domain (to know the resonance frequency instead of when the resonance occurs), it requires frequency calibration with respect to the reference laser based on f_{rep}, $f_{\mathrm{BP\,1}}$ and $f_{\mathrm{BP\,2}}$. As shown in Fig.4.2, each time a group of four calibration markers is generated in the time domain, the laser scans over one f_{rep} in the frequency domain. As the precise frequency difference between any two adjacent calibration markers is known, assuming that the ECDLs scan uniformly in each f_{rep} interval, the instantaneous (relative) frequency of any data point can be interpolated based on f_{rep}, $f_{\mathrm{BP\,1}}$ and $f_{\mathrm{BP\,2}}$. The reference laser sets the frequency reference for the absolute frequency calibration. Figure 4.3 shows all the recorded data including the transmission spectrum, the calibration markers and the reference marker, with different scales ($\times$20 and $\times$500) showing the data details.

The precision of the frequency calibration is limited by two factors: a 2.2 MHz/point error due to the oscilloscope's maximum 10 million data points per trace over 22 THz (1355 – 1505 nm) scan range and the error due to $\Gamma/2\pi \approx 2$ MHz bandwidths of BPs. Error in reading the f_{rep} leads to a systematic error in the relative frequency calibration, however f_{rep} is read very precisely with precision better than 1 Hz and the systematic error is negligible compared with the other two errors. Therefore the total error is estimated as 4.2 MHz/point. However

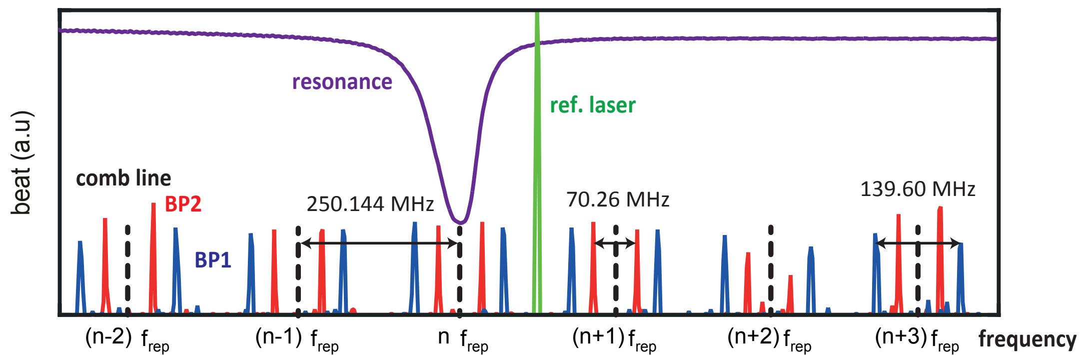

Figure 4.2 – Signals recorded by the oscilloscope in each laser scan. The calibration markers (blue, red) and the reference markers (green) are denoted. Two BPs are used in order to generate double calibration markers for better frequency determination. Each group of calibration markers is indexed by the comb line that generates it (black dashed lines).

such error will not be prominent for resonances with >100 MHz linewidth, as the resonant frequency is usually obtained by line profile fitting whose precision is then limited by the signal quality, background fluctuation, fitting function used, resonance splitting etc.

The reference laser's frequency f_{ref} is read either from an optical spectrum analyzer (OSA) which has an imprecision of few gigahertz or from a wavelength-meter which has an imprecision of few hundred MHz. Such imprecision will introduce a global offset to the absolute frequency calibration, but will not affect the continuity of the trace combination and the relative frequency calibration with respect to f_{ref}. The global offset (i.e. an absolute frequency measurement) is much less important for certain measurements such as the dispersion measurement of microresonators where the entire frequency scan needs to exhibit a precise relative frequency calibration, but not necessarily an absolute frequency calibration.

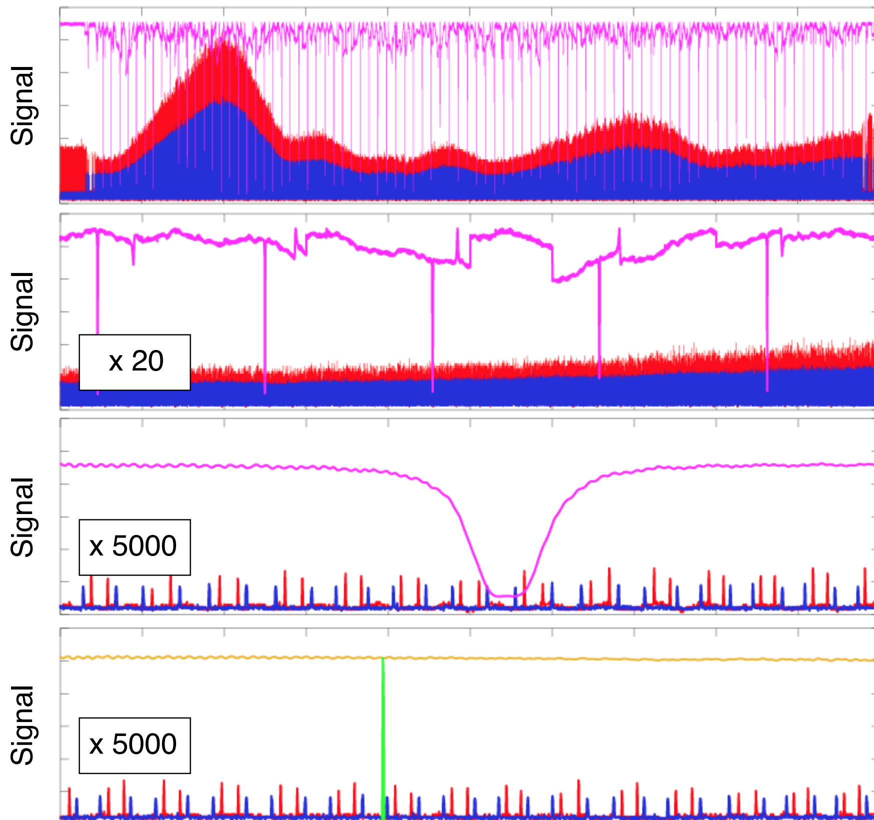

Figure 4.3 – Data traces showing all the recorded data including the transmission spectrum, the calibration markers and the reference marker. The representation at different scales ($\times 20$ and $\times 500$) shows the data details.

4.1.2 Dispersion Characterization with Cascaded Diode Lasers

The method based on frequency-comb-assisted diode laser spectroscopy is able to measure the dispersion parameter D_2 of microresonators. However, to measure the higher order dispersion such as D_3 and D_4, frequency-comb-assisted diode laser spectroscopy has the bandwidth limitation, as the effect from higher-order dispersion becomes strong only for resonances with large index μ. Therefore, increasing the measurement bandwidth is required to measure higher order dispersion.

The measurement bandwidth is determined by two factors: the wavelength tuning range of the used laser and the range of the frequency comb. Usually the second one can be satisfied easily, as a spectrally broadened frequency comb can cover hundreds of nanometres range, e.g. the Menlo frequency comb that we use covers one octave from 1050 nm to 2100 nm. Therefore the main limitation becomes the wavelength tuning range of the used laser. One solution is to use more than one laser to cover different ranges, and combine the individual data into a single one. In this section a method to extend the measurement bandwidth by cascading two widely tunable lasers covering the wavelength range from 1355 nm to 1630 nm is demonstrated. The validity of our method is examined by molecular absorption spectroscopy. Subsequently this method is used to characterize the dispersion of a Si_3N_4 microresonator whose FSR is approximately 1 THz, as an example.

The setup is shown in Fig.4.4. Compared to the setup shown in the previous section, ECDL 2 working in the range of 1355 – 1505 nm is added. Thus the full bandwidth becomes 1355 – 1630 nm (184 - 221 THz). In addition, a 1310 nm/1550 nm wavelength-division multiplexer (WDM) splits the frequency comb into two branches. Two optical switches are synchronized, such that ECDL 1 beats with the 1310 nm branch, and successively ECDL 2 beats with the

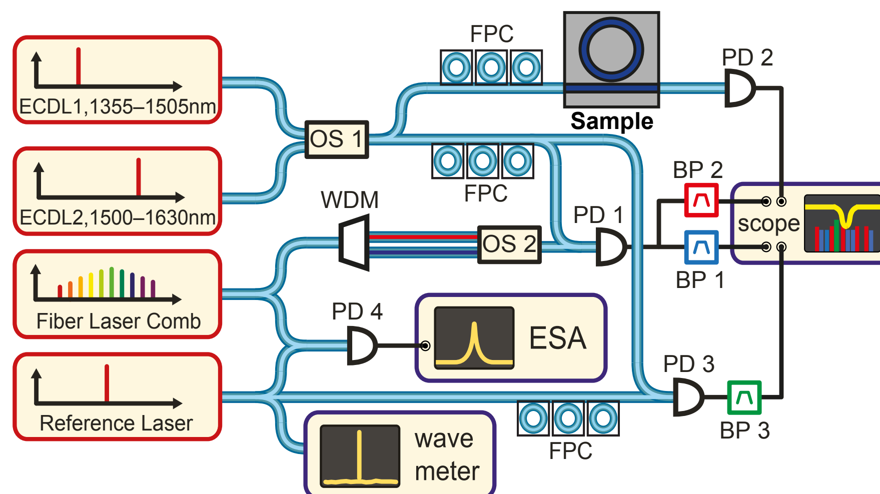

Figure 4.4 – Schematic of the setup used for cascaded frequency comb assisted diode laser spectroscopy. OS: optical switch; WDM: wavelength-division multiplexer; ESA: electrical spectrum analyzer.

1550 nm branch. The purpose of using the WDM and synchronizing the optical switches is to suppress the comb lines which do not contribute to the beat signals, thus to prevent the photodiode saturation and to improve the signal-to-noise ratio of the beat signals especially for the 1310 branch.

The two ECDLs scan one after the other with a scan speed of 10 nm/s. By using the band-pass filters labeled as BP 1 and BP 2 (center frequencies $f_{\mathrm{BP}\,1}$ and $f_{\mathrm{BP}\,2}$), the scanning ECDL generates four "calibration markers" per f_{rep} interval when the frequency distance to its nearest comb line is $\pm f_{\mathrm{BP}\,1}$ or $\pm f_{\mathrm{BP}\,2}$ [298]. The key problem is the combination of the two individual traces generated by the two ECDL scans into a single continuous trace which covers the full measurement range. This is solved by using an auxiliary reference laser (New Focus Velocity) whose wavelength λ_{ref} is set in the 1500 – 1505 nm range where both ECDLs overlap spectrally. With a low-pass filter (BP 3), in each trace a "reference marker" is recorded when the

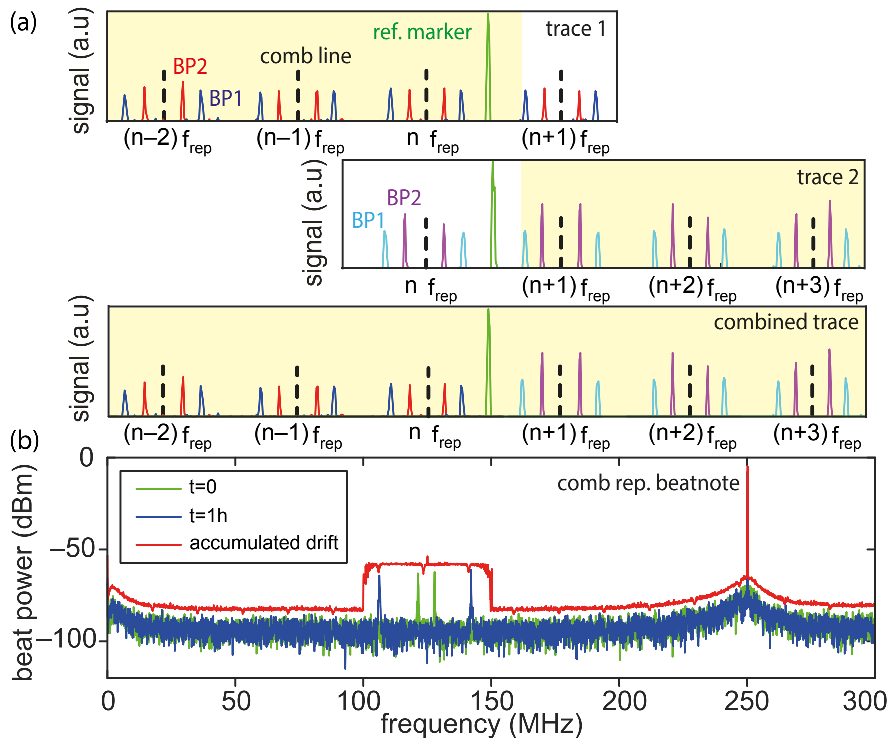

Figure 4.5 – Procedure to combine two ECDL scan traces using the reference laser. (a) The calibration markers (blue, red, cyan and purple) and the reference markers (green) are denoted in both traces. Two BPs are used in order to generate double calibration markers for better frequency determination. Each group of calibration markers is indexed by the comb line that generates it (black dashed lines). The combined trace is formed by combining the data in the yellow shaded zones of both traces. (b) Measurement of the reference laser's drift within 1 hour by beating it with the frequency comb and observing the beat note's drift on an ESA. The peak at 250 MHz is the frequency comb's repetition rate beat f_{rep}. Two peaks symmetrical to 125 MHz are due to the reference laser beating with its two nearest comb lines. Accumulated drift is recorded by using the "maximum hold" function of the ESA.

ECDL scans over the reference laser. The reference laser is set initially $f_{\text{rep}}/2$ from its nearest comb line, and its long-term drift is measured as <20 MHz/h as shown in Fig.4.5(b). As long as the reference laser drifts less than $f_{\text{rep}}/2$ from its initial position within the measurement time (≈60 s), which can be monitored by an electrical spectrum analyzer (ESA), it can be unambiguously assumed that the calibration markers adjacent to the reference marker are generated by the same comb line in both traces. Therefore, using the reference marker, the indices of the calibration markers in both traces can be matched. As shown in Fig.4.5(a), by combining the data before the reference marker in trace 1 with the data after the reference marker in trace 2, a complete continuous trace from 1355 nm to 1630 nm is formed.

4.1.3 Molecular Spectroscopy

In order to examine the validity of this method, e.g. the continuity of the combined trace and the relative frequency calibration, a molecular absorption spectroscopy of a gas cell composed of water (H_2O), carbon monoxide (CO) and acetylene (C_2H_2) is implemented and compared with the absorption line data from HITRAN*online* [313] (www.hitran.org). The normalized transmission spectrum is shown in Fig.4.6(a), and the absorption lines for each kind of molecule are marked. As the spectroscopy is not Doppler-free, Doppler broadening dominates the linewidth given by the Gaussian profile as

$$g_D(f-f_0)=\frac{\alpha}{f_0}\sqrt{\frac{Mc^2}{2\pi kT}}\exp[-\frac{Mc^2}{2kT}\frac{(f-f_0)^2}{f_0^2}] \tag{4.1}$$

The full-width-at-half-maximum (FWHM) of Doppler linewidth is $\Delta f = 2f_0(2kT\ln 2/Mc^2)^{1/2}$. The fitted linewidth distribution is shown in Fig.4.6(b). A clear trend of linewidth increase is seen from CO (28 g/mol) to H_2O (18 g/mol), as CO moves slower thus has smaller Doppler broadening effect.

The fitted line-center frequencies f_{fit} are then compared with the known frequencies f_{HIT} from HITRAN*online*, and a global offset $f_{\text{off}} \approx -98$ MHz is observed due to the reason mentioned above. Such an offset $f_{\text{off}} = -98$ MHz is introduced due to the imprecision of the wavelength-meter as mentioned above and the pressure-induced line shift [314, 315]. Subtracting the global offset, the frequency deviations defined by $\delta = f_{\text{fit}} - f_{\text{HIT}} - f_{\text{off}}$ are plotted in Fig.4.6(c). All the frequency deviations are distributed in a ±100 MHz range around 0 MHz, showing the continuity of the combined trace and a good global accuracy of the relative frequency calibration. As the CO lines suffer the least Doppler broadening effect due to the largest molecular mass of CO, their frequencies are more precisely fitted with smaller deviations. Therefore to examine the precision of the relative frequency calibration, the deviation distribution of CO lines is fitted with a Gaussian distribution and a 13.6 MHz standard deviation is shown. It should be emphasized that the 13.6 MHz standard deviation is not due to the method itself,

but mainly due to the fitting error in determining the line-center frequencies with the GHz linewidths and the pressure-induced line shifts [314, 315]. To eliminate the Doppler broadening and to demonstrate better precision, a Doppler-free spectroscopy could be built [306, 307], which requires free space optics and high laser output power.

4.1.4 Dispersion Characterization

The method is applied to characterize the dispersion of a Si_3N_4 microresonator with 1 THz FSR. By design, the microresonator has $0.87 \times 1.4\ \mu\ m^2$ cross-section and is coupled by a straight single-mode bus waveguide with approximate $0.87 \times 0.5\ \mu\ m^2$, as shown in Fig.4.7(a). If TM/TE mode is launched in the bus waveguide, both TM_{00}/TE_{00} and TM_{10}/TE_{10} modes of

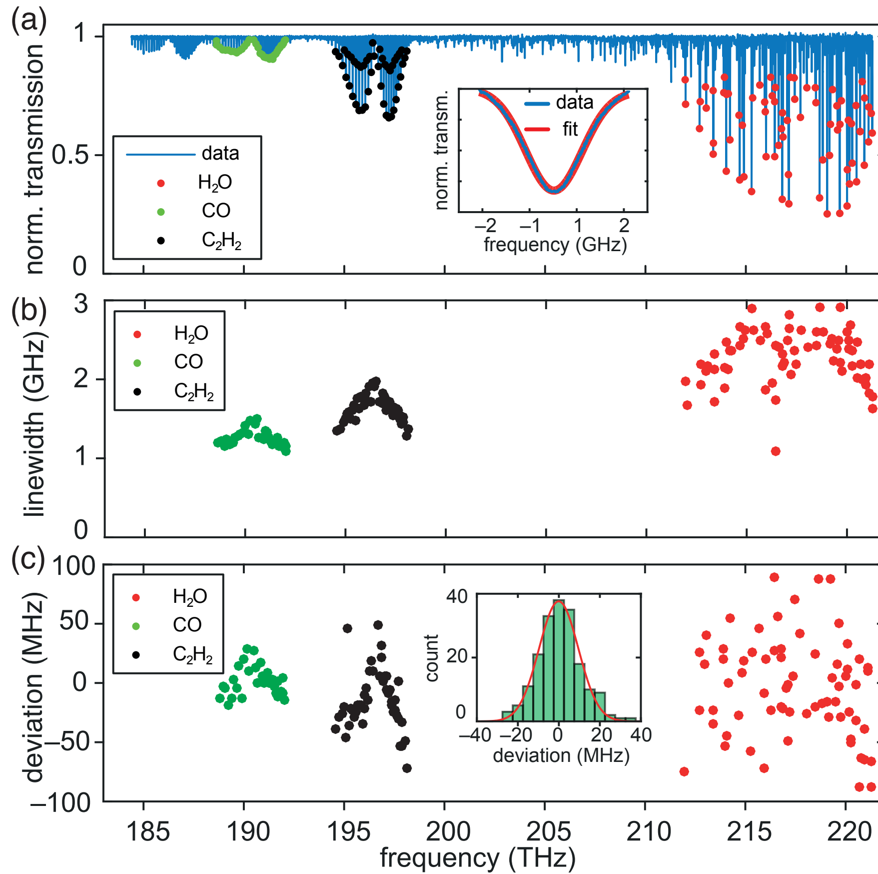

Figure 4.6 – Broadband characterization of a molecular absorption spectroscopy. (a) Normalized transmission spectrum of the gas cell. Each kind of molecule is marked according to the data from HITRAN*online*. Inset: one CO line and fit with Gaussian profile. (b) Linewidths of each absorption line fitted with Gaussian profiles. (c) Deviations of the fitted line-center frequencies from the values on HITRAN*online*. Inset: histogram of the deviations of CO lines from six repeated measurements and fit with a Gaussian distribution (red curve) with a standard deviation of 13.6 MHz.

the microresonator are excited. TM_{00}/TE_{00} and TM_{10}/TE_{10} modes can be distinguished from their different linewidths referred to the FDTD simulations as shown in Fig.4.7(b), or from their different FSRs referred to the FEM simulation. Fig.4.7(c) plots the transmission spectrum for the TM mode. Each resonance is fitted with the model derived in ref. [214] as Eq.4.2:

$$g_G = \frac{\delta_0^2 - \delta_c^2 + \beta^2 - \Delta\omega^2 + i2\delta_0\Delta\omega}{(\delta_0 + \delta_c)^2 + \beta^2 - \Delta\omega^2 + i2\Delta\omega(\delta_0 + \delta_c)} \tag{4.2}$$

The amplitude transmittance coefficient T describes the waveguide-ring resonator coupling; δ_0 describes the internal loss; $\delta_c = T^2/2\tau_0$ is the decrement the coupler device, with τ_0 is the circulation time; $\delta\omega$ is frequency detuning from unperturbed resonance.

The center frequency and the linewidth are extracted from the fit with Eq.4.2. Both a 3$^{\text{rd}}$ order and a 4$^{\text{th}}$ order weighted polynomial are used to fit the $D_{\text{int}}/2\pi$, while the reference resonance $\omega_0/2\pi$ is chosen at 193.12 THz (1553.5 nm). The fit is performed by weighting each resonance according to the inverse of its linewidth, as the center frequencies of broader resonances are less precisely fitted. By observing whether the 4$^{\text{th}}$ order weighted polynomial has significantly better fit than the 3$^{\text{rd}}$ order one, one can find if there is a necessity to consider the fourth order dispersion parameter D_4 in the fit.

Figure 4.8(b) plots the fitted linewidths of the TM_{00} mode, compared with the simulated linewidths $\kappa/2\pi$. $\kappa/2\pi$ has two components $(\kappa_{\text{ex}} + \kappa_0)/2\pi$, $\kappa_{\text{ex}}/2\pi$ is due to the wavelength-

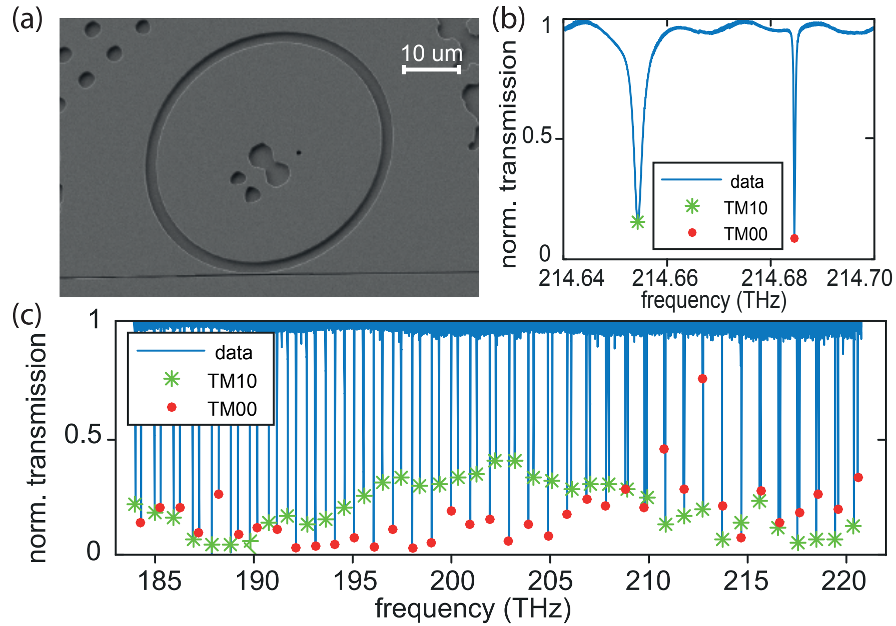

Figure 4.7 – Broadband dispersion characterization of a Si_3N_4 photonic chip-based microresonator with FSR≈1 THz. (a) SEM image of the used microresonator geometry. (b) Linewidth difference between TM_{00} and TM_{10} modes. (c) Normalized transmission spectrum of the TM mode through the microresonator.

dependent waveguide-resonator external coupling strength [47] whose value is extracted from a FDTD simulation, and $\kappa_0/2\pi$ is due to the intrinsic loss whose value is extracted from the linewidth fit and is assumed as a constant 110 MHz. In addition, an avoided modal crossing [44, 309] is identified around 213 THz where both modes have approximately the same local resonance frequency. At such a modal crossing point, the resonances deviate from the fitted dispersion curve and a local linewidth broadening is observed. Figure 4.8(c, d) plots the $D_{\text{int}}/2\pi$ and the fitted linewidths of the TM_{10} mode. Figure 4.9 plots the $D_{\text{int}}/2\pi$ and the fitted linewidths of TE_{00} and TE_{10} modes. The dispersion parameters extracted from the 4$^{\text{th}}$ order weighted polynomial fit are shown in Table. 4.1.

Table 4.1 – Fitted dispersion parameters.

Parameter	TM_{00} mode	TM_{10} mode	TE_{00} mode	TE_{10} mode
$D_1/2\pi$	980.2 GHz	958.9 GHz	991.1 GHz	962.1 GHz
$D_2/2\pi$	-26.08 MHz	-559.5 MHz	51.95 MHz	-674.0 MHz
$D_3/2\pi$	5.62 MHz	46.3 MHz	1.12 MHz	44.0 MHz
$D_4/2\pi$	-0.200 MHz	-2.03 MHz	-0.117 MHz	-1.31 MHz

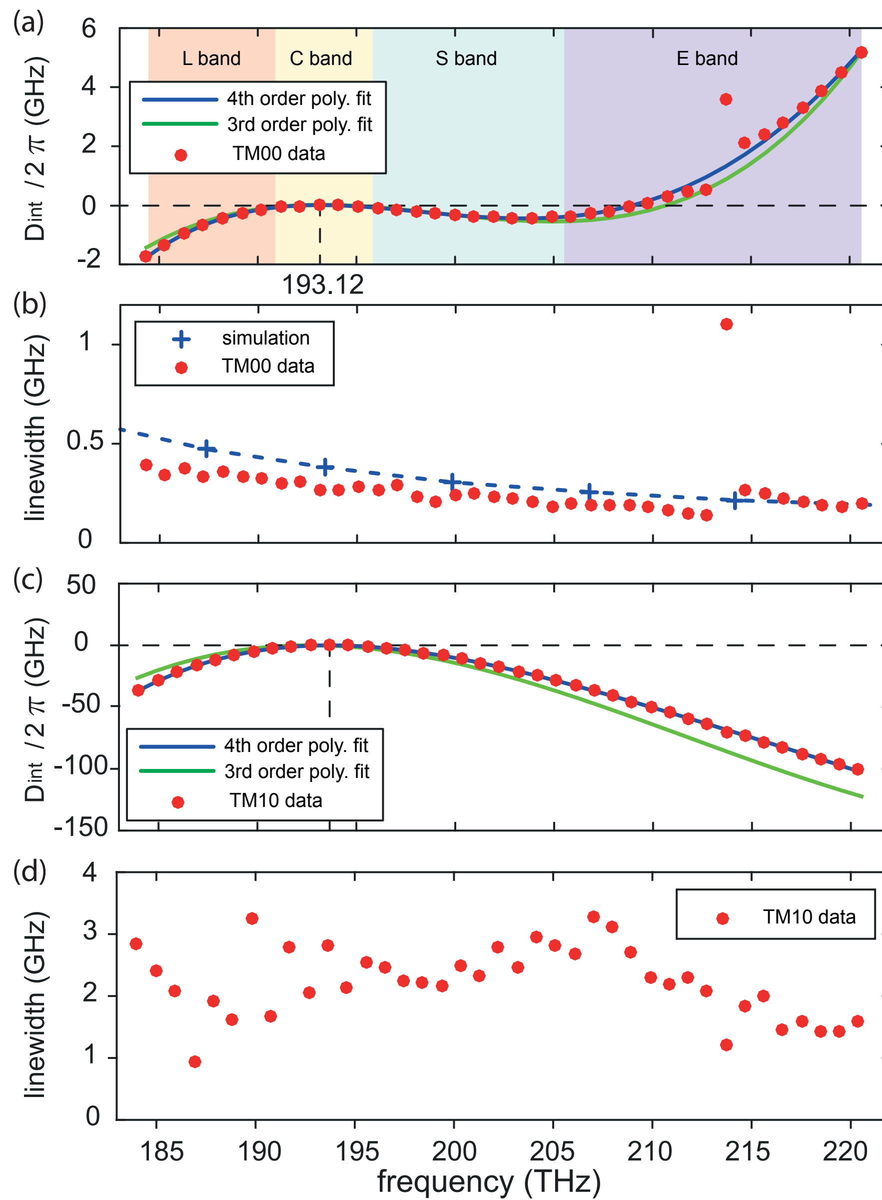

Figure 4.8 – Plot of the TM mode dispersion. (a) Plot of $D_{\text{int}}/2\pi$ of the TM_{00} mode. Red points are the measured data, green solid curve is the 3rd order weighted fitting polynomial, blue solid curve is the 4th order weighted fitting polynomial. Different optical fiber communication bands are highlighted by different color shaded zones. (b) Plot of the fitted linewidths of the TM_{00} mode and comparison to the simulated linewidths. (c) Plot of $D_{\text{int}}/2\pi$ of the TM_{10} mode. (d) Plot of the fitted linewidths of the TM_{10} mode.

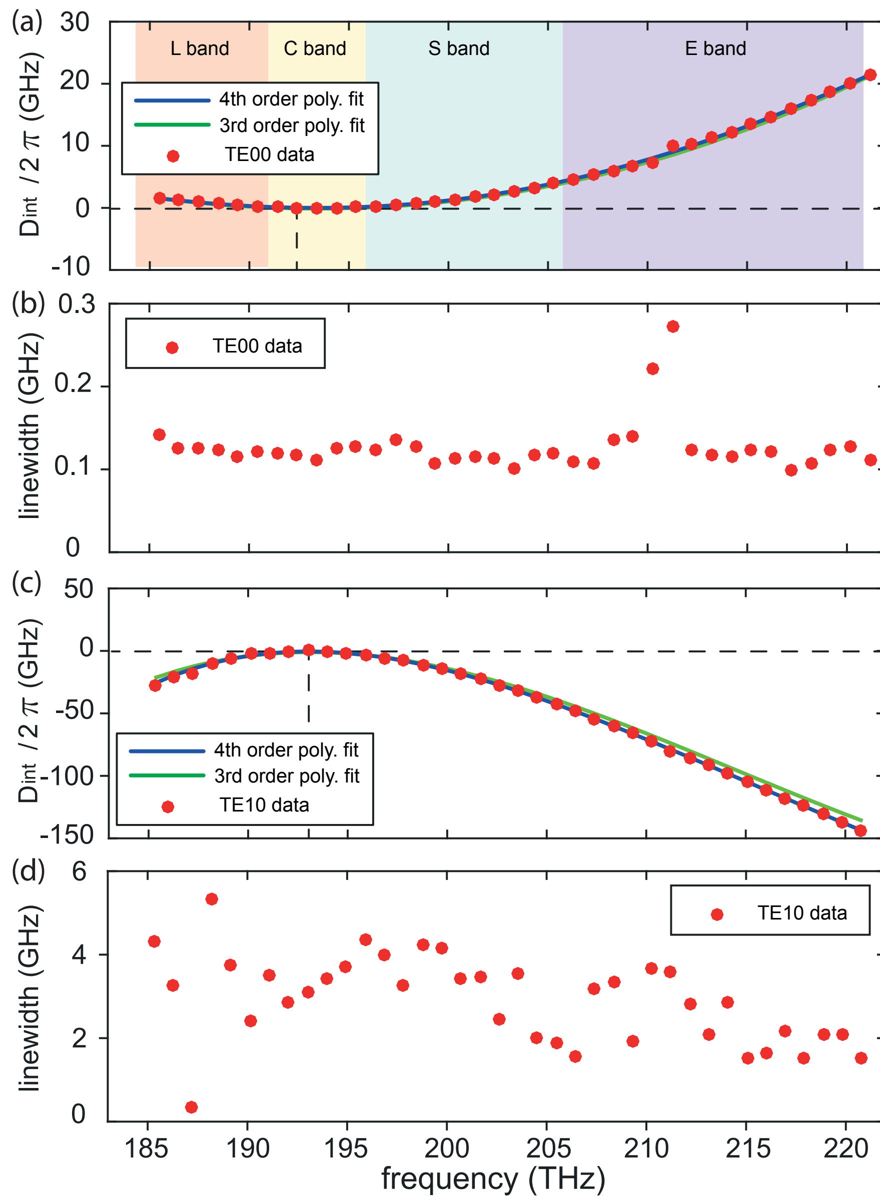

Figure 4.9 – Plot of the TE mode dispersion. (a) Plot of $D_{\text{int}}/2\pi$ of the TE_{00} mode. (b) Plot of the fitted linewidths of the TE_{00} mode. (c) Plot of $D_{\text{int}}/2\pi$ of TE_{10} mode. (d) Plot of the fitted linewidths of the TE_{10} mode.

4.2 Statistical analysis of microresonator Q factors

In this section, a systematic study of Si_3N_4 microresonators Q factors (i.e. optical losses) is presented. The main result has been published in ref. [92], "**High-yield wafer-scale fabrication of ultralow-loss, dispersion-engineered silicon nitride photonic circuits**", arXiv 2005.13949 (2020). I developed the fabrication process, designed the chip devices, fabricated the Si_3N_4 samples and led the experimental characterization of samples. Jijun He has contributed significantly to the sample characterization. Guanhao Huang has led the experiment and simulation of microresonator linear response measurement. Rui Ning Wang has contributed to the sample fabrication.

The microresonators studied here were all fabricated using the current photonic Damascene

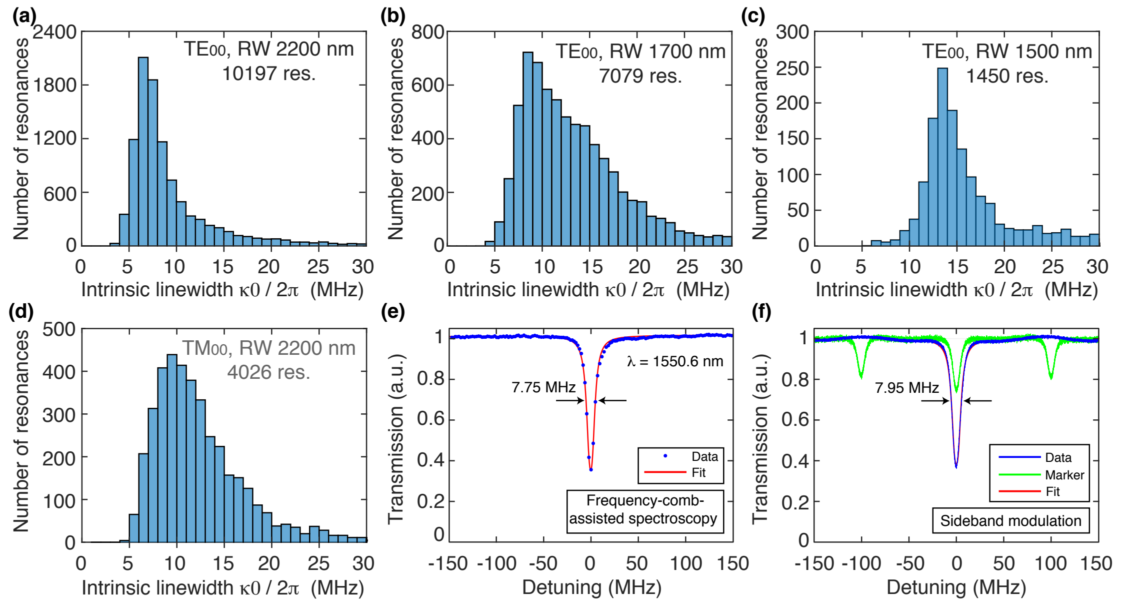

Figure 4.10 – Comparison of $\kappa_0/2\pi$ histograms of different resonator waveguide widths and in different modes. (a) Waveguide width is 2200 nm, histogram of 10197 TE_{00} resonances from twenty-six resonators of 40.6 GHz FSR shows the most probable value of $\kappa_0/2\pi \sim 6.5$ MHz (i.e. $Q_0 \sim 30 \times 10^6$). (b) Waveguide width is 1700 nm, histogram of 7079 TE_{00} resonances from nine resonators of 19.6 GHz FSR shows the most probable value of $\kappa_0/2\pi \sim 8.5$ MHz (i.e. $Q_0 \sim 23 \times 10^6$). (c) Waveguide width is 1500 nm, histogram of 1450 TE_{00} resonances from eight resonators of 98.9 GHz FSR shows the most probable value $\kappa_0/2\pi \sim 13.5$ MHz (i.e. $Q_0 \sim 15 \times 10^6$). (d) Waveguide width is 2200 nm, histogram of 3544 TM_{00} resonances from nine resonators of 40.6 GHz FSR shows the most probable value of $\kappa_0/2\pi \sim 9.5$ MHz (i.e. $Q_0 \sim 20 \times 10^6$). (e, f) The resonance measured at 193.47 THz using the frequency-comb-assisted diode laser spectroscopy (e), and the sideband modulation technique (f). The fitted values in (e) are $\kappa/2\pi \sim 7.75$ MHz and $\kappa_0/2\pi \sim 5.87$ MHz, and in (f) are $\kappa/2\pi \sim 7.95$ MHz and $\kappa_0/2\pi \sim 6.05$ MHz. Both methods agree with each other, and show $Q_0 > 32 \times 10^6$. a.u.: arbitrary unit.

process and characterized using the frequency-comb-assisted diode laser spectroscopy, as illustrated previously. The total (loaded) linewidth $\kappa/2\pi = (\kappa_0 + \kappa_{ex})/2\pi$, the intrinsic linewidth (i.e. intrinsic loss) $\kappa_0/2\pi$ and the coupling strength $\kappa_{ex}/2\pi$ are extracted from each resonance fit [214, 316]. While the coupling strength $\kappa_{ex}/2\pi$ depends on the bus-waveguide-to-resonator gap distance, the microresonator intrinsic loss $\kappa_0/2\pi$ is mainly affected by the fabrication process. Therefore, here the study is focused on the statistical performance of the intrinsic loss $\kappa_0/2\pi$. The $\kappa_0/2\pi$ of all measured resonances, from many samples, are put into a histogram. The most probable value of the $\kappa_0/2\pi$ histogram should properly represent the intrinsic Q factor ($Q_0 = \omega/\kappa_0$) of microresonators, and the quality of our fabrication process.

Here, only the fundamental transverse electric (TE_{00}) and magnetic (TM_{00}) modes are studied. Figure 4.10(a, b, c) compare the histogram of $\kappa_0/2\pi$ in the TE_{00} mode, for three waveguide widths, 2200 nm, 1700 nm and 1500 nm, while the waveguide heights are above 850 nm and nearly identical. The lowest $\kappa_0/2\pi$ is achieved at 6.5 MHz in the waveguide of 2200 nm width, from 10197 resonances measured from twenty-six 40-GHz-FSR microresonators. The $\kappa_0/2\pi \sim$ 6.5 MHz corresponds to $Q_0 > 30 \times 10^6$. A waveguide-width-dependent κ_0 is revealed, i.e. a larger waveguide width results in a lower κ_0 (thus a higher Q_0). For the Damascene process, the waveguide top surface is planarized via CMP and features sub-nanometre roughness [90, 100]. The waveguide bottom surface has superior quality determined by SiO_2 growth using thermal wet oxidation on single-crystal silicon wafers. Therefore, likely the waveguide sidewall roughness is the main reason for scattering losses. The comparison in Fig. 4.10 supports that, as a waveguide of a larger width has a weaker optical mode interaction with the waveguide sidewall, the resulted scattering losses are less and the Q_0 is higher. It also suggest that, in order to compare different fabrication processes for attaining lower losses, the geometry dependence needs to be included. Reports on large-aspect-ratio Si_3N_4 waveguides [201, 199, 100], with waveguide widths exceeding $10\mu m$, have shown exceptionally low loss ($\alpha/2\pi < 0.1$ dB/m) and high microresonator Q ($Q_0 \sim 81 \times 10^6$). These Si_3N_4 waveguides are ideal for passive elements such as delay lines and optical packet routers [196], but not suitable for soliton microcomb and supercontinuum generation due to the normal GVD and large mode area, resulting from the large waveguide width.

Figure 4.10(d) shows the histogram of $\kappa_0/2\pi$ in the TM_{00} mode, for 2200 nm waveguide width, in comparison with the TE_{00} mode shown in Fig. 4.10(a). This comparison shows that the TE_{00} mode has lower κ_0 (higher Q_0) than the TM_{00} mode. This is likely due to the fact that the waveguide aspect ratio, width / height = 2200/900, results in a larger mode area for the TM_{00} mode than for the TE_{00} mode. Therefore the TM_{00} mode has stronger interaction with the waveguide sidewall, and consequently, higher losses.

In addition to frequency-comb-assisted diode laser spectroscopy, sideband modulation technique [312] is also used to measure the resonance linewidth $\kappa/2\pi$ and to fit the intrinsic loss $\kappa_0/2\pi$. Two sidebands, each separated from the carrier by 150 MHz, are used to calibrate the resonance linewidth. Figure 4.10(e, f) compare the measured $\kappa/2\pi$ and fitted $\kappa_0/2\pi$ of the same resonance, using the frequency-comb-assisted diode laser spectroscopy ($\kappa/2\pi \sim 7.75$

MHz and $\kappa_0/2\pi \sim 5.87$ MHz) and the sideband modulation technique ($\kappa/2\pi \sim 7.95$ MHz and $\kappa_0/2\pi \sim 6.05$ MHz). Both methods agree well with each other, and show $Q_0 > 32 \times 10^6$.

4.2.1 Ringdown measurement

Furthermore, a cavity ring-down measurement to validate the measured linewidth is also performed, using an experimental setup shown in Fig. 4.11(a). An intensity modulator (IM) is used to rapidly switch on and off the pump field. The ring-down signal of the transmitted light is recorded by a 1-GHz-bandwidth low-noise photodetector. A 50-kHz square wave electrical

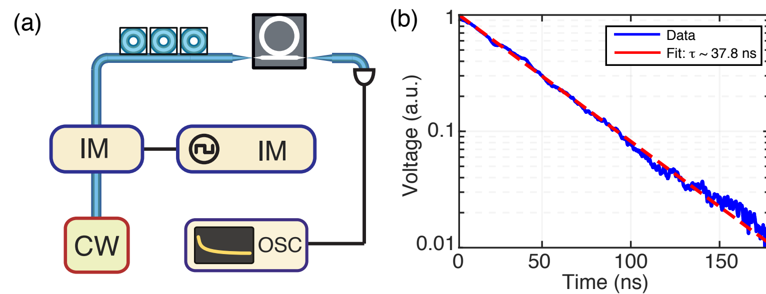

Figure 4.11 – Resonance linewidth measurement using cavity ring-down technique. (a) The experimental setup utilizing an intensity modulator (IM) to switch on and off the pump field. (b) Recorded cavity ring-down shown in log scale. The ringdown was averaged 1000 times. The exponential fit give $\tau = 37.8$ ns, corresponding to a loaded linewidth of 8.4 MHz. a.u.: arbitrary unit.

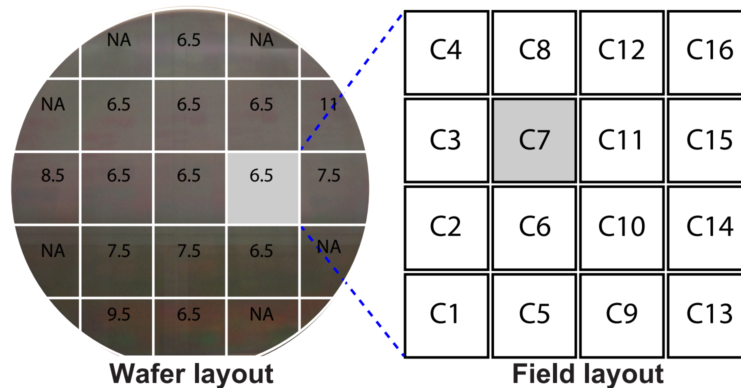

Figure 4.12 – Systematic study of $\kappa_0/2\pi$ histograms using multiple samples over the entire 4-inch wafer. DUV stepper lithography exposure layout, and the measured TE_{00}'s $\kappa_0/2\pi$ value of 40-GHz-FSR chips at different wafer positions. The reticle design containing sixteen chips of 5×5 mm^2 size, is uniformly exposed in each field over a 4-inch wafer. For the particular chip C7 containing multiple 40-GHz-FSR microresonators, the most probable value $\kappa_0/2\pi$ is extracted from the $\kappa_0/2\pi$ histogram and listed in each exposure field. NA: not applicable, due to visible photoresist coating defects or the design missing in particular fields close to the wafer edge.

drive signal is generated using a fast arbitrary waveform generator, ensuring that the light is switched off significantly faster than the resonance linewidth. The upper and lower voltage levels of the square wave are adjusted to match the maximum and minimum transmission voltage of the IM, such that the electrical overshoot and undershoot of the square wave signal do not twist the ring-down slope. A representative ring-down measurement data is shown in Fig. 4.11(b). Due to the finite extinction ratio of the IM, the residual pump field beats with the leakage of the intracavity field, producing a field ring-down signal which is affected by the detuning of the laser from the cavity mode resonances [317]. At small detunings ($\Delta << \kappa$), the effective ring-down rate is increased by the laser's detuning from cavity resonance, and thus the directly inferred quality factor is less accurate than the sideband fitting result. As most high Q resonances suffer from a certain amount of mode splitting, an effective detuning presents from the split resonances, and the ring-down results can therefore only serve as a lower bound of the loaded Q factor of the measured resonances. However, when the detuning is taken into account in the analysis, the corrected loaded linewidth $\kappa/2\pi \sim 8.4$ MHz is in agreement with the sideband fitting results, showing consistency between the three characterization methods used here.

4.2.2 Wafer-scale distribution of Q

Next, in order to prove that the current fabrication process is high-yield and reproducible, the most probable values of $\kappa_0/2\pi$ histograms of the 40-GHz-FSR microresonator samples at different positions on the same 4-inch wafer are studied. Figure 4.12 shows the DUV stepper lithography exposure layout on the wafer, as well as the reticle layout. There are 4×4 chip designs on the reticle. Each chip is in 5×5 mm^2 size, and contains multiple 40-GHz-FSR

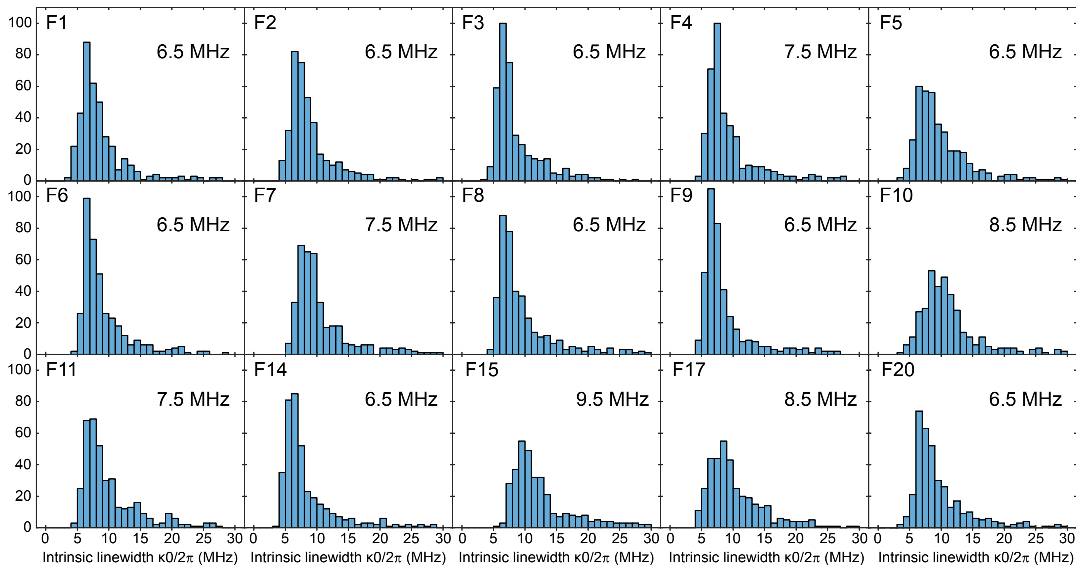

Figure 4.13 – The $\kappa_0/2\pi$ histograms of multiple 40-GHz-FSR chips.

microresonators. The DUV stepper exposes the reticle pattern (with ×5 demagnification) uniformly over the full 4-inch wafer scale in discreet fields. The chip design containing 40-GHz-FSR microresonators is C7. The most probable value of $\kappa_0/2\pi$ histograms of this C7 chip is measured and plotted in each exposure field. The individual value of the $\kappa_0/2\pi$ histograms of the C7 chip in each stepper exposure field is shown in Fig.4.13. Despite the fields at the wafer edge, which can have compromised quality due to laser focusing and photoresist coating, the most probable $\kappa_0/2\pi$ of C7 remains constant (6.5 MHz) in all fields.

In addition to the wafer-scale Q study of 40-GHz-FSR chips, below it shows that a high Q is also obtained reproducibly over the full 4-inch wafer scale with 10-GHz-FSR chips. Figure 4.14(c) shows our mask layout constituting 4×4 chip designs on the DUV stepper reticle. Each chip contains only one 10-GHz-FSR microresonator Figure 4.14(a) shows that the DUV stepper exposes uniformly the reticle pattern over the full 4-inch wafer scale in discreet fields. The calibration chip studied here is the C15 chip. The most probable value of $\kappa_0/2\pi$ histograms of this C15 chip is measured and plotted in each exposure field, as shown in Fig. 4.14(b). In most fields, $\kappa_0/2\pi < 9.5$ MHz is found. These high-Q, 10-GHz-FSR chips have been recently used to demonstrate soliton-based X-band microwave generation [78].

The wafer-scale Q study here demonstrates that our current fabrication can achieve high reproducibility and yield, i.e. all chips are crack-free and feature equally good Q factor. Further, taking advantages of the current semiconductor technology, the process can be easily applied on 8- and 12-inch wafers, thus can enable large-scale manufacture and production with low cost in the future.

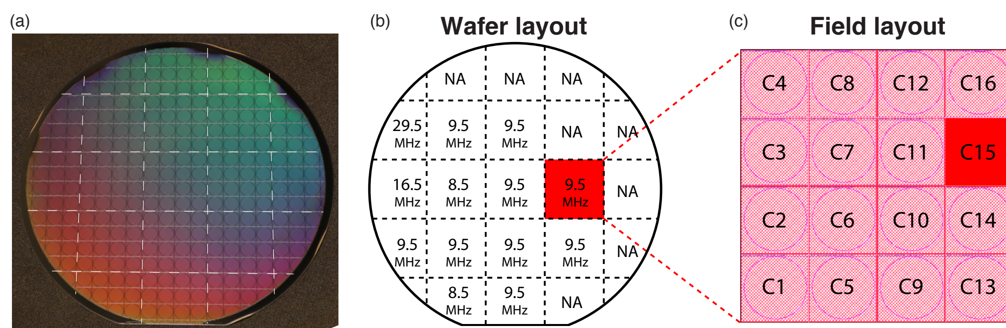

Figure 4.14 – Q distribution on a 4-inch wafer of 10-GHz-FSR chips. (a) Photo of the 4-inch wafer containing only chips of 10 GHz FSR. (b) DUV stepper lithography exposure layout, and the most probable value $\kappa_0/2\pi$ of the C15 chips at different exposure field and wafer positions. (c) The reticle design contains sixteen chips and is uniformly exposed in discrete field over a 4-inch wafer. NA: not applicable, due to visible photoresist coating defects or the design missing in particular fields close to the wafer edge.

4.2.3 Reflow's impact

The SiO_2 preform reflow is a unique step in the Damascene process, due to the fact that the thermal wet SiO_2 has a glass transition temperature below 1250 $^\circ C$, which can be achieved in our atmosphere-pressure chemical vapor deposition (APCVD) tube. Our previous work [90] shows that, in the case of lower microresonator Q (below 4×10^6), the preform reflow can lead to a Q improvement by a factor of 2, accompanied however by a waveguide cross-section deformation. Now using the new Damascene process and with the high-Q Si_3N_4 microresonator samples, it is needed to investigate and quantify the impact of the preform reflow on microresonator Q factor.

Figure 4.15(a, b) compare the histogram of $\kappa_0/2\pi$ in the TE_{00} mode, in samples of 1500 nm waveguide width and 850 nm height, with and without the preform reflow. Without reflow, the most probable value of $\kappa_0/2\pi \sim 15.5$ MHz is only marginally larger than the value $\kappa_0/2\pi \sim 14.5$ MHz with reflow. This comparison indicates that the efficacy of reflow is reduced in the current Damascene process, as the use of DUV stepper lithography and optimized dry etching result in less sidewall roughness and scattering losses, compared with the previously reported Damascene process [90]. Therefore, as the sidewall quality before reflow is already good, in the current Damascene process for high-Q Si_3N_4 microresonators, the preform reflow is not indispensable for higher Q. Indeed, subtractive processes using optimized lithography and dry etching have also achieved high microresonator $Q > 10 \times 10^6$ recently [98, 100, 318], where SiO_2 or Si_3N_4 reflow is absent.

Despite the fact that the reflow can impact Q and losses, it also deforms the waveguide cross-section. Previous report [90] shows a change in waveguide sidewall angle from 90° to 98°, after 24 hours reflow at 1250°. This waveguide deformation can cause difficulty in critical dimension control, thus is typically undesired. In the current Damascene process, by reducing the reflow time to only 3 hours, the sidewall slant effect can be significantly reduced. Figure 4.15(c, d) compare the waveguide cross-sections with and without reflow. While the sidewall angle is ~ 90° without reflow, it becomes 93° (3° difference) after 3 hours reflow. Therefore, in the current Damascene process, the impact on waveguide deformation caused by the reflow is significantly reduced.

4.3 Probing the ultimate microresonator Q limited by absorption loss

The optical losses in the telecommunication band in Si_3N_4 waveguides have two main contributions: the Rayleigh scattering loss [213, 214] caused mainly by the waveguide sidewall roughness, and the hydrogen absorption loss due to the residual nitrogen-hydrogen (N-H) and silicon-hydrogen (Si-H) bonds [217, 201]. While the hydrogen absorption loss can be efficiently eliminated via thermal annealing of Si_3N_4 at high temperature ~ 1200°C [218], efforts on loss reduction have mainly focused on reducing waveguide roughness via optimized dry

etching [223, 100], wet etching [225], and etchless process [227, 319]. In addition, small-core waveguides [201, 199] featuring large mode areas and reduced optical mode interaction with waveguide sidewalls have also been developed.

This section presents a quantitative study to analyze how much the absorption loss contributes in the total intrinsic loss of $\kappa_0/2\pi = 6.5$ MHz, and to provide an estimation of the optical loss limit of our Si_3N_4 waveguides. For this purpose, a modulation response measurement [79, 311] is used. The experimental setup is shown in Fig. 4.16(a). Two lasers, pump and probe, are used in the experiment. The pump laser is tuned to the m-th optical resonance whose resonance frequency is f_m and the thermal absorption loss κ_{abs} at this frequency is to be characterized. Meanwhile, the pump laser is intensity-modulated at frequency ω. The probe field is weakly locked (i.e. low-bandwidth locking) to the m'-th optical resonance whose resonance frequency is f'_m. The principle of linear microresonator response measurement is to characterize the resonance frequency shift $\delta f_{m'} = \chi(\omega)\delta n_{\text{ph}}$ of the probe mode $f_{m'}$ induced by the intensity modulation of the pump mode f_m. The intensity modulation of the pump laser causes intracavity power modulation (i.e. photon number modulation n_{ph}), which modulates the resonance frequency shift of the probe mode $f_{m'}$. The pump power is maintained sufficiently low, such that the steady-state frequency shift of the probe mode is small compared to the optical linewidth κ of the m'-th resonance, i.e. $\delta f_{m'} \ll \kappa$. In the linear regime, the frequency

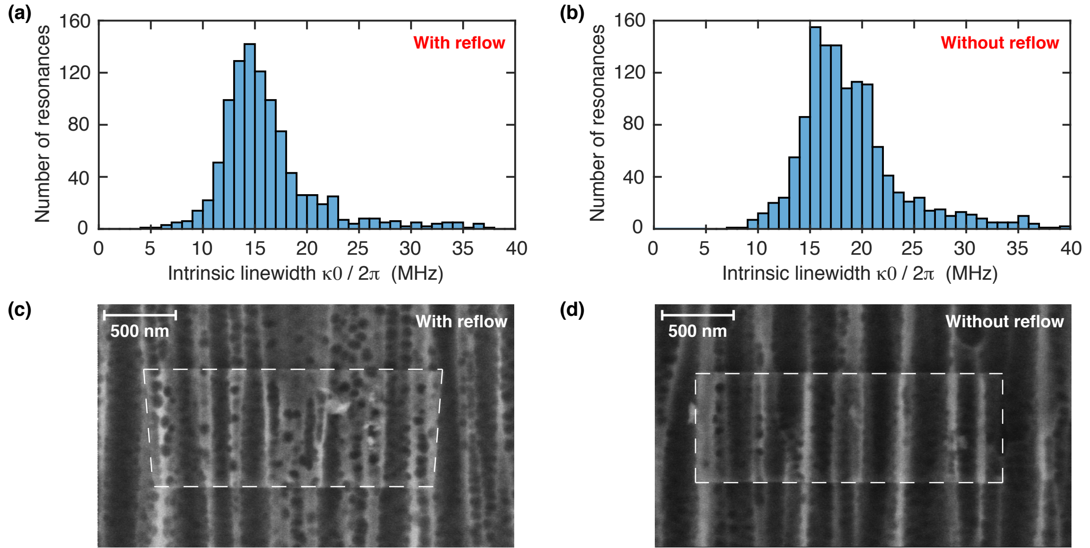

Figure 4.15 – Comparison of $\kappa_0/2\pi$ histograms and waveguide cross-section deformation in the cases with and without reflow. (a, b) The histograms of $\kappa_0/2\pi$ with and without the preform reflow. Without reflow, the most probable value of $\kappa_0/2\pi \sim 15.5$ MHz (b) is only marginally larger than the value $\kappa_0/2\pi \sim 14.5$ MHz with reflow (a). $\kappa_0/2\pi \sim 15.5$ MHz corresponds to $Q_0 \sim 13 \times 10^6$. (c, d) SEM images showing waveguide cross-sections with 90° sidewall bottom angle before reflow (c), and 93.5° angle after 3 hours (d).

response df_m to the modulated pump power dN_{ph} at modulation frequency ω is given by

$$\chi(\omega) = \frac{df_m}{dN_{\mathrm{ph}}} = \chi_{\mathrm{therm}}(\omega) + \chi_{\mathrm{Kerr}}(\omega) \tag{4.3}$$

The total response $\chi(\omega)$ consists of two parts: the Kerr response $\chi_{\mathrm{Kerr}}(\omega)$ with infinite bandwidth, and the thermal response $\chi_{\mathrm{therm}}(\omega)$ which has bandwidth up to few kilohertz. Therefore, by calibrating the response dependence on the modulation frequency ω, $\chi_{\mathrm{therm}}(\omega)$ and $\chi_{\mathrm{Kerr}}(\omega)$ can be individually identified. In the DC modulation regime ($\omega \to 0$), the Kerr response term

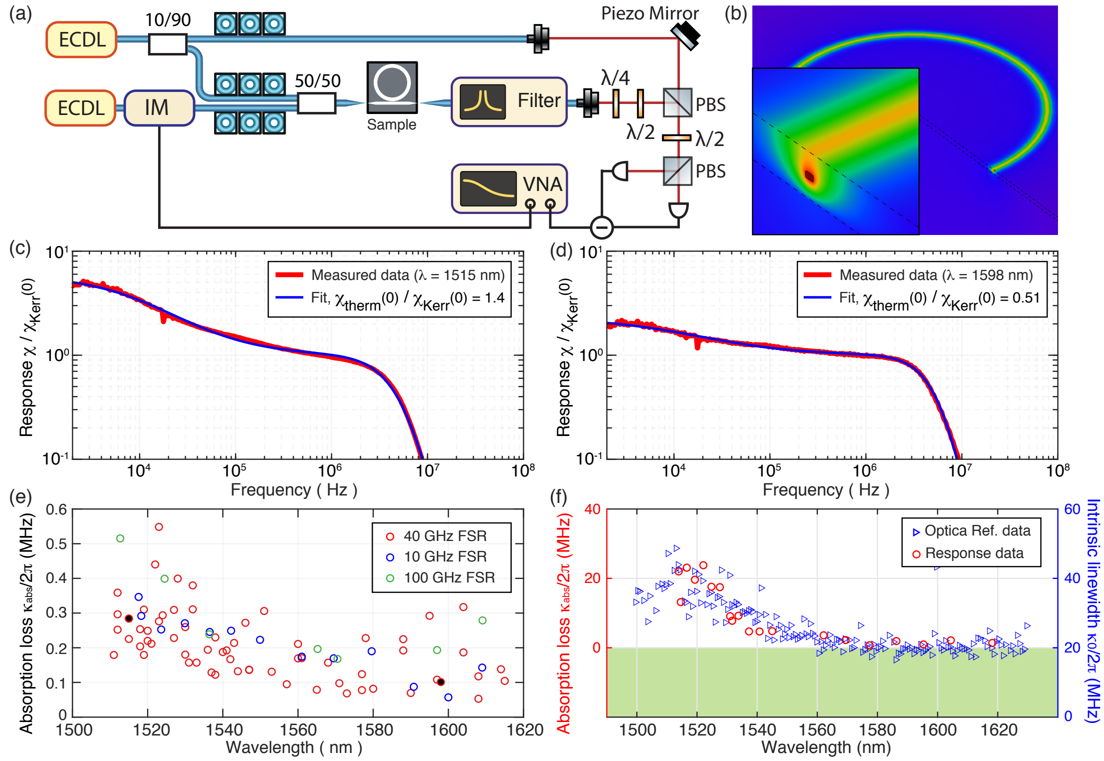

Figure 4.16 – Linear microresonator response measurement. (a) Experiment setup. ECDL: external-cavity diode lasers. IM: intensity modulator. VNA: vector network analyzer. PBS: polarization beam splitter. (b) Thermal simulation of the temperature distribution in the waveguide structures (c, d) Measured frequency response $\chi(\omega)$ normalized to χ_{Kerr}, of two representative resonances at 1515 nm and 1598 nm. The fitted thermal cutoff frequency $\omega_{\mathrm{therm}}/2\pi$ and cavity cutoff frequency $\kappa/4\pi$ are, $\omega_{\mathrm{therm}}/2\pi = 14.2$ kHz and $\kappa/4\pi = 6.2$ MHz in (c), and $\omega_{\mathrm{therm}}/2\pi = 14.9$ kHz and $\kappa/4\pi = 6.5$ MHz in (d). (e) Calculated absorption loss κ^m_{abs} of different resonances from different samples. The black solid circles correspond to the data shown in (c, d). (f) Comparison of loss characterization results using both the linear microresonator response measurement and the frequency-comb-assisted diode laser spectroscopy, on a partially annealed sample. This particular samples features prominent hydrogen absorption losses. The green-shaded zoom marks a wavelength-independent scattering loss of 20 MHz. The results from both methods are consistent.

$\chi_{\text{Kerr}}(0)$ is calculated[79] as

$$\begin{aligned}\chi_{\text{Kerr}}(0) &= \frac{df_{m,\text{Kerr}}}{dN_{\text{ph}}} \\ &= \eta\kappa h f_m \frac{df_m}{dP_{\text{in}}} \\ &= \eta\kappa h f_m \cdot 2 \cdot \frac{4\eta Q c n_2}{n_g^2 V_{\text{eff}}} \\ &= 8\eta^2 \frac{c n_2 h f_m^2}{n_g^2 V_{\text{eff}}} \\ &= 2\frac{c n_2 h f_m^2}{n_g^2 V_{\text{eff}}}\end{aligned} \tag{4.4}$$

where h is the Planck constant, $\kappa/2\pi$ is the loaded resonance linewidth, $Q = 2\pi f_m/\kappa$ is the loaded resonance Q, $n_g = 2.1$ is the group index, $\eta = \kappa_{ex}/\kappa$ is the normalized coupling strength and $\eta = 1/2$ for the case of critical coupling. The factor of 2 comes from the cross-phase-modulation, as the pump and probe modes are two distinct resonances in our experiment (i.e. $m \neq m'$ and $f_m \neq f_{m'}$).

The Thermal response term $\chi_{\text{th}}(0)$ is calculated as

$$\begin{aligned}\chi_{\text{therm}}(0) &= \frac{df_{m,\text{therm}}}{dN_{\text{ph}}} \\ &= \frac{f_m}{n_{\text{mat}}} \cdot \frac{dn_{\text{mat}}}{dN_{\text{ph}}} \\ &= \frac{f_m}{n_{\text{mat}}} \cdot \frac{dT}{dN_{\text{ph}}} \cdot \frac{dn_{\text{mat}}}{dT} \\ &= \frac{\kappa_{\text{abs}} h f_m^2}{n_{\text{mat}}} \frac{dT}{dP_{\text{abs}}} \frac{dn_{\text{mat}}}{dT}\end{aligned} \tag{4.5}$$

where we use $df_m/f_m = dn_{\text{mat}}/n_{\text{mat}}$ and $dP_{\text{abs}} = \kappa_{\text{abs}} h f_m dN_{\text{ph}}$. The material refractive index of Si_3N_4 at 1550 nm is $n_{\text{mat}} = 2.0$, and its temperature dependence [320] is $dn_{\text{mat}}/dT = 2.5 \times 10^{-5}/\text{K}$.

Using the values of $\chi_{\text{therm}}(\omega)$ and $\chi_{\text{Kerr}}(\omega)$ at DC ($\omega = 0$), the absorption rate is calculated as

$$\kappa_{\text{abs}} = \frac{2c n_{\text{mat}} n_2}{n_g^2 V_{\text{eff}} \frac{dT}{dP_{\text{abs}}} \frac{dn_{\text{mat}}}{dT}} \frac{\chi_{\text{therm}}(0)}{\chi_{\text{Kerr}}(0)} \tag{4.6}$$

where V_{eff} is the effective optical mode volume, $n_2 = 2.4 \times 10^{-19}\text{m}^2/\text{W}$ is the nonlinear index of Si_3N_4, $n_g = 2.1$ is the group index, $n_{\text{mat}} = 2.0$ is the material index and $dn_{\text{mat}}/dT = 2.5 \times 10^{-5}/\text{K}$ is the thermo-optic coefficient [320], and P_{abs} is the absorbed power.

The frequency response $\delta f_{m'}$ to the pump modulation is transduced into the probe laser's phase modulation. The phase response is measured using a balanced homodyne detection,

with the pump laser being filtered out before detection. In order to extract the actual microresonator response $\chi(\omega)$ from the experimentally photodetected $\chi'(\omega)$, the frequency response $\chi_{\mathrm{det}}(\omega)$ of the entire experiment setup and detection chain needs to be calibrated first. This is realized by direct detection of the pump power modulation $\delta P(\omega) \propto \chi_{\mathrm{det}}(\omega)$ in the absence of the probe laser and the pump filter. The measured response $\chi'(\omega)$ is normalized to the setup response $\chi_{\mathrm{det}}(\omega)$, and thus the actual microresonator response $\chi(\omega) = \chi'(\omega)/\chi_{\mathrm{det}}(\omega)$ is retrieved, with an uncertain constant factor. This constant factor is removed when retrieving $\chi_{\mathrm{therm}}(0)/\chi_{\mathrm{Kerr}}(0)$ from the two pole fitting of $\chi(\omega)$ using a fitting function

$$\chi(\omega) = \frac{\chi_{\mathrm{Kerr}}(0)}{\sqrt{1+(2\omega/\kappa)^2}} \cdot \left(1 + \frac{\chi_{\mathrm{therm}}(0)}{\chi_{\mathrm{Kerr}}(0)} \frac{1}{1+i(\omega/\omega_{\mathrm{therm}})^{\gamma}}\right) \tag{4.7}$$

with $\omega_{\mathrm{therm}}/2\pi$ and $\kappa/4\pi$ being the thermal and cavity cutoff frequencies, γ being the parameter accounting for the material inhomogeneity (that is, the Si_3N_4 waveguide has a finite dimension and is surrounded by SiO_2 cladding).

To evaluate the absorption rate κ_{abs}, the factor $\chi_{\mathrm{therm}}(0)/\chi_{\mathrm{Kerr}}(0)$ is retrieved by a two-pole fitting of the measured response $\chi(\omega)$, which presents a thermal cut-off frequency ω_{therm} and a cavity cut-off frequency $\kappa/2$. The fitting exploits the fact that the thermal response $\chi_{\mathrm{therm}}(\omega)$ dominates at frequency below 10 kHz and has a cutoff frequency $\omega_{\mathrm{therm}}/2\pi < 20$ kHz. At higher frequency, the Kerr response $\chi_{\mathrm{Kerr}}(\omega)$ dominates. Figure 4.16(c, d) present two examples of measured and fitted $\chi(\omega)$. Note that, only the normalized response $\chi(\omega)/\chi_{\mathrm{Kerr}}(0)$ is shown, with the uncertain constant factor removed.

To calculate the coefficients V_{eff} and dT/dP_{abs}, COMSOL simulations of optical mode profiles and bulk absorption heating are used, based on the actual geometry of the Si_3N_4 samples used. COMSOL Multiphysics is used to simulate the thermal response due to bulk absorption heating of our Si_3N_4 samples. The main material property coefficients of interest used in the current simulation are identical to the ones used in Ref.[173] for simulating the Si_3N_4 thermal refractive noise. First, the waveguide optical mode profile (TE_{00} mode) is simulated, from which the effective mode volume V_{eff} is calculated. Bulk absorption heating is introduced which power distribution is proportional to the intensity distribution of the optical mode f_m. From the stationary study of the sample heating, the dependence of temperature change on absorbed power, dT/dP_{abs}, is retrieved from an absorption power sweep. Figure 4.16(b) shows the temperature profile from the thermal simulation. The combined value of $V_{\mathrm{eff}} \cdot dT/dP_{\mathrm{abs}}$ is calculated as 2.09×10^{-12}K$\cdot$ m^3/W in the case of full SiO_2 cladding for samples used in Fig. 4.16(c, d, e), and is 3.84×10^{-12}K$\cdot$ m^3/W in the case of missing top SiO_2 cladding for samples used in Fig. 4.16(f).

Figure 4.16(e) shows the calculated absorption rates κ_{abs} of different resonances from four 40-GHz-FSR Si_3N_4 samples featuring $Q_0 > 30 \times 10^6$, in comparison with 10- and 100-GHz-FSR samples fabricated using the same Damascene process but from different wafers. All samples show similar trends, and present two conclusions. First, the average κ_{abs} of our ultralow-loss Si_3N_4 samples is $\kappa_{\mathrm{abs}}/2\pi \approx 0.2$ MHz. Therefore, the optical loss of our Si_3N_4 samples is

currently dominated by the non-absorptive, scattering loss. Second, $\kappa_{\text{abs}}/2\pi$ is higher (≈ 0.4 MHz) around 1520 nm wavelength, compared to the value at e.g. 1600 nm (< 0.2 MHz). Such absorption loss is caused by the residual N-H and Si-H bonds in our thermally annealed Si_3N_4. Note that, only standard LPCVD Si_3N_4 / SiO_2 films and thermal annealing are used in our fabrication to achieve such low absorption losses.

To validate these findings, the linear microresonator response measurement is further benchmarked by characterizing a partially annealed Si_3N_4 sample whose resonance linewidth data has been published in Ref. [91]. This particular sample is re-characterized, using both the linear microresonator response measurement and the frequency-comb-assisted diode laser spectroscopy, and compare the results using both methods in Fig. 4.16(f). Assuming a universal wavelength-independent scattering loss of 20 MHz, the measured hydrogen absorption loss using the response measurement agrees with the total loss measured using the frequency-comb-assisted diode laser spectroscopy.

Here, it is revealed that our waveguide loss is dominated by scattering losses. The potential microresonator Q is calculated to exceed 10^9, in the ideal cases limited only by thermal absorption losses. Thus, the optical losses could be further reduced by further reducing the scattering losses, e.g. via optimizing lithography and etching. The optimized photonic Damascene process has shown its unique advantages in terms of the PIC performance and fabrication maturity. Transferring this fabrication technology to 8- or 12-inch wafer process, our Damascene process could be readily adopted at CMOS foundry levels.

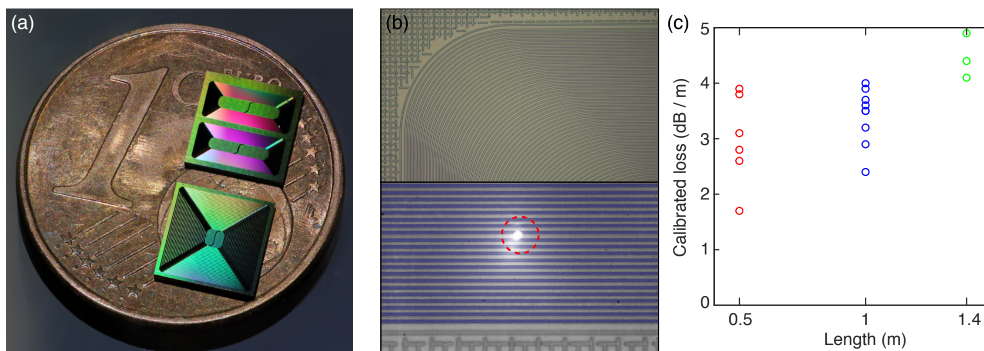

Figure 4.17 – Ultralow-loss, metre-long Si_3N_4 spiral waveguides. (a) Photograph showing Si_3N_4 chips containing two 1.0-metre-long and one 1.4-metre-long spiral waveguides. (b) Optical microscope image of the densely packed Si_3N_4 waveguides in Archimedean spirals, with yellow light camera (top) and IR camera (bottom). When 1550 nm laser light is coupled into the waveguide, light-scattering defects are observed under the IR camera (highlighted with a red circle). (c) Measured and calibrated light propagation losses in 0.5 m, 1.0 m and 1.4 m long spiral waveguides.

4.4 Metre-long spiral waveguides

In addition to the characterization of the optical losses in microresonators, here the study of the optical loss in metre-long spiral waveguides is presented. These long spiral waveguides are a key element to build photonic true-time delay lines, which find applications in feed-forward buffers in optical packet routers [321], beamforming [322] and integrated optical gyroscopes [323]. Unlike other methods to realize optical delay using resonant structures or nonlinear effects, delay lines based on physically extended spiral waveguides have infinite bandwidth and lower insertion loss. Silica wedge waveguides [209] and small-core (weak optical confinement) Si_3N_4 waveguides [201] have been studied to build delay lines with loss values below 0.1 dB/m. However, for integrated Si_3N_4 platform, similar loss performance has not yet been achieved in metre-long waveguides of tight optical confinement. Our Si_3N_4 waveguides combine ultralow loss and tight optical confinement, and offer negligible bending losses, smaller footprint, and enhanced optical nonlinearity. Therefore, these waveguides can find key applications in nonlinear photonics [187] and optical coherence tomography (OCT) [324].

Figure 4.17(a) shows a photograph of photonic chips containing Si_3N_4 waveguides longer than 1 m. Figure 4.17(b) top shows the spiral layout under microscope. The waveguides are densely packed in Archimedean spirals. Three lengths are studied here: a 0.5-metre-long spiral contains 50 coils and covers 3.1 mm^2 area; a 1.0-metre-long spiral contains 106 coils and covers 6.6 mm^2 area; a 1.4-metre-long spiral contains 130 coils and covers 20.2 mm^2 area. Light scattering defects are found with an infrared (IR) camera, as shown in Fig. 4.17(b). By counting the number of defects in high-loss spirals, each defect is estimated to cause 1-2 dB extra loss. Figure 4.17(c) shows the measured losses in multiples samples. The propagation loss is calibrated using the adjacent 5-millimetre-long waveguide, which has a fiber-chip-fiber through coupling efficiency of 33% (4.8 dB for two chip facets). The lowest loss values found are 1.7 dB/m for 0.5 m length, 2.4 dB/m for 1.0 m length, and 4.1 dB/m for 1.4 m length. These loss values are significantly higher that the value extrapolated from microresonator Q characterization (1 dB/m). In addition, an overall trend showing higher losses in longer waveguides is observed. Both observations are attributed to the extra light-scattering defects as shown in the bottom panel of Fig. 4.17(b). The probability of defects depends on the waveguide area. These defects are likely caused by particle contamination on the wafer, as we have verified that these defects are not on the DUV reticle which otherwise would generate the same defects in the same position in each exposure field.

5 Soliton Generation with Ultralow Power Threshold

In this section, I will present the soliton generation experiment and results using the high-Q Si_3N_4 devices. The generated solitons feature repetition rates from 1 THz down to 40 GHz. Most the soliton generation results were achieved without using an EDFA. The main result of this chapter has been published in ref. [91], J. Liu et al, "**Ultralow-power chip-based soliton frequency combs for photonic integration**", *Optica* **5**, 884 (2018). I designed and fabricated the Si_3N_4 samples, and led the experimental characterization of samples and soliton generation. Arslan S. Raja has contributed significantly to the experimental characterization of samples and data collection for soliton generation.

5.1 Ultralow-power single soliton

Although the soliton microcomb has been directly generated with a diode laser in a silica microresonator coupled to a tapered optical fibre recently [325], this has not been possible for integrated devices including Si_3N_4. Yet, there are remaining challenges in soliton formation in Si_3N_4 microresonators, related to: (i) The comparatively low quality (Q) factor which increases the threshold power of soliton formation, compared to e.g. crystalline and silica microresonators. (ii) Optical coupling losses from the laser to the chip device, resulting from the optical mode mismatch at chip facets. (iii) Stable access to soliton states may require the use of complex excitation techniques such as "power kicking" [64], single-sideband modulators [59] or multiple lasers [62]. The first two challenges are particularly problematic for future photonic integration, as they necessitate the use of high-power lasers. So far, for integrated Si_3N_4 microresonator devices, soliton formation with device input power of several hundreds of milliwatts has only been achieved in microresonators of 1 THz free spectral range (FSR) [89, 99, 138, 60]. Yet in these experiments input coupling loss still necessitated the use of additional amplifiers to reach the required power levels of several tens of milliwatts on the chip. Meanwhile, low microcomb initiation power at milliwatt or even sub-milliwatt level has been demonstrated in Si_3N_4 microresonators of Q exceeding 10^7 [98, 100], but solitons have not been observed due to the insufficient anomalous GVD. Consequently, soliton formation has been limited to wavelength regions where optical amplifiers are available. It is only very

recently that soliton generation in high-Q Si_3N_4 microresonators of anomalous GVD pumped by an integrated laser was reported in Ref. [101]. However in that case, the repetition rate is 200 GHz, which is not electronically detectable, resulting in limited application potentials.

In this section, I will show that the photonic Damascene reflow process illustrated in the previous chapter can overcome the outlined challenges and significantly reduce the required input power for soliton formation in Si_3N_4 microresonators. Single soliton formation in Si_3N_4 microresonators of $Q_0 > 8.2 \times 10^6$ at 88 GHz is demonstrated, which is electronically detectable, with 48.6 mW power at the chip input facet (30.3 mW in the bus waveguide). In addition, by further improving the microresonator Q factors to $Q_0 > 15 \times 10^6$, single soliton formation of 99 GHz repetition rate with a record-low input power of 9.8 mW (6.2 mW in the waveguide) is demonstrated. Using only a tunable diode laser without an optical amplifier, the single soliton states are accessed in eleven consecutive resonances in the telecom L-band and five in the telecom C-band, via simple laser piezo tuning. Such low-power soliton microcombs of sub-100-GHz repetition rate can significantly simplify the recently demonstrated dual-comb ultrafast distance measurements [129] and optical coherent communication [128], which required EDFA to amplify the input power to above 1 Watt. In addition, the soliton microcombs demonstrated here have shown great potential for future photonic integrated microwave generators, and chip-based frequency synthesizers [138] via integration of on-chip lasers, semiconductor optical amplifiers and nonlinear microresonators. Soliton microcombs formed in wavelength regions where amplifiers are not available could unlock new applications such as optical coherent tomography (OCT) at 1.3 μm [326] and sensing of toxic gases and greenhouse gases e.g. methane at 1.6 μm [327].

5.1.1 Solitons of repetition rates below 100 GHz

In the first part, the single soliton formation in 88-GHz-FSR microresonators, with the fundamental TE mode (TE_{00}), is presented. Figure 5.1(a) shows the microscope image of the 88-GHz-FSR microresonators. The microresonator samples described in this section have no SiO_2 top cladding, as shown in Fig. 5.1(a) inset. Meander bus waveguides are used to densely pack a large number of devices on one chip. The Si_3N_4 microresonator has a cross-section, width×height, of 1.58×0.75 μm^2, and is coupled to a multi-mode bus waveguide of the same cross-section for high coupling ideality [290]. The polarization of the incident light to the chip is controlled by fibre polarization controllers, and the polarization state is measured using linear polarizers. The microresonator transmission trace is obtained from 1500 to 1630 nm using frequency-comb-assisted diode laser spectroscopy [298, 119]. The precise frequency of each data point is calibrated using a commercial femtosecond optical frequency comb with 250 MHz repetition rate. For the TE_{00} mode family, the FSR of the microresonator and the anomalous GVD are extracted from the calibrated transmission trace by identifying the precise frequency of each resonance. The total (loaded) linewidth $\kappa/2\pi = (\kappa_0 + \kappa_{ex})/2\pi$, the intrinsic linewidth (intrinsic loss) $\kappa_0/2\pi$ and the coupling strength $\kappa_{ex}/2\pi$ are extracted from each resonance fit [214, 316].

The measured linewidths of each TE_{00} resonance are shown in Fig. 5.1(d). These resonances are all undercoupled. Larger linewidths are found in the wavelength region from 1500 to 1550 nm, due the absorption by the nitrogen-hydrogen (N-H) and silicon-hydrogen (Si-H) bonds in LPCVD Si_3N_4 material [217, 201]. These bonds are introduced during standard LPCVD Si_3N_4 process based on SiH_2Cl_2 and NH_3 precursors [216], and can be partially removed by thermal annealing. Figure 5.1(b) shows the resonance at $\lambda = 1558.0$ nm. The resonance fit shows a loaded linewidth of $\kappa/2\pi = 30.3$ MHz, and the estimated intrinsic loss based on the resonance fit is $\kappa_0/2\pi \sim 23.3$ MHz, corresponding to the intrinsic $Q_0 > 8.2 \times 10^6$. Figure 5.1(c) shows the resonance at $\lambda = 1620.0$ nm, with a loaded linewidth of $\kappa/2\pi = 28.7$ MHz, and the estimated intrinsic loss is $\kappa_0/2\pi \sim 17.3$ MHz, corresponding to the intrinsic $Q_0 > 10.7 \times 10^6$. Figure 5.1(e) shows the measured microresonator integrated GVD, defined as $D_{\text{int}}(\mu) = \omega_\mu - \omega_0 - D_1\mu = D_2\mu^2/2 + D_3\mu^3/6 + ...$ Here $\omega_\mu/2\pi$ is the frequency of the μ-th resonance relative to the reference resonance $\omega_0/2\pi = 192.6$ THz ($\lambda_0 = 1558.0$ nm, as shown in Fig.5.1(b)). The fit values obtained from the dispersion measurement are $D_1/2\pi \sim 88.63$ GHz, $D_2/2\pi \sim 1.10$ MHz and $D_3/2\pi \sim \mathcal{O}(1)$ kHz.

When the pump laser scans over the resonance from the blue-detuned side to the red-detuned side, a step in the transmission trace can be observed, indicating to the soliton formation

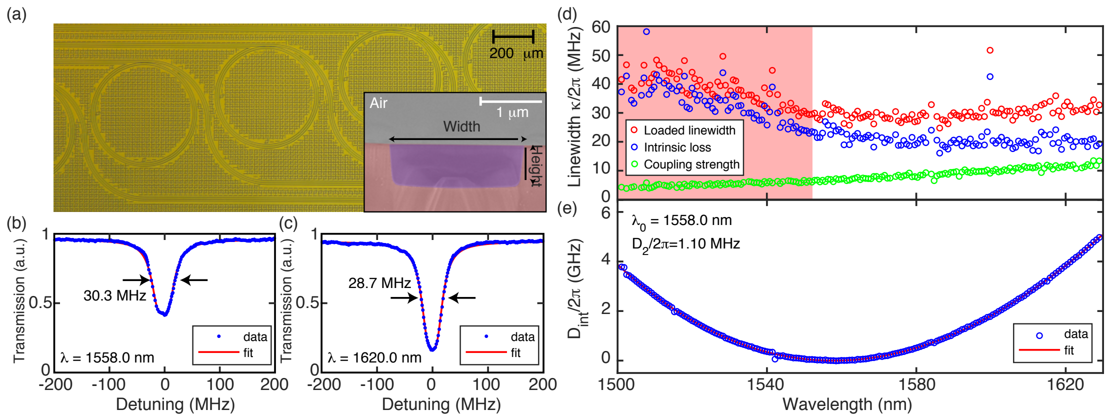

Figure 5.1 – Dispersion and resonance linewidth characterization of an 88-GHz-FSR microresonator. (a) Microscope image of densely packed 88-GHz-FSR microresonators, using meander bus waveguides. These samples have no SiO_2 top cladding. Inset: SEM image of the cross-section of a Si_3N_4 waveguide without SiO_2 top cladding. The Si_3N_4 waveguide is blue shaded, the SiO_2 bottom cladding is red shaded, the air is not color shaded. (b) The pump resonance at $\lambda = 1558.0$ nm and its fit, with the loaded linewidth of $\kappa/2\pi = 30.3$ MHz and fitted intrinsic loss of $\kappa_0/2\pi \sim 23.2$ MHz, corresponding to $Q_0 > 8.2 \times 10^6$. (c) The resonance at $\lambda = 1620.0$ nm and its fit, with the loaded linewidth of $\kappa/2\pi = 28.7$ MHz and fitted intrinsic loss of $\kappa_0/2\pi \sim 17.3$ MHz, corresponding to $Q_0 > 10.7 \times 10^6$. (d) Loaded linewidth, intrinsic loss and coupling strength of each TE_{00} resonance. Larger intrinsic losses are found in the wavelength region from 1500 to 1550 nm (red shaded area), due to the absorption by the N-H and Si-H bonds in LPCVD Si_3N_4. (e) Measured GVD of the TE_{00} mode family. Several avoided mode crossings are observed, where resonance linewidth increases.

[44]. Fibre-chip-fibre transmission of 40% (coupling efficiency of 63% per device facet) is achieved via double-inverse nanotapers on the chip facets [239]. The input power (P_{in}) is defined as the power measured before the input lensed fibre which couples light into the chip device. Thus the optical power in the bus waveguide (P_{b}) on the chip, which directly pumps the microresonator, is calculated as $P_{\text{b}} = 0.63 P_{\text{in}}$.

In our setup, the output power of the diode laser can go as high as 23 mW, with few milliwatt power variation depending on the wavelength. An EDFA is used to slightly amplify the optical power to $P_{\text{in}} = 48.6$ mW ($P_{\text{b}} = 30.6$ mW). To access the single soliton state, a single-sideband modulator [59] is used, and a single soliton spectrum is observed as shown in Fig. 5.2(b), verified by the system response measurement using vector network analyzer (VNA) [58]. The observed double resonance response shown in Fig. 5.2(b) inset corresponds to the cavity resonance of the continuous wave ("*C*-resonance"), and the soliton-induced resonance ("*S*-resonance"). These two resonances can be distinguished by increasing the detuning of the soliton state [58]. Figure 5.2(a) shows the simulation of soliton formation based on Lugiato-Lefever equation [51, 77] using the measured microresonator parameters. The simulated

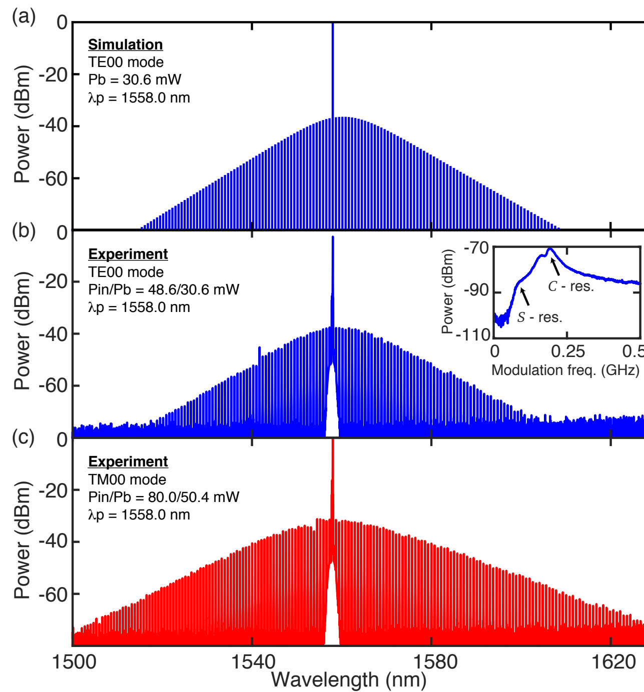

Figure 5.2 – Ultralow-power single soliton formation in the 88-GHz-FSR microresonator. (a) Simulated single soliton spectrum based on the measured microresonator's parameters, in the TE_{00} mode. $P_{\text{b}} = 30.6$ mW corresponds to $P_{\text{in}} = 48.6$ mW. (b) Single soliton spectrum pumped at $\lambda_{\text{p}} = 1558.0$ nm in the TE_{00} mode, with a pump power of $P_{\text{in}} = 48.6$ mW ($P_{\text{b}} = 30.6$ mW). Inset: cavity response measurement using the VNA, verifying that the spectrum is a single soliton state. (c) Single soliton spectrum pumped at $\lambda_{\text{p}} = 1558.0$ nm in the TM_{00} mode, with the pump power $P_{\text{in}} = 80.0$ mW ($P_{\text{b}} = 50.4$ mW).

soliton spectrum is nearly identical to the measured one. A single soliton in the TM_{00} mode is also generated ($D_1/2\pi \sim 86.35$ GHz, $D_2/2\pi \sim 0.967$ MHz, $D_3/2\pi \sim 5.4$ kHz) pumped at the wavelength $\lambda_p = 1558.0$ nm, with the input power $P_{in} = 80.0$ mW ($P_b = 50.6$ mW), as shown in Fig. 5.2(c). This soliton spectrum is broader than the one in the TE_{00} mode shown in Fig. 5.2(b), likely due to the lower D_2 value and higher power. The estimated power conversion efficiency from the CW pump to the soliton pulse is around 1.5%, with the power per comb line around 20 μW in the 3 dB bandwidth. Compared to prior works shown in Ref. [128, 129] which use solitons of repetition rate less than 100 GHz with input power exceeding 1 Watt, the current result shown here represents a significant power reduction, while the power per comb line of 20 μW still can achieve the same goals.

5.1.2 99 GHz soliton generation without EDFA

In this subsection, single soliton formation in 99-GHz-FSR microresonators without using EDFA is presented. Figure 5.1(d) shows that hydrogen absorption is the main loss reason which prevents the generation of 88 GHz soliton with lower power. Note that, the hydrogen is likely introduced due to the incomplete thermal annealing, or moisture in the air which forms a thin water film on the sample surface, or a combination of both two. Therefore in a new wafer fabrication run, the LPCVD Si_3N_4 is annealed via deposition - annealing - deposition -

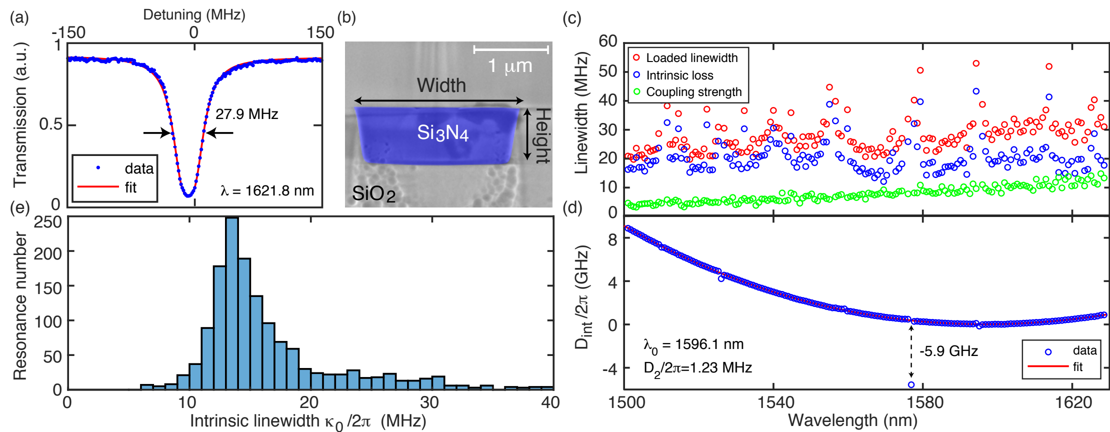

Figure 5.3 – Dispersion and resonance linewidth characterization of a 99-GHz-FSR microresonator. (a) The critically coupled resonance at $\lambda = 1621.8$ nm and its fit, with the loaded linewidth of $\kappa/2\pi = 27.9$ MHz and fitted intrinsic loss of $\kappa_0/2\pi \sim 13.7$ MHz. (b) SEM image of the cross-section of a Si_3N_4 waveguide with full SiO_2 cladding. The Si_3N_4 waveguide is blue shaded, the SiO_2 cladding is not color shaded. (c) Loaded linewidth, intrinsic loss and coupling strength of each TE_{00} resonance. No prominent hydrogen absorption loss is observed in the wavelength region from 1500 to 1550 nm. (d) Measured GVD of the TE_{00} mode family. Several avoided mode crossings are observed, where resonance linewidth increases. A strong mode crossing is found at 1577 nm, with -5.9 GHz resonance frequency deviation. (e) Histogram of intrinsic loss from the measurement of eight under-coupled samples. The most probable value of the histogram is around 13 - 14 MHz, which represents the Q factor of $Q_0 > 15 \times 10^6$.

annealing cycles, as described in Ref. [218]. To prevent water film formation on the wafer, a thick SiO_2 top cladding composed of TEOS and low temperature oxide (LTO) was deposited via LPCVD on the Si_3N_4 waveguides (SEM image of the waveguide cross-section is shown in Fig. 5.3(b)), followed by thermal annealing. Figure 5.3(c) shows the loaded linewidth, intrinsic loss and coupling strength of each TE_{00} resonance of a Si_3N_4 microresonator whose cross-section, width×height, is $1.58 \times 0.81\ \mu m^2$. The microresonator FSR is $D_1/2\pi \sim 98.9$ GHz. Compared with Fig. 5.1(d), Fig. 5.3(c) shows significant reduction of intrinsic loss in the wavelength range from 1500 to 1550 nm, demonstrating the successful removal of hydrogen in LPCVD Si_3N_4. Some resonances with large linewidth are caused by avoided mode crossings, in accordance with the observed avoided mode crossings in the dispersion measurement shown in Fig. 5.3(d). The measured GVD is $D_2/2\pi \sim 1.23$ MHz, with respect to $\omega_0/2\pi = 188.0$ THz ($\lambda_0 = 1596.1$ nm as the pump resonance in Fig. 5.4). Figure 5.3(e) shows the histogram of intrinsic loss from the measurement of eight under-coupled samples. These samples have the same waveguide cross-section but different bus-waveguide-to-microresonator gap distance. The most probable value of the histogram is around 13 - 14 MHz, which represents the Q factor of $Q_0 > 15 \times 10^6$. Figure 5.3(a) shows the resonance at $\lambda = 1621.8$ nm and its fit, with the loaded linewidth of $\kappa/2\pi = 27.9$ MHz and fitted intrinsic loss of $\kappa_0/2\pi \sim 13.7$ MHz.

Silicon nitride microresonators of anomalous GVD and Q factor exceeding 10×10^6 have been reported [98, 100], however single soliton generation has not been demonstrated. In those works, large waveguide width ($\geq 2.5\ \mu$m) was used. Despite the fact that the large waveguide

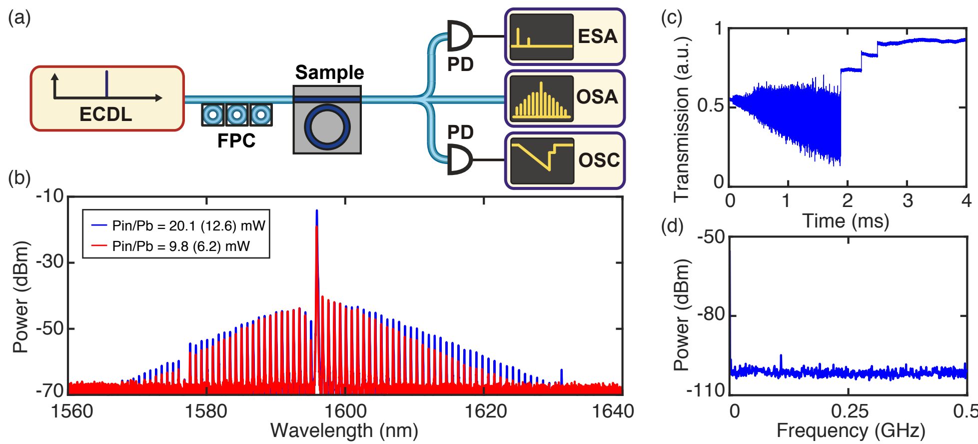

Figure 5.4 – Single soliton formation in a 99-GHz-FSR microresonator without EDFA. (a) Experimental setup. ECDL: external-cavity diode laser. OSC: oscilloscope. OSA: optical spectrum analyzer. ESA: electrical spectrum analyzer. FPC: fibre polarization controller. PD: photodiode. (b) Single soliton spectra pumped at $\lambda_p = 1596.1$ nm in the TE_{00} mode, with the input pump powers of $P_{in} = 9.8$ mW ($P_b = 6.2$ mW, red) and $P_{in} = 20.1$ mW ($P_b = 12.6$ mW, blue). (c) A representative soliton step of several hundred of microsecond, sufficiently long for accessing the single soliton state via simple laser piezo tuning. (d) Low-frequency RF spectrum of the optical spectrum with $P_{in} = 9.8$ mW (red), demonstrating the soliton nature of the spectrum.

width reduces optical mode interaction with the sidewall roughness, and thus reduces the scattering loss caused by the sidewall roughness, the resulted weak anomalous GVD due to the large waveguide width is insufficient for single soliton generation with low power. Here, with the high Q and strong anomalous GVD ($D_2/2\pi \sim 1.23$ MHz), a single soliton of 99 GHz repetition rate is generated with 9.8 mW input power (6.2 mW power in the bus waveguide), directly from the diode laser, without EDFA. The experimental setup is shown in Fig. 5.4(a), and the single soliton spectra are shown in Fig. 5.4(b). Parametric oscillation which generates frequency sidebands is observed around 1.7 mW input power. When the diode laser scans over the resonance, the observed soliton step varies from several hundred of microsecond to a millisecond (a representative soliton step in the transmission trace is shown in Fig. 5.4(c)), which is sufficiently long for accessing the single soliton state via simple laser piezo tuning [44]. Increasing power to the maximum laser output (around 20.1 mW) increases the soliton bandwidth. The estimated power conversion efficiency from the CW pump to the soliton pulse is around 1.7%. To identify the soliton nature of the spectrum, in this case a VNA measurement is difficult to implement due to the large EOM insertion loss and the limited diode laser output power. Instead, the soliton nature is revealed by the low-frequency radio frequency (RF) spectrum, as shown in Fig. 5.4(d), which can be well distinguished from the recorded noisy comb spectrum (modulation instability, not shown here). it is observed that, the single soliton generation with less than 10 mW input power is highly reproducible in resonances close to avoided mode crossings. In our case, without the EDFA and its gain bandwidth limitation, the diode laser frequency is tuned to a resonance which is close to a mode crossing, and investigate the minimum power for single soliton generation. Several samples have been experimentally measured. It is observed that such sub-10-mW-power single soliton generation is highly reproducible in these resonances, all of which feature long soliton steps (similar to the one shown in Fig. 5.4(c)). It appears that the mode crossings can facilitate single soliton formation with lower power, compared with normal resonances far from mode crossings. This phenomenon is likely due to single soliton generation assisted by spatial mode-interactions [328].

The single soliton formation over the full tuning range of the diode laser is further investigated. Figure 5.5(a, b) show the measured resonance linewidth and microresonator dispersion of a different 99-GHz-FSR microresonator ($D_1/2\pi \sim 98.9$ GHz, $D_2/2\pi \sim 1.19$ MHz, $D_3/2\pi \sim -1.1$ kHz). Figure 5.5(c) shows the single soliton spectra pumped at twenty selected resonances, eleven of which are consecutive in the telecom L-band, and five of which are consecutive in the telecom C-band. These spectra are generated with laser output power around 22 mW, and all accessed via simple laser piezo tuning. The complete hydrogen removal facilitates the soliton generation in the hydrogen absorption band. The minimum power to generate soliton in these resonances is not investigated. Single or few-soliton states in other resonances in the same sample are also generated, in addition to the ones shown in Fig. 5.5(c). The single soliton generation in a broad range of resonances demonstrates the reliability of the fabrication process, and offers extra flexibility to investigate spectrally localized effects, such as avoided mode crossings, which can enable the formation of dark pulses in the normal GVD

region [329, 96], and breathing solitons [330].

5.1.3 Sub-milliwatt-power soliton generation

In addition to the microresonators of sub-100-GHz FSR, the last part presents results from 1-THz-FSR microresonators, with the fundamental TE mode (TE_{00}). The Si_3N_4 microresonators have a cross-section, width×height, of 1.545×0.75 μm^2. The microresonator is critically coupled to a single-mode bus waveguide, for high coupling ideality [290]. Figure 5.6(b) shows the measured resonance linewidth versus wavelength. Figure 5.6(c) shows the measured resonance at 1564.8 nm and the linewidth fit [214, 316], which is pumped to generate soliton microcomb. This critically coupled resonance shows a total linewidth of $\kappa/2\pi = 61.3$ MHz, corresponding to an intrinsic loss $\kappa_0/2\pi \sim 30.7$ MHz and an intrinsic $Q_0 > 6.2 \times 10^6$. Figure 5.6(d) shows the measured microresonator integrated GVD. The fit values based on the measurement

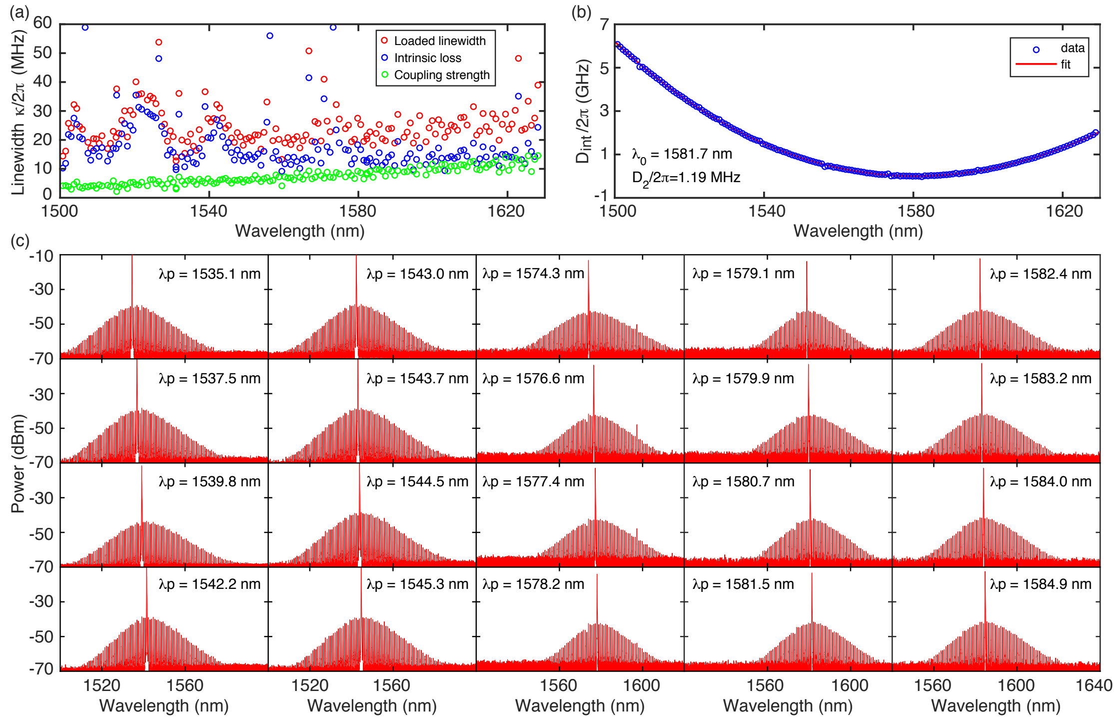

Figure 5.5 – Characterization of a different 99-GHz-FSR microresonator, and single soliton formation in multiple resonances. (a) Loaded linewidth, intrinsic loss and coupling strength of each TE_{00} resonance. (b) Measured GVD of the TE_{00} mode family. Several avoided mode crossings are observed, where resonance linewidth increases. (c) Single soliton formation in twenty selected resonances, eleven of which are consecutive in the telecom L-band, and five of which are consecutive in the telecom C-band. λ_p is the wavelength of the pumped resonance. Single or few soliton states are generated also in other resonances, which are not shown here. The complete hydrogen removal facilitates the soliton generation in the hydrogen absorption band.

are $D_1/2\pi \sim 1024$ GHz, $D_2/2\pi \sim 123$ MHz and $D_3/2\pi \sim 4.0$ kHz.

To generate and characterize soliton states, the setup used is shown in Fig.5.7(a). Note that no EDFA is used here. The soliton spectra with varying optical input power P_{in} is studied. As shown in Fig. 5.7(b), comb initiation is observed when P_{in} (P_{b}) reaches 800 (500) μW. Due to the high GVD ($D_2/2\pi \sim 123$ MHz) and the low linewidth ($\kappa/2\pi = 61.3$ MHz), corresponding to $\sqrt{\kappa/D_2} < 1$, the first sidebands start oscillating in the resonance modes adjacent to the pump at $\lambda_{\text{p}} = 1564.8$ nm. As the soliton step length is longer than 1 ms, the single soliton state can be accessed with the simple forward laser piezo tuning method [44]. A single soliton spectrum is observed, when P_{in} (P_{b}) reaches 6.6 (4.1) mW. The spectrum is further broadened with higher laser power, until the maximum power of the laser is reached at around 23 mW. At P_{in} (P_{b}) of 23.3 (14.6) mW, the single soliton shows a spectral bandwidth exceeding 300 nm, with a prominent Raman-induced soliton self-frequency shift [87]. The estimated power conversion efficiency from the CW pump to the soliton pulse is around 40%. Fig. 5.7(c) and (d) show that, the two spectra with $P_{\text{in}} = 6.6$ mW and $P_{\text{in}} = 23.3$ mW are indeed single soliton states, as verified by the system response measurement using vector network analyzer (VNA) [58]. The C-resonance and the S-resonance can be clearly distinguished by increasing the detuning of the soliton state [58].

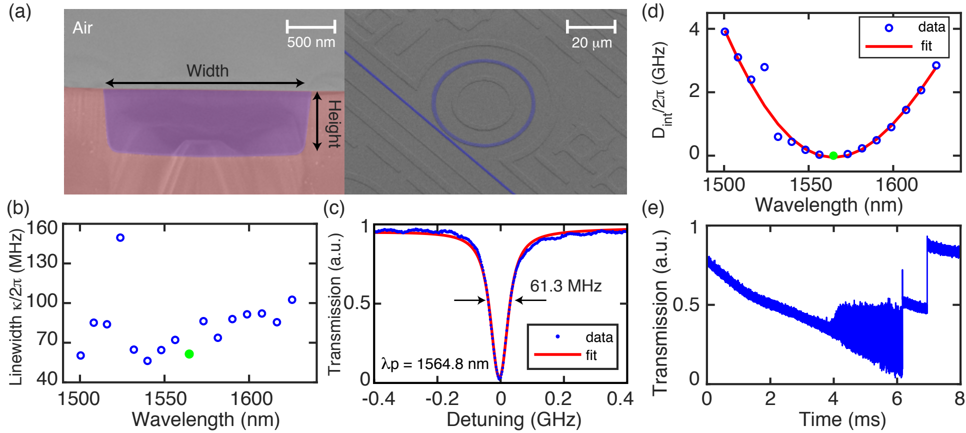

Figure 5.6 – Device design and characterization of the 1-THz-FSR microresonators. (a) Left: Scanning electron microscope (SEM) image of the sample's cross-section. Si_3N_4 waveguide is blue shaded. SiO_2 bottom cladding is red shaded. Unshaded area is air. Right: SEM image of the tilted view of the sample. Si_3N_4 waveguide is blue shaded. (b) Measured linewidth versus wavelength of each resonance of the 1-THz-FSR microresonator's TE_{00} mode family. (c) The resonance at $\lambda_{\text{p}} = 1564.8$ nm and its fit, which is marked as a green solid circle in (b) and (d) and is the pump resonance for DKS formation in Fig. 5.7. This critically coupled resonance shows a total linewidth of 61.3 MHz, corresponding to an intrinsic loss $\kappa_0/2\pi \sim 30.7$ MHz and an intrinsic $Q_0 > 6.2 \times 10^6$. (d) Measured dispersion properties of the 1-THz-FSR microresonator's TE_{00} mode family. A strong mode crossing is observed around 1530 nm. (e) A soliton step longer than 1 ms is observed when the laser scans over the resonance from the blue-detuned side to the red-detuned side.

5.1.4 40 GHz soliton generation without EDFA

Here, we demonstrate soliton microcomb generation at 40.6 GHz repetition rate, with only 10.2 mW optical power on chip (16 mW input power in the fibre), without using EDFA. Such a soliton repetition rate at microwave K_a and Q bands can be detected by fast photodetectors and be electronically processed. The microresonator features intrinsic $Q_0 \sim 30 \times 10^6$, and is critically coupled with loaded $Q \sim 15 \times 10^6$. Figure 5.8(a) shows the intrinsic loss $\kappa_0/2\pi$, coupling strength $\kappa_{ex}/2\pi$, and loaded linewidth $\kappa/2\pi$ of each TE_{00} resonance, measured from 1500 nm to 1630 nm using frequency-comb-assisted diode laser spectroscopy. The sample shows an estimated $\kappa_0/2\pi \sim 6.5$ MHz. Figure 5.8(b) shows the measured microresonator integrated dispersion. The FSR is $D_1/2\pi \sim 40.6$ GHz, and the GVD is $D_2/2\pi \sim 224$ kHz, obtained from fitting the measured dispersion profile. Using only a diode laser without an EDFA, the single soliton is generated with 10.2 mW power on the chip (input pump powers of $P_{in} = 16.0$ mW), as shown in Fig. 5.8(c). The single soliton state is accessed via only laser piezo frequency tuning, and does not require complex soliton tuning methods.

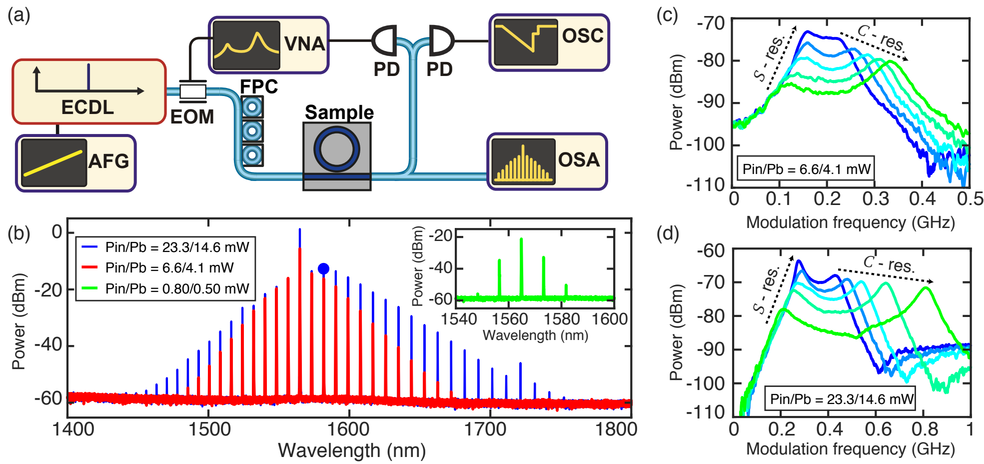

Figure 5.7 – Ultralow-power comb initiation and single soliton formation in the 1-THz-FSR microresonator. (a) Experimental setup. ECDL: external-cavity diode laser. VNA: vector network analyzer. OSC: oscilloscope. OSA: optical spectrum analyzer. AFG: arbitrary function generator. FPC: fibre polarization controller. EOM: electro-optic modulator. PD: photodiode. Note the lack of an EDFA. (b) Ultralow-power comb initiation spectrum (green), single soliton spectrum with low laser power (red), and single soliton spectrum with high laser power (blue), pumped at $\lambda_p = 1564.8$ nm. The blue circle marks the maximum of the soliton spectral envelope, showing the Raman-induced soliton self-frequency shift. (c, d) Cavity response measurement using, verifying that the two spectra shown in (b), red and blue, are both in a single soliton state. The evolution of the characteristic C- and S-resonances is shown for each state with increasing pump-cavity detuning.

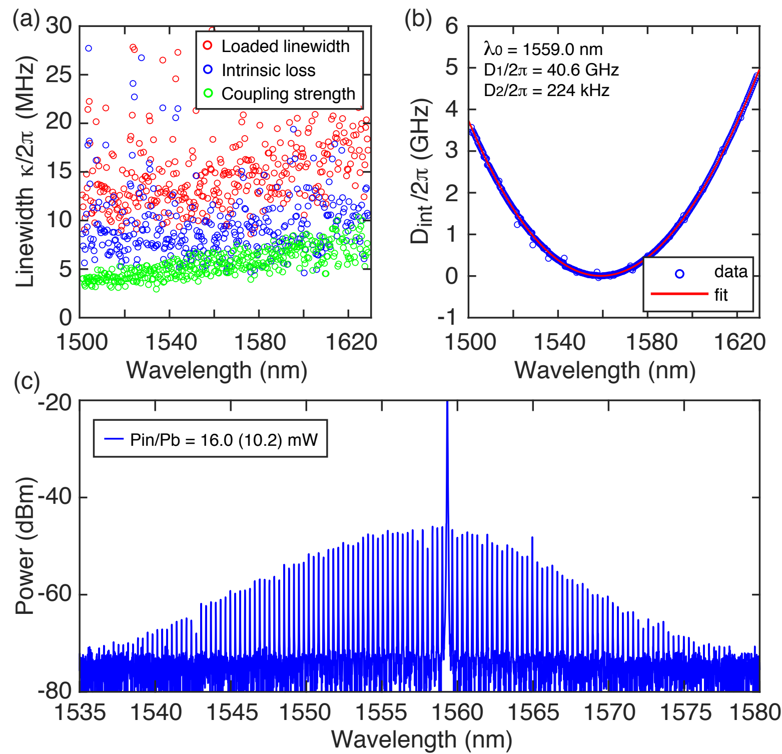

Figure 5.8 – Direct generation of single soliton of 40 GHz repetition rate using only diode laser, without optical amplifier. (a) Loaded linewidth, intrinsic loss, and coupling strength of each TE_{00} resonance from 1500 nm to 1550 nm. This sample has an estimated $\kappa_0/2\pi \sim 6.5$ MHz. (b) Measured GVD of the TE_{00} mode family. Avoided mode crossings of MHz resonance frequency deviation are observed. (c) Single-soliton spectra pumped at $\lambda_p = 1559.0$ nm in the TE_{00} mode, with the input pump powers of $P_{\text{in}} = 16.0$ mW to the chip ($P_{\text{b}} = 10.2$ mW on the chip), using only a diode laser, without an optical amplifier.

5.2 Soliton formation via laser self-injection locking

Laser self-injection locking is a phenomenon that the laser dynamics is impacted by external feedback light in the case without an optical isolator [331]. For example, in the case of laser self-injection locking of a DFB laser chip is to a high-Q microresonator, the back-reflected light from the microresonator due to the bulk Rayleigh scattering, impacts the laser dynamics and can significantly reduce the laser frequency noise in the presence of this passive optical feedback. This scheme, when using crystalline microresonators, has been used to demonstrate an ultra-narrow linewidth laser [332]. In addition, thanks to the high microresonator Q, once the laser power exceeds a certain threshold, nonlinear parametric oscillator and soliton formation can occur in the presence of laser self-injection locking [81, 333]. This scheme has been used to demonstrate an ultralow-noise microwave oscillator based on the photodetection of the generated soliton repetition rate [81].

Employing laser self-injection locking for soliton generation in Si_3N_4 chip device has a key advantage that, since the optical isolator is not required, the entire microcomb modulate can be compact, consisting of only a DFB laser chip or a laser diode, with a high-Q Si_3N_4 chip. In this section, the first work showing soliton formation via laser self-injection locking in integrated Si_3N_4 chip devices is presented. In fact, so far, only Si_3N_4 has been used to demonstrate this novel soliton generation scheme, due to the high microresonator Q exceeding 10×10^6 compared with other integrated platforms. By directly butt-coupling a multi-mode laser diode to a Si_3N_4 chip, solitons are generated via laser self-injection locking with sufficient on-chip power. it is observed that the current tuning of the laser diode can induce transitions from the chaotic microcomb state to breather solitons, and finally to stable multiple and single soliton solitons. The entire device of a compact form, consisting of only a laser diode and a Si_3N_4 chip, consumes less than 1 Watt electrical power for soliton microcombs with repetition rates below 150 GHz.

The main result has been published in ref. [170], A. S. Raja et al, "**Electrically pumped photonic integrated soliton microcomb**", *Nature Communications* 10, 680 (2019). The experimental and theoretical works were performed mainly by Arslan S. Raja, Andrey Voloshin and Hairun Guo. I designed and fabricated all the Si_3N_4 chip devices used in this work and led the sample characterization.

5.2.1 Schematic with a laser diode

Figure 5.9(a) presents the photo showing a Si_3N_4 chip butt-coupled to a multi-mode laser diode chip. The overall butt coupling loss is 3.6 dB. Figure 5.9(b) shows the schematic of soliton generation via laser self-injection locking. by tuning the frequency of the light emitted from the laser diode to a high-Q resonance of the Si_3N_4 microresonator, light is coupled into the microresonator. The bulk and surface Rayleigh scattering in the microresonator injects a fraction of light back into the laser diode, which triggers the laser self-injection locking.

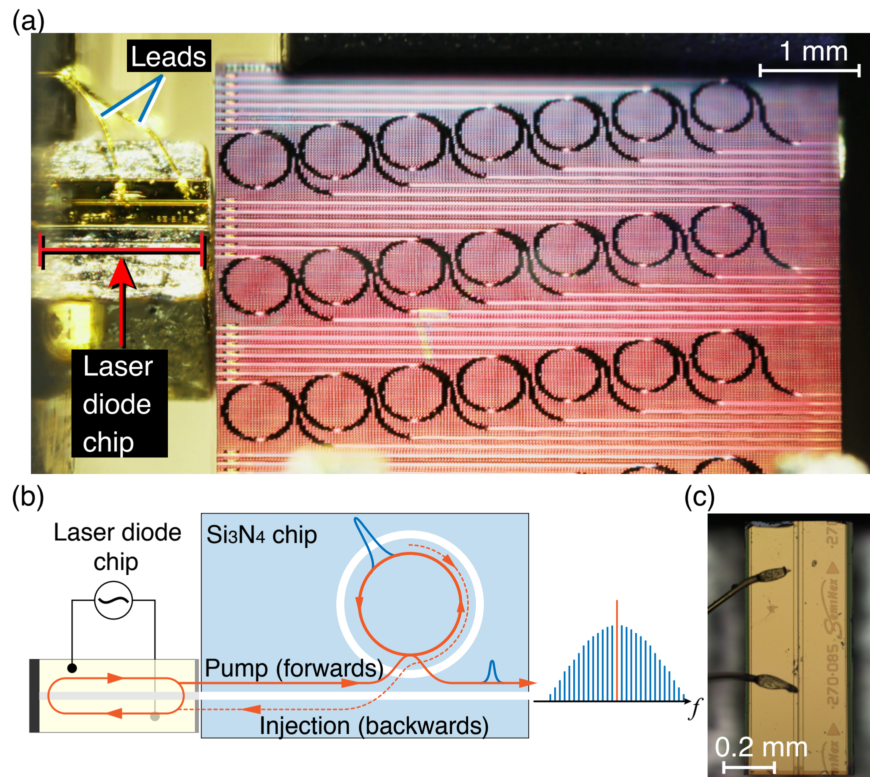

Figure 5.9 – Principle of laser self-injection locking using a laser diode chip and a Si_3N_4 chip. (a) Photo of the laser diode chip butt-coupled to a Si_3N_4 photonic chip, which contains several microresonators. (b) Schematic representation of the laser-injection-locked soliton microcomb formation. (c) An optical image of the InP laser diode chip.

Such back-reflection provides a frequency-selective optical feedback to the laser, leading to single-frequency operation and a significant reduction of the laser linewidth.

Initially, the free-running laser diode has multi-frequency light emission spectrum and a maximum optical output power of ∼ 100 mW. The measured linewidth is ∼ 60 MHz and an estimated short-time linewidth of ∼ 2 MHz. By tuning the laser frequency via diode current tuning, the initial multi-frequency emission spectrum switches to a single-frequency emission, indicative of laser self-injection locking. It is observed that, most resonances enabling laser self-injection locking feature visible mode splitting as a result of backscattering. The experimentally measured and fitted laser linewidth with self-injection locking has a Gaussian contribution of 186 kHz and Lorentzian contribution is 0.7 kHz. Since the self-injection locking leads to a reduction of the white noise of the laser diode [331], the reduction in the Lorentzian contribution in the Voigt profile corresponds to a more than 1000-fold reduction in the linewidth.

Theoretically, the presence of backscattering leads to an amplitude reflection coefficient r

from the passive microresonator on resonance to the laser diode, as:

$$r \approx \frac{2\eta\Gamma}{1+\Gamma^2}, \tag{5.1}$$

where $\eta = \kappa_{\mathrm{ex}}/\kappa$ characterizes the coupling efficiency ($\kappa = \kappa_0 + \kappa_{\mathrm{ex}}$, with $\eta = 1/2$ being the critical coupling), and $\Gamma = \gamma/\kappa$ is the normalized mode-coupling parameter that describes the visibility of the resonance split. According to Ref. [331], this reflection can initiate self-injection locking, and induce laser linewidth narrowing, as:

$$\delta\omega \approx \delta\omega_{\mathrm{free}} \frac{Q_{\mathrm{LD}}^2}{Q^2} \frac{1}{16r^2(1+\alpha_g^2)}, \tag{5.2}$$

where $Q = \omega/\kappa$ is the microresonator quality factor, Q_{LD} is the quality factor of the laser diode, $\omega/2\pi$ is the laser frequency, $\delta\omega_{\mathrm{free}}/2\pi$ is the linewidth of the free-running laser. The phase-amplitude coupling factor α_g is the linewidth enhancement factor, given by the ratio of the variation of the real refractive index to the imaginary refractive index of the laser diode active region, in response to a carrier density fluctuation [334]. The factor α_g takes typical values from 1.6 to 7. The InGaAsP/InP multiple-quantum-well laser diode has $\alpha_g = 2.5$.

In the presence of self-injection locking, the "**injection pulling**" allows a frequency detuning between the laser frequency and microresonator resonance. This frequency detuning, enabled by injection pulling, is imperative for soliton generation. The injection pulling is a result of slight phase difference between the emitted laser frequency from the diode and its feedback from the microresonator, leading to partial locking [331]. The locking range $\Delta\omega_{\mathrm{lock}}$ is defined as the frequency range over which laser self-injection locks happens, and has the follows expression [331]:

$$\Delta\omega_{\mathrm{lock}} \approx r\sqrt{1+\alpha_g^2}\,\frac{\omega}{Q_{\mathrm{LD}}}. \tag{5.3}$$

The laser output power reduces from the free-running state to the self-injection-locked state, due to the single-longitudinal-mode operation. Since our Si_3N_4 devices allow soliton generation threshold power at few milliwatt power, solitons can be generated concurrent to the laser self-injection locking with tens of milliwatt on-chip power. Figure 5.10(a) shows the self-injection-locked microcomb generation in a microresonator with an FSR of 149 GHz. Concurrent to laser self-injection locking, via current tuning, a chaotic comb is observed as shown in Fig. 5.10(a). Increasing the laser current slightly by $\mathcal{O}$(mA) that changes the laser detuning by injection pulling, the chaotic comb is switched to an intermediate oscillatory state, as shown in Fig. 5.10(b). This oscillatory state is identified as a breather soliton [335], where the soliton exhibits periodic oscillations. Further increasing the laser current, a transition to a low-noise comb state is observed, signalling the formation of stable soliton as shown in Fig. 5.10(c). The spectral envelope exhibits a secant-squared profile, corresponding to a single soliton. This transition is realized by only laser diode current tuning.

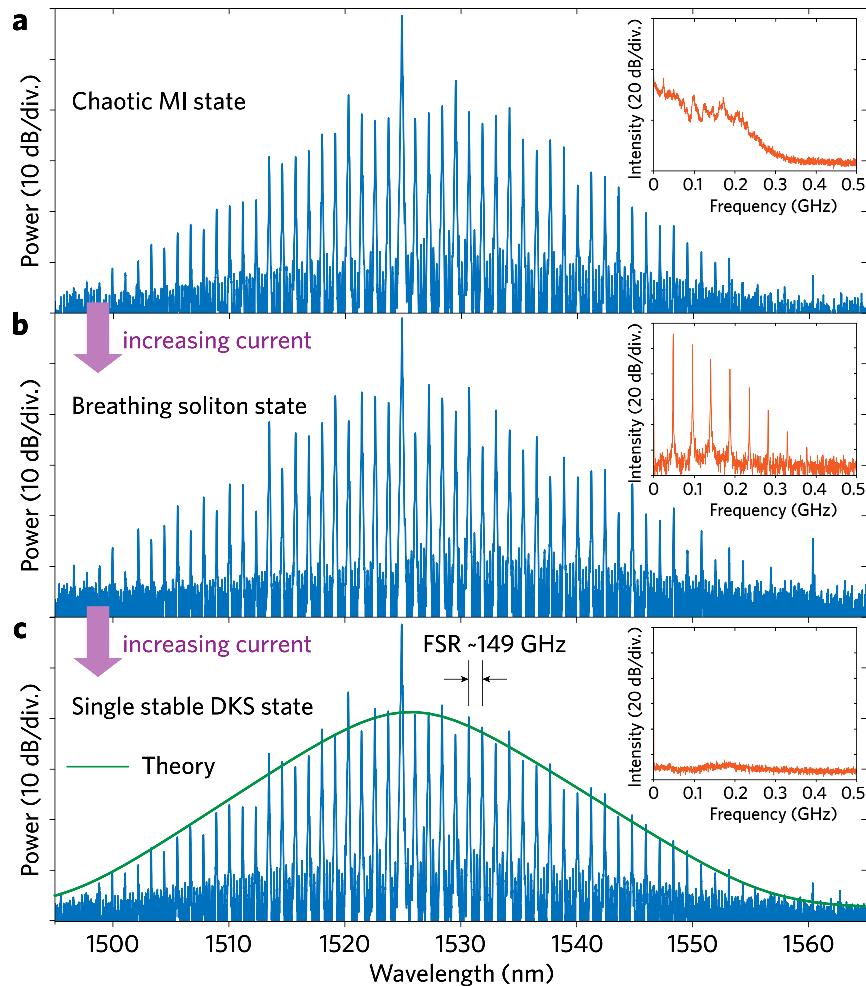

Figure 5.10 – Lase-injection-locked soliton switching (a) Chaotic comb (modulation instability). (b) Breathing soliton (c) Single soliton. The spectrum is fitted with a hyperbolic secant envelope (green-solid line). Each inset shows the low-frequency RF spectrum.

In a follow up work, a highly-compact soliton microcomb module with 30 GHz soliton repetition rate is presented. This module is based on a DFB laser chip self-injection-locked a Si_3N_4 microresonator chip of 30 GHz FSR. It is revealed theoretically and experimentally, that soliton states can be accessed using both the forward and backward laser frequency tuning [44, 58] while in the laser self-injection locking regime. The self-injection locking regime is experimentally characterized, and different soliton states are observed, depending on the laser frequency detuning locking phase. To corroborate the experimental observation, a theoretical model of nonlinear laser self-injection locking, i.e. laser self-injection-locked to a high-Q microresonator where the intracavity power is sufficiently high to induce parametric oscillation and comb formation via Kerr nonlinearity. It is shown that, in the locked state, attainable effective laser detuning values might not cover the full soliton existence range. Meanwhile, the maximum attainable effective laser detuning for soliton generation depends on the direction

of the laser frequency scan. Compared to the case where a multi-mode laser diode is used, the DFB laser chip avoids mode competition effects and offers higher laser output power above 100 mW. The main result has been published in "**Dynamics of laser self-injection locked soliton microcombs in integrated microresonators**", arXiv: 1912.11303 (2019). The experimental and theoretical works were performed at RQC by Andrey Voloshin and Nikita Kondratiev The Si_3N_4 chip devices were fabricated by myself.

6 Generation and Application of Microwave-Repetition-Rate Solitons

The synthesis, distribution and processing of radio and microwave signals is ubiquitous in our information society for radars, wireless networks, and satellite communications. With the looming bandwidth bottleneck in telecommunications [336] (due to e.g. future requirements of 5G and the Internet of Things), the tendency is to use carriers in higher frequency bands. As it becomes progressively difficult to generate and digitize electronic signals with increasing carrier frequency, using photonics to process ultra-wideband signals has been extensively explored, commonly referred to “microwave photonics” [337]. Microwave photonic technologies [337, 185], which up-shift the carrier into the optical domain to facilitate the generation and processing of ultra-wideband electronic signals at vastly reduced fractional bandwidths, have the potential to achieve superior performance compared to conventional electronics for targeted functions. Landmark demonstrations of microwave photonics, such as radar [338], analogue-to-digital converter [339], radio-over-fibre [340], and waveform generation [341] have achieved bandwidth not attainable using conventional electronics. For microwave photonic applications such as filters [342], coherent radars [338], subnoise detection [343], optical communications [344] and low-noise microwave generation [27], frequency combs are key building blocks. Similarly, the synthesis of low-noise microwave signals, paramount in a large variety of modern applications such as time-frequency metrology [345] and wireless broadband communications [346], have attained unrivalled performance in terms of spectral purity (i.e. noise) [27, 347, 81], by using optical synthesis approaches based on frequency combs. However, the future deployment of these technologies critically depends on achieving such performance enhancements with photonic *integrated* components [185]. In this context, soliton microcomb could be key building blocks as sources of multiple coherent optical carriers for microwaves synthesis, and as sources to implement microwave photonic functionalities which require multiple coherent carriers [348, 349, 350]. Silicon nitride based soliton microcombs have given rise to photonic integrated microcombs operating with low power and can be integrated with compact lasers [101, 170], thus allowing further optical or electrical functionalities [97, 116]. However, the unfavourable scaling of the soliton threshold power, which increases for low quality factors and low repetition rates, has prevented the repetition rates f_{rep} of integrated microcombs from being reduced below ~ 100 GHz in microwave bands

that can easily be processed by regular optoelectronic components.

So far, soliton microcombs of repetition rates in the microwave K- and X-band (f_{rep} < 20 GHz) have been demonstrated only on low-refractive-index materials such as silica and bulk-polished crystalline microresonators [84, 81]. These microresonators can only operate with air cladding, thus exhibit limited capability of scalable manufacture using CMOS-compatible foundry process, and are sensitive to contamination and challenging to integrate with active tuning components such as piezoelectric actuators and metallic heaters [97, 116]. On fully integrated platforms such as Si_3N_4, the main challenges hindering soliton generation at microwave repetition rates are related to the comparatively low quality (Q) factor and thermal effects. Laser power up to several Watts is required to obtain microwave-repetition-rate solitons, not only due to the decreasing resonator finesse, but also the decreasing Q caused

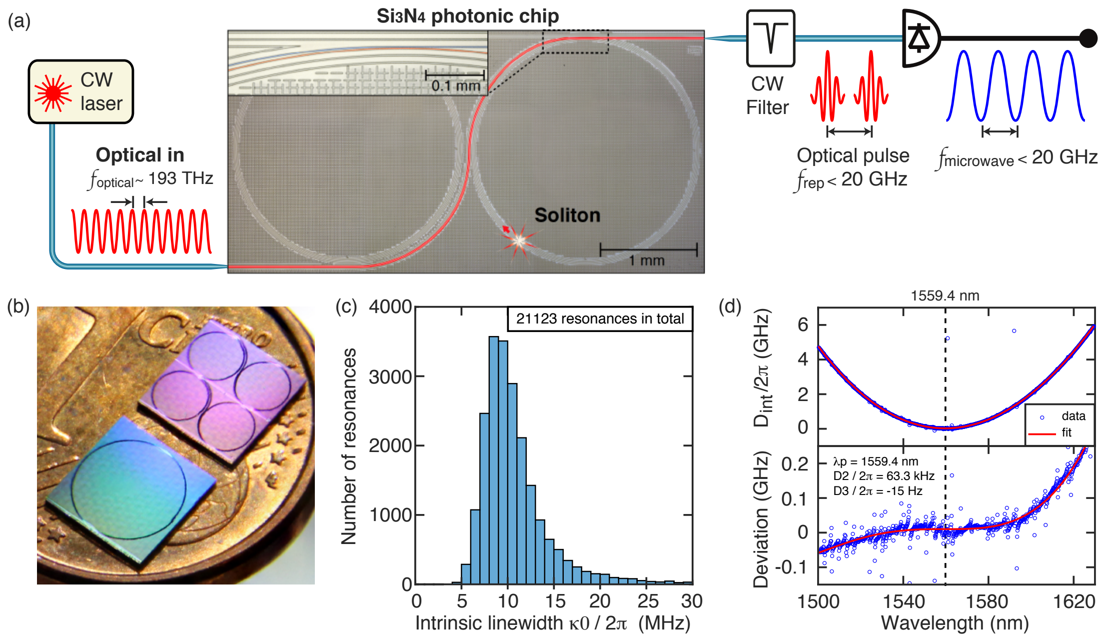

Figure 6.1 – Principle of nanophotonic microwave synthesizers based on integrated soliton microcombs, and characteristics of Si_3N_4 microresonators. (a) Concept of the photonic microwave synthesizer based on an integrated Si_3N_4 soliton microcomb driven by a c.w. laser. The microscope image of the Si_3N_4 photonic chip highlights the bus-waveguide-to-ring-resonator coupling, and stress-release patterns for Si_3N_4 film crack prevention. (b) Photograph of Si_3N_4 photonic chips which are 5×5 mm^2 in size, in comparison with a 1-cent Euro coin. The chip color is due to the light interference caused by the SiO_2 cladding. (c) Histogram of the intrinsic loss $\kappa_0/2\pi$ of 21123 resonances. The most probable value is $\kappa_0/2\pi = 8.5$ MHz, corresponding to $Q_0 > 22 \times 10^6$. (e) Top: Fitted microresonator dispersion $D_{int}/2\pi$, with $D_1/2\pi \sim 19.6$ GHz and $D_2/2\pi \sim 63.3$ kHz, referred to $\lambda_p = 1559.4$ nm. Bottom: Resonance frequency deviation from a D_2-dominant parabolic profile, defined as $(D_{int} - D_2\mu^2/2)/2\pi$, in order to outline mode crossings and $D_3/2\pi \sim -15$ Hz. Mode crossings well below 50 MHz are revealed due the high resonance Q (loaded linewidth $\kappa/2\pi \sim 18$ MHz).

by fabrication-related defects such as lithography stitching errors. Stitching errors tend to accumulate in larger pattern areas, resulting in serious device failure and low fabrication yield for long waveguides or large rings. Complex resonator shapes have been utilized to avoid stitching errors [114, 98], and 20 GHz FSR resonators with Q exceeding 10×10^6 have been demonstrated [98]. However, the significantly enhanced mode crossings in these microresonators, caused by the spatial mode coupling in the waveguide bending sections, likely prohibited single soliton formation [114, 98]. In addition, thermal effects in Si_3N_4 lead to short "soliton steps" [99], which make more difficulty to access the (single) soliton state via simple laser frequency tuning. Complex techniques [59] can be used to overcome this challenge, at the expense of requiring additional electronic and optical components.

In this chapter, integrated Si_3N_4 soliton microcombs operating in the microwave X- and K-band are presented and their phase noise performances are experimentally characterized. This result has been published in ref. [78], J. Liu et al, "**Photonic microwave generation in the X- and K-band using integrated soliton microcombs**", *Nature Photonics* (2020). I designed and fabricated all the Si_3N_4 chip devices used in this work, and led the sample characterization and soliton generation. Multiple people have contributed significantly to this result, particularly Erwan Lucas who lead the characterization and analysis of the phase noise of soliton repetition rates.

6.1 Principle and sample description

The principle of microwave oscillators based on integrated soliton microcombs is depicted in Fig. 6.1(a). A photonic integrated microresonator is driven by a near-infrared c.w. laser to produce an optical pulse stream, which upon photodetection generates a microwave signal, whose frequency depends on the microresonator FSR. As the soliton generation power increases with decreasing FSR, the key challenge here is to use nanofabrication process to make macroscopic resonators of centimetre-scale dimensions, and simultaneously generate soliton pulses, ideally with power levels compatible with integrated lasers [351, 206]. This challenge is overcome by using the photonic Damascene reflow process, which allows scalable manufacture of high-Q integrated microresonators based on ultralow-loss Si_3N_4 waveguides (linear propagation loss $\alpha \approx 1.4$ dB/m) with high fabrication yield and reproducibility. Such low loss and high yield are achieved by using several key fabrication techniques, including DUV stepper lithography based on KrF at 248 nm to pattern the waveguides with reduced stitching errors and superior quality, and stress-release patterns to prevent crack formation in the thick Si_3N_4 film required to obtain a strong anomalous geometric GVD. The advantages of DUV stepper lithography over electron beam lithography (EBL), besides the higher yield and lower cost, are: 1. The stitching errors on the wafer are 4 or 5 times smaller than the ones on the reticle used in the industrial standard 4 or 5 demagnification lens systems; 2. The reticle writing using standard photolithography (~ 1 hour) is much faster than the wafer writing using EBL (> 10 hours), thus the field-to-field (or stripe-to-stripe) time delay is significantly shorter with DUV than with EBL, leading to smaller stitching errors caused by the beam drift; 3. The

field (or stripe) size of photolithography for reticle writing is much larger than the field size of EBL for wafer writing, leading to fewer stitching errors; 4. Multipass for reticle writing can be easily adapted with reasonable cost increases. Consequently, DUV stepper lithography can provide superior lithography quality, and has been used in recently demonstrated integrated Brillouin laser[200] based on low-confinement Si_3N_4 waveguides of optical propagation loss below 1 dB/m[201, 199].

In addition, in order to minimize the spatial mode coupling between the soliton mode and other waveguide modes, the microresonators are designed in a perfectly circular shape, whose diameters are 2.30 (4.60) mm for ~ 20 (10) GHz FSR. The microresonator is coupled to a multi-mode bus waveguide of the same cross-section for high coupling ideality [290]. Both the straight and pulley bus waveguides are studied in this work, however no prominent performance difference is observed, likely due to the high Q. Figure 6.1(b) shows a photo of the final Si_3N_4 photonic chips in 5×5 mm^2 size, in comparison with a 1-cent Euro coin. For each resonance, the loaded linewidth $\kappa/2\pi = (\kappa_0 + \kappa_{ex})/2\pi$, intrinsic loss $\kappa_0/2\pi$, and coupling strength $\kappa_{ex}/2\pi$ are extracted from each resonance fit. Figure 6.1(c) shows the histogram of $\kappa_0/2\pi$ of 21123 fitted resonances, from 14 characterized 10-GHz-FSR samples. The most probable value is $\kappa_0/2\pi$ = 8.5 MHz, corresponding to a statistical intrinsic quality factor $Q_0 > 22 \times 10^6$. Figure 6.1(d) shows the measured $D_{int}/2\pi$ and outlines the resonance frequency deviation from a D_2-dominant parabolic profile, defined as $(D_{int} - D_2\mu^2/2)/2\pi$, in order to reveal mode crossings and the D_3 term. As evidenced by Fig. 6.1(d), our fabrication and design yield an ideal anomalous GVD with significantly reduced mode crossings compared with previous work [114, 98].

Using the Damascene reflow process, microresonators with FSRs in the microwave K- and X-band are fabricated. Light is coupled into and out of the chip device via double-inverse nanotapers [239]. The coupling loss is ~ 3 dB per facet, corresponding to ~ 25% fibre-chip-fibre coupling efficiency. More than 20 samples are tested and single solitons are generated in every sample. Only four selected samples (A, B, C and D) are shown here. Samples A and B are used to generate 19.6-GHz-repetition-rate solitons. Sample A is undercoupled, with a loaded linewidth $\kappa/2\pi \sim 18$ MHz and a coupling coefficient $\eta = \kappa_{ex}/\kappa \sim 1/3$. Sample B is overcoupled, with $\kappa/2\pi \sim 27$ MHz and $\eta \sim 2/3$, and the soliton generated in this chip is used later for the K-band soliton phase noise characterization. Samples C and D are used to generate 9.78-GHz-repetition-rate soliton. Sample C is undercoupled, with $\kappa/2\pi \sim 14$ MHz and $\eta \sim 2/5$, and the soliton generated in this chip is used later for the X-band soliton phase noise characterization. Sample D is overcoupled, with $\kappa/2\pi \sim 22$ MHz and $\eta \sim 2/3$. The waveguide cross-sections, width × height, are 1700×950 nm^2 for samples A and B, and 2100×950 nm^2 for sample C and D, respectively.

6.2 K- and X-band soliton generation

Using the setup shown in Fig. 6.2(a), single solitons are generated using simple laser piezo frequency tuning [44, 58] in all tested samples. As shown in Fig. 6.2(b), in sample A (red), the single soliton is generated with 38 mW power in the bus waveguide on the chip (76 mW power in the input lensed fibre), while parametric oscillation is observed with 7 mW power. The single soliton spectrum fit shows a 3-dB-bandwidth of 11.0 nm, corresponding to a pulse duration of 232 fs. Not only is it the first single soliton of a K-band repetition rate among all integrated

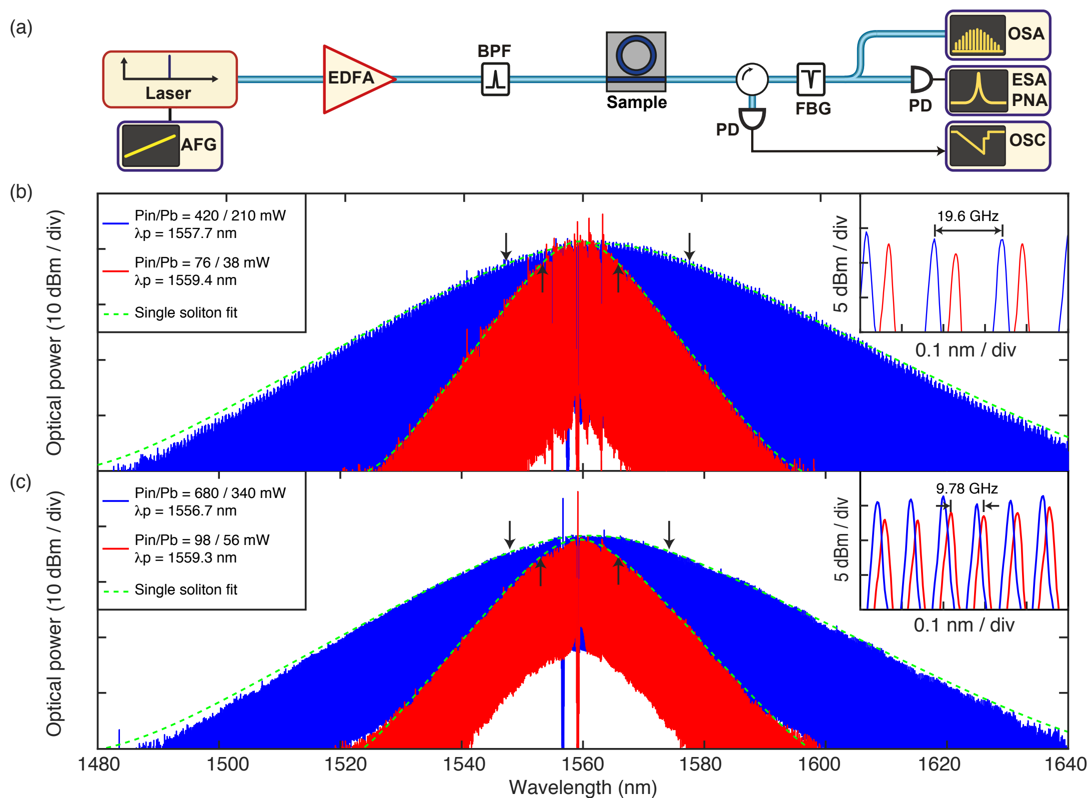

Figure 6.2 – Single solitons of microwave K- and X-band repetition rates. (a) Experimental setup to generate single solitons and to characterize the soliton phase noise. EDFA: erbium-doped fibre amplifier. AFG: arbitrary function generator. BPF: band-pass filter. FBG: fibre Bragg grating. OSA: optical spectrum analyzer. OSC: oscilloscope. PD: photodiode. ESA / PNA: electrical spectrum analyzer / phase noise analyzer. (b) Single soliton spectra of 19.6 GHz repetition rate with 38 mW power in sample A (red), and with 210 mW power in sample B (blue), and their spectrum fit (green). Arrows mark the 3-dB-bandwidths. Inset: Spectrum zoom-in showing the 19.6 GHz mode spacing. (c) Single soliton spectra of 9.78 GHz repetition rate with 56 mW power in sample C (red=), and with 340 mW power in sample D (blue=), and their spectrum fit (green). Arrows mark the 3-dB-bandwidths. Inset: Spectrum zoom-in showing the 9.78 GHz mode spacing. Note: for soliton spectra in (b) and (c), a BPF is used to filter out the EDFA's amplified spontaneous emission (ASE) noise in the pump laser, and an FBG is used to filter out the pump laser in the soliton spectra.

waveguide platforms, but it also represents an extremely low threshold power for soliton formation, on par with the power values in silica and crystalline microresonators [81, 84]. This power level is compatible with state-of-art integrated lasers [351, 206], which enables realistic prospects for fully integrated microwave photonic systems, especially in conjunction with resonator actuators (such as piezoelectric actuator [116] and metallic heaters [97]) to tune or stabilize the operation frequency. In sample B, the single soliton is generated with 210 mW power, and features 170 comb lines within the 3-dB-bandwidth of 26.9 nm (94.6 fs pulse duration), ideal for creating dense wavelength-division multiplexing (WDM) channels for coherent communications [145]. Single solitons at 9.78 GHz repetition rate in the X-band is also generated, as shown in Fig. 6.2(c), with a power of 56 mW in sample C (red) and 340 mW in sample D (blue). The 3-dB-bandwidths are 12.5 nm (red, 158 comb lines, 203 fs pulse duration) and 25.8 nm (blue, 327 comb lines, 98.6 fs pulse duration), respectively. The Raman self-frequency-shift [87, 352] is observed of ~ 4.9 nm in sample B and of ~ 4.4 nm in sample D. The c.w.-to-single-soliton power conversion efficiency is approximately 0.4% in sample A and 0.2% in sample C. For K-band single soliton generation, further power budget reduction to below 100 mW input requires a higher microresonator Q factor, and may also be achieved by increasing the anomalous GVD (D_2) via e.g. coupled resonators exhibiting mode hybridization [256], which increases the soliton pulse duration and c.w.-to-soliton power conversion efficiency.

Besides the single solitons, multi-solitons of K- and X-band microwave repetition rates with lower laser power are also generated. Figure 6.3 shows the multi-soliton spectra of 19.6 GHz repetition rate with 48 mW input power (24 mW on the chip) in sample A, and 9.78 GHz repetition rate with 56 mW input power (32 mW on the chip) in sample C.

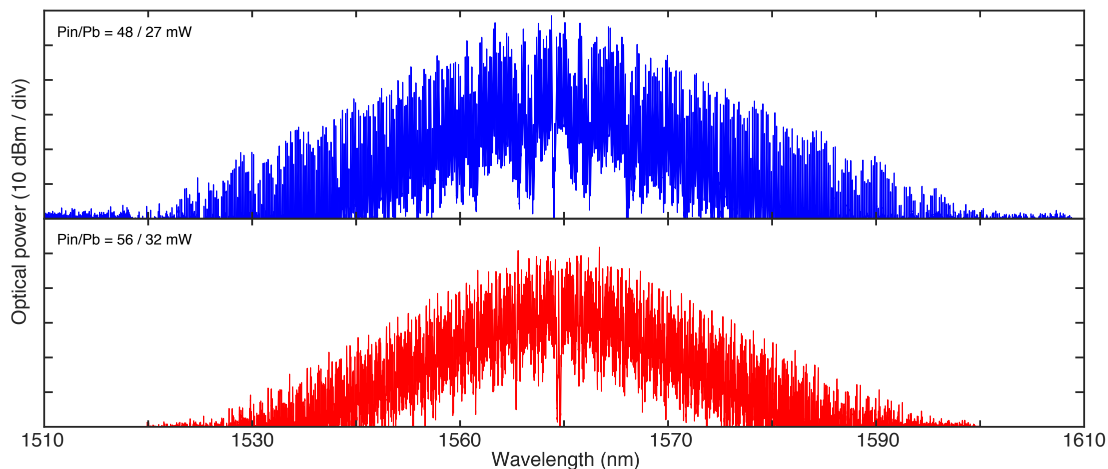

Figure 6.3 – Multi-soliton spectrum of K- and X-band repetition rate. Top: 19.6 GHz multi-soliton with 48 mW input power (24 mW on the chip). Bottom: 9.78 GHz multi-soliton with 56 mW input power (32 mW on the chip).

6.3 Phase noise characterization

Next, the phase fluctuations of the soliton-based K- and X-band microwave carriers is systematically analyzed. The measurement setup is shown in Fig. 6.2(a): the soliton pulse stream is driven by a c.w. ECDL (Toptica CTL). After the resonator, the excess c.w. pump light is rejected using a narrow-band optical notch filter, before the photodetection of the soliton repetition rate on a fast InGaAs photodiode (Discovery Semi. DSC40) whose output electrical signal is fed to a phase noise analyzer (PNA, Rohde & Schwarz FSW43). The soliton repetition rates around 9.78 GHz are characterized in the free-running state, i.e. neither the laser frequency and power nor the resonator are stabilized. A slow frequency modulation at ~ 5 Hz rate is observed (see Fig. 6.5(c)), which is likely caused by the unstable chip coupling using suspended lensed fibres, susceptible to vibrations. To increase the coupling stability, ultrahigh-numerical aperture fibres are glued to the chip using a photonic packaging technique [353], as shown in Fig. 6.4(a). The comparison of the relative Allan deviation before and after packaging the same 9.78-GHz-FSR chip, shown in Fig. 6.4(c), proves that the chip packaging largely improves the soliton stability.

Figure 6.4(b) shows the measured free-running phase noise of the 9.78 GHz soliton repetition rate before and after packaging the same chip, in comparison with the phase noise of a K-band soliton in an unpackaged 19.6-GHz-FSR chip. Note that in the case of unpackaged 19.6 GHz soliton, though lensed fibres are used to couple light into and out of the chip, the power transmitted through the chip is stabilized, which is to imitate the case of packaged chip with stable fibre-chip coupling. This is realized by using two auxiliary soliton stabilization techniques: the first one is to stabilize the transmitted power through the chip using an acousto-optic modulator (AOM), which varies the pump power. A power servo based on a proportional-integral-derivative (PID) controller is used to keep constant the power at the chip output. The second method is to actively stabilize the cavity-pump detuning using an offset sideband Pound-Drever-Hall (PDH) lock [59] with feedback applied to the pump laser power, which can effectively compensate the cavity resonance jitter induced by coupling fluctuations. Two cases are investigated in Fig. 6.4(d): In case A, with the power-stabilization, the soliton is driven by a diode laser (Toptica) and the PNA used is the FSW43; In case B, with the detuning-stabilization, the soliton is driven by a fibre laser (Koheras AdjustiK), and, besides the FSW43, an additional PNA (Rohde & Schwarz FSUP, with cross-correlations) is used only for measuring the 10 kHz – 1 MHz offset frequency range. Note that, due to the fact that the current soliton phase noise is mainly limited by the laser used (laser phase noise or relative intensity noise), using these soliton stabilization techniques do not necessarily result in prominent soliton phase noise reduction. The full experimental setup with auxiliary components for soliton stabilization is shown in Fig 6.5(a). First, the drift of the photodetected soliton repetition rate around 19.67 GHz is characterized in the free-running state. An oscillation at low frequency ~ 5 Hz is observed, as shown in Fig. 6.5(b) left, which is likely caused by the unstable chip coupling using suspended lensed fibres, susceptible to vibrations. Several experimental technique can be used to mitigate this effect, including stabilizing the transmitted power through the

chip using an AOM with a power servo based on a PID controller, or stabilizing the cavity-pump detuning using an offset sideband PDH lock [59] with feedback applied to the pump laser power. Both methods can significantly improve the soliton stability, as the observed low-frequency oscillation in the free-running situation is significantly reduced, as shown in Fig. 6.5(b).

Thanks to the chip packaging, the soliton phase noise at low offset frequency < 30 Hz is reduced. However, no prominent phase noise reduction at higher offset frequencies is observed before and after chip packaging. Furthermore, no prominent phase noise difference is observed between the unpackaged 19.6 and 9.78 GHz solitons in that frequency range. To further investigate the source of the phase noise limitation, the following study only focuses on unpackaged 19.6 GHz soliton.

To investigate the role of laser noises in the generated microwave signal, the laser phase noise is measured and correlated with the soliton repetition rate noise, and the conversion of optical

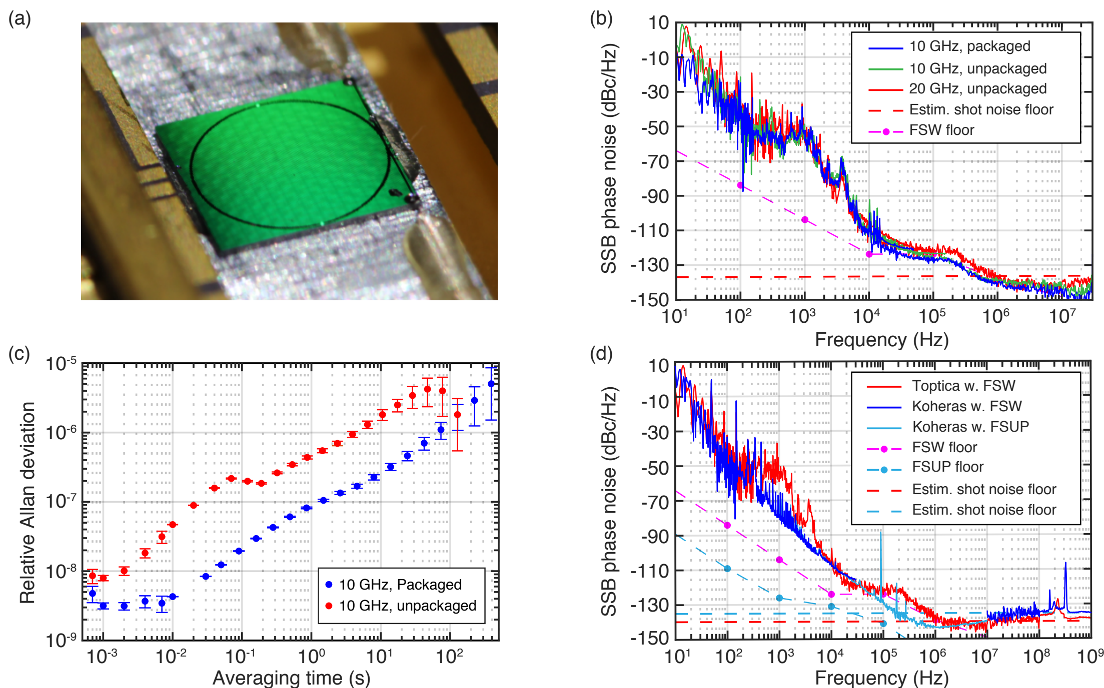

Figure 6.4 – Phase noise characterization of the soliton repetition rate. (a) Photo of a packaged Si_3N_4 chip for X-band soliton generation, with input and output fibres glued to the chip. (b) Comparison of free-running soliton phase noises using packaged and unpackaged X-band soliton chips, and an unpackaged K-band soliton chip. (c) Measured relative Allan deviation of the X-band soliton repetition rate before and after packaging the same chip, revealing the stability improvement. (d) SSB phase noise measured with the stabilized cavity-pump detuning at $\delta\omega/2\pi \sim 400$ MHz, using different lasers and PNAs (PNA noise floors are indicated). The estimated shot noise floors are –140 dBc/Hz with Toptica laser (red), and –135 dBc/Hz with Koheras laser (blue).

to microwave noise is estimated as −55 dB. This is measured by comparing the laser phase noise (obtained by beating it against an ultra-stable laser) and the phase noise of soliton repetition rate, which enables the estimation of the optical to microwave phase transduction (PM2PM). In particular, the Toptica CTL diode laser features a typical noise bump around 3 kHz. Under usual condition, i.e. out of "quiet point" regime [159], the measured PM2PM coefficient is approximately −55 dB, as shown in Fig. 6.6(a). This conversion factor arises from the conversion of detuning fluctuations to repetition rate fluctuations, which we mainly attribute to the Raman self-frequency shift [352, 87].

In addition, the conversion of laser relative intensity noise (RIN) to the phase noise of soliton repetition rate is also experimentally measured. A calibrated pure power-modulation of the pump laser is applied using a 0th-order AOM at frequencies ranging from 10^3 to 10^5 Hz. The resulting phase modulation strength of the soliton repetition rate is measured by integrating the corresponding peak of the phase noise power spectrum density (PSD). The result of the AM2PM transfer function measurement is shown in Fig. 6.6(b). From this measurement, it appears that the AM2PM conversion mostly follows a $1/f^2$ slope (red line in Fig. 6.6(b)), meaning that, in fact the amplitude modulation leads to frequency modulation of the repetition rate as:

$$\delta f_{\mathrm{rep}} = \alpha \delta P_{\mathrm{in}} \tag{6.1}$$

conversion coefficient is estimated as $\alpha = 79$ Hz/mW to match the measurement (the power is defined as the input power in the lensed fibre, before coupled into the chip). This conversion

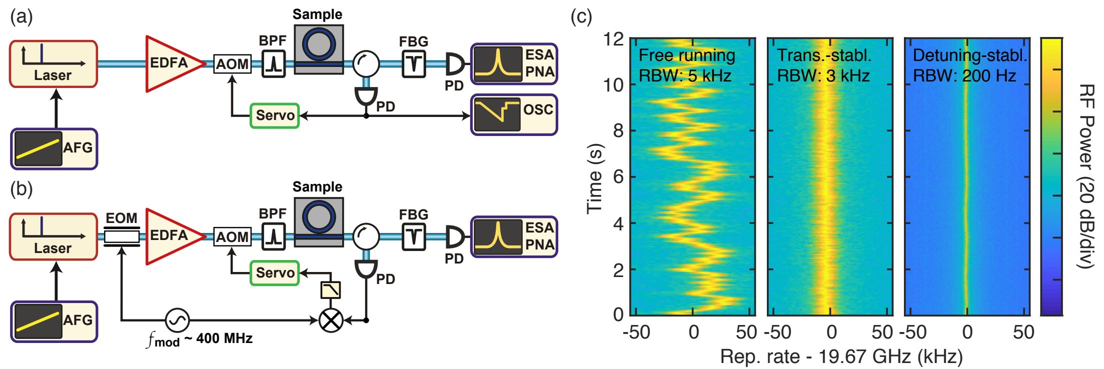

Figure 6.5 – Experimental setup for soliton stabilization, and spectrogram of the soliton repetition rate. (a) The experimental setup with auxiliary components for chip transmission stabilization. AOM: acousto-optic modulator. EDFA: erbium-doped fibre amplifier. AFG: arbitrary function generator. BPF: band-pass filter. FBG: fibre Bragg grating. OSA: optical spectrum analyzer. OSC: oscilloscope. PD: photodiode. ESA / PNA: electrical spectrum analyzer / phase noise analyzer. (b) Experimental setup with auxiliary components for offset PDH detuning stabilization. EOM: electro-optic modulator. (c) Spectrogram of the soliton repetition rate in the free-running state, with transmitted power stabilization, and with cavity-pump detuning stabilization. RBW: resolution bandwidth.

coefficient is on the same order of magnitude as the transduction expected from the conversion of intensity fluctuations to frequency fluctuation via the Kerr effect [354].

When the soliton is driven by the Toptica laser, as shown in the red curves in Fig. 6.4(b, d), the noise feature within 100 Hz – 10 kHz offset frequency is caused by the Toptica laser phase noise, while the step-like feature within 20 kHz – 1 MHz is caused by the FSW43 noise floor. In a different case, when the soliton is driven by a fibre laser (Koheras AdjustiK) featuring a lower phase noise level, the soliton phase noise is reduced as shown in the blue curve in Fig. 6.4(d). An additional PNA (Rohde & Schwarz FSUP, with cross-correlations) is used here, in order to overcome the FSW43 device limitation, which however results in the phase noise within 200 kHz – 10 MHz being marginally below the shot noise floor, likely caused by parasitic anti-correlation effects in FSUP[355]. The absolute single-sideband (SSB) phase noise power spectral density of the microwave carrier reaches ~ −80 dBc/Hz at 1 kHz offset Fourier frequency, ~ −110 dBc/Hz at 10 kHz and ~ −130 dBc/Hz at 100 kHz. Analysis shows that, when using the fibre laser, the main phase noise limitation is the laser RIN for offset frequencies < 1 MHz, with a contribution from the impact of the thermo-refractive noise (TRN) [173] in Si_3N_4 on the detuning within 10 – 100 kHz offset frequencies.

Laser technical noises: From the previous conversion estimations, the origins of the main noise limitations of the measured soliton repetition rate can be analyzed below. In the case with the Toptica diode laser, as shown in Fig. 6.7(a), the conversions of the laser phase noise and RIN show that the main limiting factor is the laser phase noise, using the previously determined coefficients. Furthermore, FSW43 without cross-correlations is used in this measurement, which limits the measurement precision of phase noise within 30 kHz – 1 MHz range. At high Fourier frequencies, the shot noise defines the white noise floor.

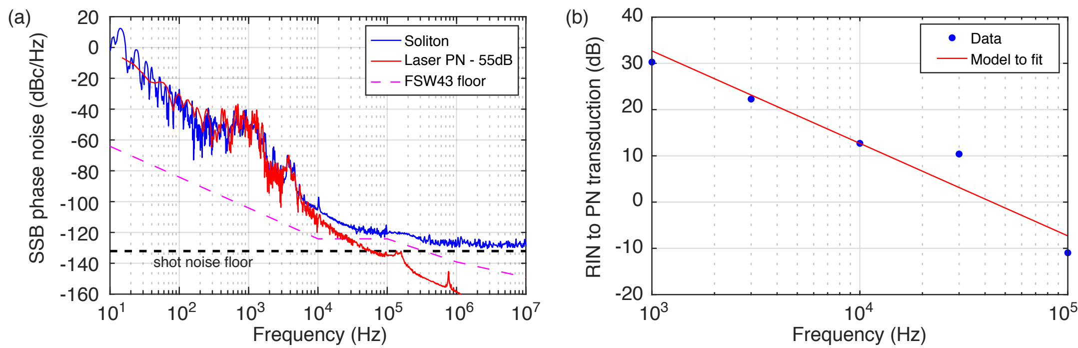

Figure 6.6 – Analysis of laser noise transduction. (a) Transduction of the laser phase noise to the microwave phase noise of the soliton repetition rate. The correlation between the optical phase noise of the Toptica laser (red) and the microwave phase noise of the soliton repetition rate (blue) yields an estimation for the PM2PM coefficient of −55 dB. (b) Transduction of the laser RIN into the phase noise of soliton repetition rate. Measured conversion of the pump relative intensity modulation to soliton phase modulation (dots). The red line shows the model $(\alpha/f)^2$ where $\alpha = 79$ Hz/mW.

The same analysis with Koheras fibre laser shows that the situation is reversed. As shown in Fig. 6.7(b), the Koheras laser RIN is the main source of phase noise limitation. This is to be expected as fibre lasers typically have lower phase noise than diode lasers. Furthermore, in this measurement, FSUP with cross-correlations is employed to measure the phase noise in the offset frequency range within 30 kHz – 1 MHz (10^5 cross-correlations applied), which alleviates the limitation of the PNA floor. However, this cross-correlation measurement also shows a noise floor that is below the expected shot noise level. This artefact is attributed to a potential correlation between amplitude and phase quadrature of the microwave noise which are known to produce artificially low results [355]. At high offset frequency with FSW43, our measurement verifies that the signal follows the white shot noise floor.

Microresonator thermo-refractive noise: Besides the laser technical noises, it is also important to consider the impact of the microresonator thermo-refractive noise (TRN) on the soliton phase noise. The fundamental thermal fluctuations within the optical mode volume of the microresonators lead to a refractive index fluctuation. This fluctuation leads to the fluctuation of the microresonator FSR [356, 173, 357], and thereby the resonance jitter (magnified by the mode index $m \approx 10^4$). The simulated resonance jitter plotted in the unit of dBc / Hz is shown in Fig. 6.8, using a simulation method described in ref. [173]. Here, two schemes leading

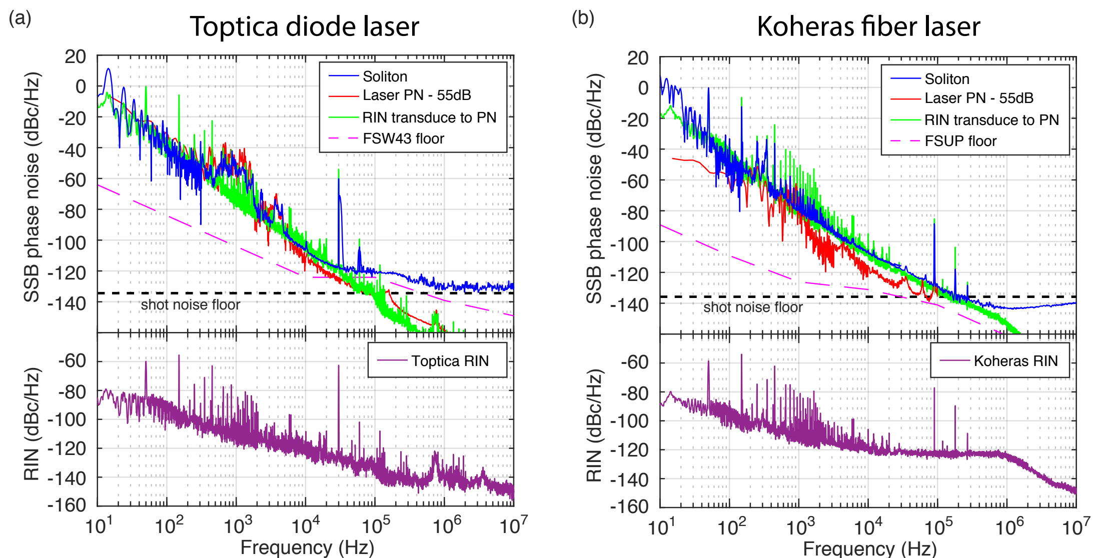

Figure 6.7 – Technical limitations of the soliton phase noise with the Toptica diode laser and the Koheras fibre laser. (a) The main source of phase noise limitation is the Toptica laser phase noise. The Toptica laser RIN is shown in the bottom panel and its transduction to soliton phase noise is plotted in the top panel (green). The Toptica RIN shows a modulation peak at 10 kHz, which is used to measure the transfer function in Fig. 6.6(b). The black dashed line shows the expected shot noise floor. (b) The main source of phase noise limitation is the Koheras laser RIN, as shown in the bottom panel. Its transduction to soliton phase noise is also plotted in the top panel (green), in comparison with the Koheras laser phase noise (red). The black dashed line shows the expected shot noise floor.

to two limits on soliton phase noise, caused by TRN, are discussed. The first scheme is the resonance jitter caused by TRN, which affects the soliton phase noise in a manner similar to the laser phase noise (i.e. fluctuation of the soliton detuning). As mentioned earlier, there is a transduction of ∼ –55 dB from optical detuning phase noise to the microwave phase noise of soliton repetition rate, to account for the PM2PM conversion. Note that the impact of this optical noise can be mitigated by operating at a quiet point (reduction of the PM2PM coefficient). The second scheme, which is fundamental, is the noise transduction limit given by the optical-to-microwave division. The division factor is calculated as $n = 193\text{THz}/19.6\text{GHz} \approx 10^4$, thus the phase noise reduction due to the optical-to-microwave division is $n^2 = 10^8$ (80 dB). The FSR fluctuations via the optical-to-microwave division set a fundamental limit to the soliton phase noise. For a microresonator of 20 GHz FSR, the resonance jitter induced by TRN, the TRN translated by –55 dB, and the TRN translated by – 80 dB, are compared in Fig. 6.8, together with the case of a microresonator of 12 GHz FSR. Based on the estimated noise for a 20-GHz-FSR microresonator, the estimated impact of TRN is shown in Fig. 6.9 together with the measured soliton phase noise. The fundamental fluctuation are much lower than the currently measured phase noise level that appear to be limited by the laser RIN at low frequencies and by the optical short noise at higher frequencies. Therefore, we believe that current soliton phase noise performance is mainly limited by the lasers used.

Quiet point operation: In addition, another solution to reduce the phase noise is to operate the soliton at a "quiet point". The phase noise measurements with different cavity-pump detunings are performed with stabilized transmitted power through the chip, as shown in Fig. 6.10. The detuning is measured using a vector network analyser (VNA) to probe the resonance frequency relative to the laser [58]. A "quiet point" [159], caused by mode crossings, is observed at the detuning of $\delta\omega/2\pi \sim 439$ MHz, and provides the best phase noise perfor-

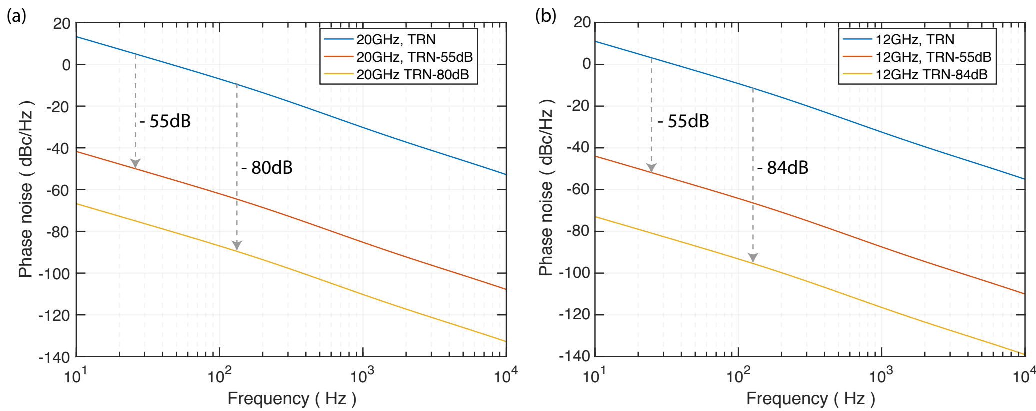

Figure 6.8 – Simulated resonance jitter induced by TRN, and the estimated impact of TRN on soliton phase noise. Here two microresonator FSRs are compared, i.e. 20 GHz (a) and 12 GHz (b). The estimated TRN limit on the soliton detuning (with –55 dB transduction) and the fundamental limit due to the optical-to-microwave division (with –80 dB transduction) are added. The TRN simulation method is presented in ref. [173].

mance compared with other detuning values. To evidence the phase noise reduction at the quiet point, the repetition rate shift and the phase noise value at 3.691 kHz Fourier offset frequency, where the laser phase noise exhibits a characteristic feature, are measured with different detunings, as shown in Fig. 6.10.

However, note that the quiet point may not be found in every (multi-)soliton state. Theoretically the presence of quiet points could be engineered. At the quiet point with the detuning $\delta\omega/2\pi \sim 439$ MHz, the Raman self-frequency-shift [87, 352], which is the soliton center frequency shift according to $\Omega_{\text{Raman}} = -32D_1^2\tau_R\delta\omega^2/15\kappa D_2$ (τ_R is the Raman shock term), is compensated by the recoil Ω_{Recoil} caused by a mode-crossing-induced dispersive wave [358], such that $\Omega(\delta\omega) = \Omega_{\text{Raman}}(\delta\omega) + \Omega_{\text{Recoil}}(\delta\omega) \approx 0$. The quiet point is reflected on the repetition rate stability since $2\pi f_{\text{rep}} = D_1 + D_2\Omega(\delta\omega)/D_1$. This point gives the best phase noise performance compared with other detuning values. However, we emphasize that a quiet point can be engineered via the third-order dispersion D_3 that skews the soliton spectrum and leads to a repetition rate shift with detuning [359], such that

$$
\begin{aligned}
2\pi f_{\text{rep}} = D_1 + D_2\frac{\Omega_{\text{Raman}}(\delta\omega)}{D_1} \\
+ \frac{D_3}{3}\left(\frac{\Omega_{\text{Raman}}(\delta\omega)}{D_1}\right)^2 + \frac{1}{3}\frac{D_3}{D_2}\delta\omega
\end{aligned}
\tag{6.2}
$$

Thus the dependence of the repetition rate f_{rep} on the detuning $\delta\omega$ could be mitigated over a broader bandwidth based on a more reliable effect (via D_3) than mode crossings.

Envisioned methods to reduce the soliton phase noise: In sum. there are several envisioned methods to reduce the soliton phase noise: 1. Operating the soliton at a quiet point, as dis-

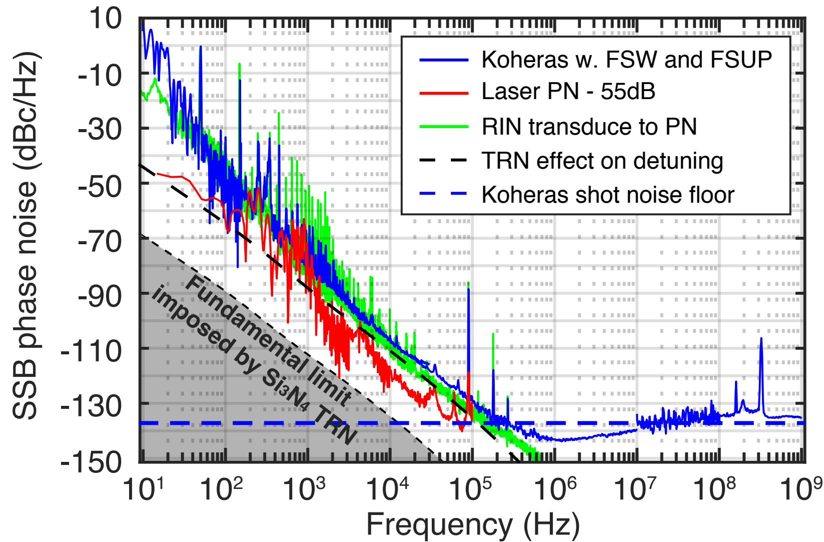

Figure 6.9 – Comparison of the TRN limit with the measured soliton phase noise of 20 GHz repetition rate.

cussed above, will reduce the optical-to-microwave phase noise transduction. 2. Using a fast actuator to tightly lock the resonance to the laser or vice versa, in order to eliminate the soliton detuning fluctuations. 3. A very nonlinear microresonator (i.e. high Kerr index and strong light confinement) yields a strong intensity-to-phase-noise transduction. Microresonators made of low-nonlinearity materials such as Hydex [197], or with large mode area such as concentric resonators [256], can be employed in order to reduce the effective nonlinearity, thus to reduce the transduction to soliton phase noise from laser RIN. In addition, large mode area can also reduce the photon-thermal noise. However, the lower nonlinearity also increases the threshold power for soliton generation, so here reaching high microresonator Q is of utmost importance. 4. The ultimate limit of soliton phase noise is posed by the TRN of the microresonator, which can be reduced by using microresonators made of athermal material. Note that an intrinsically athermal material might be difficult to find, however some material properties, such as photorefraction, can counteract thermal-optic effect, thus rendering the material effectively athermal. This effect has been recently employed to generate self-starting solitons in lithium niobate [65].

6.4 Soliton injection-locking

The low soliton repetition rate allows soliton injection-locking to an external microwave source [74], which can discipline the soliton repetition rate and improve the long-term soliton stability, which is key for applications requiring a stable and referenced comb line spacing. The modified experimental setup is shown in Fig. 6.11(a). A phase modulation is applied on the c.w. pump laser, with a swept frequency f_{inj} around 19.678 GHz, while the microwave spectrum evolution is recorded as shown in Fig. 6.4(b). The soliton injection-locking, i.e. synchronization of the soliton repetition rate f_{rep} to the modulation frequency f_{inj}, is observed when $|f_{rep} - f_{inj}| < 40$ kHz. This injection-locking range is more than a 100-fold increase compared to that measured in MgF_2 resonators (~ 300 Hz in ref. [74]), likely caused by the lower Q in

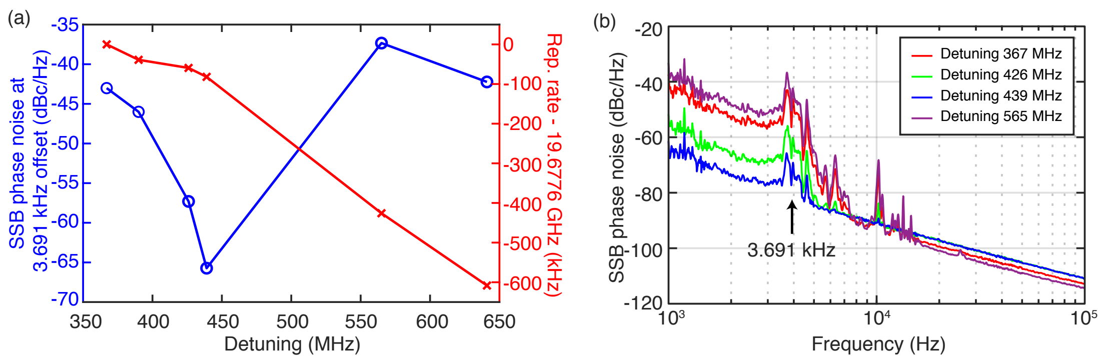

Figure 6.10 – Phase noise measured at the quiet point. (a) SSB phase noise at 3.691 kHz offset Fourier frequency and measured repetition rate shift with different cavity-pump detunings. (b) SSB phase noise measured at different cavity-pump detunings with power stabilization. A quiet point is observed at the detuning of ~ 439 MHz.

Si_3N_4. The phase noise spectra of the injection-locked soliton (blue), the microwave source used (black), and the soliton with a stabilized cavity-pump detuning (red), are compared in Fig. 6.4(c). The phase noise of the injection-locked soliton closely follows the microwave source's phase noise at offset frequency below 10 kHz, apart from a residual bump at 1 kHz which originates from the pump laser. For offset Fourier frequencies above 10 kHz, the soliton-induced spectral purification effect is revealed, as the soliton phase noise departs from the injected microwave phase noise, and becomes similar to the case with only active cavity-pump detuning stabilization.

6.5 Comparison of microwave oscillators

The demonstrated soliton microcombs above are promising building blocks for microwave photonic applications, such as low-noise microwave oscillators. Figure 6.12 compares our soliton-based microwave oscillators to other compact photonics-based microwave oscillators [360, 361, 362, 363, 200, 81] and a commercial dielectric resonator oscillator (DRO) based on GaN [364], as well as the limit imposed by TRN in Si_3N_4. The measured phase noise in our work is still 30 dB higher than the fundamental limit, revealing the considerable potential for further phase noise reduction, which can be accessed by using lasers with suppressed phase noise and RIN, and microresonators of higher Q. It is worth to mention that, compared with commercial DROs, soliton-based microwave oscillators already show competitive phase noise performance. In addition, though DRO is currently a mature technology for low-noise

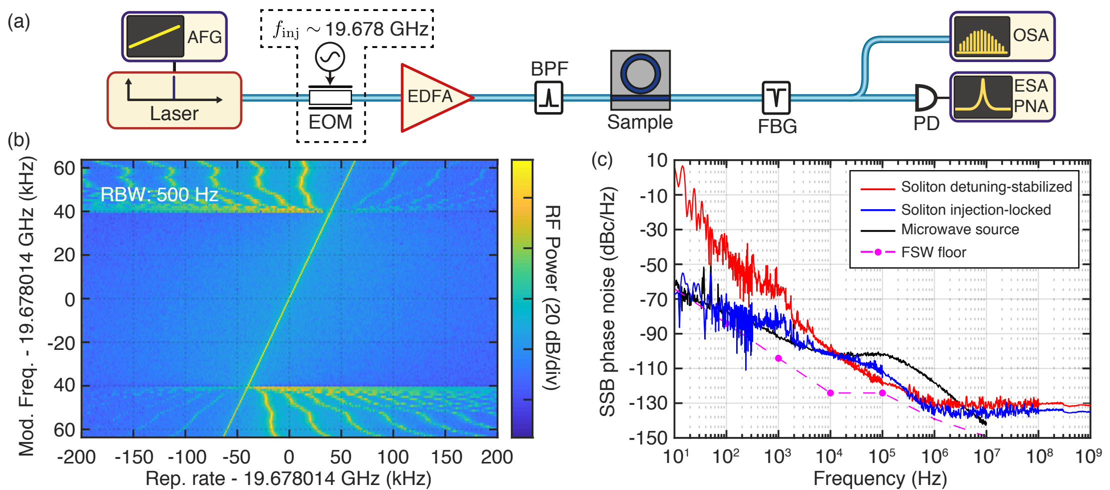

Figure 6.11 – Soliton injection-locking to an external microwave source. (a) Experimental setup for soliton injection-locking. EOM: electro-optic modulator. (b) Microwave spectrum evolution showing the injection locking of the soliton repetition rate f_{rep} with the modulation frequency f_{inj} on the c.w. pump, when $|f_{\text{rep}} - f_{\text{inj}}| < 40$ kHz. (c) SSB phase noise spectrum comparison of the injection-locked soliton, the microwave source used to discipline the soliton, and the soliton with a stabilized cavity-pump detuning. The soliton spectral purification effect is revealed above 10 kHz offset Fourier frequency.

microwave synthesis up to 40 GHz, which is challenging to achieve using other integrated electronics-based technology such as surface and bulk acoustic wave resonators that typically work at few GHz frequency, it is well known that the quality factor of the DRO decreases with higher operation frequency, resulting in compromised phase noise performance. On the contrary, soliton-based microwave oscillators have more advantages working at higher microwave frequency (i.e. repetition rate), and could achieve better phase noise performance than DROs. Moreover, soliton combs are coherent multi-carrier optical sources, where the microwave signal is naturally encoded into optical carriers, thus allow distributing the microwave signal directly via optical fibres. Therefore, integrated soliton microcombs with microwave repetition rates represent a critical step towards fully integrated soliton-based low-noise microwave oscillators for future architectures of radars and information processing networks, fostering wide deployment of these technologies in our information society.

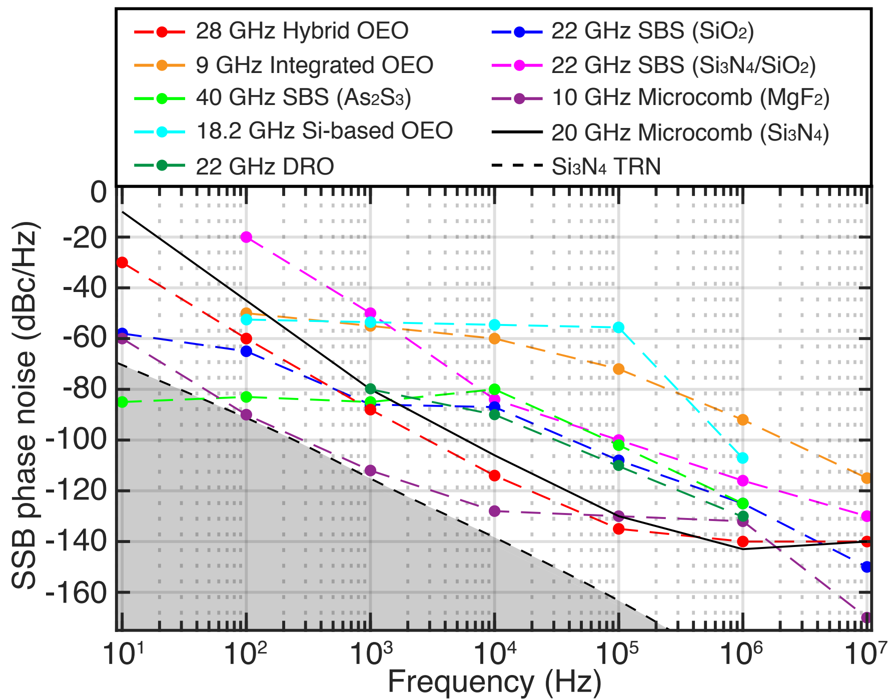

Figure 6.12 – Comparison of demonstrated compact photonics-based microwave oscillators. 28 GHz hybrid optoelectronic oscillators (OEO) (OEwaves HI-Q^{TM} Nano-OEO), 9 GHz integrated OEO [360], 40 GHz OEO using stimulated Brillouin scattering (SBS) in As_2S_3 chalcogenide [361], 18.2 GHz silicon-based OEO [362], 22 GHz DRO (Microwave Dynamics DRO-1500), 22 GHz SBS in SiO_2 [363], 22 GHz SBS in Si_3N_4 / SiO_2 [200], 10 GHz microcomb in MgF_2 [81], and 20 GHz microcomb in Si_3N_4 (this work). The region below the fundamental limit imposed by TRN in Si_3N_4 [173] (dashed black) is grey-shaded.

6.6 Fully packaged device: DARPA DODOS deliverable

The microwave-repetition-rate Si_3N_4 soliton microcomb chip devices described above have been used in DARPA **DODOS** project, a joint effort together with Caltech, UCSB and EPFL, aiming to build fully packaged soliton microcomb modules. The main result has been published in ref. [69], B. Shen, L. Chang, J. Liu et al, "**Integrated turnkey soliton microcombs**", *Nature* (2020). I designed and fabricated all the Si_3N_4 chip devices used in this work, and led the Si_3N_4 sample characterization, with the assistance from Rui Ning Wang, Jijun He and Tianyi Liu. UCSB team led the device packaging and project coordination. Caltech team performed the experiment and developed the theoretical model. This joint collaboration work will be described in this section.

A packaged module contains a Si_3N_4 chip, a DFB laser chip, and a butterfly package with a fibre output and a temperature / mechanics stabilization mount. The Si_3N_4 chips, fabricated using the photonic Damascene process at EPFL by me and Rui Ning Wang, have Q factors above 15×10^6 and FSRs of 15, 20, and 40 GHz. The DFB laser chip, fabricated by **Freedom Photonics**, has high-reflection coatings at the backside facet and anti-reflection coatings at the front side facet, and a total output power of 120 mW. The DFB laser chip was re-packaged and assembled at UCSB. The DFB laser chip is butt-coupled to the Si_3N_4 chip, with an overall coupling loss of 6 dB (i.e. 30 mW pump power in Si_3N_4 waveguide). Both chips are mounted in the butterfly package, thus the entire device is very compact, as shown in Fig. 6.13.

The soliton generation experiment was performed at Caltech. The soliton generation employs laser self-injection locking, described in the previous chapter. Thanks to the lases self-injection locking and high Q of Si_3N_4 microresonators, it is observed that the laser frequency noise is reduced by ~ 30 dB compared with that of a free-running DFB laser. Moreover, the entire soliton microcomb package allows **turnkey** operation, i.e. deterministic soliton formation by simple power-on of the pump laser. Once generated, the soliton maintains for hours without any active feedback control. Simulations of the injection locking dynamics suggest that the feedback phase (i.e. the phase difference between the laser emission light and the reflected light from the microresonator) and the pump laser power (above a certain threshold) are the two most critical parameters which determine if the entire system enables turnkey operation. The effective pump laser power can be increased by improving the mode match between the DFB output mode and the Si_3N_4 inverse taper coupler mode. The feedback phase can be varied by changing the gap distance between the DFB laser chip and the Si_3N_4 chip, or including a phase shifter (e.g. metallic heaters) on the waveguide between the butt-coupled facet and the Si_3N_4 microresonator which allows to finely tune the optical path length. This new regime of turnkey soliton generation via laser self-injection locking significantly simplifies the soliton generation complexity, and also reduces the frequency noise of the pump laser which could in turn reduce the phase noise of the soliton repetition rate, critical for soliton-based microwave synthesis.

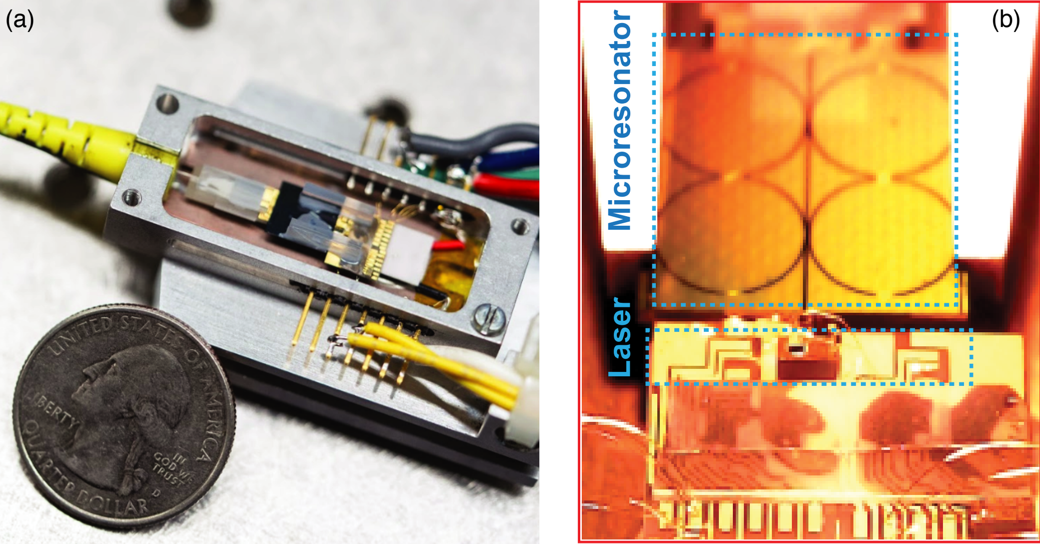

Figure 6.13 – Fully packaged soliton microcomb module containing a Si_3N_4 chip and a DFB laser chip in a butterfly package with a fibre output. (a) Photo of the packaged module. (b) Magnified photo image showing the butt-coupling between the Si_3N_4 chip and the DFB laser chip. This figure is taken from ref. [69].

7 Monolithic Piezoelectric Control of Soliton Microcombs

For many metrology applications of laser frequency combs, the capability to achieve high-speed actuation of comb teeth, as well as the repetition rate, is critical [2]. For example, locking combs to microwave standards is key in optical frequency synthesis [365]. Phase-locking of combs to stable reference cavities is also central for low-noise microwave generation via optical frequency division [9]. Optical clocks require frequency combs to be locked to atomic transitions [366], and higher-bandwidth actuators are needed to keep pace with the improvement in clock fractional frequency uncertainty [5]. Frequency combs based on mode-locked lasers have established elaborate techniques for wideband frequency actuation, typically realized using bulk phase or amplitude modulators within the laser cavity. In contrast, measurement-based high-speed feedback stabilization of chip-based microcombs is currently only achieved with off-chip bulk modulators that actuate on the pump laser. Therefore, high-speed actuators on-chip are highly desirable for integrated soliton microcombs. While integrated piezoelectric modulators on Si_3N_4 waveguides have been demonstrated [115], they have not yet been used to initiate or control microcombs. Other modulators integrated with Si_3N_4, e.g. based on the electro-absorption of graphene [189, 190, 367, 368] and ferroelectric lead-zirconate-titanate (PZT) [192, 193, 194], have not yet demonstrated compatibility with soliton generation which requires maintaining ultralow optical losses in Si_3N_4 waveguides. As a result, current integrated actuation techniques for soliton microcombs rely primarily on metallic heaters [97, 54], which have limited actuation bandwidth up to 10 kHz. In addition, heaters exhibit uni-directional tuning, and typically consume electrical power exceeding 30 mW [101], higher than the threshold optical power for soliton formation in state-of-the-art integrated devices [101, 170], and are not compatible with cryogenic operation [369, 115]. Alternatively, the direct generation of solitons in Pockels materials such as AlN [370, 371, 104, 103] and $LiNbO_3$ [107, 65, 106] would allow high-speed actuation, however these platforms are not yet as mature as Si_3N_4.

In this chapter, integrated piezoelectric modulators to actuate soliton microcombs are demonstrated, which overcome these limitations. These piezoelectric modulators are based on aluminium nitride (AlN), a commercial micro-electro-mechanical-systems (MEMS) technique

to build microwave filters in modern cellular phone technology [372]. It is shown that the piezoelectric control employing the stress-optic effect [373] allows deterministic soliton initiation, switching, tuning, long-term stabilization, and phase locking with 0.6 MHz bandwidth. These integrated piezoelectric actuators that are linear, fast, non-absorptive, bi-directional, and consume ultralow electric power endow integrated soliton microcombs with novel capability in power-critical applications e.g. in space, data centres and portable atomic clocks, in extreme environment such as cryogenic temperatures, or in emerging applications for coherent LiDAR [158, 137], frequency synthesizers [138] and RF photonics [348, 349].

The main result of this chapter has been published in ref. [178], J. Liu et al, "**Monolithic piezoelectric control of soliton microcombs**", *Nature* (2020). Multiple people have contributed significantly to this result, particularly Hao Tian and Sunil A. Bhave who developed and performed the AlN process; Erwan Lucas, Arslan S. Raja and Grigory Lihachev who lead the experiments on soliton locking and LiDAR.

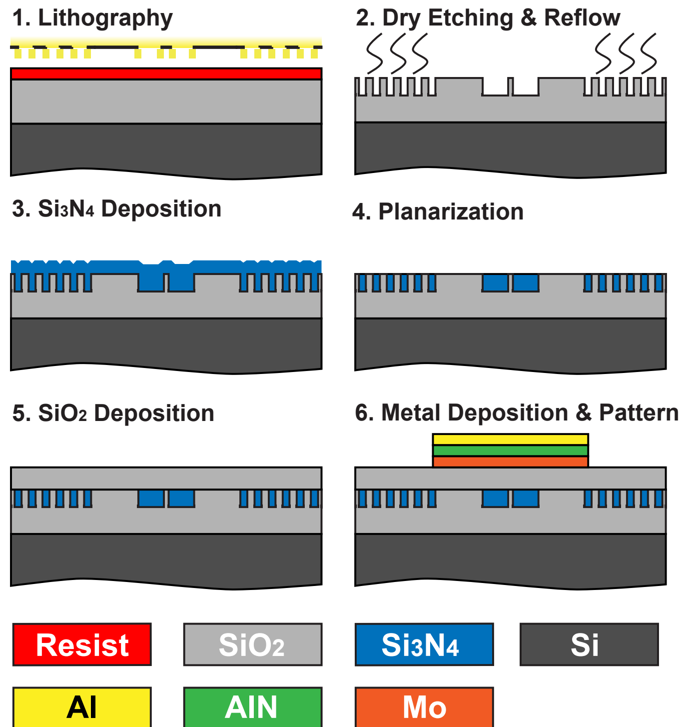

Figure 7.1 – Process flow of hybrid Si_3N_4-AlN photonic circuits and actuators.

7.1 Integrated Aluminium Nitride Actuators on Silicon Nitride Circuits

Reliable and fast resonance tuning of Si_3N_4 microresonators is an important asset and requirement for multiple applications in integrated photonics. However, due to the lack of Pockels nonlinearity in Si_3N_4 (which is amorphous), electro-optic modulation of the refractive index of Si_3N_4 is challenging. In contrast to silicon, Si_3N_4 requires heterogeneous or hybrid integration with other materials to achieve active tuning or modulation. Metallic heaters employing thermo-optic effect is widely used to realize Si_3N_4 microresonator tuning [97, 54], which however presents low tuning speed (< 10 kHz), high power consumption (> 10 mW), and thermal cross-talk. Other methods using materials e.g. graphene [189, 190, 367, 368] and PZT [192, 193, 194] are still facing challenges related to CMOS-compatibility, fabrication complexity, and optical losses. To fully utilize the maturity and advantages of ultralow-loss Si_3N_4 photonics, new tuning mechanisms which retain the original optical properties are needed.

The stress-optical effect, discovered over a hundred years ago, has recently gained attention for its role in the modulation of Si_3N_4 waveguides and microring resonators both theoretically [374, 373] and experimentally [192, 194], thanks to the advances in micro-electro-mechanical-systems (MEMS) [375]. Here, by integrating AlN piezoelectric actuators on top of Si_3N_4 photonic circuits, integrated acousto-optic modulation of Si_3N_4 microresonators is presented Aluminium nitride [376], a commercial MEMS technology to build microwave filters in modern cellular phone technology [372] and aeroacoustic microphones [377], forms the main piezoelectric material to realize such acousto-optic modulation. Driving the AlN actuator harmonically at a microwave frequency, fast and efficient acousto-optic modulation is realized by exciting high-overtone bulk acoustic wave resonances (HBAR) in the substrate stack. The AlN actuators feature linear and bi-directional tuning, free from hysteresis, and operated at ultralow electrical power. Therefore, this novel capability is important for tuning and stabilization of soliton microcombs, and may allow soliton injection locking for stabilization and microwave synthesis [71, 74].

Figure 7.1 shows the fabrication process flow of hybrid Si_3N_4-AlN photonic circuits and actuators. The AlN actuators are monolithically integrated on ultralow-loss Si_3N_4 waveguides. In order to preserve the ultralow waveguide loss, thick SiO_2 top cladding is deposited on the Si_3N_4 waveguides, before the piezoelectric actuators are deposited and patterned. The piezoelectric actuators are made from polycrystalline AlN as the main piezoelectric material, molybdenum (Mo) as the bottom electrode (ground) and the substrate to grow polycrystalline AlN, and aluminium (Al) as the top electrode. The polycrystalline AlN has a piezoelectric coefficient [378] $C_{33} \sim 1.55$ C/m^2, and Mo is chosen in order to minimize the acoustic impedance with AlN [379] compared to gold or titanium. Using physical vapour deposition (PVD), 100 nm Mo and 1 μm polycrystalline AlN films are sputtered on the substrate through foundry services (commercial service via *OEM Group*). To pattern the actuators, this process is performed at Birck Nanotechnology Center at Purdue University by Hao Tian. The AlN actuator is patterned

by AZ1518 photoresist, and dry etched using Cl_2 and BCl_3 in a Panasonic E620 Etcher. The dry etching of the bottom electrode (Mo) is performed using Cl_2 in the same Panasonic E620 Etcher. Finally, the top 100 nm Al is evaporated by a PVD electron-beam evaporator, and patterned using a standard lift-off process. Afterwards, the entire wafer is diced into individual chips using the standard chip release process.

When a vertical electric field is applied, i.e. voltage applied between Al and Mo electrode, the piezoelectric AlN is deformed and generate stress beneath the AlN, where the Si_3N_4 waveguide sits. As shown in Fig. 7.2(a, b), a disk-shaped actuator is placed on top of the Si_3N_4 microresonator. The AlN actuator is slightly larger than the Si_3N_4 microresonator. The Si_3N_4 waveguide is positioned 3 μm to the inner edge of the AlN disk actuator. The bus-waveguide-to-microresonator coupling region is opened, in order to prevent any actuation-induced perturbation of light coupling (however, the impact might be very negligible). Figure 7.2(b) shows the microscope image of the fabricated $_3N_4$ microresonator covered by an AlN disk actuator. Figure 7.2(c) shows the SEM image of the sample cross-section, including the optical mode in the Si_3N_4 waveguide.

7.1.1 Stress-optic tuning

The stress-optic tuning [374] of the microresonator resonances in the fundamental transverse-electric mode (TE_{00}) is characterized first. The experimental setup to characterize the reso-

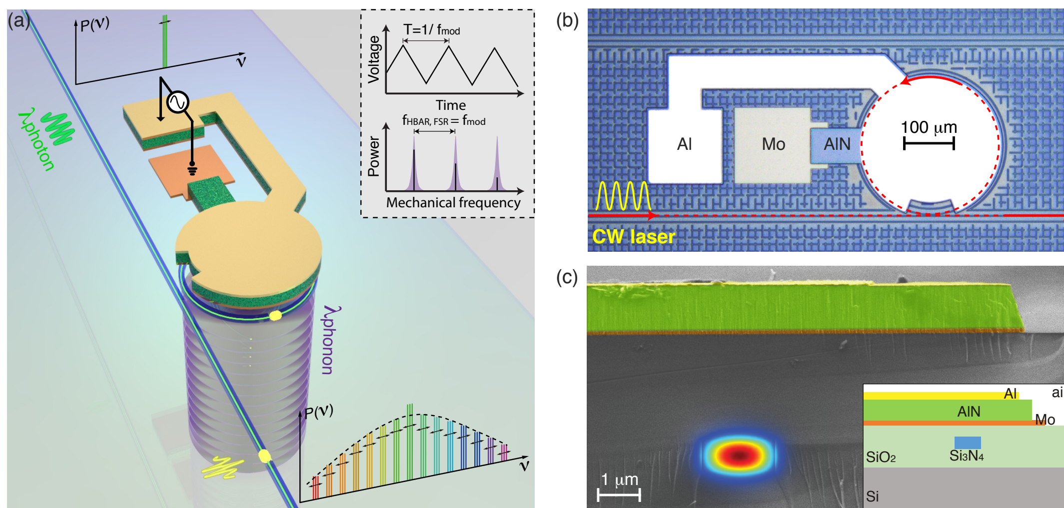

Figure 7.2 – Design and fabrication of integrated Si_3N_4 microresonators with AlN actuators. (a) Schematic of using the piezoelectric AlN to actuate the light (or soliton microcomb), via either stress-optic effect or HBAR modes. (b) Microscope image of the sample with a disk-shape AlN actuator. (c) False-coloured SEM image of the sample cross-section, including the optical mode in the Si_3N_4 waveguide. Inset: Schematic of the materials and layers shown in the SEM image.

nance frequency tuning versus voltage applied on the AlN actuator is shown in Fig. 7.3(d). A tunable laser (Toptica CTL) is locked to a S_3N_4 microresonator resonance, via a PDH lock loop using an EOM. When the resonance is tuned by varying the applied voltage, the laser frequency follows the resonance shift. The beat signal between the laser locked to the resonance and a reference laser (another Toptica CTL) is measured using a fast photodiode and an electrical spectrum analyzer (ESA). A programmable DC power supply (Keithley 2400) is used to apply the voltage on the AlN actuator. A ramp signal is applied on the power supply in order to output the voltage between ±140 V with a voltage increment / decrement of 2.8 V. The interval time between two subsequent measurements is 200 ms. The change in the two lasers' beatnote signal recorded by the ESA corresponds to the resonance frequency shift, as one laser is locked to the resonance and the other is frequency-fixed. These measurements are repeated continuously for multiple (3 to 5) scans between ±140 V in order to confirm the tuning hysteresis.

Figure 7.3(a) shows the low-speed (DC) tuning curve, i.e. resonance frequency shift versus the applied voltage up to ±140 V, of a TE_{00} resonance at 1556 nm. The average linear tuning coefficient at DC is $\delta\nu/\delta V$ = 15.7 MHz/V. Note that, this resonance tuning is *bi-directional*, in contrast to the uni-direction thermal tuning using heaters. A weak hysteresis is observed when cycling the voltage between ±140 V. While crystalline AlN is non-ferroelectric, such hysteresis is commonly caused by the trapped charges accumulated at AlN interfaces or combined with bulk defects [380]. Since the AlN actuator is capacitive, the operation current at high voltage is measured to be less than 2 nA, corresponding to less than 300 nW power consumption at

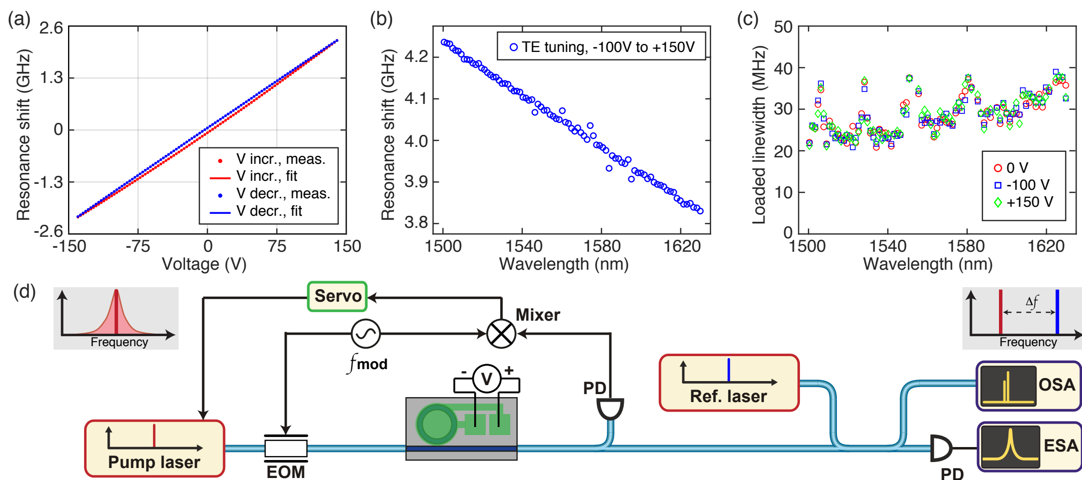

Figure 7.3 – Characterization of stress-optic tuning. (a) Resonance shift versus applied voltage. The linear tuning coefficient at DC is $\delta\nu/\delta V$ = 15.7 MHz/V. A weak hysteresis is observed. (b) Resonance shift for all TE_{00} resonances in the wavelength range from 1500 nm to 1630 nm, when the applied voltage changes from −100 V to +150 V. The wavelength-dependent tuning results from ~ 5 MHz change of microresonator FSR. (c) Comparison of loaded linewidths with different applied voltages. No voltage-dependent linewidth change is observed. (d) Experimental setup to characterize the resonance tuning versus voltage applied.

150 V voltage. The calculated capacity based on the device geometry is 3.3 pF, corresponding to stored energy of 37 nJ at 150 V voltage. Therefore, the main power consumption comes from the leakage current, likely caused by the defects and free charge carriers in polycrystalline AlN.

Figure 7.3(b) shows the frequency tuning for all TE_{00} resonances in the wavelength range from 1500 nm to 1630 nm, calibrated using frequency-comb-assisted diode laser spectroscopy. The wavelength-dependent tuning rate results from a change of the microresonator FSR (~ 5 MHz of 191 GHz FSR). Figure 7.3(c) compares the measured loaded linewidths with different applied voltages. The resonances remain critically coupled, and no linewidth change is observed when varying the voltage. The estimated intrinsic quality factor, $Q_0 > 15 \times 10^6$, with integrated AlN actuators is identical to bare microresonators without AlN [91], demonstrating that the monolithically integrated AlN actuators are compatible with ultralow-loss Si_3N_4 waveguide platform (linear optical loss of ~ 1 dB/m).

7.1.2 High-overtone bulk acoustic wave resonances

When the AlN actuator is driven harmonically, vibration of the actuator launches acoustic waves vertically into the substrate, as shown in Fig. 7.2(a). Since the bottom (backside) surface of the substrate (i.e. the interface between Si and air) is smooth and flat, the acoustic wave is reflected and subsequently bounce back and forth between the top and bottom device surfaces (frontside and backside). Therefore, the entire substrate works as an acoustic Fabry-Pérot (FP) cavity, and can lead to the formation of standing-wave acoustic waves if the acoustic cavity length (i.e. the substrate thickness) is an integer number of the acoustic wavelength. In this case, the acoustic energy is coherently built up inside the acoustic FP cavity. These bulk acoustic standing waves, also called as "**high-overtone bulk acoustic resonator (HBAR) mode**", further enhance the stress field around the Si_3N_4 waveguides, and allows to modulate the effective refractive index through stress-optical effect.

The following experimental characterization of HBAR modes was performed by Hao Tian in the group of Sunil A. Bhave at Purdue University. The electromechanical reflection parameter S_{11}, describing the conversion from the electrical signal to acoustic waves is shown in Fig. 7.4(a). A series of resonance dips is evenly distributed over multiple octaves in the microwave domain. A spectrum zoom-in is illustrated in Fig. 7.4(d), highlighting the mechanical resonance shape, linewidth of ~3 MHz, and acoustic FSR of around 17.5 MHz. The narrow linewidth demonstrates a mechanical Q of ~1000, which is mainly limited by the intrinsic acoustic loss in the substrate and phonon scattering at material interfaces. Meanwhile, the envelope of these sharp resonances varies slowly and smoothly with a period of ~ 490 MHz. This is caused by the resonances inside the 5.4-μm-thick SiO_2 cladding, which form from the acoustic wave reflection at the Si-SiO_2 interface due to the acoustic impedance mismatch. The SiO_2 resonances are located at the node of the envelope, whereas the anti-resonances are located at the anti-node. At the frequency of anti-resonances of the SiO_2 layer, the SiO_2-Si interface works as an acoustic anti-reflection coating, such that the acoustic power transmission into

the Si substrate is maximum. This situation corresponds to the maximum acoustic impedance, and thus maximum electromechanical power conversion. When the acoustic wave's half wavelength matches the 1 μm AlN thickness, the fundamental acoustic resonance mode of the AlN layer is excited. In this case, acoustic waves of 4 – 4.3 GHz frequency is efficiently excited. Note that, by varying the AlN and SiO_2 thickness, the resonances of these two acoustic cavities can be misaligned to engineer the acoustic wave excitation.

The S_{21} measurement describes the acousto-optic modulation (transduction). By setting the input laser frequency at the slope of the optical resonance, the output laser intensity is modulated. The S_{21} measurement is performed for both the TE and TM fundamental mode resonance, as shown in Fig. 7.4(b, c). Again, periodic peaks in S_{21} are observed, corresponding to each HBAR mode.

An simulated bulk acoustic mode is shown in Fig. 7.4(h). The acoustic standing wave distributes uniformly over the entire substrate, revealing that the Si_3N_4 photonic circuits can be buried deeply inside the SiO_2 cladding. This enables the photonic circuits to be free from the trade-off between the actuation efficiency and the absorption losses caused by the metal above. Meanwhile, with microwave frequencies, the acoustic wavelength comparable to the optical wavelength and the waveguide cross-section size is achieved in macroscopic actuators. It can be seen from Fig. 7.4(h) that the acoustic mode is mainly confined beneath the actuator

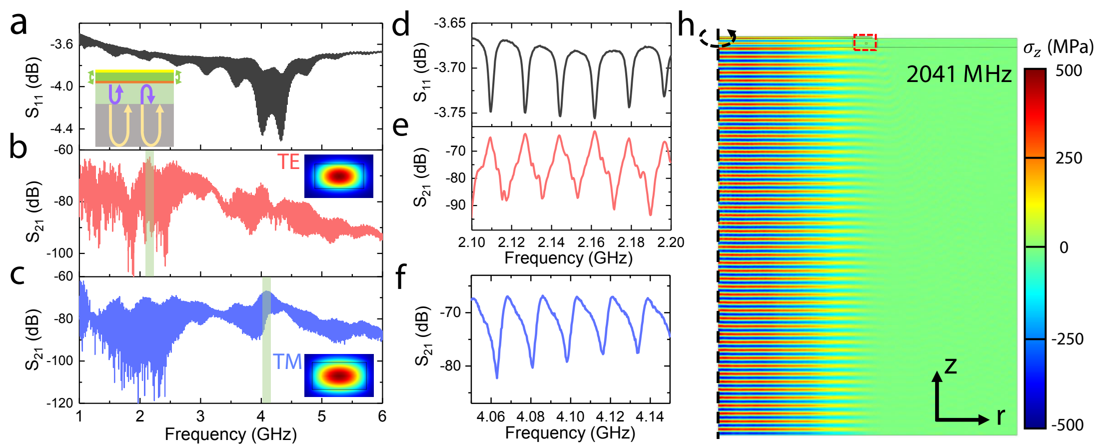

Figure 7.4 – Electro-mechanical-optic transduction in the microwave domain. (a) Electromechanical S_{11} spectrum from 1 to 6 GHz. The inset schematic illustrates the acoustic wave reflection at material interfaces. (b, c) Optomechanical S_{21} responses of TE and TM modes. Due to the different optical mode profiles (insets) and thus the acousto-optic mode overlap, TE and TM modes show different S_{21} spectra. (d) The zoom-in of S_{11} (e) The zoom in of TE mode's S_{21} within the green-shaded area in (b) around 2 GHz. (f) The zoom-in of TM mode's S_{21} within the green-shaded area in (c) around 4 GHz. The resonances distribute evenly with an FSR of 17.5 MHz in (a-f). (h) Numerical simulation of vertical stress σ_z distribution for one typical acoustic resonant mode at 2.041 GHz under 1 V driving voltage. **Note**: This figure is adapted from ref. [116].

which reduces electromechanical cross-talk between adjacent devices.

7.2 Monolithic piezoelectric control of soliton microcombs

For many applications of frequency combs, such as optical frequency synthesis [13], frequency division [9], and dual-comb spectroscopy [381], the capability to achieve megahertz-bandwidth actuation of comb teeth, as well as the repetition rate, is critical. In contrast to femtosecond laser frequency combs which have developed a wide range of fast actuators within the laser cavity, measurement-based feedback stabilization of photonic chip-based microcombs still relies on off-chip, bulk acousto-optic modulators (AOM) or electro-optic modulators (EOM) that actuate on the pump laser. Therefore, high-speed actuators integrated on chip are highly desirable for microcombs. While integrated modulators on Si_3N_4 waveguides have been demonstrated, e.g. based on the electro-absorption of graphene [189, 190, 368] and ferroelectric lead-zirconate-titanate (PZT) [192, 193, 194], these methods are not well suited for integrated microcomb applications. Graphene-based actuators are not compatible with wafer-scale manufacture using foundry process, and ferroelectric PZT actuators exhibit tuning hysteresis which poses challenges for soliton initiation and switching. Importantly, these methods have not yet demonstrated compatibility with soliton generation, which requires maintaining ultralow optical losses in Si_3N_4 waveguides. Therefore, current integrated actuation techniques for soliton microcombs rely primarily on metallic heaters [97, 54], which have only kilohertz actuation bandwidth, limited by the thermal relaxation time. In addition, heaters exhibit uni-directional tuning, and typically consume electrical power exceeding 30 mW [101], higher than the threshold optical power for soliton formation in state-of-art integrated devices [101, 170, 69] and not compatible with cryogenic operation [369, 115].

The integrated AlN piezoelectric actuators described in the previous section can overcome these limitations. In this section, the piezoelectric control employing the stress-optic effect [374, 373] is presented, which allows deterministic soliton initiation, switching, tuning, long-term stabilization, and phase locking with ~ 0.6 MHz bandwidth. Such integrated piezoelectric actuators that are linear, fast, non-absorptive, bi-directional, and consume ultralow electric power endow integrated Si_3N_4 soliton microcombs with novel capability.

7.2.1 Voltage-controlled soliton microcombs

A c.w. laser is coupled into the microresonator, and soliton is initiated by strain-tuning the resonance to the laser [97] via varying the voltage, using the setup shown in Fig. 7.5(a). The laser is initially set blue-detuned by 1 GHz from a microresonator resonance, and launches 15 mW power into the waveguide (60% coupling efficiency per chip facet). A typical soliton step of millisecond duration is shown in Fig. 7.5(b). Though not required for soliton initiation, the resonance-laser detuning is monitored using an EOM and a vector network analyser (VNA) [58]. As shown in Fig. 7.5(c), the resonance is initially tuned to the laser (0 V→71 V), and subsequently generates modulation instability (MI, 81 V) and a multi-soliton state (MS, 85 V). Next, the AlN voltage is reduced such that the backward tuning enables switching [58] to the single soliton state (SS, 79 V). The voltage is increased again (90 V) to increase the soliton

bandwidth. Figure 7.5(d) shows different soliton states with different applied voltages.

The voltage-controlled AlN actuator can be used to implement feedback and eliminate detuning fluctuations over a long term. The experimental setup to stabilize the soliton microcomb over 5 hours is shown in Fig. 7.5(f). A feedback loop is applied in order to fix the soliton detuning at 317 MHz and eliminate the detuning fluctuation over a long term. The VNA is used only to monitor the soliton detuning over a long term. The final soliton loss after 5 hours

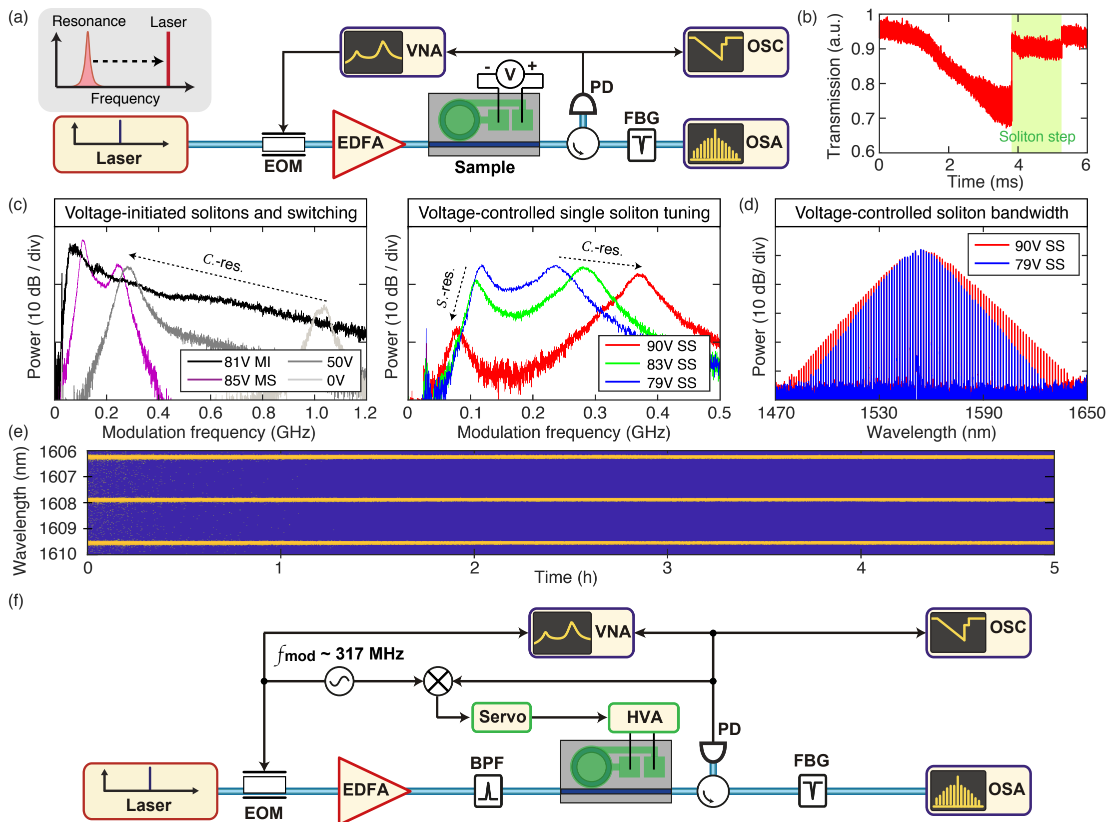

Figure 7.5 – Experimental demonstration of soliton control via AlN actuation. (a) Experimental setup. OSC: oscilloscope. FBG: Fibre Bragg grating. Inset: the soliton initiation employed here is to tune the resonance from the red detuning to the blue detuning of the fixed laser frequency. (b) A typical soliton step featuring millisecond length. (c) Soliton detuning control via AlN actuation. Left: Initially the resonance is 1 GHz blue-detuned from the laser (0 V). The resonance is tuned to the laser, and generate modulation instability (MI, 81 V) and a multi-soliton state (MS, 85 V). Right: Once the multi-soliton is generated (85 V), the voltage is reduced to switch to a single soliton state (SS, 79 V). The soliton detuning, as well as the bandwidth, is further increased via increasing the voltage (90 V). *S*-res.: Soliton resonance. *C*-res.: Cavity resonance. (d) Different soliton states with different applied voltage. (e) Soliton stabilization over 5 hour, realized by locking the resonance to the laser and maintaining the soliton detuning. (f) Experimental setup for long-term stabilization of the soliton microcomb. HVA: high voltage amplifier. BPF: bandpass filter.

is caused by the drift of the fibre-chip coupling using suspended lensed fibres, and can be mitigated via gluing the fibres to the chip [353]. Figure 7.5(e) shows the evolution of three soliton comb lines over 5 hours.

As seen from the previous section, the resonance tuning via stress-optic effect achieves 1 GHz range with more than 60 V applied voltage. Assuming that initially the laser and the resonance have the same frequency, for soliton initiation, soliton detuning of $\sim 20\kappa/2\pi$ is needed to access the soliton regime. This means that, the resonance linewidth $\kappa_2\pi$ must be below 50 MHz in the case of critical coupling, i.e. the intrinsic loss $\kappa_0/2\pi$ must be below 25 MHz. Therefore, it is worth to emphasize that, the key reason why the piezoelectric AlN actuator can be used to initiate solitons with our Si_3N_4 integrated photonics is due to the ultralow loss (i.e. high microresonator Q) of our Si_3N_4 waveguides.

7.2.2 Fast soliton actuation and locking

Next, fast modulation of the microresonator using the AlN actuation is shown. Such an actuation can be utilized to stabilize the soliton repetition rate. Figure 7.6(a) shows the experimental setup to characterize the frequency transduction $S_{21}(\omega)$ from the electrical to the optical domain. As shown in Fig. 7.6(d), the measured $S_{21}(\omega)$ has multiple peaks extending from 200 kHz, which correspond to different mechanical modes of the photonic chip, excited by the AlN actuator. The mechanical modes with frequency from 246 kHz to $\sim$ 17 MHz are contour modes [382] of the entire chip. Figure 7.6(b) shows the simulated contour modes around 246 kHz, using finite element modelling based on the actual chip size of 4.96×4.96 mm^2. These contour modes only exist with free boundary conditions. The broad peak at $\sim$ 17 MHz is the fundamental HBAR mode, confined vertically over the chip thickness

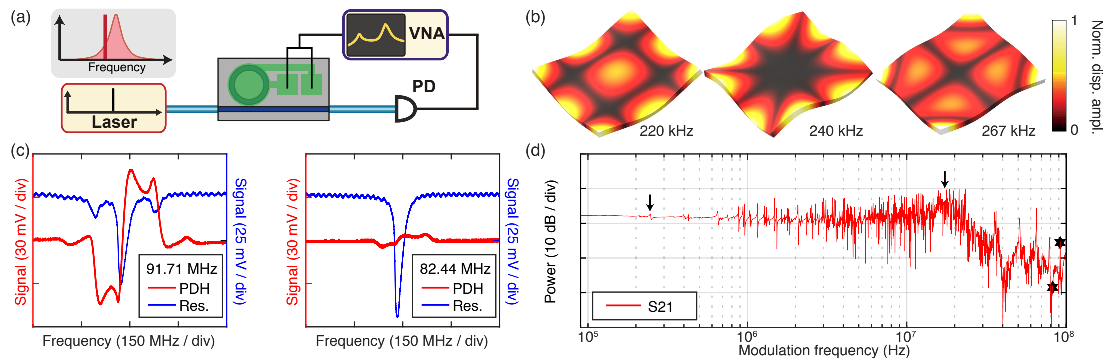

Figure 7.6 – High-speed piezoelectric actuation for on-chip PDH error signal generation. (a) Experimental setup to measure $S_{21}(\omega)$. The laser frequency is set on the resonance slope. (b) Simulated contour modes of the photonic chip starting from 220 kHz. The color represents the displacement amplitude. (c) Generated PDH error signals when modulating the AlN at 91.71 and 82.44 MHz, marked with stars in (d). (d) Electrical to optical signal transduction $S_{21}(\omega)$ of the AlN actuator. Arrows mark the contour mode at 246 kHz and the fundamental HBAR mode at $\sim$ 17 MHz.

and material stack (8.4 μm SiO_2 and 213 μm Si). The resonances at multiple of ~ 17 MHz are higher-order HBAR modes.

Though narrowband, the HBAR modes provide novel functionality such as for error signal generation using the Pound-Drever-Hall (PDH) technique. Figure 7.7(a) shows the experimental setup to generate PDH error signals using HBAR modes induced by the AlN actuation. Figure 7.6(c) compares the generated PDH error signals, when applying 82.44 MHz and 91.71 MHz modulation frequency directly on the AlN actuator. The error signal with 91.71 MHz frequency is ×10 stronger than the one of 82.44 MHz frequency, since only the 91.71 MHz corresponds to an HBAR frequency, marked in Fig. 7.6(d). In addition, the measured $S_{21}(\omega)$ response of the AlN actuation, up to 400 MHz, is plotted in the linear frequency scale in Fig. 7.7(b), showing both cases when the laser is on- and off-resonance. Different modulation frequencies corresponding to different HBAR modes are investigated, which are marked with stars in Fig. 7.7(b). The PDH error signals modulated at these HBAR frequencies are shown in Fig. 7.7(c), as well as the studied microresonator resonance. A microwave source providing ~ 8 dBm RF power is used to modulate the Si_3N_4 microresonator via AlN actuation. The same RF power is used for modulation at all the HBAR frequencies. The decrease in error signal contrast at higher HBAR frequency is likely caused by the lower acousto-optic transduction S_{21}.

The relatively flat $S_{21}(\omega)$ response up to ~ 800 kHz allows soliton repetition rate stabilization via AlN actuation. As the soliton repetition rate, ν_{rep} = 191 GHz, is not directly measurable, an electro-optic frequency comb (EO comb) of 14.6974 GHz line spacing is utilized, and the beat signal between the -1st line of the microcomb and the -13th line of the EO comb is measured, as illustrated in Fig. 7.8(a). Figure 7.8(d) shows the experimental setup to stabilize the soliton repetition rate referenced to an EO comb. The EO comb is generated using a

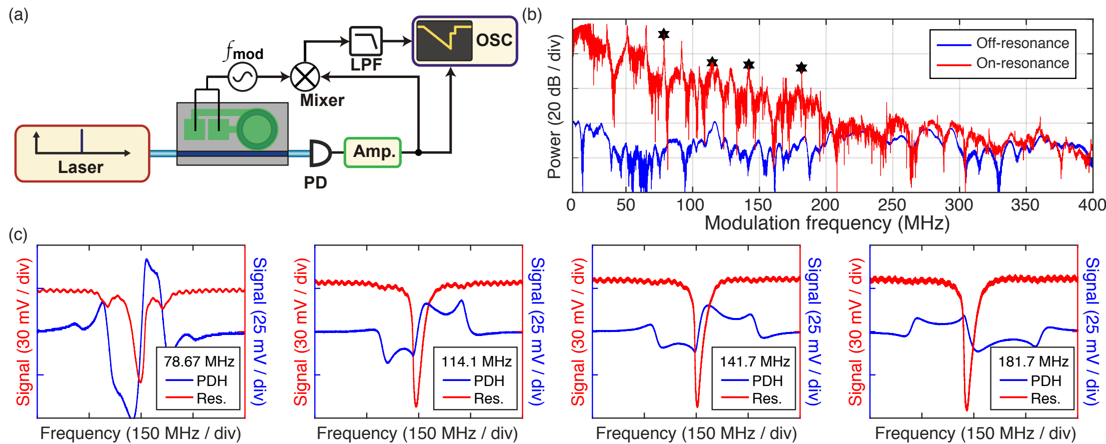

Figure 7.7 – On-chip generation of PDH error signals using the HBAR modes induced by the AlN actuation. (a) Experimental setup. LPF: low-pass filter. Amp.: RF power amplifier. (b) The measured $S_{21}(\omega)$ response of the AlN actuator in the linear frequency scale. Both cases, when the laser is on- and off-resonance, are measured. (c) The PDH error signals modulated at the HBAR frequencies marked with stars in (b).

scheme described in Ref. [71, 75], and has a comb line spacing of 14.6974 GHz. The EO comb and soliton microcomb are pumped by the same laser (Toptica CTL). The measure the beat signal between the -1st line of the microcomb and the -13th line of the EO comb, is further compared to a reference signal of 60.0 MHz. The error signal is applied directly on the AlN actuator, such that the actuation on the microresonator stabilizes the soliton repetition rate to the EO comb line spacing. Figure 7.8(b, c) compare the measured beat signal between the -1st line of the microcomb and the -13th line of the EO comb, and the phase noise of the beat signal in the cases of free-running and locked states, in comparison with the phase noise of the 60.0 MHz reference microwave. The locking bandwidth, determined by the merging point of two phase noise curves, is 0.6 MHz. Note that 0.6 MHz is a large bandwidth for piezoelectric optical frequency actuators, compared to conventional lasers where the piezo response is typically limited to few kilohertz, similar to integrated heaters.

To measure the *out-of-loop* beat signal and its phase noise, a modified setup is used as shown in Fig. 7.9(a). The pump laser's frequency to generate the soliton microcomb is shifted by 77.0 MHz via a fibre-coupled acousto-optic modulator (AOM). The reason to shift the micro-comb's pump frequency is to cancel out the drift and noise caused by the imbalanced paths in delayed self-homodyne measurement, by detecting the beatnote (77.0 MHz shift) between the

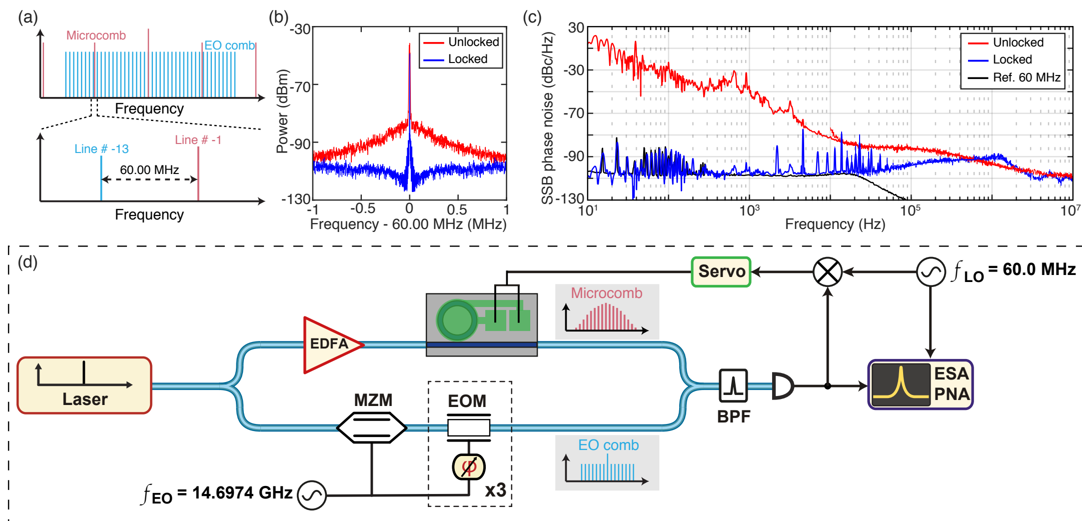

Figure 7.8 – High-speed piezoelectric actuation for soliton repetition rate stabilization using an EO comb. (a) Schematic of soliton repetition rate stabilization using an EO comb with 14.6974 GHz line spacing. The -1st line of the microcomb and the -13th line of the EO comb are locked, referenced to a 60.0 MHz microwave signal. (b) Measured beatnote signal of the -1st line of the microcomb and the -13th line of the EO comb, in the cases of locked and unlocked (free-running) states. Resolution bandwidth (RBW) is 1 kHz. (c) Measured phase noise of the beat signal, in comparison to the 60.0 MHz microwave signal. The locking bandwidth of the AlN actuator is 0.6 MHz. (d) Experimental setup to characterize the *in-loop* phase noise of the beat signal between the -1st line of the microcomb and the -13th line of the EO comb.

pump lines of the microcomb and the EO comb. By down-mixing the 77.0 MHz heterodyne beatnote signal using the same microwave source that drives the AOM, the feedback signal is applied to the laser current such that the pump laser's frequency is stabilized and the noise in the delayed self-homodyne measurement is removed.

Then, the beatnote between the $+1^{st}$ line of the microcomb and $+13^{th}$ line of the EO comb is detected and referenced to a 20.0 MHz microwave signal, in order to stabilize the microcomb repetition rate. The entire schematic of referencing the microcomb to the EO comb is shown in Fig. 7.9(b). Figure 7.9(c) compares the single-sideband (SSB) phase noise of the beat signals, for:

- Dashed red: The free-running phase noise of the beat signal between the $+1^{st}$ line of the microcomb and the $+13^{th}$ line of the EO comb while the pump laser's frequency is locked.
- Dashed blue: The free-running phase noise of the beat signal between the -1st line of the microcomb and the -13th line of the EO comb while the pump laser's frequency is locked.

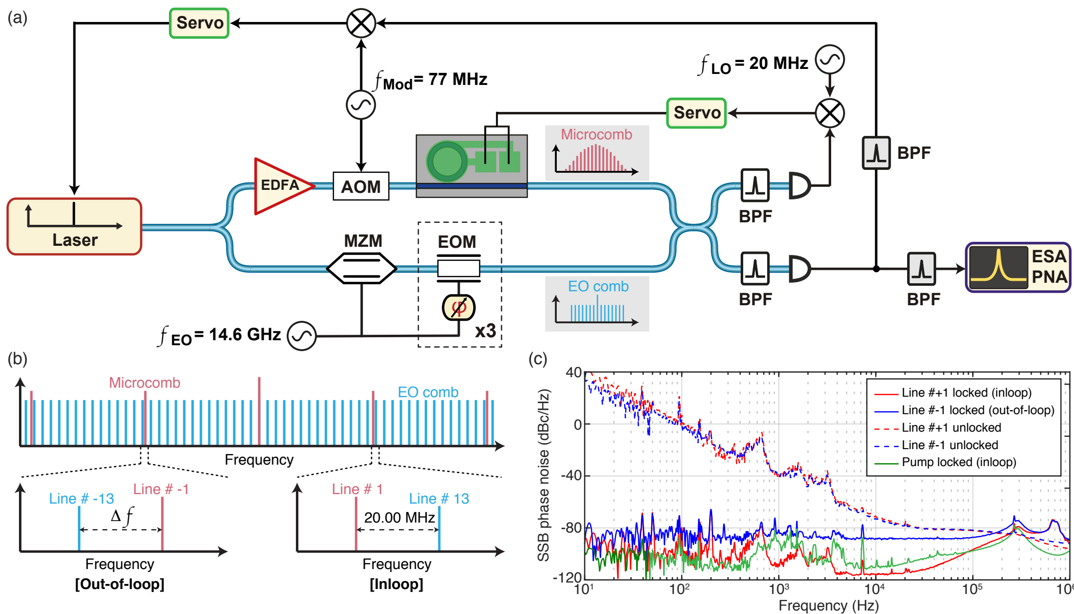

Figure 7.9 – Out-of-loop beat signal characterization using a modified setup. (a) Modified experimental setup to characterize the *out-of-loop* phase noise of the beat signal between the -1st line of the microcomb and the $+13^{th}$ line of the EO comb. (b) Schematic of referencing the microcomb to the EO comb. The beatnote (in-loop) between the $+1^{st}$ line of the microcomb and $+13^{th}$ line of the EO comb is detected and referenced to a 20.0 MHz microwave signal. The beatnote (out-of-loop) between the -1st line of the microcomb and -13th line of the EO comb is characterized. (c) Comparison of SSB phase noises measured in different cases.

- Solid green: When the pump laser's frequency is locked, the phase noise between the EO comb's pump and the microcomb's pump (shifted by 77 MHz).

- Solid red: The *in-loop*, locked phase noise of the beat signal between the $+1^{st}$ line of the microcomb and the $+13^{th}$ line of the EO comb.

- Solid blue: The *out-of-loop* phase noise of the beat signal between the -1st line of the microcomb and the -13th line of the EO comb, when the $+1^{st}$ line of the microcomb and the $+13^{th}$ line of the EO comb are locked.

In the out-of-loop phase noise of the beat signal between the -1st line of the microcomb and the -13th line of the EO comb, a reduction in phase noise is observed with the AlN actuation. The locking bandwidth in this case is > 300 kHz.

To further evaluate the long-term stability of the locked system, frequency counting measurements of the relative Allan deviations are performed, as shown in Fig. 7.10. The 77 MHz microwave source (used to lock the pump laser's frequency) is referenced to the 20 MHz microwave oscillator (used to down-mix the in-loop beat signal to derive the error signal). Similarly, the microwave source driving the EOMs (14.6974 GHz) for EO comb generation is also referenced to the same 20 MHz microwave oscillator. The relative Allan deviation of the beat signals between the free-running microcomb and EO comb are not converging, while the beat signal between the locked pump lines of the microcomb and EO comb show 10^{-2} at 1 s averaging time. After locking the soliton repetition rate to the EO comb by actuating on AlN, the in-loop and the out-of-loop beat signals show similar frequency stability.

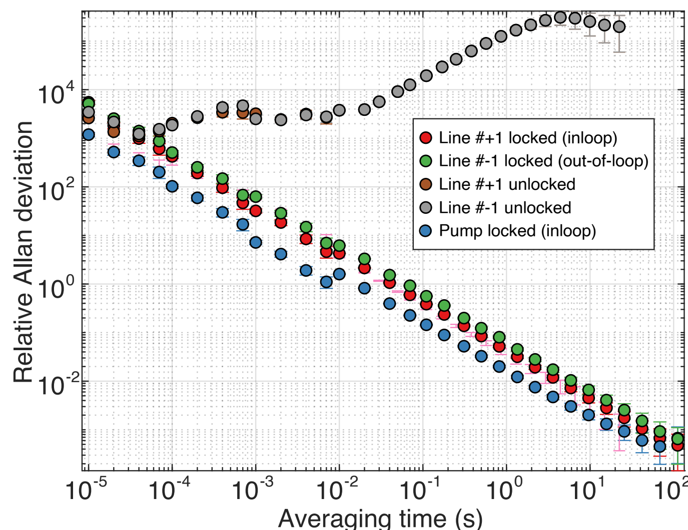

Figure 7.10 – Comparison of measured relative Allan deviation for the microcomb and EO comb beat signals in different cases, to evaluate the long-term stability of the locked system.

7.2.3 Soliton-based parallel LiDAR engine

The AlN actuator can be a key component for a soliton-based, parallel, frequency-modulated continuous-wave (FMCW) LiDAR [137]. Figure 7.11 outlines the operation principle of an FMCW LiDAR. A continuous-wave laser sends a frequency-chirped signal to a moving object, and receives the reflected signal from the object. The heterodyne beatnote between the emitted signal and the received signal provides two key parameters, f_u and f_d, which allow to recover the profile of the received signal. Compared with the emitted signal, the received signal has a time-delay Δt and a frequency-shift Δf_D. The time-delay Δt is due to the photon's time of flight, which allows to calculate the distance between the laser emitter and the moving object. The frequency-shift Δf_D is caused by the Doppler effect, which allows to calculate the moving speed and direction of the object. Therefore, the FMCW LiDAR can perform both the distance and speed measurement at the same time.

The scheme of a soliton-based FMCW LiDAR relies on scanning the pump laser's frequency ν_L over the soliton existence range [335] $\Delta\nu_\mathrm{s} = \nu_2 - \nu_1$, i.e. $\nu_\mathrm{c} - \nu_\mathrm{L} \in [\nu_1, \nu_2]$, with ν_c being the resonance frequency, ν_1 and ν_2 being the boundary of soliton existence detuning range. This results in transferring the pump frequency chirp to all soliton comb teeth, as shown in Fig. 7.12(a). Combined with diffractive optics that disperses multiple frequency lines,

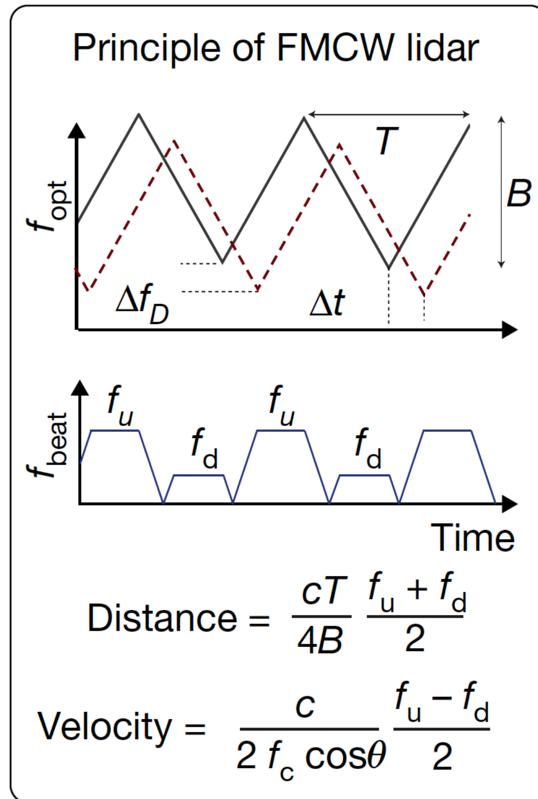

Figure 7.11 – Operation principle of an FMCW LiDAR. This figure is took from Ref. [137].

this approach to FMCW LiDAR allows high-speed parallel acquisition of both velocity and position in each pixel. However, the varying soliton detuning has several limitations. First, the varying soliton detuning $\nu_c - \nu_L$ leads to variations in soliton spectrum bandwidth and power, which limits the number of usable optical channels. Second, the Raman self-frequency shift [87, 159] causes a varying soliton repetition rate (i.e. comb line spacing). Third, GHz frequency excursion of the pump laser ($\Delta\nu_L$) requires GHz-wide soliton existence range ($\Delta\nu_s$), necessitating to elevate the pump power to several Watts.

These limitations can be overcome using the AlN actuation on the microresonator, such that the microresonator resonance ν_c is *modulated synchronously* to the pump frequency ν_L, in order to maintain a constant soliton detuning $\nu_c - \nu_L$. Both schemes are experimentally investigated, i.e. (a) scanning the pump laser within the soliton existence range, and (b) synchronously modulating the pump laser and the microresonator resonance ("feed-forward"). For the feed-forward scheme, a triangular signal of frequency f_{mod} is applied on both the pump laser and the AlN actuator. A phase shifter, an attenuator and a high-voltage amplifier (HVA) are used to modify the triangular signals in order to synchronize the resonance tuning to the laser tuning and to achieve the same frequency excursions of the laser and the resonance. Figure 7.12 shows the experimental setup to synchronously scan the microresonator and the

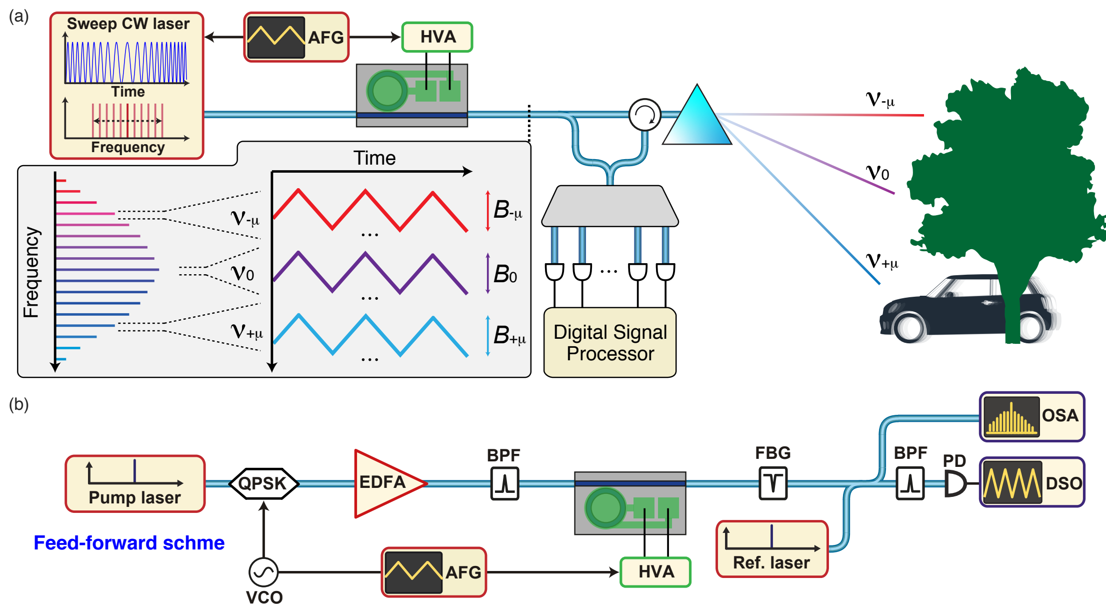

Figure 7.12 – Schematic and experimental setup of hybrid AlN-Si_3N_4 soliton LiDAR engine. (a) Schematic of soliton-based parallel FMCW LiDAR. A chirped pump transduces synchronous modulation to other comb lines, with the same modulation rate and frequency excursion. (b) Experimental setup for synchronous scan of the laser frequency and the microresonator resonance, using the feed-forward scheme. VCO: voltage-controlled oscillator. AFG: arbitrary waveform generator. QPSK: quadrature phase shift keying. DSO: digital storage oscilloscope.

pump laser (i.e. the feed-forward scheme. A single-sideband modulator driven by a voltage-controlled oscillator (VCO) is used to fast scan the laser frequency, instead of directly scanning the laser piezo due to the limited piezo scan speed of our laser (~ 200 Hz). A voltage ramp signal from the same dual-channel arbitrary waveform generator (AWG) is applied on the VCO and on the AlN actuator. The ramp signal sent to the AlN actuator is further amplified by the HVA with ×50 voltage amplification and 3-dB bandwidth of ~ 5 MHz. The synchronous scan of the laser frequency and the microresonator resonance is performed by adjusting the amplitude and the phase of the ramp signal applied on the VCO. A PDH lock can further improve the synchronization by locking the resonance to the laser with a constant frequency difference [59]. Initially, a ramp signal from the AWG with a peak-to-peak voltage V_{pp} of 3 V (HVA amplifies to 150 V) and 10 kHz scanning rate is applied on the AlN. The amplitude V_{pp} and the phase of the ramp signal driving the VCO is adjusted until stable *C*-resonance is observed on VNA. The tuning into soliton states is realized either by changing the laser frequency via laser piezo tuning, or by turning on and off the VCO which allows fast tuning of the laser to the effectively red-detuned side of the resonance. A reference laser is used to probe the chirp of different comb lines (the pump line, $\pm 10^{th}$ comb lines etc). A fast oscilloscope of 2 GHz bandwidth and 5 GSamples/s is used to capture the heterodyne beatnote detected on the fast photodiode, for further off-line data processing such as fast Fourier transform and fitting triangular signal.

Figure 7.13(a) compares the soliton spectra using both schemes, i.e. (a) scanning the pump laser within the soliton existence range, and (b) feed-forward scheme. Figure 7.13(a, b, c) illustrate the differences in soliton spectrum, soliton detuning and integrated soliton pulse power using both schemes, and highlight the advantages of the feed-forward scheme using the AlN actuator. First, the pump frequency chirp $\Delta\nu_{\mathrm{L}}$ can be significantly larger than the soliton existence range $\Delta\nu_{\mathrm{s}}$, while simultaneously allows operating the soliton with tens of milliwatt power, compatible with state-of-art integrated laser [351, 206, 383]. Second, the soliton spectrum and the repetition rate are nearly constant and not affected by the pump frequency chirp.

Figure 7.13(d) compares the frequency excursions of different soliton comb line. The scheme of soliton detuning scan, at frequency f_{mod} = 10 kHz (blue), shows a frequency excursion dependence on the comb line number, resulted from the soliton repetition rate change $\Delta\nu_{\mathrm{rep}} \approx$ 17.4 MHz per 0.383 GHz pump frequency excursion. Using feed-forward scheme with modulation frequency f_{mod} = 10 kHz and 100 kHz (red, solid lines), frequency excursion of ~ 2 GHz is achieved, which is more than ×5 larger than the soliton existence range ($\Delta\nu_{\mathrm{s}} \approx$ 400 MHz). Moreover, the soliton repetition rate change is reduced to $\Delta f_{\mathrm{rep}} \approx$ 0.066 MHz per 2.04 GHz pump frequency excursion with f_{mod} = 10 kHz. Figure 7.13(e) shows the time-frequency diagram of different comb lines chirping at 10 kHz modulation frequency, with frequency excursion of 2.04 GHz. More importantly, the HBAR and contour mechanical modes of our device enable modulation with higher frequency and efficiency (red, dashed lines). By applying modulation with f_{mod} = 18.308 MHz, coinciding with the fundamental HBAR mode and a contour mode, pump frequency excursion of 1.6 GHz is imparted without using the HVA, i.e.

the voltage applied on the AlN is only 7.48 V, a CMOS-compatible voltage. In addition, this modulation corresponds to an equivalent tuning speed of 58.6 PHz/s. The corresponding resonance tuning coefficient is $\delta\nu/\delta V = 219$ MHz/V, which is $\times 14$ larger than the DC tuning value of $\delta\nu/\delta V = 15.7$ MHz/V. Applying modulation with $f_{\mathrm{mod}} = 18.322$ MHz, while still coinciding the fundamental HBAR mode but not a contour mode, the tuning coefficient is reduced to $\delta\nu/\delta V = 133$ MHz/V.

The integrated AlN piezoelectric actuators allow tuning and control of soliton microcombs.

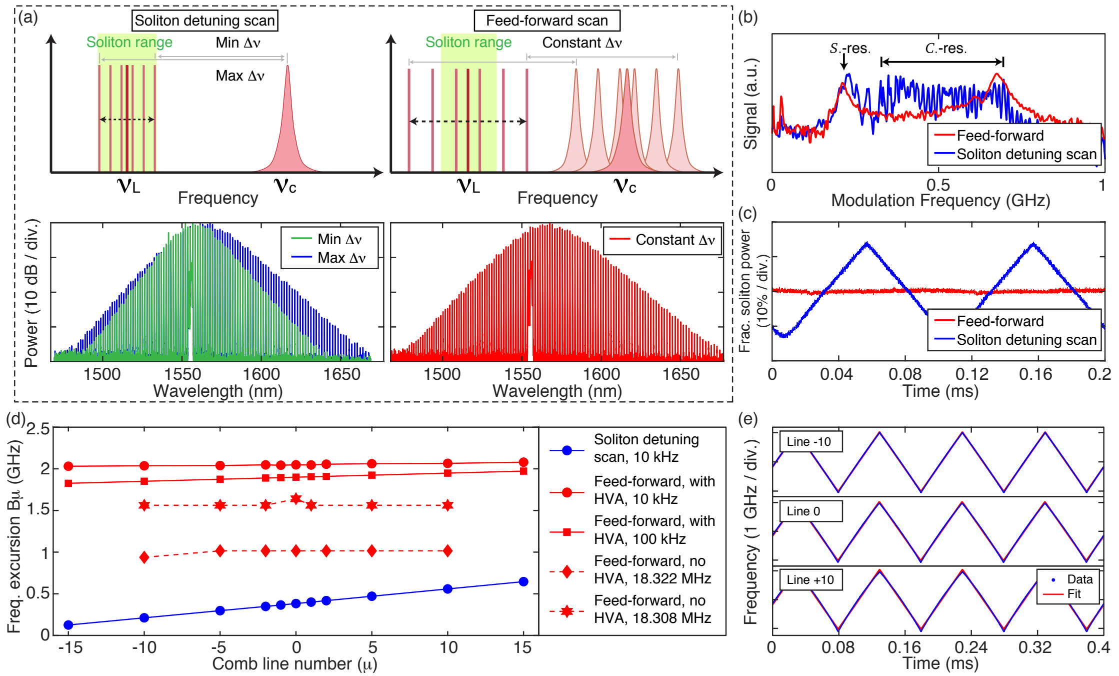

Figure 7.13 – Results of hybrid AlN-Si_3N_4 soliton LiDAR engine. (a) Comparison of two schemes for soliton-based FMCW LiDAR. Left: The scheme employing soliton detuning scan, with a fixed microresonator resonance ν_c, and a pump centered at ν_L chirping within the soliton existence range (green shaded). By varying the soliton detuning $\Delta\nu$, the soliton spectrum varies correspondingly, as shown in the bottom. Right: Feed-forward scheme employing synchronous modulation of the pump frequency ν_L and the resonance ν_c, such that the soliton detuning $\Delta\nu$ is constant, resulting in also a constant soliton spectrum shown in the bottom. Note that in this scheme, the pump frequency excursion can be significantly larger than the soliton existence range (green shaded) (b) Comparison of both schemes for the soliton response on VNA [58]. The soliton detuning scan shows a varying C-resonance, while the feed-forward scheme shows a fixed C-resonance. (c) Comparison of both schemes for the integrated soliton pulse power. The soliton detuning scan shows a varying soliton pulse power, while the feed-forward scheme shows a constant power. (d) Comparison of the frequency excursions of different soliton comb lines, using different approaches. (e) Time-frequency diagram of different comb lines chirping at 10 kHz modulation frequency, with frequency excursion of 2.04 GHz.

This novel capability not only benefits existing applications, but also allows synchronous scanning of the pump laser and photonic microresonator, as required for massively parallel FMCW LiDAR. While polycrystalline AlN is used in our current work, the operation voltage can be reduced by more than ×2 using scandium-doped AlN [384, 385]. By future co-integration of CMOS electronic circuitry on a closeby die, compactly packaged soliton microcombs with rapid electronic actuation is attainable.

8 Conclusion and Outlook

In my perspective, the most important result of this PhD thesis is the development and optimization of the photonic Damascene fabrication process of ultralow-loss, dispersion-engineered Si_3N_4 photonic integrated circuits. The ultralow loss and the high microresonator Q, together with the extremely low thermal absorption loss, are the key reasons for the success of the soliton generation with ultralow power and microwave repetition rates, the soliton generation via laser self-injection locking, and the piezoelectric control of solitons. While certainly more applications using soliton microcombs can be envisaged in the near future, further reduction of the optical losses in integrated waveguides via improving the fabrication process and developing new techniques will still be the central topics of Si_3N_4 integrated photonics. In addition, the current Si_3N_4 photonic Damascene process has used LPCVD Si_3N_4 and high temperature thermal annealing of Si_3N_4 and SiO_2, thus this process is only compatible to other CMOS processes if the Damascene process is performed in the front-end (e.g. different materials processed on the planarized Si_3N_4 Damascene substrate. Therefore, a Si_3N_4 process fully operated at a CMOS temperature (i.e. below 450°C) can be very helpful for photonic integration of Si_3N_4 and other materials. In this case, low-loss Si_3N_4 photonic integrated circuits can also be used as a back-end process.

For the two abovementioned reasons, based on my understanding and knowledge of Si_3N_4 photonics developed in this PhD thesis, I outline one future topic that can be key for a wider use of low-loss Si_3N_4 photonic integrated circuits in the future.

8.1 Novel Si_3N_4 and SiO_2 CVD processes using silicon tetrachloride

A key reason enabling ultralow loss of our Si_3N_4 integrated waveguides is the LPCVD technology which is used to grow Si_3N_4 and SiO_2, followed by thorough thermal annealing at a temperature above 1200°C. This combined process enables not only high-quality Si_3N_4 and SiO_2 (high density, low porosity, excellent stoichiometry etc), but more importantly the ultralow thermal absorption losses below 0.2 MHz presented in Chapter 4. However, the LPCVD Si_3N_4 deposition temperature and the thermal annealing temperature of Si_3N_4 and

SiO_2 are both too high to be compatible with CMOS electronic circuits. If PECVD Si_3N_4 and SiO_2 are used (at a process temperature below 450°C), without thermal annealing, the optical loss will be dominated by hydrogen absorption losses. Therefore, an important future topic is to develop hydrogen-free Si_3N_4 and SiO_2 CVD processes that are operated at a process temperature below 450°C.

Recently, there are few reports on PECVD Si_3N_4 and SiO_2 processes using deuterated silane (SiD_4), in contrast to the commonly used silane (SiH_4) precursor for Si_3N_4 and SiO_2 PECVD process. The Si-D and N-D bonds have absorption peaks out of the telecommunication bands around 1550 nm, where the absorption peaks of Si-H and N-H are. In ref. [248], J. Chiles *et al* reported a Si_3N_4 PECVD process using SiD_4 and NH_3. In ref. [386], W. Jin *et al* reported a SiO_2 PECVD process using SiD_4 and O_2. Both processes are operated at a temperature around 350°C.

Within this PhD thesis, though still ongoing and not conclusive yet, I have also participated and lead the development of novel PECVD Si_3N_4 and SiO_2 processes using silicon tetrachloride ($SiCl_4$) precursor. The chemical reactions are: $3\,SiCl_4 + 2\,N_2 \longrightarrow Si_3N_4 + 6\,Cl_2$, and $SiCl_4 + O_2 \longrightarrow SiO_2 + 2\,Cl_2$. As immediately seen, both processes result in materials hydrogen-free. In addition, the deposition by-product Cl_2 could remove any metal impurities introduced due to the precursors or contaminations. As Si-Cl bond has higher bonding energy than Si-H (as a proof, at room temperature SiH_4 is gas but $SiCl_4$ is liquid), the absorption peak is also removed from the telecommunication wavelength. It is worth to note that, $SiCl_4$ is a key chemicals not only for semiconductor products but also for optical fibers. For example, the precursor $SiCl_2H_2$ used for LPCVD Si_3N_4 process is synthesized from $SiCl_4$. High-quality glass used for optical fibers are generated via the **hydrolysis** of $SiCl_4$, as $SiCl_4 + 2\,H_2O \longrightarrow SiO_2 + 4\,HCl$. More details of the **flame hydrolysis process** will be given in the next section.

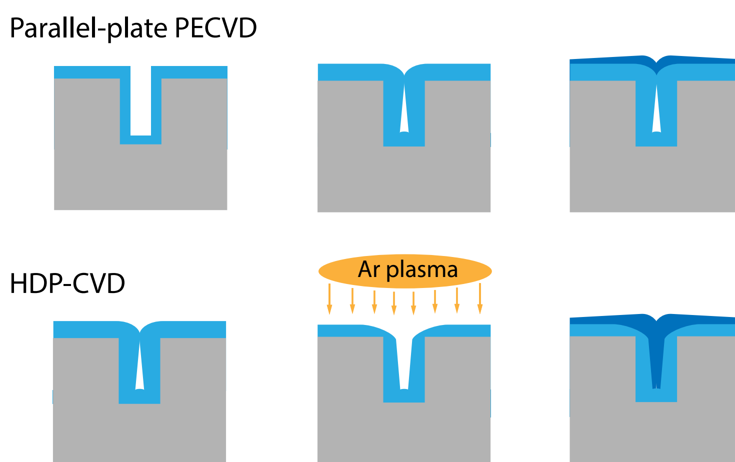

Figure 8.1 – Difference in the topography of deposited films using PECVD and HDP-CVD. The gap filling capability of the HDP-CVD is highlighted.

As the Si-Cl bonds has a high bonding energy, common high-temperature process used in LPCVD cannot break the $SiCl_4$ molecules. Therefore, to realize the film deposition, plasma driven by high power is needed. For this purpose, a high-density-plasma chemical vapour deposition (HDP-CVD) tool is used. As mentioned briefly in Chapter 2, an HDP-CVD tool performs deposition and etching in the dual-mode, and offers the following advantages:

- The precursors used, $SiCl_4$, N_2, and O_2 are inherently hydrogen-free.
- Better dissociation of $SiCl_4$ precursors and radical reaction due to the high-density plasma.
- The deposition by-product Cl_2 could remove any metal impurities introduced due to the precursors or contaminations.
- The in-situ ion bombardment due to the plasma bias increases the film density.
- The gap-filling capability offered by HDP-CVD, which is absent in standard PECVD process. This feature is detailed below.

Gap filling: The conformal deposition of thin films is critical. Voids can form if the deposition process does not have sufficient conformality, as shown in Chapter 2, which can compromise the device performance. For our Damascene process, the conformality of LPCVD Si_3N_4, as a result of surface thermo-dynamics, is critical to fill the preform trenches. For the standard subtractive process, conformality of SiO_2 is required to fill the gap between the bus waveguide and the ring resonator, to achieve the minimum perturbation of the optical mode in the Si_3N_4 waveguide core. If gas-phase nucleation dominates surface thermo-dynamics, voids can often form in the SiO_2 cladding if the wafer has patterned structures. Therefore, the HDP-CVD process is intrinsically beneficial as compared to the standard PECVD process where film material is mainly formed directly in the gas phase. In fact, the "void filling" is one of the main motivations for the invention of HDP-CVD for microelectronic circuit manufacturing. The high-density plasma not only offers high deposition rate, but also offer in-situ physical etching (i.e. sputter). Figure 2.17 illustrates the principle of gap filling using an HDP-CVD. If a void is about to form, the sharp edge attracts more impinging ions due to the edge charge effects, thus has a higher etch rate. The net effect of deposition and etching creates an excellent performance on gap filling and deposition conformality. A side-effect which can be also

Parameter	Si_3N_4	SiO_2
Refractive index	1.976 ± 0.001	1.464 ± 0.001
Stress	Compressive	Compressive or tensile
Deposition rate	<20 nm / min	-
Deposition uniformity	4.09%	4.75%
BHF etch rate	-	420 nm/min

Table 8.1 – Film parameters of Si_3N_4 and SiO_2 deposited with $SiCl_4$ precursor.

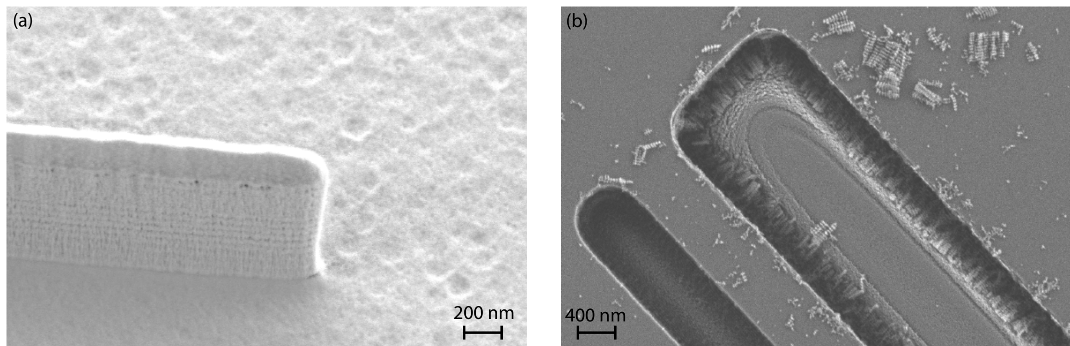

Figure 8.2 – SEM images of Si_3N_4 deposited with $SiCl_4$ precursor. (a) SEM top view of Si_3N_4 waveguide after CMP. (b) SEM side view of dry-etched Si_3N_4 waveguide.

beneficial is that the sputter further densifies the film and alter the film stress. By optimizing the sputter strength, it is possible to make the dielectric film compressive, while the chemical reaction and temperature cooling down usually make the film tensile.

During my PhD thesis, with my colleague Michael Zervas, we have started investigating this novel $SiCl_4$-based CVD processes using an HDP-CVD tool. So far, we can obtain stable Si_3N_4 and SiO_2 films. Table 8.1 lists the measured film parameters of Si_3N_4 and SiO_2. Except the density (reflected from the BHF etch rate), the SiO_2 process with $SiCl_4$ precursor is nearly accomplished.

However the Si_3N_4 film has more problems. Figure 8.2 shows the SEM image of Si_3N_4 waveguides after CMP and dry etching. Two things are observed: 1. The Si_3N_4 film shows multi-layer structures like the "Italian Lasagna", which is due to the unoptimized alternating deposition-sputter cycles. 2. The film density is low and cannot sustain CMP. Both problems limit us to further process the wafers and measure the optical losses of this $SiCl_4$-based Si_3N_4 dielectric film. **This work will be continued after this PhD thesis**.

One should note that, these two $SiCl_4$-based CVD processes can be useful, not only to achieve lower loss in Si_3N_4 but also offer hydrogen-free, annealing-free dielectric films for other integrated materials. For the subtractive processes of $LiNbO_3$, AlGaAs, GaP, Ta_2O_5 and crystalline AlN, the SiO_2 process can be useful due to the gap filling capability and requiring no high-temperature thermal annealing to remove hydrogen. Therefore, this $SiCl_4$-based, low-temperature Si_3N_4 fabrication technology can foster a wider use of low-loss Si_3N_4 photonic circuits integrated with other materials in the future.

8.2 Ultra-pure SiO_2 deposition via flame hydrolysis

The **flame hydrolysis deposition** (FHD) is a CVD technique to deposit ultra-pure SiO_2 on silicon wafer substrates [387, 388]. This process features fast deposition rate (thus ideal to grow SiO_2 films of thickness up to 50 μm), and flexibility of doping SiO_2 with germanium,

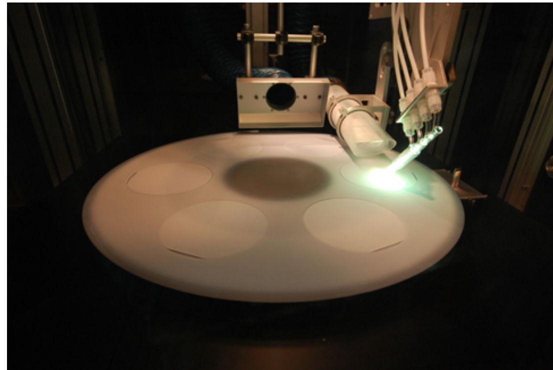

Figure 8.3 – Photo showing the FHD of SiO_2 on a rotating plate that contains six 6-inch wafers. The flame looks green due to the presence of boron. This photo is taken from *Zepler Institute* (https://www.zeplerinstitute.ac.uk/facilities/fhd).

phosphorous and boron. These dopants can allow modification of the optical (e.g. refractive index and UV photo-sensitivity) and mechanical (e.g. stress and density) properties of the SiO_2 film. Particularly, the high photo-sensitivity for direct UV laser writing is advantageous to fabricate SiO_2 photonic integrated waveguides for applications e.g. chip-based quantum computing [389].

The FHD process shares the same physical and chemical principles as vapour axial deposition which has been widely used in industrial production of optical fibers. The chemical reaction is slightly different from the one used in the ICP-CVD shown in the previous section, as here, H_2 is also involved. Equivalently, the $SiCl_4$ precursor reacts with H_2O, as $SiCl_4 + 2H_2 + O_2 \longrightarrow SiO_2 + 4HCl$, at the reaction temperature of 1200°C. That is why this process gets the name "flame hydrolysis". The dopants of germanium, phosphorous and boron are introduced by adding BCl_3 / BBr_3, PCl_3 / $POCl_3$ and $GeCl_4$. All these chloride precursors have low saturated vapour pressure, and are liquid at room temperature (except BCl_3). Therefore, **bubbler** systems are often used, in which flowing N_2 gas is used to bring precursors to the reaction chamber. Figure **??** shows the photo of ongoing SiO_2 FHD on a rotating plate that contains six 6-inch wafers. The flame looks green due to the presence of boron. During FHD, SiO_2 soot is produced on the wafer. To consolidate / density the SiO_2 soot, high temperature annealing (above 1200°C) for hours is needed.

During the development of ICP-CVD $SiCl_4$ processes, we also performed FHD SiO_2 deposition as the top SiO_2 cladding on our Damascene wafers. This process was performed in the University of Southampton, with the courtesy of Dr. James Gates, Dr. Matthew Posner, and Prof. Peter Smith. After the FHD top SiO_2 deposition, the wafers were sent back to EPFL. Following steps for wafer release were performed. The final chips were also measured. Figure 8.4(a) shows a representative data of the resonance linewidth (loss) characterization. The intrinsic loss is $\kappa_0/2\pi \approx 400$ MHz, significantly larger than our normal linewidth value (below 20 MHz), meaning that this FHD process is currently not compatible with our Damascene ultralow-loss Si_3N_4 process. To understand the reason for loss increase, a chip was cleaved

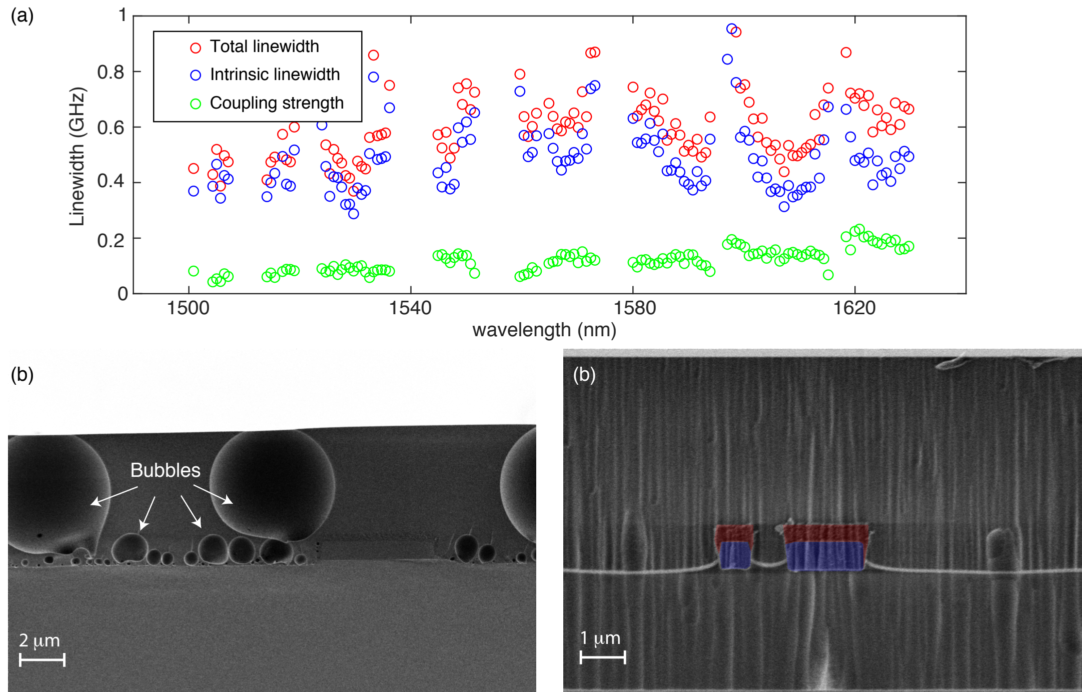

Figure 8.4 – Characterization of Damascene process using FHD SiO_2 as the top cladding. (a) Resonance linewidth (loss) characterization of the final chip. The intrinsic loss is $\kappa_0/2\pi \approx 400$ MHz. (b) SEM image of the sample cross-section showing the generated bubbles in the FHD SiO_2 cladding. (c) SEM image of the sample cross-section showing the material diffusion (red) from the Si_3N_4 waveguides (blue).

and the cross-section was examined. Figure 8.4(c, d) shows the sample cross-section. Bubbles were found in the FHD SiO_2 cladding. Meanwhile, material diffusion (maybe nitrogen atoms) from the Si_3N_4 waveguide cores was also observed. These two issues need to be resolved before using the FHD process for our Damascene process.

8.3 Beyond lithography limit – patterning nano structures with photolithography

Besides the waveguide loss, another type of losses which can be further reduced is the fiber-to-chip coupling loss using inverse nanotapers. Double inverse nanotapers have already been illustrated in Chapter 3 as well as Ref. [239]. Polarization-insensitive coupling with a coupling loss down to 1.7 dB per facet at 1550 nm wavelength has been demonstrated. However, the taper design and fabrication could still be improved, for lower losses or coupling at shorter wavelengths (e.g. 1064 nm and 780 nm, for applications of e.g. optical atomic clocks).

The key factor limiting the fiber-to-chip coupling is the mode match between the fiber mode and the taper mode. As detailed in Chapter 3, typically the fiber mode is larger than the taper mode. Therefore, making the taper smaller increases the size of the taper mode, and improves

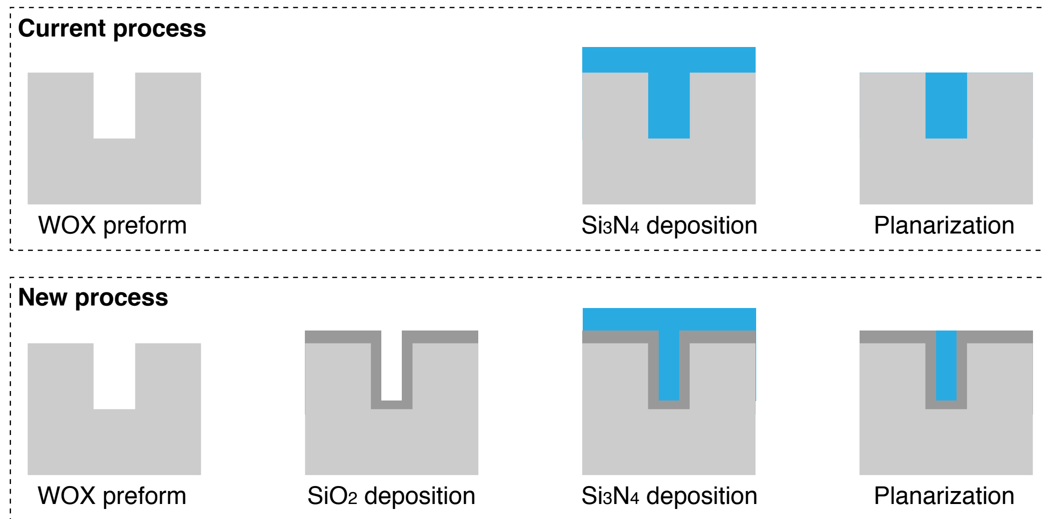

Figure 8.5 – Comparison of the current (standard) process to fabricate the inverse nanotapers for edge coupling with fibers, and the new process. The new process has a taper of a reduced size, using conformal deposition of SiO_2 on thermal wet SiO_2 preform before LPCVD Si_3N_4 deposition.

the mode match to the fiber mode. For this purpose, the key point here is to further reduce the taper size.

A feasible solution through modified fabrication is shown in Fig. 8.5. The key idea here is to deposit *conformal* SiO_2 before the LPCVD Si_3N_4 deposition. The conformal deposition of SiO_2 on the thermal wet SiO_2 preform narrows the etched trench and reduces its size. For example, for a trench of width w and depth h, the SiO_2 deposition of thickness t makes the trench of width $w-2t$ and depth h. The conformal SiO_2 deposition makes the trench narrower, and increases the aspect ratio (depth / width). Here, the conformality of SiO_2 deposition is key, thus the ideal process could be LPCVD TEOS or HTO process (see Chapter 2 on LPCVD).

The SEM image of the fabricated taper using the conformal LPCVD TEOS deposition before the LPCVD Si_3N_4 deposition is shown in Fig. 8.6. The top CD is 280 nm (merely resolvable with our DUV stepper), and the bottom CD is 108 nm (unresolvable with our DUV stepper). Yet, interestingly, the maximum measured fiber-chip-fiber coupling efficiency, at 1550 nm, using the tapers fabricated via this process, is still below 50%, not significantly higher than what has been achieved in Chapter 3 and Ref. [239]. Therefore, to better see the improvement of coupling using this type of tapers, it would be ideal to experiment at 1064 nm or 780 nm, where normal tapers will fail due to the large sizes.

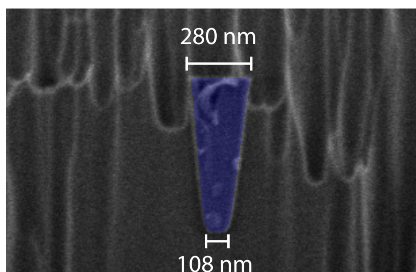

Figure 8.6 – SEM image showing the taper with a reduced size using the conformal LPCVD TEOS deposition before the LPCVD Si_3N_4 deposition. The Si_3N_4 taper is blue-shaded.

Bibliography

[1] T. Udem, R. Holzwarth, and T. W. Hänsch, "Optical frequency metrology," *Nature*, vol. 416, p. 233, 03 2002.

[2] S. T. Cundiff and J. Ye, "Colloquium: Femtosecond optical frequency combs," *Rev. Mod. Phys.*, vol. 75, pp. 325–342, Mar 2003.

[3] S. A. Diddams, K. Vahala, and T. Udem, "Optical frequency combs: Coherently uniting the electromagnetic spectrum," *Science*, vol. 369, no. 6501, 2020.

[4] N. R. Newbury, "Searching for applications with a fine-tooth comb," *Nature Photonics*, vol. 5, p. 186, 03 2011.

[5] T. Fortier and E. Baumann, "20 years of developments in optical frequency comb technology and applications," *Communications Physics*, vol. 2, no. 1, p. 153, 2019.

[6] T. W. Hänsch, "Nobel lecture: Passion for precision," *Rev. Mod. Phys.*, vol. 78, pp. 1297–1309, Nov 2006.

[7] J. L. Hall, "Nobel lecture: Defining and measuring optical frequencies," *Rev. Mod. Phys.*, vol. 78, pp. 1279–1295, Nov 2006.

[8] R. Holzwarth, T. Udem, T. W. Hänsch, J. C. Knight, W. J. Wadsworth, and P. S. J. Russell, "Optical frequency synthesizer for precision spectroscopy," *Phys. Rev. Lett.*, vol. 85, pp. 2264–2267, Sep 2000.

[9] T. M. Fortier, M. S. Kirchner, F. Quinlan, J. Taylor, J. C. Bergquist, T. Rosenband, N. Lemke, A. Ludlow, Y. Jiang, C. W. Oates, and S. A. Diddams, "Generation of ultrastable microwaves via optical frequency division," *Nature Photonics*, vol. 5, pp. 425–429, jun 2011.

[10] H. R. Telle, G. Steinmeyer, A. E. Dunlop, J. Stenger, D. H. Sutter, and U. Keller, "Carrier-envelope offset phase control: A novel concept for absolute optical frequency measurement and ultrashort pulse generation," *Applied Physics B*, vol. 69, no. 4, pp. 327–332, 1999.

[11] S. Diddams, "The evolving optical frequency comb [invited]," *J. Opt. Soc. Am. B*, vol. 27, no. B51-B62, 2010.

[12] S. A. Diddams, D. J. Jones, J. Ye, S. T. Cundiff, J. L. Hall, J. K. Ranka, R. S. Windeler, R. Holzwarth, T. Udem, and T. W. Hänsch, “Direct link between microwave and optical frequencies with a 300 thz femtosecond laser comb,” *Phys. Rev. Lett.*, vol. 84, pp. 5102–5105, May 2000.

[13] D. J. Jones, S. A. Diddams, J. K. Ranka, A. Stentz, R. S. Windeler, J. L. Hall, and S. T. Cundiff, “Carrier-envelope phase control of femtosecond mode-locked lasers and direct optical frequency synthesis,” *Science*, vol. 288, no. 5466, pp. 635–639, 2000.

[14] R. Ell, U. Morgner, F. X. Kärtner, J. G. Fujimoto, E. P. Ippen, V. Scheuer, G. Angelow, T. Tschudi, M. J. Lederer, A. Boiko, and B. Luther-Davies, “Generation of 5-fs pulses and octave-spanning spectra directly from a ti:sapphire laser,” *Opt. Lett.*, vol. 26, pp. 373–375, Mar 2001.

[15] T. M. Fortier, A. Bartels, and S. A. Diddams, “Octave-spanning ti:sapphire laser with a repetition rate >1 ghz for optical frequency measurements and comparisons,” *Opt. Lett.*, vol. 31, pp. 1011–1013, Apr 2006.

[16] J. K. Ranka, R. S. Windeler, and A. J. Stentz, “Visible continuum generation in air–silica microstructure optical fibers with anomalous dispersion at 800 nm,” *Opt. Lett.*, vol. 25, pp. 25–27, Jan 2000.

[17] L.-S. Ma, M. Zucco, S. Picard, L. Robertsson, and R. S. Windeler, “A new method to determine the absolute mode number of a mode-locked femtosecond-laser comb used for absolute optical frequency measurements,” *IEEE Journal of Selected Topics in Quantum Electronics*, vol. 9, no. 4, pp. 1066–1071, 2003.

[18] L. E. Hargrove, R. L. Fork, and M. A. Pollack, “Locking of he–ne laser modes induced by synchronous intracavity modulation,” *Applied Physics Letters*, vol. 5, no. 1, pp. 4–5, 1964.

[19] F. Tauser, A. Leitenstorfer, and W. Zinth, “Amplified femtosecond pulses from an er:fiber system: Nonlinear pulse shortening and self-referencing detection of the carrier-envelope phase evolution,” *Opt. Express*, vol. 11, pp. 594–600, Mar 2003.

[20] B. R. Washburn, S. A. Diddams, N. R. Newbury, J. W. Nicholson, M. F. Yan, and C. G. Jørgensen, “Phase-locked, erbium-fiber-laser-based frequency comb in the near infrared,” *Opt. Lett.*, vol. 29, pp. 250–252, Feb 2004.

[21] A. Schliesser, N. Picqué, and T. W. Hänsch, “Mid-infrared frequency combs,” *Nature Photonics*, vol. 6, no. 7, pp. 440–449, 2012.

[22] C. Gohle, T. Udem, M. Herrmann, J. Rauschenberger, R. Holzwarth, H. A. Schuessler, F. Krausz, and T. W. Hänsch, “A frequency comb in the extreme ultraviolet,” *Nature*, vol. 436, no. 7048, pp. 234–237, 2005.

[23] S. A. Diddams, T. Udem, J. C. Bergquist, E. A. Curtis, R. E. Drullinger, L. Hollberg, W. M. Itano, W. D. Lee, C. W. Oates, K. R. Vogel, and D. J. Wineland, “An optical clock based on a single trapped 199hg+ ion,” *Science*, vol. 293, no. 5531, pp. 825–828, 2001.

[24] A. D. Ludlow, T. Zelevinsky, G. K. Campbell, S. Blatt, M. M. Boyd, M. H. G. de Miranda, M. J. Martin, J. W. Thomsen, S. M. Foreman, J. Ye, T. M. Fortier, J. E. Stalnaker, S. A. Diddams, Y. Le Coq, Z. W. Barber, N. Poli, N. D. Lemke, K. M. Beck, and C. W. Oates, "Sr lattice clock at 1 × 10–16 fractional uncertainty by remote optical evaluation with a ca clock," *Science*, vol. 319, no. 5871, pp. 1805–1808, 2008.

[25] T. Rosenband, D. B. Hume, P. O. Schmidt, C. W. Chou, A. Brusch, L. Lorini, W. H. Oskay, R. E. Drullinger, T. M. Fortier, J. E. Stalnaker, S. A. Diddams, W. C. Swann, N. R. Newbury, W. M. Itano, D. J. Wineland, and J. C. Bergquist, "Frequency ratio of al+ and hg+ single-ion optical clocks; metrology at the 17th decimal place," *Science*, vol. 319, no. 5871, pp. 1808–1812, 2008.

[26] L.-S. Ma, Z. Bi, A. Bartels, L. Robertsson, M. Zucco, R. S. Windeler, G. Wilpers, C. Oates, L. Hollberg, and S. A. Diddams, "Optical frequency synthesis and comparison with uncertainty at the 10-19 level," *Science*, vol. 303, no. 5665, pp. 1843–1845, 2004.

[27] X. Xie, R. Bouchand, D. Nicolodi, M. Giunta, W. Hänsel, M. Lezius, A. Joshi, S. Datta, C. Alexandre, M. Lours, P.-A. Tremblin, G. Santarelli, R. Holzwarth, and Y. Le Coq, "Photonic microwave signals with zeptosecond-level absolute timing noise," *Nature Photonics*, vol. 11, p. 44, 11 2016.

[28] B. C. Young, F. C. Cruz, W. M. Itano, and J. C. Bergquist, "Visible lasers with subhertz linewidths," *Phys. Rev. Lett.*, vol. 82, pp. 3799–3802, May 1999.

[29] A. Marian, M. C. Stowe, J. R. Lawall, D. Felinto, and J. Ye, "United time-frequency spectroscopy for dynamics and global structure," *Science*, vol. 306, no. 5704, pp. 2063–2068, 2004.

[30] S. A. Diddams, L. Hollberg, and V. Mbele, "Molecular fingerprinting with the resolved modes of a femtosecond laser frequency comb," *Nature*, vol. 445, no. 7128, pp. 627–630, 2007.

[31] N. Picqué and T. W. Hänsch, "Frequency comb spectroscopy," *Nature Photonics*, vol. 13, no. 3, pp. 146–157, 2019.

[32] A. Hugi, G. Villares, S. Blaser, H. Liu, and J. Faist, "Mid-infrared frequency comb based on a quantum cascade laser," *Nature*, vol. 492, no. 7428, p. 229, 2012.

[33] I. Coddington, W. C. Swann, and N. R. Newbury, "Coherent multiheterodyne spectroscopy using stabilized optical frequency combs," *Phys. Rev. Lett.*, vol. 100, p. 013902, Jan 2008.

[34] B. Bernhardt, A. Ozawa, P. Jacquet, M. Jacquey, Y. Kobayashi, T. Udem, R. Holzwarth, G. Guelachvili, T. W. Hänsch, and N. Picqué, "Cavity-enhanced dual-comb spectroscopy," *Nature Photonics*, vol. 4, no. 1, pp. 55–57, 2010.

[35] I. Coddington, N. Newbury, and W. Swann, "Dual-comb spectroscopy," *Optica*, vol. 3, no. 4, pp. 414–426, 2016.

[36] P. Del'Haye, A. Schliesser, O. Arcizet, T. Wilken, R. Holzwarth, and T. J. Kippenberg, "Optical frequency comb generation from a monolithic microresonator," *Nature*, vol. 450, no. 7173, pp. 1214–1217, 2007.

[37] A. A. Savchenkov, A. B. Matsko, V. S. Ilchenko, I. Solomatine, D. Seidel, and L. Maleki, "Tunable optical frequency comb with a crystalline whispering gallery mode resonator," *Phys. Rev. Lett.*, vol. 101, p. 093902, Aug 2008.

[38] A. Bartels, D. Heinecke, and S. A. Diddams, "10-ghz self-referenced optical frequency comb," *Science*, vol. 326, no. 5953, pp. 681–681, 2009.

[39] K. J. Vahala, "Optical microcavities," *Nature*, vol. 424, p. 839, 08 2003.

[40] A. A. Savchenkov, A. B. Matsko, V. S. Ilchenko, and L. Maleki, "Optical resonators with ten million finesse," *Opt. Express*, vol. 15, pp. 6768–6773, May 2007.

[41] T. J. Kippenberg, S. M. Spillane, and K. J. Vahala, "Kerr-nonlinearity optical parametric oscillation in an ultrahigh-q toroid microcavity," *Phys. Rev. Lett.*, vol. 93, p. 083904, Aug 2004.

[42] G. New, *Introduction to Nonlinear Optics.* Cambridge University Press, 2011.

[43] T. Herr, K. Hartinger, J. Riemensberger, C. Y. Wang, E. Gavartin, R. Holzwarth, M. L. Gorodetsky, and T. J. Kippenberg, "Universal formation dynamics and noise of kerr-frequency combs in microresonators," *Nature Photonics*, vol. 6, p. 480, 06 2012.

[44] T. Herr, V. Brasch, J. D. Jost, C. Y. Wang, N. M. Kondratiev, M. L. Gorodetsky, and T. J. Kippenberg, "Temporal solitons in optical microresonators," *Nature Photonics*, vol. 8, p. 145, 12 2013.

[45] T. J. Kippenberg, A. L. Gaeta, M. Lipson, and M. L. Gorodetsky, "Dissipative kerr solitons in optical microresonators," *Science*, vol. 361, no. 6402, 2018.

[46] D. K. Armani, T. J. Kippenberg, S. M. Spillane, and K. J. Vahala, "Ultra-high-q toroid microcavity on a chip," *Nature*, vol. 421, no. 6926, pp. 925–928, 2003.

[47] M. Cai, O. Painter, and K. J. Vahala, "Observation of critical coupling in a fiber taper to a silica-microsphere whispering-gallery mode system," *Phys. Rev. Lett.*, vol. 85, pp. 74–77, 2000.

[48] S. M. Spillane, T. J. Kippenberg, O. J. Painter, and K. J. Vahala, "Ideality in a fiber-taper-coupled microresonator system for application to cavity quantum electrodynamics," *Phys. Rev. Lett.*, vol. 91, p. 043902, 2003.

[49] M. A. Foster, A. C. Turner, J. E. Sharping, B. S. Schmidt, M. Lipson, and A. L. Gaeta, "Broad-band optical parametric gain on a silicon photonic chip," *Nature*, vol. 441, p. 960, 06 2006.

[50] F. Ferdous, H. Miao, D. E. Leaird, K. Srinivasan, J. Wang, L. Chen, L. T. Varghese, and A. M. Weiner, "Spectral line-by-line pulse shaping of on-chip microresonator frequency combs," *Nature Photonics*, vol. 5, no. 12, pp. 770–776, 2011.

[51] L. A. Lugiato and R. Lefever, "Spatial dissipative structures in passive optical systems," *Phys. Rev. Lett.*, vol. 58, pp. 2209–2211, May 1987.

[52] F. Leo, S. Coen, P. Kockaert, S.-P. Gorza, P. Emplit, and M. Haelterman, "Temporal cavity solitons in one-dimensional kerr media as bits in an all-optical buffer," *Nature Photonics*, vol. 4, no. 7, pp. 471–476, 2010.

[53] P. Grelu and N. Akhmediev, "Dissipative solitons for mode-locked lasers," *Nature Photonics*, vol. 6, no. 2, pp. 84–92, 2012.

[54] X. Xue, Y. Xuan, C. Wang, P.-H. Wang, Y. Liu, B. Niu, D. E. Leaird, M. Qi, and A. M. Weiner, "Thermal tuning of kerr frequency combs in silicon nitride microring resonators," *Opt. Express*, vol. 24, pp. 687–698, Jan 2016.

[55] T. Carmon, L. Yang, and K. J. Vahala, "Dynamical thermal behavior and thermal self-stability of microcavities," *Opt. Express*, vol. 12, pp. 4742–4750, Oct 2004.

[56] D. C. Cole, E. S. Lamb, P. Del'Haye, S. A. Diddams, and S. B. Papp, "Soliton crystals in kerr resonators," *Nature Photonics*, vol. 11, no. 10, pp. 671–676, 2017.

[57] M. Karpov, M. H. P. Pfeiffer, H. Guo, W. Weng, J. Liu, and T. J. Kippenberg, "Dynamics of soliton crystals in optical microresonators," *Nature Physics*, vol. 15, no. 10, pp. 1071–1077, 2019.

[58] H. Guo, M. Karpov, E. Lucas, A. Kordts, M. H. P. Pfeiffer, V. Brasch, G. Lihachev, V. E. Lobanov, M. L. Gorodetsky, and T. J. Kippenberg, "Universal dynamics and deterministic switching of dissipative kerr solitons in optical microresonators," *Nature Physics*, vol. 13, p. 94, 09 2016.

[59] J. R. Stone, T. C. Briles, T. E. Drake, D. T. Spencer, D. R. Carlson, S. A. Diddams, and S. B. Papp, "Thermal and nonlinear dissipative-soliton dynamics in kerr-microresonator frequency combs," *Phys. Rev. Lett.*, vol. 121, p. 063902, Aug 2018.

[60] T. C. Briles, J. R. Stone, T. E. Drake, D. T. Spencer, C. Fredrick, Q. Li, D. Westly, B. R. Ilic, K. Srinivasan, S. A. Diddams, and S. B. Papp, "Interlocking kerr-microresonator frequency combs for microwave to optical synthesis," *Opt. Lett.*, vol. 43, pp. 2933–2936, Jun 2018.

[61] T. Wildi, V. Brasch, J. Liu, T. J. Kippenberg, and T. Herr, “Thermally stable access to microresonator solitons via slow pump modulation,” *Opt. Lett.*, vol. 44, no. 18, pp. 4447–4450, 2019.

[62] H. Zhou, Y. Geng, W. Cui, S.-W. Huang, Q. Zhou, K. Qiu, and C. Wei Wong, “Soliton bursts and deterministic dissipative kerr soliton generation in auxiliary-assisted microcavities,” *Light: Science & Applications*, vol. 8, no. 1, p. 50, 2019.

[63] S. Zhang, J. M. Silver, L. D. Bino, F. Copie, M. T. M. Woodley, G. N. Ghalanos, A. Ø. Svela, N. Moroney, and P. Del’Haye, “Sub-milliwatt-level microresonator solitons with extended access range using an auxiliary laser,” *Optica*, vol. 6, pp. 206–212, Feb 2019.

[64] V. Brasch, M. Geiselmann, M. H. P. Pfeiffer, and T. J. Kippenberg, “Bringing short-lived dissipative kerr soliton states in microresonators into a steady state,” *Opt. Express*, vol. 24, pp. 29312–29320, Dec 2016.

[65] Y. He, Q.-F. Yang, J. Ling, R. Luo, H. Liang, M. Li, B. Shen, H. Wang, K. Vahala, and Q. Lin, “Self-starting bi-chromatic linbo3 soliton microcomb,” *Optica*, vol. 6, pp. 1138–1144, Sep 2019.

[66] A. A. Savchenkov, A. B. Matsko, D. Strekalov, V. S. Ilchenko, and L. Maleki, “Enhancement of photorefraction in whispering gallery mode resonators,” *Phys. Rev. B*, vol. 74, p. 245119, Dec 2006.

[67] Y. Furukawa, K. Kitamura, S. Takekawa, A. Miyamoto, M. Terao, and N. Suda, “Photorefraction in linbo3 as a function of [li]/[nb] and mgo concentrations,” *Applied Physics Letters*, vol. 77, pp. 2494–2496, 2020/04/15 2000.

[68] M. Asobe, O. Tadanaga, T. Yanagawa, H. Itoh, and H. Suzuki, “Reducing photorefractive effect in periodically poled zno- and mgo-doped linbo3 wavelength converters,” *Applied Physics Letters*, vol. 78, pp. 3163–3165, 2020/04/15 2001.

[69] B. Shen, L. Chang, J. Liu, H. Wang, Q.-F. Yang, C. Xiang, R. N. Wang, J. He, T. Liu, W. Xie, J. Guo, D. Kinghorn, L. Wu, Q.-X. Ji, T. J. Kippenberg, K. Vahala, and J. E. Bowers, “Integrated turnkey soliton microcombs,” *Nature*, vol. 582, no. 7812, pp. 365–369, 2020.

[70] A. S. Voloshin, J. Liu, N. M. Kondratiev, G. V. Lihachev, T. J. Kippenberg, and I. A. Bilenko, “Dynamics of soliton self-injection locking in a photonic chip-based microresonator,” *arXiv*, vol. 1912.11303.

[71] E. Obrzud, S. Lecomte, and T. Herr, “Temporal solitons in microresonators driven by optical pulses,” *Nature Photonics*, vol. 11, pp. 600 EP –, 08 2017.

[72] T. Kobayashi, H. Yao, K. Amano, Y. Fukushima, A. Morimoto, and T. Sueta, “Optical pulse compression using high-frequency electrooptic phase modulation,” *IEEE Journal of Quantum Electronics*, vol. 24, no. 2, pp. 382–387, 1988.

[73] J. K. Jang, A. Klenner, X. Ji, Y. Okawachi, M. Lipson, and A. L. Gaeta, "Synchronization of coupled optical microresonators," *Nature Photonics*, vol. 12, no. 11, pp. 688–693, 2018.

[74] W. Weng, E. Lucas, G. Lihachev, V. E. Lobanov, H. Guo, M. L. Gorodetsky, and T. J. Kippenberg, "Spectral purification of microwave signals with disciplined dissipative kerr solitons," *Phys. Rev. Lett.*, vol. 122, p. 013902, Jan 2019.

[75] M. H. Anderson, R. Bouchand, J. Liu, W. Weng, E. Obrzud, T. Herr, and T. J. Kippenberg, "Photonic chip-based resonant supercontinuum," *arXiv*, vol. 1909.00022, 2019.

[76] Y. K. Chembo and N. Yu, "Modal expansion approach to optical-frequency-comb generation with monolithic whispering-gallery-mode resonators," *Physical Review A*, vol. 82, no. 3, p. 033801, 2010.

[77] S. Coen, H. G. Randle, T. Sylvestre, and M. Erkintalo, "Modeling of octave-spanning kerr frequency combs using a generalized mean-field lugiato lefever model," *Opt. Lett.*, vol. 38, no. 1, pp. 37–39, 2013.

[78] J. Liu, E. Lucas, A. S. Raja, J. He, J. Riemensberger, R. N. Wang, M. Karpov, H. Guo, R. Bouchand, and T. J. Kippenberg, "Photonic microwave generation in the x- and k-band using integrated soliton microcombs," *Nature Photonics*, 2020.

[79] D. J. Wilson, K. Schneider, S. Hönl, M. Anderson, Y. Baumgartner, L. Czornomaz, T. J. Kippenberg, and P. Seidler, "Integrated gallium phosphide nonlinear photonics," *Nature Photonics*, vol. 14, no. 1, pp. 57–62, 2020.

[80] L. Chang, W. Xie, H. Shu, Q.-F. Yang, B. Shen, A. Boes, J. D. Peters, W. Jin, C. Xiang, S. Liu, G. Moille, S.-P. Yu, X. Wang, K. Srinivasan, S. B. Papp, K. Vahala, and J. E. Bowers, "Ultra-efficient frequency comb generation in algaas-on-insulator microresonators," *Nature Communications*, vol. 11, no. 1, p. 1331, 2020.

[81] W. Liang, D. Eliyahu, V. S. Ilchenko, A. A. Savchenkov, A. B. Matsko, D. Seidel, and L. Maleki, "High spectral purity kerr frequency comb radio frequency photonic oscillator," *Nature Communications*, vol. 6, p. 7957, 08 2015.

[82] H. Lee, T. Chen, J. Li, K. Y. Yang, S. Jeon, O. Painter, and K. J. Vahala, "Chemically etched ultrahigh-Q wedge-resonator on a silicon chip," *Nature Photonics*, vol. 6, pp. 369–373, 6 2012.

[83] X. Yi, Q.-F. Yang, K. Y. Yang, M.-G. Suh, and K. Vahala, "Soliton frequency comb at microwave rates in a high-q silica microresonator," *Optica*, vol. 2, pp. 1078–1085, Dec 2015.

[84] K. Y. Yang, D. Y. Oh, S. H. Lee, Q.-F. Yang, X. Yi, B. Shen, H. Wang, and K. Vahala, "Bridging ultrahigh-q devices and photonic circuits," *Nature Photonics*, vol. 12, no. 5, pp. 297–302, 2018.

[85] J. Riemensberger, K. Hartinger, T. Herr, V. Brasch, R. Holzwarth, and T. J. Kippenberg, “Dispersion engineering of thick high-q silicon nitride ring-resonators via atomic layer deposition,” , *Opt. Express*, vol. 20, pp. 27661–27669, Dec 2012.

[86] V. Brasch, M. Geiselmann, T. Herr, G. Lihachev, M. H. P. Pfeiffer, M. L. Gorodetsky, and T. J. Kippenberg, “Photonic chip–based optical frequency comb using soliton cherenkov radiation,” *Science*, vol. 351, no. 6271, pp. 357–360, 2016.

[87] M. Karpov, H. Guo, A. Kordts, V. Brasch, M. H. P. Pfeiffer, M. Zervas, M. Geiselmann, and T. J. Kippenberg, “Raman self-frequency shift of dissipative kerr solitons in an optical microresonator,” *Phys. Rev. Lett.*, vol. 116, p. 103902, Mar 2016.

[88] M. H. P. Pfeiffer, A. Kordts, V. Brasch, M. Zervas, M. Geiselmann, J. D. Jost, and T. J. Kippenberg, “Photonic damascene process for integrated high-q microresonator based nonlinear photonics,” *Optica*, vol. 3, no. 1, pp. 20–25, 2016.

[89] M. H. P. Pfeiffer, C. Herkommer, J. Liu, H. Guo, M. Karpov, E. Lucas, M. Zervas, and T. J. Kippenberg, “Octave-spanning dissipative kerr soliton frequency combs in si3n4 microresonators,” *Optica*, vol. 4, pp. 684–691, Jul 2017.

[90] M. H. P. Pfeiffer, J. Liu, A. S. Raja, T. Morais, B. Ghadiani, and T. J. Kippenberg, “Ultra-smooth silicon nitride waveguides based on the damascene reflow process: fabrication and loss origins,” *Optica*, vol. 5, pp. 884–892, Jul 2018.

[91] J. Liu, A. S. Raja, M. Karpov, B. Ghadiani, M. H. P. Pfeiffer, B. Du, N. J. Engelsen, H. Guo, M. Zervas, and T. J. Kippenberg, “Ultralow-power chip-based soliton microcombs for photonic integration,” *Optica*, vol. 5, pp. 1347–1353, Oct 2018.

[92] J. Liu, G. Huang, R. N. Wang, J. He, A. S. Raja, T. Liu, N. J. Engelsen, and T. J. Kippenberg, “High-yield wafer-scale fabrication of ultralow-loss, dispersion-engineered silicon nitride photonic circuits,” *arXiv*, 2020.

[93] J. S. Levy, A. Gondarenko, M. A. Foster, A. C. Turner-Foster, A. L. Gaeta, and M. Lipson, “Cmos-compatible multiple-wavelength oscillator for on-chip optical interconnects,” *Nature Photonics*, vol. 4, pp. 37–40, 01 2010.

[94] A. Gondarenko, J. S. Levy, and M. Lipson, “High confinement micron-scale silicon nitride high q ring resonator,” *Opt. Express*, vol. 17, no. 14, pp. 11366–11370, 2009.

[95] K. Luke, A. Dutt, C. B. Poitras, and M. Lipson, “Overcoming si3n4 film stress limitations for high quality factor ring resonators,” *Opt. Express*, vol. 21, pp. 22829–22833, Sep 2013.

[96] X. Xue, Y. Xuan, Y. Liu, P.-H. Wang, S. Chen, J. Wang, D. E. Leaird, M. Qi, and A. M. Weiner, “Mode-locked dark pulse kerr combs in normal-dispersion microresonators,” *Nature Photonics*, vol. 9, p. 594, 08 2015.

[97] C. Joshi, J. K. Jang, K. Luke, X. Ji, S. A. Miller, A. Klenner, Y. Okawachi, M. Lipson, and A. L. Gaeta, “Thermally controlled comb generation and soliton modelocking in microresonators,” *Opt. Lett.*, vol. 41, pp. 2565–2568, Jun 2016.

[98] Y. Xuan, Y. Liu, L. T. Varghese, A. J. Metcalf, X. Xue, P.-H. Wang, K. Han, J. A. Jaramillo-Villegas, A. A. Noman, C. Wang, S. Kim, M. Teng, Y. J. Lee, B. Niu, L. Fan, J. Wang, D. E. Leaird, A. M. Weiner, and M. Qi, “High-q silicon nitride microresonators exhibiting low-power frequency comb initiation,” *Optica*, vol. 3, pp. 1171–1180, Nov 2016.

[99] Q. Li, T. C. Briles, D. A. Westly, T. E. Drake, J. R. Stone, B. R. Ilic, S. A. Diddams, S. B. Papp, and K. Srinivasan, “Stably accessing octave-spanning microresonator frequency combs in the soliton regime,” *Optica*, vol. 4, pp. 193–203, Feb 2017.

[100] X. Ji, F. A. S. Barbosa, S. P. Roberts, A. Dutt, J. Cardenas, Y. Okawachi, A. Bryant, A. L. Gaeta, and M. Lipson, “Ultra-low-loss on-chip resonators with sub-milliwatt parametric oscillation threshold,” *Optica*, vol. 4, pp. 619–624, Jun 2017.

[101] B. Stern, X. Ji, Y. Okawachi, A. L. Gaeta, and M. Lipson, “Battery-operated integrated frequency comb generator,” *Nature*, vol. 562, no. 7727, pp. 401–405, 2018.

[102] H. Jung, C. Xiong, K. Y. Fong, X. Zhang, and H. X. Tang, “Optical frequency comb generation from aluminum nitride microring resonator,” *Opt. Lett.*, vol. 38, pp. 2810–2813, Aug 2013.

[103] Z. Gong, A. Bruch, M. Shen, X. Guo, H. Jung, L. Fan, X. Liu, L. Zhang, J. Wang, J. Li, J. Yan, and H. X. Tang, “High-fidelity cavity soliton generation in crystalline aln micro-ring resonators,” *Opt. Lett.*, vol. 43, pp. 4366–4369, Sep 2018.

[104] X. Liu, C. Sun, B. Xiong, L. Wang, J. Wang, Y. Han, Z. Hao, H. Li, Y. Luo, J. Yan, T. Wei, Y. Zhang, and J. Wang, “Integrated high-q crystalline aln microresonators for broadband kerr and raman frequency combs,” *ACS Photonics*, vol. 5, pp. 1943–1950, 05 2018.

[105] M. Zhang, C. Wang, R. Cheng, A. Shams-Ansari, and M. Lončar, “Monolithic ultra-high-q lithium niobate microring resonator,” *Optica*, vol. 4, pp. 1536–1537, Dec 2017.

[106] C. Wang, M. Zhang, M. Yu, R. Zhu, H. Hu, and M. Loncar, “Monolithic lithium niobate photonic circuits for kerr frequency comb generation and modulation,” *Nature Communications*, vol. 10, no. 1, p. 978, 2019.

[107] Z. Gong, X. Liu, Y. Xu, M. Xu, J. B. Surya, J. Lu, A. Bruch, C. Zou, and H. X. Tang, “Soliton microcomb generation at 2 μm in z-cut lithium niobate microring resonators,” *Opt. Lett.*, vol. 44, pp. 3182–3185, Jun 2019.

[108] M. Pu, L. Ottaviano, E. Semenova, and K. Yvind, “Efficient frequency comb generation in algaas-on-insulator,” *Optica*, vol. 3, no. 8, pp. 823–826, 2016.

[109] L. Razzari, D. Duchesne, M. Ferrera, R. Morandotti, S. Chu, B. E. Little, and D. J. Moss, “Cmos-compatible integrated optical hyper-parametric oscillator,” *Nature Photonics*, vol. 4, no. 1, pp. 41–45, 2010.

[110] J. Wang, Z. Lu, W. Wang, F. Zhang, J. Chen, Y. Wang, X. Zhao, J. Zheng, S. T. Chu, W. Zhao, B. E. Little, X. Qu, and W. Zhang, “Long distance measurement using single soliton microcomb,” *arXiv*, vol. 2002.10565.

[111] H. Jung, S.-P. Yu, D. R. Carlson, T. E. Drake, T. C. Briles, and S. B. Papp, “Kerr solitons with tantala ring resonators,” in *Nonlinear Optics (NLO)*, p. NW2A.3, Optical Society of America, 2019.

[112] M. Yu, Y. Okawachi, A. G. Griffith, M. Lipson, and A. L. Gaeta, “Mode-locked mid-infrared frequency combs in a silicon microresonator,” *Optica*, vol. 3, no. 8, pp. 854–860, 2016.

[113] B. J. M. Hausmann, I. Bulu, V. Venkataraman, P. Deotare, and M. Lončar, “Diamond nonlinear photonics,” *Nature Photonics*, vol. 8, pp. 369 EP –, 04 2014.

[114] A. R. Johnson, Y. Okawachi, J. S. Levy, J. Cardenas, K. Saha, M. Lipson, and A. L. Gaeta, “Chip-based frequency combs with sub-100 ghz repetition rates,” *Opt. Lett.*, vol. 37, pp. 875–877, Mar 2012.

[115] P. R. Stanfield, A. J. Leenheer, C. P. Michael, R. Sims, and M. Eichenfield, “Cmos-compatible, piezo-optomechanically tunable photonics for visible wavelengths and cryogenic temperatures,” *Opt. Express*, vol. 27, pp. 28588–28605, Sep 2019.

[116] H. Tian, J. Liu, B. Dong, J. C. Skehan, M. Zervas, T. J. Kippenberg, and S. A. Bhave, “Hybrid integrated photonics using bulk acoustic resonators,” *arXiv*, vol. 1907.10177, 2019.

[117] Y. Okawachi, M. R. E. Lamont, K. Luke, D. O. Carvalho, M. Yu, M. Lipson, and A. L. Gaeta, “Bandwidth shaping of microresonator-based frequency combs via dispersion engineering,” *Opt. Lett.*, vol. 39, pp. 3535–3538, Jun 2014.

[118] J. P. Epping, *Dispersion Engineering Silicon Nitride Waveguides for Broadband Nonlinear Frequency Conversion.* Phd thesis, University of Twente, Sept. 2015.

[119] J. Liu, V. Brasch, M. H. P. Pfeiffer, A. Kordts, A. N. Kamel, H. Guo, M. Geiselmann, and T. J. Kippenberg, “Frequency-comb-assisted broadband precision spectroscopy with cascaded diode lasers,” *Opt. Lett.*, vol. 41, pp. 3134–3137, Jul 2016.

[120] J. K. Jang, M. Erkintalo, S. G. Murdoch, and S. Coen, “Observation of dispersive wave emission by temporal cavity solitons,” *Opt. Lett.*, vol. 39, pp. 5503–5506, Oct 2014.

[121] C. Milián and D. Skryabin, “Soliton families and resonant radiation in a micro-ring resonator near zero group-velocity dispersion,” *Opt. Express*, vol. 22, pp. 3732–3739, Feb 2014.

[122] V. Brasch, E. Lucas, J. D. Jost, M. Geiselmann, and T. J. Kippenberg, "Self-referenced photonic chip soliton kerr frequency comb," *Light: Science & Applications*, vol. 6, no. 1, pp. e16202–e16202, 2017.

[123] S.-P. Yu, T. C. Briles, G. T. Moille, X. Lu, S. A. Diddams, K. Srinivasan, and S. B. Papp, "Tuning kerr-soliton frequency combs to atomic resonances," *Phys. Rev. Applied*, vol. 11, p. 044017, Apr 2019.

[124] P. Del'Haye, T. Herr, E. Gavartin, M. L. Gorodetsky, R. Holzwarth, and T. J. Kippenberg, "Octave spanning tunable frequency comb from a microresonator," *Phys. Rev. Lett.*, vol. 107, p. 063901, Aug 2011.

[125] J. D. Jost, T. Herr, C. Lecaplain, V. Brasch, M. H. P. Pfeiffer, and T. J. Kippenberg, "Counting the cycles of light using a self-referenced optical microresonator," *Optica*, vol. 2, pp. 706–711, Aug 2015.

[126] P. Del'Haye, A. Coillet, T. Fortier, K. Beha, D. C. Cole, K. Y. Yang, H. Lee, K. J. Vahala, S. B. Papp, and S. A. Diddams, "Phase-coherent microwave-to-optical link with a self-referenced microcomb," *Nature Photonics*, vol. 10, no. 8, pp. 516–520, 2016.

[127] W. C. Jiang, J. Zhang, N. G. Usechak, and Q. Lin, "Dispersion engineering of high-q silicon microresonators via thermal oxidation," *, Applied Physics Letters*, vol. 105, no. 3, 2014.

[128] P. Marin-Palomo, J. N. Kemal, M. Karpov, A. Kordts, J. Pfeifle, M. H. P. Pfeiffer, P. Trocha, S. Wolf, V. Brasch, M. H. Anderson, R. Rosenberger, K. Vijayan, W. Freude, T. J. Kippenberg, and C. Koos, "Microresonator-based solitons for massively parallel coherent optical communications," *Nature*, vol. 546, p. 274, 06 2017.

[129] P. Trocha, M. Karpov, D. Ganin, M. H. P. Pfeiffer, A. Kordts, S. Wolf, J. Krockenberger, P. Marin-Palomo, C. Weimann, S. Randel, W. Freude, T. J. Kippenberg, and C. Koos, "Ultrafast optical ranging using microresonator soliton frequency combs," *Science*, vol. 359, no. 6378, pp. 887–891, 2018.

[130] M.-G. Suh and K. J. Vahala, "Soliton microcomb range measurement," *Science*, vol. 359, no. 6378, pp. 884–887, 2018.

[131] E. Obrzud, M. Rainer, A. Harutyunyan, M. H. Anderson, J. Liu, M. Geiselmann, B. Chazelas, S. Kundermann, S. Lecomte, M. Cecconi, A. Ghedina, E. Molinari, F. Pepe, F. Wildi, F. Bouchy, T. J. Kippenberg, and T. Herr, "A microphotonic astrocomb," *Nature Photonics*, vol. 13, no. 1, pp. 31–35, 2019.

[132] M.-G. Suh, X. Yi, Y.-H. Lai, S. Leifer, I. S. Grudinin, G. Vasisht, E. C. Martin, M. P. Fitzgerald, G. Doppmann, J. Wang, D. Mawet, S. B. Papp, S. A. Diddams, C. Beichman, and K. Vahala, "Searching for exoplanets using a microresonator astrocomb," *Nature Photonics*, vol. 13, no. 1, pp. 25–30, 2019.

[133] M.-G. Suh, Q.-F. Yang, K. Y. Yang, X. Yi, and K. J. Vahala, "Microresonator soliton dual-comb spectroscopy," *Science*, vol. 354, no. 6312, pp. 600–603, 2016.

[134] M. Yu, Y. Okawachi, A. G. Griffith, N. Picqué, M. Lipson, and A. L. Gaeta, "Silicon-chip-based mid-infrared dual-comb spectroscopy," *Nat. Commun.*, vol. 9, no. 1, p. 1869, 2018.

[135] A. Dutt, C. Joshi, X. Ji, J. Cardenas, Y. Okawachi, K. Luke, A. L. Gaeta, and M. Lipson, "On-chip dual-comb source for spectroscopy," *Science Advances*, vol. 4, no. 3, 2018.

[136] Q.-F. Yang, B. Shen, H. Wang, M. Tran, Z. Zhang, K. Y. Yang, L. Wu, C. Bao, J. Bowers, A. Yariv, and K. Vahala, "Vernier spectrometer using counterpropagating soliton microcombs," *Science*, vol. 363, no. 6430, pp. 965–968, 2019.

[137] J. Riemensberger, A. Lukashchuk, M. Karpov, W. Weng, E. Lucas, J. Liu, and T. J. Kippenberg, "Massively parallel coherent laser ranging using a soliton microcomb," *Nature*, vol. 581, no. 7807, pp. 164–170, 2020.

[138] D. T. Spencer, T. Drake, T. C. Briles, J. Stone, L. C. Sinclair, C. Fredrick, Q. Li, D. Westly, B. R. Ilic, A. Bluestone, N. Volet, T. Komljenovic, L. Chang, S. H. Lee, D. Y. Oh, M.-G. Suh, K. Y. Yang, M. H. P. Pfeiffer, T. J. Kippenberg, E. Norberg, L. Theogarajan, K. Vahala, N. R. Newbury, K. Srinivasan, J. E. Bowers, S. A. Diddams, and S. B. Papp, "An optical-frequency synthesizer using integrated photonics," *Nature*, vol. 557, no. 7703, pp. 81–85, 2018.

[139] S. B. Papp, K. Beha, P. Del'Haye, F. Quinlan, H. Lee, K. J. Vahala, and S. A. Diddams, "Microresonator frequency comb optical clock," *Optica*, vol. 1, pp. 10–14, Jul 2014.

[140] Z. L. Newman, V. Maurice, T. Drake, J. R. Stone, T. C. Briles, D. T. Spencer, C. Fredrick, Q. Li, D. Westly, B. R. Ilic, B. Shen, M.-G. Suh, K. Y. Yang, C. Johnson, D. M. S. Johnson, L. Hollberg, K. J. Vahala, K. Srinivasan, S. A. Diddams, J. Kitching, S. B. Papp, and M. T. Hummon, "Architecture for the photonic integration of an optical atomic clock," *Optica*, vol. 6, pp. 680–685, May 2019.

[141] X. Ji, X. Yao, A. Klenner, Y. Gan, A. L. Gaeta, C. P. Hendon, and M. Lipson, "Chip-based frequency comb sources for optical coherence tomography," *Opt. Express*, vol. 27, pp. 19896–19905, Jul 2019.

[142] P. J. Marchand, J.-J. Ho, M. H. Pfeiffer, J. Liu, C. Hauger, T. Lasser, and T. J. Kippenberg, "Soliton microcomb based spectral domain optical coherence tomography," *arXiv*, vol. 1902.06985, 2019.

[143] H. Guo, W. Weng, J. Liu, F. Yang, W. Hansel, C. S. Bres, L. Thevenaz, R. Holzwarth, and T. J. Kippenberg, "Nanophotonic supercontinuum based mid-infrared dual-comb spectroscopy," *arXiv*, vol. 1908.00871, 2019.

[144] J. Pfeifle, V. Brasch, M. Lauermann, Y. Yu, D. Wegner, T. Herr, K. Hartinger, P. Schindler, J. Li, D. Hillerkuss, R. Schmogrow, C. Weimann, R. Holzwarth, W. Freude, J. Leuthold, T. J. Kippenberg, and C. Koos, “Coherent terabit communications with microresonator kerr frequency combs,” *Nature Photonics*, vol. 8, no. 5, pp. 375–380, 2014.

[145] M. Mazur, M.-G. Suh, A. Fülöp, J. Schröder, V. Torres-Company, M. Karlsson, K. J. Vahala, and P. A. Andrekson, “Enabling high spectral efficiency coherent superchannel transmission with soliton microcombs,” *arXiv*, vol. 1812.11046, 2018.

[146] T. Steinmetz, T. Wilken, C. Araujo-Hauck, R. Holzwarth, T. W. Hänsch, L. Pasquini, A. Manescau, S. D’Odorico, M. T. Murphy, T. Kentischer, W. Schmidt, and T. Udem, “Laser frequency combs for astronomical observations,” *Science*, vol. 321, no. 5894, pp. 1335–1337, 2008.

[147] C.-H. Li, A. J. Benedick, P. Fendel, A. G. Glenday, F. X. Kärtner, D. F. Phillips, D. Sasselov, A. Szentgyorgyi, and R. L. Walsworth, “A laser frequency comb that enables radial velocity measurements with a precision of 1 cm s-1,” *Nature*, vol. 452, no. 7187, pp. 610–612, 2008.

[148] Q.-F. Yang, X. Yi, K. Y. Yang, and K. Vahala, “Counter-propagating solitons in microresonators,” *Nature Photonics*, vol. 11, no. 9, pp. 560–564, 2017.

[149] C. Joshi, A. Klenner, Y. Okawachi, M. Yu, K. Luke, X. Ji, M. Lipson, and A. L. Gaeta, “Counter-rotating cavity solitons in a silicon nitride microresonator,” *Opt. Lett.*, vol. 43, pp. 547–550, Feb 2018.

[150] E. Lucas, G. Lihachev, R. Bouchand, N. G. Pavlov, A. S. Raja, M. Karpov, M. L. Gorodetsky, and T. J. Kippenberg, “Spatial multiplexing of soliton microcombs,” *Nature Photonics*, vol. 12, no. 11, pp. 699–705, 2018.

[151] J. D. Jost, J. L. Hall, and J. Ye, “Continuously tunable, precise, single frequency optical signal generator,” *Opt. Express*, vol. 10, pp. 515–520, Jun 2002.

[152] M. T. Hummon, S. Kang, D. G. Bopp, Q. Li, D. A. Westly, S. Kim, C. Fredrick, S. A. Diddams, K. Srinivasan, V. Aksyuk, and J. E. Kitching, “Photonic chip for laser stabilization to an atomic vapor with 10−11 instability,” *Optica*, vol. 5, pp. 443–449, Apr 2018.

[153] J. Kitching, “Chip-scale atomic devices,” *Applied Physics Reviews*, vol. 5, p. 031302, 2020/05/09 2018.

[154] S. Knappe, V. Shah, P. D. D. Schwindt, L. Hollberg, J. Kitching, L.-A. Liew, and J. Moreland, “A microfabricated atomic clock,” *Applied Physics Letters*, vol. 85, pp. 1460–1462, 2020/04/12 2004.

[155] L.-A. Liew, S. Knappe, J. Moreland, H. Robinson, L. Hollberg, and J. Kitching, “Microfabricated alkali atom vapor cells,” *Applied Physics Letters*, vol. 84, pp. 2694–2696, 2020/04/26 2004.

[156] M. Fleischhauer, A. Imamoglu, and J. P. Marangos, “Electromagnetically induced transparency: Optics in coherent media,” *Rev. Mod. Phys.*, vol. 77, pp. 633–673, Jul 2005.

[157] S. Kim, D. A. Westly, B. J. Roxworthy, Q. Li, A. Yulaev, K. Srinivasan, and V. A. Aksyuk, “Photonic waveguide to free-space gaussian beam extreme mode converter,” *Light: Science & Applications*, vol. 7, no. 1, p. 72, 2018.

[158] N. Kuse and M. E. Fermann, “Frequency-modulated comb lidar,” *APL Photonics*, vol. 4, no. 10, p. 106105, 2019.

[159] X. Yi, Q.-F. Yang, X. Zhang, K. Y. Yang, X. Li, and K. Vahala, “Single-mode dispersive waves and soliton microcomb dynamics,” *Nature Communications*, vol. 8, p. 14869, 03 2017.

[160] Z. Jiang, C.-B. Huang, D. E. Leaird, and A. M. Weiner, “Optical arbitrary waveform processing of more than 100 spectral comb lines,” *Nature Photonics*, vol. 1, no. 8, pp. 463–467, 2007.

[161] S. T. Cundiff and A. M. Weiner, “Optical arbitrary waveform generation,” *Nature Photonics*, vol. 4, no. 11, pp. 760–766, 2010.

[162] A. M. Weiner, “Femtosecond pulse shaping using spatial light modulators,” *Review of Scientific Instruments*, vol. 71, pp. 1929–1960, 2020/04/16 2000.

[163] J. P. Heritage, A. M. Weiner, and R. N. Thurston, “Picosecond pulse shaping by spectral phase and amplitude manipulation,” *Opt. Lett.*, vol. 10, pp. 609–611, Dec 1985.

[164] V. Brasch, Q.-F. Chen, S. Schiller, and T. J. Kippenberg, “Radiation hardness of high-q silicon nitride microresonators for space compatible integrated optics,” *Opt. Express*, vol. 22, pp. 30786–30794, Dec 2014.

[165] D. Z. Anderson, V. Mizrahi, and J. E. Sipe, “Model for second-harmonic generation in glass optical fibers based on asymmetric photoelectron emission from defect sites,” *Opt. Lett.*, vol. 16, pp. 796–798, Jun 1991.

[166] A. Billat, D. Grassani, M. H. P. Pfeiffer, S. Kharitonov, T. J. Kippenberg, and C.-S. Brès, “Large second harmonic generation enhancement in si3n4 waveguides by all-optically induced quasi-phase-matching,” *Nature Communications*, vol. 8, no. 1, p. 1016, 2017.

[167] F. Gyger, J. Liu, F. Yang, J. He, A. S. Raja, R. N. Wang, S. A. Bhave, T. J. Kippenberg, and L. Thévenaz, “Observation of stimulated brillouin scattering in silicon nitride integrated waveguides,” *Phys. Rev. Lett.*, vol. 124, p. 013902, Jan 2020.

[168] M. J. Shaw, J. Guo, G. A. Vawter, S. Habermehl, and C. T. Sullivan, “Fabrication techniques for low-loss silicon nitride waveguides,” in *Proc.SPIE*, vol. 5720, 1 2005.

[169] B. Stern, X. Ji, A. Dutt, and M. Lipson, “Compact narrow-linewidth integrated laser based on a low-loss silicon nitride ring resonator,” *Opt. Lett.*, vol. 42, no. 21, pp. 4541–4544, 2017.

[170] A. S. Raja, A. S. Voloshin, H. Guo, S. E. Agafonova, J. Liu, A. S. Gorodnitskiy, M. Karpov, N. G. Pavlov, E. Lucas, R. R. Galiev, A. E. Shitikov, J. D. Jost, M. L. Gorodetsky, and T. J. Kippenberg, "Electrically pumped photonic integrated soliton microcomb," *Nature Communications*, vol. 10, no. 1, p. 680, 2019.

[171] D. Liang and J. E. Bowers, "Recent progress in lasers on silicon," *Nature Photonics*, vol. 4, p. 511, 07 2010.

[172] Z. Wang, K. Van Gasse, V. Moskalenko, S. Latkowski, E. Bente, B. Kuyken, and G. Roelkens, "A iii-v-on-si ultra-dense comb laser," *Light: Science & Applications*, vol. 6, no. 5, pp. e16260–e16260, 2017.

[173] G. Huang, E. Lucas, J. Liu, A. S. Raja, G. Lihachev, M. L. Gorodetsky, N. J. Engelsen, and T. J. Kippenberg, "Thermorefractive noise in silicon-nitride microresonators," *Phys. Rev. A*, vol. 99, p. 061801, Jun 2019.

[174] C. Xiang, W. Jin, J. Guo, J. D. Peters, M. J. Kennedy, J. Selvidge, P. A. Morton, and J. E. Bowers, "Narrow-linewidth iii-v/si/si3n4 laser using multilayer heterogeneous integration," *Optica*, vol. 7, pp. 20–21, Jan 2020.

[175] T. Komljenovic, M. Davenport, J. Hulme, A. Y. Liu, C. T. Santis, A. Spott, S. Srinivasan, E. J. Stanton, C. Zhang, and J. E. Bowers, "Heterogeneous silicon photonic integrated circuits," *Journal of Lightwave Technology*, vol. 34, pp. 20–35, Jan 2016.

[176] H. Park, C. Zhang, M. A. Tran, and T. Komljenovic, "Heterogeneous silicon nitride photonics," *Optica*, vol. 7, pp. 336–337, Apr 2020.

[177] D. Liang, G. Roelkens, R. Baets, and J. Bowers, "Hybrid integrated platforms for silicon photonics," *Materials*, vol. 3, pp. 1782–1802, 2010.

[178] J. Liu, H. Tian, E. Lucas, A. S. Raja, G. Lihachev, R. N. Wang, J. He, T. Liu, M. H. Anderson, W. Weng, S. A. Bhave, and T. J. Kippenberg, "Monolithic piezoelectric control of soliton microcombs," *Nature*, 2020.

[179] M. Churaev, S. Hööhl, T. Liu, J. C. Skehan, J. Riemensberger, D. Caimi, J. Liu, P. Seidler, and T. J. Kippenberg, "Hybrid si3n4-linbo3 integrated platform for electro-optic conversion," *CLEO 2020, STh1F.3*, 2020.

[180] A. Rickman, "The commercialization of silicon photonics," *Nature Photonics*, vol. 8, no. 8, pp. 579–582, 2014.

[181] D. Thomson, A. Zilkie, J. E. Bowers, T. Komljenovic, G. T. Reed, L. Vivien, D. Marris-Morini, E. Cassan, L. Virot, J.-M. Fédéli, J.-M. Hartmann, J. H. Schmid, D.-X. Xu, F. Boeuf, P. O'Brien, G. Z. Mashanovich, and M. Nedeljkovic, "Roadmap on silicon photonics," *Journal of Optics*, vol. 18, p. 073003, jun 2016.

[182] J. Michel, J. Liu, and L. C. Kimerling, "High-performance ge-on-si photodetectors," *Nature Photonics*, vol. 4, p. 527, 07 2010.

[183] M. Smit, X. Leijtens, H. Ambrosius, E. Bente, J. van der Tol, B. Smalbrugge, T. de Vries, E.-J. Geluk, J. Bolk, R. van Veldhoven, L. Augustin, P. Thijs, D. D'Agostino, H. Rabbani, K. Lawniczuk, S. Stopinski, S. Tahvili, A. Corradi, E. Kleijn, D. Dzibrou, M. Felicetti, E. Bitincka, V. Moskalenko, J. Zhao, R. Santos, G. Gilardi, W. Yao, K. Williams, P. Stabile, P. Kuindersma, J. Pello, S. Bhat, Y. Jiao, D. Heiss, G. Roelkens, M. Wale, P. Firth, F. Soares, N. Grote, M. Schell, H. Debregeas, M. Achouche, J.-L. Gentner, A. Bakker, T. Korthorst, D. Gallagher, A. Dabbs, A. Melloni, F. Morichetti, D. Melati, A. Wonfor, R. Penty, R. Broeke, B. Musk, and D. Robbins, "An introduction to inp-based generic integration technology," vol. 29, no. 8, p. 083001, 2014.

[184] T. Horikawa, D. Shimura, H. Okayama, S. Jeong, H. Takahashi, J. Ushida, Y. Sobu, A. Shiina, M. Tokushima, K. Kinoshita, and T. Mogami, "A 300-mm silicon photonics platform for large-scale device integration," *IEEE Journal of Selected Topics in Quantum Electronics*, vol. 24, pp. 1–15, July 2018.

[185] D. Marpaung, J. Yao, and J. Capmany, "Integrated microwave photonics," *Nature Photonics*, vol. 13, no. 2, pp. 80–90, 2019.

[186] B. J. Eggleton, C. G. Poulton, P. T. Rakich, M. J. Steel, and G. Bahl, "Brillouin integrated photonics," *Nature Photonics*, vol. 13, no. 10, pp. 664–677, 2019.

[187] A. L. Gaeta, M. Lipson, and T. J. Kippenberg, "Photonic-chip-based frequency combs," *Nature Photonics*, vol. 13, no. 3, pp. 158–169, 2019.

[188] C. Wang, M. Zhang, X. Chen, M. Bertrand, A. Shams-Ansari, S. Chandrasekhar, P. Winzer, and M. Lončar, "Integrated lithium niobate electro-optic modulators operating at cmos-compatible voltages," *Nature*, vol. 562, no. 7725, pp. 101–104, 2018.

[189] N. Gruhler, C. Benz, H. Jang, J.-H. Ahn, R. Danneau, and W. H. P. Pernice, "High-quality si3n4 circuits as a platform for graphene-based nanophotonic devices," *Opt. Express*, vol. 21, pp. 31678–31689, Dec 2013.

[190] C. T. Phare, Y.-H. Daniel Lee, J. Cardenas, and M. Lipson, "Graphene electro-optic modulator with 30 ghz bandwidth," *Nature Photonics*, vol. 9, no. 8, pp. 511–514, 2015.

[191] I. Datta, S. H. Chae, G. R. Bhatt, M. A. Tadayon, B. Li, Y. Yu, C. Park, J. Park, L. Cao, D. N. Basov, J. Hone, and M. Lipson, "Low-loss composite photonic platform based on 2d semiconductor monolayers," *Nature Photonics*, vol. 14, no. 4, pp. 256–262, 2020.

[192] N. Hosseini, R. Dekker, M. Hoekman, M. Dekkers, J. Bos, A. Leinse, and R. Heideman, "Stress-optic modulator in triplex platform using a piezoelectric lead zirconate titanate (pzt) thin film," *Opt. Express*, vol. 23, pp. 14018–14026, Jun 2015.

[193] K. Alexander, J. P. George, J. Verbist, K. Neyts, B. Kuyken, D. Van Thourhout, and J. Beeckman, "Nanophotonic pockels modulators on a silicon nitride platform," *Nature Communications*, vol. 9, no. 1, p. 3444, 2018.

[194] W. Jin, R. G. Polcawich, P. A. Morton, and J. E. Bowers, "Piezoelectrically tuned silicon nitride ring resonator," *Opt. Express*, vol. 26, pp. 3174–3187, Feb 2018.

[195] C. O. de Beeck, B. Haq, L. Elsinger, A. Gocalinska, E. Pelucchi, B. Corbett, G. Roelkens, and B. Kuyken, "Heterogeneous iii-v on silicon nitride amplifiers and lasers via microtransfer printing," *Optica*, vol. 7, pp. 386–393, May 2020.

[196] D. J. Blumenthal, R. Heideman, D. Geuzebroek, A. Leinse, and C. Roeloffzen, "Silicon nitride in silicon photonics," *Proceedings of the IEEE*, vol. 106, no. 12, pp. 2209–2231, 2018.

[197] D. J. Moss, R. Morandotti, A. L. Gaeta, and M. Lipson, "New cmos-compatible platforms based on silicon nitride and hydex for nonlinear optics," *Nature Photonics*, vol. 7, p. 597, 07 2013.

[198] A. Kovach, D. Chen, J. He, H. Choi, A. H. Dogan, M. Ghasemkhani, H. Taheri, and A. M. Armani, "Emerging material systems for integrated optical kerr frequency combs," *Adv. Opt. Photon.*, vol. 12, pp. 135–222, Mar 2020.

[199] D. T. Spencer, J. F. Bauters, M. J. R. Heck, and J. E. Bowers, "Integrated waveguide coupled si3n4 resonators in the ultrahigh-q regime," *Optica*, vol. 1, pp. 153–157, Sep 2014.

[200] S. Gundavarapu, G. M. Brodnik, M. Puckett, T. Huffman, D. Bose, R. Behunin, J. Wu, T. Qiu, C. Pinho, N. Chauhan, J. Nohava, P. T. Rakich, K. D. Nelson, M. Salit, and D. J. Blumenthal, "Sub-hertz fundamental linewidth photonic integrated brillouin laser," *Nature Photonics*, vol. 13, no. 1, pp. 60–67, 2019.

[201] J. F. Bauters, M. J. R. Heck, D. D. John, J. S. Barton, C. M. Bruinink, A. Leinse, R. G. Heideman, D. J. Blumenthal, and J. E. Bowers, "Planar waveguides with less than 0.1 db/m propagation loss fabricated with wafer bonding," *Opt. Express*, vol. 19, pp. 24090–24101, Nov 2011.

[202] Z. Ye, A. Fülöp, Óskar Bjarki Helgason, P. A. Andrekson, and V. Torres-Company, "Low-loss high-q silicon-rich silicon nitride microresonators for kerr nonlinear optics," *Opt. Lett.*, vol. 44, pp. 3326–3329, Jul 2019.

[203] H. E. Dirani, L. Youssef, C. Petit-Etienne, S. Kerdiles, P. Grosse, C. Monat, E. Pargon, and C. Sciancalepore, "Ultralow-loss tightly confining si3n4 waveguides and high-q microresonators," *Opt. Express*, vol. 27, pp. 30726–30740, Oct 2019.

[204] S. K. Selvaraja, P. D. Heyn, G. Winroth, P. Ong, G. Lepage, C. Cailler, A. Rigny, K. K. Bourdelle, W. Bogaerts, D. V. Thourhout, J. V. Campenhout, and P. Absil, "Highly uniform and low-loss passive silicon photonics devices using a 300mm cmos platform," in *Optical Fiber Communication Conference*, p. Th2A.33, Optical Society of America, 2014.

[205] C. Ciminelli, F. Dell'Olio, M. N. Armenise, F. M. Soares, and W. Passenberg, "High performance inp ring resonator for new generation monolithically integrated optical gyroscopes," *Opt. Express*, vol. 21, pp. 556–564, Jan 2013.

[206] D. Huang, M. A. Tran, J. Guo, J. Peters, T. Komljenovic, A. Malik, P. A. Morton, and J. E. Bowers, “High-power sub-khz linewidth lasers fully integrated on silicon,” *Optica*, vol. 6, pp. 745–752, Jun 2019.

[207] M. Aspelmeyer, T. J. Kippenberg, and F. Marquardt, “Cavity optomechanics,” *Rev. Mod. Phys.*, vol. 86, pp. 1391–1452, Dec 2014.

[208] J. Wang, F. Sciarrino, A. Laing, and M. G. Thompson, “Integrated photonic quantum technologies,” *Nature Photonics*, 2019.

[209] H. Lee, T. Chen, J. Li, O. Painter, and K. J. Vahala, “Ultra-low-loss optical delay line on a silicon chip,” *Nature Communications*, vol. 3, no. 1, p. 867, 2012.

[210] A. A. Savchenkov, A. B. Matsko, V. S. Ilchenko, N. Yu, and L. Maleki, “Whispering-gallery-mode resonators as frequency references. ii. stabilization,” *J. Opt. Soc. Am. B*, vol. 24, pp. 2988–2997, Dec 2007.

[211] E. Agrell, M. Karlsson, A. R. Chraplyvy, D. J. Richardson, P. M. Krummrich, P. Winzer, K. Roberts, J. K. Fischer, S. J. Savory, B. J. Eggleton, M. Secondini, F. R. Kschischang, A. Lord, J. Prat, I. Tomkos, J. E. Bowers, S. Srinivasan, M. Brandt-Pearce, and N. Gisin, “Roadmap of optical communications,” *Journal of Optics*, vol. 18, p. 063002, may 2016.

[212] P. Muñoz, P. W. L. van Dijk, D. Geuzebroek, M. Geiselmann, C. Domínguez, A. Stassen, J. D. Doménech, M. Zervas, A. Leinse, C. G. H. Roeloffzen, B. Gargallo, R. Baños, J. Fernández, G. M. Cabanes, L. A. Bru, and D. Pastor, “Foundry developments toward silicon nitride photonics from visible to the mid-infrared,” *IEEE Journal of Selected Topics in Quantum Electronics*, vol. 25, no. 5, pp. 1–13, 2019.

[213] F. P. Payne and J. P. R. Lacey, “A theoretical analysis of scattering loss from planar optical waveguides,” *Optical and Quantum Electronics*, vol. 26, no. 10, pp. 977–986, 1994.

[214] M. L. Gorodetsky, A. D. Pryamikov, and V. S. Ilchenko, “Rayleigh scattering in high-q microspheres,” *J. Opt. Soc. Am. B*, vol. 17, pp. 1051–1057, Jun 2000.

[215] G. N. Parsons, J. H. Souk, and J. Batey, “Low hydrogen content stoichiometric silicon nitride films deposited by plasma-enhanced chemical vapor deposition,” *Journal of Applied Physics*, vol. 70, pp. 1553–1560, 2019/07/11 1991.

[216] J. Yota, J. Hander, and A. A. Saleh, “A comparative study on inductively-coupled plasma high-density plasma, plasma-enhanced, and low pressure chemical vapor deposition silicon nitride films,” *J. Vac. Sci. Technol. A*, vol. 18, no. 2, pp. 372–376, 2000.

[217] S. C. Mao, S. H. Tao, Y. L. Xu, X. W. Sun, M. B. Yu, G. Q. Lo, and D. L. Kwong, “Low propagation loss sin optical waveguide prepared by optimal low-hydrogen module,” *Opt. Express*, vol. 16, pp. 20809–20816, Dec 2008.

[218] K. Luke, Y. Okawachi, M. R. E. Lamont, A. L. Gaeta, and M. Lipson, "Broadband mid-infrared frequency comb generation in a si3n4 microresonator," *Opt. Lett.*, vol. 40, pp. 4823–4826, Nov 2015.

[219] J. H. Jang, W. Zhao, J. W. Bae, D. Selvanathan, S. L. Rommel, I. Adesida, A. Lepore, M. Kwakernaak, and J. H. Abeles, "Direct measurement of nanoscale sidewall roughness of optical waveguides using an atomic force microscope," *Applied Physics Letters*, vol. 83, pp. 4116–4118, 2019/07/12 2003.

[220] S. P. Roberts, X. Ji, J. Cardenas, A. Bryant, and M. Lipson, "Sidewall roughness in si3n4 waveguides directly measured by atomic force microscopy," in *Conference on Lasers and Electro-Optics*, p. SM3K.6, Optical Society of America, 2017.

[221] C. A. Mack, "Reducing roughness in extreme ultraviolet lithography," 2017.

[222] J. O. J. C. S. H. T. B. S. K. W. G. S. E. Nathan Marchack, Marwan Khater, "Reducing line edge roughness in si and sin through plasma etch chemistry optimization for photonic waveguide applications," 2017.

[223] C. J. Mogab, A. C. Adams, and D. L. Flamm, "Plasma etching of si and sio2—the effect of oxygen additions to cf4 plasmas," *Journal of Applied Physics*, vol. 49, pp. 3796–3803, 2019/07/12 1978.

[224] F. Ren, S. J. Pearton, J. R. Lothian, C. R. Abernathy, and W. S. Hobson, "Reduction of sidewall roughness during dry etching of sio2," *Journal of Vacuum Science & Technology B: Microelectronics and Nanometer Structures Processing, Measurement, and Phenomena*, vol. 10, pp. 2407–2411, 2019/07/12 1992.

[225] Y. Huang, Q. Zhao, L. Kamyab, A. Rostami, F. Capolino, and O. Boyraz, "Sub-micron silicon nitride waveguide fabrication using conventional optical lithography," *Opt. Express*, vol. 23, pp. 6780–6786, Mar 2015.

[226] M. H. P. Pfeiffer, C. Herkommer, J. Liu, T. Morais, M. Zervas, M. Geiselmann, and T. J. Kippenberg, "Photonic damascene process for low-loss, high-confinement silicon nitride waveguides," *IEEE Journal of Selected Topics in Quantum Electronics*, vol. 24, no. 4, pp. 1–11, 2018.

[227] A. Griffith, J. Cardenas, C. B. Poitras, and M. Lipson, "High quality factor and high confinement silicon resonators using etchless process," *Opt. Express*, vol. 20, pp. 21341–21345, Sep 2012.

[228] S. Han, D.-G. Kim, J. Hwang, I. H. Do, D. Jeong, Y.-H. Lee, D.-Y. Choi, and H. Lee, "On-chip stimulated brillouin lasers based on chalcogenide glass resonators with 10 million q-factor," in *Conference on Lasers and Electro-Optics*, p. SM4O.2, Optical Society of America, 2019.

[229] K. N. Andersen, W. E. Svendsen, T. Stimpel-Lindner, T. Sulima, and H. Baumgärtner, "Annealing and deposition effects of the chemical composition of silicon-rich nitride," *Applied Surface Science*, vol. 243, no. 1, pp. 401–408, 2005.

[230] V. E. Vamvakas, N. Vourdas, and S. Gardelis, "Optical characterization of si-rich silicon nitride films prepared by low pressure chemical vapor deposition," *Microelectronics Reliability*, vol. 47, no. 4, pp. 794–797, 2007.

[231] T. J. Kippenberg, A. L. Tchebotareva, J. Kalkman, A. Polman, and K. J. Vahala, "Purcell-factor-enhanced scattering from si nanocrystals in an optical microcavity," *Phys. Rev. Lett.*, vol. 103, p. 027406, Jul 2009.

[232] N. Akhmediev and M. Karlsson, "Cherenkov radiation emitted by solitons in optical fibers," *Phys. Rev. A*, vol. 51, pp. 2602–2607, Mar 1995.

[233] Y. Z. Hu, R. J. Gutmann, and T.-S. Chow, *Silicon Nitride Chemical Mechanical Polishing Mechanisms*, vol. 145. 11 1998.

[234] D. Zhao and X. Lu, "Chemical mechanical polishing: Theory and experiment," *Friction*, vol. 1, no. 4, pp. 306–326, 2013.

[235] K. H. Nam, I. H. Park, and S. H. Ko, "Patterning by controlled cracking," *Nature*, vol. 485, p. 221, 05 2012.

[236] H. Guo, C. Herkommer, A. Billat, D. Grassani, C. Zhang, M. H. P. Pfeiffer, W. Weng, C.-S. Brès, and T. J. Kippenberg, "Mid-infrared frequency comb via coherent dispersive wave generation in silicon nitride nanophotonic waveguides," *Nat. Photonics*, vol. 12, no. 6, pp. 330–335, 2018.

[237] L. Chang, M. H. P. Pfeiffer, N. Volet, M. Zervas, J. D. Peters, C. L. Manganelli, E. J. Stanton, Y. Li, T. J. Kippenberg, and J. E. Bowers, "Heterogeneous integration of lithium niobate and silicon nitride waveguides for wafer-scale photonic integrated circuits on silicon," *Opt. Lett.*, vol. 42, pp. 803–806, Feb 2017.

[238] R. A. Gottscho, C. W. Jurgensen, and D. J. Vitkavage, "Microscopic uniformity in plasma etching," *J. Vac. Sci. Technol. B*, vol. 10, no. 5, pp. 2133–2147, 1992.

[239] J. Liu, A. S. Raja, M. H. P. Pfeiffer, C. Herkommer, H. Guo, M. Zervas, M. Geiselmann, and T. J. Kippenberg, "Double inverse nanotapers for efficient light coupling to integrated photonic devices," *Opt. Lett.*, vol. 43, pp. 3200–3203, Jul 2018.

[240] H. Guo, J. Liu, W. Weng, and T. J. Kippenberg, "Soliton-induced mid-infrared cherenkov radiation in nano-photonic hybrid waveguides," in *Advanced Photonics 2018 (BGPP, IPR, NP, NOMA, Sensors, Networks, SPPCom, SOF)*, p. JTu6B.1, Optical Society of America, 2018.

[241] V. R. Almeida, R. R. Panepucci, and M. Lipson, "Nanotaper for compact mode conversion," *Opt. Lett.*, vol. 28, no. 15, pp. 1302–1304, 2003.

[242] R. J. Bojko, J. Li, L. He, T. Baehr-Jones, M. Hochberg, and Y. Aida, "Electron beam lithography writing strategies for low loss, high confinement silicon optical waveguides," *Journal of Vacuum Science & Technology B*, vol. 29, p. 06F309, 2018/08/06 2011.

[243] M. I. Ojovan, "Configurons: Thermodynamic parameters and symmetry changes at glass transition," *Entropy*, vol. 10, pp. 334–364, 2008.

[244] J. P. Epping, M. Hoekman, R. Mateman, A. Leinse, R. G. Heideman, A. van Rees, P. J. van der Slot, C. J. Lee, and K.-J. Boller, "High confinement, high yield si3n4 waveguides for nonlinear optical applications," *Opt. Express*, vol. 23, pp. 642–648, Jan 2015.

[245] H. E. Dirani, M. Casale, S. Kerdiles, C. Socquet-Clerc, X. Letartre, C. Monat, and C. Sciancalepore, "Crack-free silicon-nitride-on-insulator nonlinear circuits for continuum generation in the ${c}$ -band," *IEEE Photonics Technology Letters*, vol. 30, no. 4, pp. 355–358, 2018.

[246] P. Temple-Boyer, C. Rossi, E. Saint-Etienne, and E. Scheid, "Residual stress in low pressure chemical vapor deposition sinx films deposited from silane and ammonia," *Journal of Vacuum Science & Technology A*, vol. 16, no. 4, pp. 2003–2007, 1998.

[247] A. Gorin, A. Jaouad, E. Grondin, V. Aimez, and P. Charette, "Fabrication of silicon nitride waveguides for visible-light using pecvd: a study of the effect of plasma frequency on optical properties," *Opt. Express*, vol. 16, pp. 13509–13516, Sep 2008.

[248] J. Chiles, N. Nader, D. D. Hickstein, S. P. Yu, T. C. Briles, D. Carlson, H. Jung, J. M. Shainline, S. Diddams, S. B. Papp, S. W. Nam, and R. P. Mirin, "Deuterated silicon nitride photonic devices for broadband optical frequency comb generation," *Opt. Lett.*, vol. 43, no. 7, pp. 1527–1530, 2018.

[249] L. Wang, W. Xie, D. V. Thourhout, Y. Zhang, H. Yu, and S. Wang, "Nonlinear silicon nitride waveguides based on a pecvd deposition platform," *Opt. Express*, vol. 26, pp. 9645–9654, Apr 2018.

[250] C. Yang and J. Pham, "Characteristic study of silicon nitride films deposited by lpcvd and pecvd," *Silicon*, vol. 10, pp. 2561–2567, Nov 2018.

[251] C. J. Krückel, A. Fülöp, T. Klintberg, J. Bengtsson, P. A. Andrekson, and V. Torres-Company, "Linear and nonlinear characterization of low-stress high-confinement silicon-rich nitride waveguides," *Opt. Express*, vol. 23, pp. 25827–25837, Oct 2015.

[252] X. Liu, M. Pu, B. Zhou, C. J. Krückel, A. Fülöp, V. Torres-Company, and M. Bache, "Octave-spanning supercontinuum generation in a silicon-rich nitride waveguide," *Opt. Lett.*, vol. 41, pp. 2719–2722, Jun 2016.

[253] C. J. Krückel, A. Fülöp, Z. Ye, P. A. Andrekson, and V. Torres-Company, "Optical bandgap engineering in nonlinear silicon nitride waveguides," *Opt. Express*, vol. 25, pp. 15370–15380, Jun 2017.

[254] G. Moille, Q. Li, S. Kim, D. Westly, and K. Srinivasan, “Phased-locked two-color single soliton microcombs in dispersion-engineered si3n4 resonators,” *Opt. Lett.*, vol. 43, pp. 2772–2775, Jun 2018.

[255] M. Soltani, A. Matsko, and L. Maleki, “Enabling arbitrary wavelength frequency combs on chip,” *Laser & Photonics Reviews*, vol. 10, pp. 158–162, 2019/07/10 2016.

[256] S. Kim, K. Han, C. Wang, J. A. Jaramillo-Villegas, X. Xue, C. Bao, Y. Xuan, D. E. Leaird, A. M. Weiner, and M. Qi, “Dispersion engineering and frequency comb generation in thin silicon nitride concentric microresonators,” *Nature Communications*, vol. 8, no. 1, p. 372, 2017.

[257] M. Karpov, M. H. P. Pfeiffer, J. Liu, A. Lukashchuk, and T. J. Kippenberg, “Photonic chip-based soliton frequency combs covering the biological imaging window,” *Nature Communications*, vol. 9, no. 1, p. 1146, 2018.

[258] A. Taflove and S. C. Hagness, *Computational Electrodynamics: The Finite-Difference Time-Domain Method, Third Edition.* Artech House; 3 edition, 2005.

[259] J. B. Schneider, *Understanding the Finite-Difference Time-Domain Method.* www.eecs.wsu.edu/ schneidj/ufdtd, 2010.

[260] J.-P. Berenger, *Perfectly Matched Layer (PML) for Computational Electromagnetics.* Morgan & Claypool, 2007.

[261] D. Taillaert, F. V. Laere, M. Ayre, W. Bogaerts, D. V. Thourhout, P. Bienstman, and R. Baets, “Grating couplers for coupling between optical fibers and nanophotonic waveguides,” *Jpn. J. Appl. Phys*, vol. 45, no. 8R, p. 6071, 2006.

[262] L. Yang, D. Dai, B. Yang, Z. Sheng, and S. He, “Characteristic analysis of tapered lens fibers for light focusing and butt-coupling to a silicon rib waveguide,” *Appl. Opt.*, vol. 48, pp. 672–678, Feb 2009.

[263] H. S. Presby, “Near 100% efficient fiber microlenses,” in *Digest of Conference on Optical Fiber Communication*, p. PD24, Optical Society of America, 1992.

[264] O. Svelto, *Principles of Lasers (5th Edition).* Springer, 2010.

[265] A. Andryieuski and A. V. Lavrinenko, “Nanocouplers for infrared and visible light,” *Advances in OptoElectronics*, vol. 2012, no. 839747, 2012.

[266] G. Ren, S. Chen, Y. Cheng, and Y. Zhai, “Study on inverse taper based mode transformer for low loss coupling between silicon wire waveguide and lensed fiber,” *Optics Communications*, vol. 284, no. 19, pp. 4782 – 4788, 2011.

[267] R. Hunsperger, *Integrated Optics: Theory and Technology.* Advanced texts in physics, Springer New York, 2009.

[268] A. Christ, S. G. Tikhodeev, N. A. Gippius, J. Kuhl, and H. Giessen, "Waveguide-plasmon polaritons: Strong coupling of photonic and electronic resonances in a metallic photonic crystal slab," *Phys. Rev. Lett.*, vol. 91, p. 183901, 2003.

[269] R. M. Briggs, J. Grandidier, S. P. Burgos, E. Feigenbaum, and H. A. Atwater, "Efficient coupling between dielectric-loaded plasmonic and silicon photonic waveguides," *Nano Letters*, vol. 10, no. 12, pp. 4851–4857, 2010.

[270] K. Shiraishi, H. Yoda, A. Ohshima, H. Ikedo, and C. S. Tsai, "A silicon-based spot-size converter between single-mode fibers and si-wire waveguides using cascaded tapers," *Applied Physics Letters*, vol. 91, no. 14, p. 141120, 2007.

[271] H. Park, S. Kim, J. Park, J. Joo, and G. Kim, "A fiber-to-chip coupler based on si/sion cascaded tapers for si photonic chips," *Opt. Express*, vol. 21, no. 24, pp. 29313–29319, 2013.

[272] A. Sure, T. Dillon, J. Murakowski, C. Lin, D. Pustai, and D. W. Prather, "Fabrication and characterization of three-dimensional silicon tapers," *Opt. Express*, vol. 11, no. 26, pp. 3555–3561, 2003.

[273] B. Jalali and S. Fathpour, "Silicon photonics," *J. Lightwave Technol.*, vol. 24, no. 12, pp. 4600–4615, 2006.

[274] R. Nagarajan, C. H. Joyner, R. P. Schneider, J. S. Bostak, T. Butrie, A. G. Dentai, V. G. Dominic, P. W. Evans, M. Kato, M. Kauffman, D. J. H. Lambert, S. K. Mathis, A. Mathur, R. H. Miles, M. L. Mitchell, M. J. Missey, S. Murthy, A. C. Nilsson, F. H. Peters, S. C. Pennypacker, J. L. Pleumeekers, R. A. Salvatore, R. K. Schlenker, R. B. Taylor, H.-S. Tsai, M. F. Van Leeuwen, J. Webjorn, M. Ziari, D. Perkins, J. Singh, S. G. Grubb, M. S. Reffle, D. G. Mehuys, F. A. Kish, and D. F. Welch, "Large-scale photonic integrated circuits," *IEEE J. Sel. Top. Quantum Electron.*, vol. 11, no. 1, pp. 50–65, 2005.

[275] M. Cherchi, S. Ylinen, M. Harjanne, M. Kapulainen, and T. Aalto, "Dramatic size reduction of waveguide bends on a micron-scale silicon photonic platform," *Opt. Express*, vol. 21, no. 15, pp. 17814–17823, 2013.

[276] L.-W. Luo, N. Ophir, C. P. Chen, L. H. Gabrielli, C. B. Poitras, K. Bergmen, and M. Lipson, "WDM-compatible mode-division multiplexing on a silicon chip," *Nat. Commun.*, vol. 5, no. 3069, 2014.

[277] A. C. Turner, C. Manolatou, B. S. Schmidt, M. Lipson, M. A. Foster, J. E. Sharping, and A. L. Gaeta, "Tailored anomalous group-velocity dispersion in silicon channel waveguides," *Opt. Express*, vol. 14, no. 10, pp. 4357–4362, 2006.

[278] C. W. Gardiner and M. J. Collett, "Input and output in damped quantum systems: Quantum stochastic differential equations and the master equation," *Phys. Rev. A*, vol. 31, pp. 3761–3774, Jun 1985.

[279] V. B. Braginsky, M. L. Gorodetsky, and V. S. Ilchenko, "Quality-factor and nonlinear properties of optical whispering-gallery modes," *Phys. Lett. A*, vol. 137, no. 7, pp. 393–397, 1989.

[280] J. C. Knight, G. Cheung, F. Jacques, and T. A. Birks, "Phase-matched excitation of whispering-gallery-mode resonances by a fiber taper," *Opt. Letters*, vol. 22, no. 15, pp. 1129–1131, 1997.

[281] M. L. Gorodetsky and V. S. Ilchenko, "Optical microsphere resonators: optimal coupling to high-Q whispering gallery modes," *J. Opt. Soc. Am. B*, vol. 16, no. 1, pp. 147–164, 1999.

[282] C. Reimer, M. Kues, P. Roztocki, B. Wetzel, F. Grazioso, B. E. Little, S. T. Chu, T. Johnston, Y. Bromberg, L. Caspani, D. J. Moss, and R. Morandotti, "Generation of multiphoton entangled quantum states by means of integrated frequency combs," *Science*, vol. 351, no. 6278, pp. 1176–1180, 2016.

[283] A. Dutt, K. Luke, S. Manipatruni, A. L. Gaeta, P. Nussenzveig, and M. Lipson, "On-chip optical squeezing," *Phys. Rev. Applied*, vol. 3, p. 044005, Apr 2015.

[284] M. Soltani, S. Yegnanarayanan, and A. Adibi, "Ultra-high Q planar silicon microdisk resonators for chip-scale silicon photonics," *Opt. Express*, vol. 15, no. 8, pp. 4694–4704, 2007.

[285] E. S. Hosseini, S. Yegnanarayanan, A. H. Atabaki, M. Soltani, and A. Adibi, "Systematic design and fabrication of high-Q single-mode pulley-coupled planar silicon nitride microdisk resonators at visible wavelengths," *Opt. Express*, vol. 18, no. 3, pp. 2127–2136, 2010.

[286] M. Ghulinyan, F. Ramiro-Manzano, N. Prtljaga, R. Guider, I. Carusotto, A. Pitanti, G. Pucker, and L. Pavesi, "Oscillatory vertical coupling between a whispering-gallery resonator and a bus waveguide," *Phys. Rev. Lett.*, vol. 110, no. 16, p. 163901, 2013.

[287] F. Xia, L. Sekaric, and Y. A. Vlasov, "Mode conversion losses in silicon-on-insulator photonic wire based racetrack resonators," *Opt. Express*, vol. 14, no. 9, pp. 3872–3886, 2006.

[288] A. Li, T. Van Vaerenbergh, P. De Heyn, P. Bienstman, and W. Bogaerts, "Backscattering in silicon microring resonators: a quantitative analysis," *Laser Photon. Rev.*, vol. 431, pp. 0–13, 2016.

[289] T. Herr, V. Brasch, J. D. Jost, I. Mirgorodskiy, G. Lihachev, M. L. Gorodetsky, and T. J. Kippenberg, "Mode spectrum and temporal soliton formation in optical microresonators," *Phys. Rev. Lett.*, vol. 113, p. 123901, 2014.

[290] M. H. P. Pfeiffer, J. Liu, M. Geiselmann, and T. J. Kippenberg, "Coupling ideality of integrated planar high-q microresonators," *Phys. Rev. Applied*, vol. 7, p. 024026, Feb 2017.

[291] C. W. Gardiner and M. J. Collet, “Input and output in damped quantum systems: Quantum stochastic differential equations and the master equation,” *Phys. Rev. A*, vol. 31, pp. 3761–3774, June 1985.

[292] H. A. Haus, *Waves and Fields in Optoelectronics.* Prentice-Hall Series in Solid State Physical Electronics, Prentice Hall, Incorporated, 1984.

[293] T. Kippenberg and K. Vahala, “Cavity opto-mechanics,” *Opt. Express*, vol. 15, pp. 17172–17205, Dec 2007.

[294] D. R. Rowland and J. D. Love, “Evanescent wave coupling of whispering gallery modes of a dielectric cylinder,” *IEE Proceedings J-Optoelectronics*, vol. 140, no. 3, p. 177, 1993.

[295] A. Yariv, “Universal relations for coupling of optical power between microresonators and dielectric waveguides,” *Electron. Lett.*, vol. 36, no. 4, pp. 321–322, 2000.

[296] A. Yariv, “Coupled-mode theory for guided-wave optics,” *IEEE J. Quant. Electron.*, vol. 9, no. 9, pp. 919–933, 1973.

[297] B. E. Little, S. T. Chu, H. A. Haus, J. Foresi, and J. Laine, “Microring resonator channel dropping filters,” *J. Lightwave Technol.*, vol. 15, pp. 998–1005, Jun. 1997.

[298] P. Del’Haye, O. Arcizet, M. L. Gorodetsky, R. Holzwarth, and T. J. Kippenberg, “Frequency comb assisted diode laser spectroscopy for measurement of microcavity dispersion,” *Nature Photonics*, vol. 3, pp. 529–533, 09 2009.

[299] A. Taflove and S. C. Hagness, *Computational Electrodynamics: The Finite-Difference Time-Domain Method.* Artech House antennas and propagation library, Artech House, 2005.

[300] W. W. Lui, T. Hirono, K. Yokoyama, and W.-P. Huang, “Polarization rotation in semiconductor bending waveguides: a coupled-mode theory formulation,” *J. Lightwave Technol.*, vol. 16, no. 5, pp. 929–936, 1998.

[301] L. Liu, Y. Ding, K. Yvind, and J. M. Hvam, “Efficient and compact TE–TM polarization converter built on silicon-on-insulator platform with a simple fabrication process,” *Opt. Lett.*, vol. 36, no. 7, pp. 1059–1061, 2011.

[302] E. Baumann, F. R. Giorgetta, I. Coddington, L. C. Sinclair, K. Knabe, W. C. Swann, and N. R. Newbury, “Comb-calibrated frequency-modulated continuous-wave ladar for absolute distance measurements,” *Opt. Lett.*, vol. 38, pp. 2026–2028, Jun 2013.

[303] E. Baumann, F. R. Giorgetta, J.-D. Deschênes, W. C. Swann, I. Coddington, and N. R. Newbury, “Comb-calibrated laser ranging for three-dimensional surface profiling with micrometer-level precision at a distance,” *Opt. Express*, vol. 22, pp. 24914–24928, Oct 2014.

[304] F. R. Giorgetta, I. Coddington, E. Baumann, W. C. Swann, and N. R. Newbury, “Fast high-resolution spectroscopy of dynamic continuous-wave laser sources,” *Nature Photonics*, vol. 4, no. 12, pp. 853–857, 2010.

[305] K. Urabe and O. Sakai, “Absorption spectroscopy using interference between optical frequency comb and single-wavelength laser,” *Applied Physics Letters*, vol. 101, no. 5, 2012.

[306] A. Nishiyama, D. Ishikawa, and M. Misono, “High resolution molecular spectroscopic system assisted by an optical frequency comb,” *J. Opt. Soc. Am. B*, vol. 30, pp. 2107–2112, Aug 2013.

[307] A. Nishiyama, A. Matsuba, and M. Misono, “Precise frequency measurement and characterization of a continuous scanning single-mode laser with an optical frequency comb,” *Opt. Lett.*, vol. 39, pp. 4923–4926, Aug 2014.

[308] P. Del'Haye, A. Coillet, W. Loh, K. Beha, S. B. Papp, and S. A. Diddams, “Phase steps and resonator detuning measurements in microresonator frequency combs,” *Nat Commun*, vol. 6, 01 2015.

[309] A. Kordts, M. H. P. Pfeiffer, H. Guo, V. Brasch, and T. J. Kippenberg, “Higher order mode suppression in high-q anomalous dispersion sin microresonators for temporal dissipative kerr soliton formation,” *Opt. Lett.*, vol. 41, pp. 452–455, Feb 2016.

[310] M. J. Thorpe, R. J. Jones, K. D. Moll, J. Ye, and R. Lalezari, “Precise measurements of optical cavity dispersion and mirror coating properties via femtosecond combs,” *Opt. Express*, vol. 13, pp. 882–888, Feb 2005.

[311] A. Schliesser, C. Gohle, T. Udem, and T. W. Hänsch, “Complete characterization of a broadband high-finesse cavity using an optical frequency comb,” *Opt. Express*, vol. 14, pp. 5975–5983, Jun 2006.

[312] J. Li, H. Lee, K. Y. Yang, and K. J. Vahala, “Sideband spectroscopy and dispersion measurement in microcavities,” *Opt. Express*, vol. 20, pp. 26337–26344, Nov 2012.

[313] L. S. Rothman *et al*, “The hitran2012 molecular spectroscopic database,” , *J. Quant. Spectrosc. Radiat. Trans.*, vol. 130, pp. 4–50, 11 2013.

[314] W. C. Swann and S. L. Gilbert, “Pressure-induced shift and broadening of 1510–1540-nm acetylene wavelength calibration lines,” *J. Opt. Soc. Am. B*, vol. 17, pp. 1263–1270, Jul 2000.

[315] W. C. Swann and S. L. Gilbert, “Pressure-induced shift and broadening of 1560–1630-nm carbon monoxide wavelength-calibration lines,” *J. Opt. Soc. Am. B*, vol. 19, pp. 2461–2467, Oct 2002.

[316] Q. Li, A. A. Eftekhar, Z. Xia, and A. Adibi, "Unified approach to mode splitting and scattering loss in high-q whispering-gallery-mode microresonators," *Phys. Rev. A*, vol. 88, p. 033816, Sep 2013.

[317] S. Wójtewicz, A. Cygan, J. Domysławska, K. Bielska, P. Morzyński, P. Masłowski, R. Ciuryło, and D. Lisak, "Response of an optical cavity to phase-controlled incomplete power switching of nearly resonant incident light," *Opt. Express*, vol. 26, no. 5, pp. 5644–5654, 2018.

[318] Z. Ye, K. Twayana, P. A. Andrekson, and V. Torres-Company, "High-q si3n4 microresonators based on a subtractive processing for kerr nonlinear optics," *Opt. Express*, vol. 27, pp. 35719–35727, Nov 2019.

[319] D.-G. Kim, S. Han, J. Hwang, I. H. Do, D. Jeong, J.-H. Lim, Y.-H. Lee, M. Choi, Y.-H. Lee, D.-Y. Choi, and H. Lee, "Universal light-guiding geometry for high-nonlinear resonators having molecular-scale roughness," *arXiv*, vol. 1909.13594, 2019.

[320] A. Arbabi and L. L. Goddard, "Measurements of the refractive indices and thermo-optic coefficients of si3n4 and siox using microring resonances," *Opt. Lett.*, vol. 38, pp. 3878–3881, Oct 2013.

[321] E. F. Burmeister, D. J. Blumenthal, and J. E. Bowers, "A comparison of optical buffering technologies," *Optical Switching and Networking*, vol. 5, no. 1, pp. 10–18, 2008.

[322] R. L. Moreira, J. Garcia, W. Li, J. Bauters, J. S. Barton, M. J. R. Heck, J. E. Bowers, and D. J. Blumenthal, "Integrated ultra-low-loss 4-bit tunable delay for broadband phased array antenna applications," *IEEE Photonics Technology Letters*, vol. 25, no. 12, pp. 1165–1168, 2013.

[323] T. Huffman, M. Davenport, M. Belt, J. E. Bowers, and D. J. Blumenthal, "Ultra-low loss large area waveguide coils for integrated optical gyroscopes," *IEEE Photonics Technology Letters*, vol. 29, no. 2, pp. 185–188, 2017.

[324] X. Ji, X. Yao, Y. Gan, A. Mohanty, M. A. Tadayon, C. P. Hendon, and M. Lipson, "On-chip tunable photonic delay line," *APL Photonics*, vol. 4, p. 090803, 2020/02/23 2019.

[325] N. Volet, X. Yi, Q. Yang, E. J. Stanton, P. A. Morton, K. Y. Yang, K. J. Vahala, and J. E. Bowers, "Micro-resonator soliton generated directly with a diode laser," *Laser Photonics Rev.*, vol. 0, no. 0, p. 1700307, 2018.

[326] S. H. Yun, G. J. Tearney, B. E. Bouma, B. H. Park, and J. F. de Boer, "High-speed spectral-domain optical coherence tomography at 1.3 μm wavelength," *Opt. Express*, vol. 11, pp. 3598–3604, Dec 2003.

[327] L. Tombez, E. J. Zhang, J. S. Orcutt, S. Kamlapurkar, and W. M. J. Green, "Methane absorption spectroscopy on a silicon photonic chip," *Optica*, vol. 4, pp. 1322–1325, Nov 2017.

[328] C. Bao, Y. Xuan, D. E. Leaird, S. Wabnitz, M. Qi, and A. M. Weiner, "Spatial mode-interaction induced single soliton generation in microresonators," *Optica*, vol. 4, pp. 1011–1015, Sep 2017.

[329] Y. Liu, Y. Xuan, X. Xue, P.-H. Wang, S. Chen, A. J. Metcalf, J. Wang, D. E. Leaird, M. Qi, and A. M. Weiner, "Investigation of mode coupling in normal-dispersion silicon nitride microresonators for kerr frequency comb generation," *Optica*, vol. 1, pp. 137–144, Sep 2014.

[330] H. Guo, E. Lucas, M. H. P. Pfeiffer, M. Karpov, M. Anderson, J. Liu, M. Geiselmann, J. D. Jost, and T. J. Kippenberg, "Intermode breather solitons in optical microresonators," *Phys. Rev. X*, vol. 7, p. 041055, Dec 2017.

[331] N. M. Kondratiev, V. E. Lobanov, A. V. Cherenkov, A. S. Voloshin, N. G. Pavlov, S. Koptyaev, and M. L. Gorodetsky, "Self-injection locking of a laser diode to a high-Q WGM microresonator," *Optics Express*, vol. 25, pp. 28167–28178, Nov. 2017.

[332] W. Liang, V. S. Ilchenko, D. Eliyahu, A. A. Savchenkov, A. B. Matsko, D. Seidel, and L. Maleki, "Ultralow noise miniature external cavity semiconductor laser," *Nature Communications*, vol. 6, no. 1, p. 7371, 2015.

[333] N. G. Pavlov, S. Koptyaev, G. V. Lihachev, A. S. Voloshin, A. S. Gorodnitskiy, M. V. Ryabko, S. V. Polonsky, and M. L. Gorodetsky, "Narrow-linewidth lasing and soliton kerr microcombs with ordinary laser diodes," *Nature Photonics*, vol. 12, no. 11, pp. 694–698, 2018.

[334] C. Henry, "Theory of the linewidth of semiconductor lasers," *IEEE Journal of Quantum Electronics*, vol. 18, no. 2, pp. 259–264, 1982.

[335] E. Lucas, M. Karpov, H. Guo, M. L. Gorodetsky, and T. J. Kippenberg, "Breathing dissipative solitons in optical microresonators," *Nature Communications*, vol. 8, p. 736, Sept. 2017.

[336] J. Hecht, "The bandwidth bottleneck that is throttling the internet," *Nature News*, vol. 536, no. 7615, p. 139, 2016.

[337] J. Capmany and D. Novak, "Microwave photonics combines two worlds," *Nature Photonics*, vol. 1, p. 319, 06 2007.

[338] P. Ghelfi, F. Laghezza, F. Scotti, G. Serafino, A. Capria, S. Pinna, D. Onori, C. Porzi, M. Scaffardi, A. Malacarne, V. Vercesi, E. Lazzeri, F. Berizzi, and A. Bogoni, "A fully photonics-based coherent radar system," *Nature*, vol. 507, p. 341, 03 2014.

[339] A. Khilo, S. J. Spector, M. E. Grein, A. H. Nejadmalayeri, C. W. Holzwarth, M. Y. Sander, M. S. Dahlem, M. Y. Peng, M. W. Geis, N. A. DiLello, J. U. Yoon, A. Motaledi, J. S. Orcutt, J. P. Wang, C. M. Sorace-Agaskar, M. A. Popovic, J. Sun, G.-R. Zhou, H. Byun, J. Chen, J. L. Hoyt, H. I. Smith, R. J. Ram, M. Perrott, T. M. Lyszczarz, E. P. Ippen, and F. X. Kartner,

"Photonic adc: overcoming the bottleneck of electronic jitter," *Optics Express*, vol. 20, no. 4, pp. 4454–4469, 2012.

[340] C. Lim, A. Nirmalathas, M. Bakaul, P. Gamage, K.-L. Lee, Y. Yang, D. Novak, and R. Waterhouse, "Fiber-wireless networks and subsystem technologies," *Journal of Lightwave Technology*, vol. 28, no. 4, pp. 390–405, 2010.

[341] M. H. Khan, H. Shen, Y. Xuan, L. Zhao, S. Xiao, D. E. Leaird, A. M. Weiner, and M. Qi, "Ultrabroad-bandwidth arbitrary radiofrequency waveform generation with a silicon photonic chip-based spectral shaper," *Nature Photonics*, vol. 4, no. 2, p. 117, 2010.

[342] V. Supradeepa, C. M. Long, R. Wu, F. Ferdous, E. Hamidi, D. E. Leaird, and A. M. Weiner, "Comb-based radiofrequency photonic filters with rapid tunability and high selectivity," *Nature Photonics*, vol. 6, no. 3, p. 186, 2012.

[343] V. Ataie, D. Esman, B.-P. Kuo, N. Alic, and S. Radic, "Subnoise detection of a fast random event," *Science*, vol. 350, no. 6266, pp. 1343–1346, 2015.

[344] E. Temprana, E. Myslivets, B.-P. Kuo, L. Liu, V. Ataie, N. Alic, and S. Radic, "Overcoming kerr-induced capacity limit in optical fiber transmission," *Science*, vol. 348, no. 6242, pp. 1445–1448, 2015.

[345] F. Riehle, "Optical clock networks," *Nature Photonics*, vol. 11, p. 25, 01 2017.

[346] T. S. Rappaport, J. N. Murdock, and F. Gutierrez, "State of the art in 60-ghz integrated circuits and systems for wireless communications," *Proceedings of the IEEE*, vol. 99, no. 8, pp. 1390–1436, 2011.

[347] J. Li, X. Yi, H. Lee, S. A. Diddams, and K. J. Vahala, "Electro-optical frequency division and stable microwave synthesis," *Science*, vol. 345, no. 6194, pp. 309–313, 2014.

[348] V. Torres-Company and A. M. Weiner, "Optical frequency comb technology for ultra-broadband radio-frequency photonics," *Laser & Photonics Reviews*, vol. 8, pp. 368–393, 2019/01/18 2014.

[349] J. Wu, X. Xu, T. G. Nguyen, S. T. Chu, B. E. Little, R. Morandotti, A. Mitchell, and D. J. Moss, "Rf photonics: An optical microcombs'perspective," *IEEE Journal of Selected Topics in Quantum Electronics*, vol. 24, no. 4, pp. 1–20, 2018.

[350] X. Xu, J. Wu, M. Tan, T. G. Nguyen, S. Chu, B. Little, R. Morandotti, A. Mitchell, and D. J. Moss, "Micro-comb based photonic local oscillator for broadband microwave frequency conversion," *Journal of Lightwave Technology*, pp. 1–1, 2019.

[351] P. A. Morton and M. J. Morton, "High-power, ultra-low noise hybrid lasers for microwave photonics and optical sensing," *J. Lightwave Technol.*, vol. 36, pp. 5048–5057, Nov 2018.

[352] X. Yi, Q.-F. Yang, K. Y. Yang, and K. Vahala, "Theory and measurement of the soliton self-frequency shift and efficiency in optical microcavities," *Opt. Lett.*, vol. 41, pp. 3419–3422, Aug 2016.

[353] A. S. Raja, J. Liu, N. Volet, R. N. Wang, J. He, E. Lucas, R. Bouchandand, P. Morton, J. Bowers, and T. J. Kippenberg, "Chip-based soliton microcomb module using a hybrid semiconductor laser," *Opt. Express*, vol. 28, pp. 2714–2721, Feb 2020.

[354] E. Lucas, P. Brochard, R. Bouchand, S. Schilt, T. Südmeyer, and T. J. Kippenberg, "Ultralow-noise photonic microwave synthesis using a soliton microcomb-based transfer oscillator," *Nature Communications*, vol. 11, no. 1, p. 374, 2020.

[355] C. W. Nelson, A. Hati, and D. A. Howe, "A collapse of the cross-spectral function in phase noise metrology," *Review of Scientific Instruments*, vol. 85, p. 024705, feb 2014.

[356] N. M. Kondratiev and M. L. Gorodetsky, "Thermorefractive noise in whispering gallery mode microresonators: Analytical results and numerical simulation," *Physics Letters A*, vol. 382, no. 33, pp. 2265–2268, 2018.

[357] T. E. Drake, T. C. Briles, J. R. Stone, D. T. Spencer, D. R. Carlson, D. D. Hickstein, Q. Li, D. Westly, K. Srinivasan, S. A. Diddams, and S. B. Papp, "Terahertz-rate kerr-microresonator optical clockwork," *Phys. Rev. X*, vol. 9, p. 031023, Aug 2019.

[358] Q.-F. Yang, X. Yi, K. Y. Yang, and K. Vahala, "Spatial-mode-interaction-induced dispersive waves and their active tuning in microresonators," *Optica*, vol. 3, pp. 1132–1135, Oct 2016.

[359] A. V. Cherenkov, V. E. Lobanov, and M. L. Gorodetsky, "Dissipative kerr solitons and cherenkov radiation in optical microresonators with third-order dispersion," *Phys. Rev. A*, vol. 95, p. 033810, Mar 2017.

[360] J. Tang, T. Hao, W. Li, D. Domenech, R. B. nos, P. M. noz, N. Zhu, J. Capmany, and M. Li, "Integrated optoelectronic oscillator," *Opt. Express*, vol. 26, pp. 12257–12265, Apr 2018.

[361] M. Merklein, B. Stiller, I. V. Kabakova, U. S. Mutugala, K. Vu, S. J. Madden, B. J. Eggleton, and R. Slavík, "Widely tunable, low phase noise microwave source based on a photonic chip," *Opt. Lett.*, vol. 41, pp. 4633–4636, Oct 2016.

[362] P. T.Do, C. Alonso-Ramos, X. L. Roux, I. Ledoux, B. Journet, and E. Cassan, "Wideband tunable microwave signal generation in a silicon-based optoelectronic oscillator," *arXiv*, vol. 1903.01137, 2019.

[363] J. Li, H. Lee, and K. J. Vahala, "Microwave synthesizer using an on-chip brillouin oscillator," *Nature Communications*, vol. 4, p. 2097, 06 2013.

[364] P. Rice, M. Moore, A. R. Barnes, M. J. Uren, N. Malbert, N. Labat, and R. Sloan, "A 10 ghz dielectric resonator oscillator using gan technology," in *2004 IEEE MTT-S International*

Microwave Symposium Digest (IEEE Cat. No.04CH37535), vol. 3, pp. 1497–1500 Vol.3, 2004.

[365] R. J. Jones and J.-C. Diels, "Stabilization of femtosecond lasers for optical frequency metrology and direct optical to radio frequency synthesis," *Phys. Rev. Lett.*, vol. 86, pp. 3288–3291, Apr 2001.

[366] M. Takamoto, F.-L. Hong, R. Higashi, and H. Katori, "An optical lattice clock," *Nature*, vol. 435, no. 7040, pp. 321–324, 2005.

[367] B. Yao, S.-W. Huang, Y. Liu, A. K. Vinod, C. Choi, M. Hoff, Y. Li, M. Yu, Z. Feng, D.-L. Kwong, *et al.*, "Gate-tunable frequency combs in graphene–nitride microresonators," *Nature*, vol. 558, no. 7710, p. 410, 2018.

[368] J. Wang, Z. Cheng, C. Shu, and H. K. Tsang, "Optical absorption in graphene-on-silicon nitride microring resonators," *IEEE Photonics Technology Letters*, vol. 27, no. 16, pp. 1765–1767, 2015.

[369] G. Moille, X. Lu, A. Rao, Q. Li, D. A. Westly, L. Ranzani, S. B. Papp, M. Soltani, and K. Srinivasan, "Kerr-microresonator soliton frequency combs at cryogenic temperatures," *Phys. Rev. Applied*, vol. 12, p. 034057, Sep 2019.

[370] C. Xiong, W. H. P. Pernice, X. Sun, C. Schuck, K. Y. Fong, and H. X. Tang, "Aluminum nitride as a new material for chip-scale optomechanics and nonlinear optics," *New Journal of Physics*, vol. 14, no. 9, p. 095014, 2012.

[371] H. Jung, K. Y. Fong, C. Xiong, and H. X. Tang, "Electrical tuning and switching of an optical frequency comb generated in aluminum nitride microring resonators," *Opt. Lett.*, vol. 39, pp. 84–87, Jan 2014.

[372] M.-A. Dubois and P. Muralt, "Properties of aluminum nitride thin films for piezoelectric transducers and microwave filter applications," *Applied Physics Letters*, vol. 74, pp. 3032–3034, 2019/11/25 1999.

[373] P. J. M. van der Slot, M. A. G. Porcel, and K.-J. Boller, "Surface acoustic waves for acousto-optic modulation in buried silicon nitride waveguides," *Opt. Express*, vol. 27, pp. 1433–1452, Jan 2019.

[374] M. Huang, "Stress effects on the performance of optical waveguides," *International Journal of Solids and Structures*, vol. 40, no. 7, pp. 1615–1632, 2003.

[375] L. Midolo, A. Schliesser, and A. Fiore, "Nano-opto-electro-mechanical systems," *Nature nanotechnology*, vol. 13, no. 1, p. 11, 2018.

[376] S. Trolier-McKinstry and P. Muralt, "Thin film piezoelectrics for mems," *Journal of Electroceramics*, vol. 12, no. 1, pp. 7–17, 2004.

[377] M. D. Williams, B. A. Griffin, T. N. Reagan, J. R. Underbrink, and M. Sheplak, "An aln mems piezoelectric microphone for aeroacoustic applications," *Journal of Microelectromechanical Systems*, vol. 21, no. 2, pp. 270–283, 2012.

[378] K. Tsubouchi and N. Mikoshiba, "Zero-temperature-coefficient saw devices on aln epitaxial films," *IEEE Transactions on Sonics and Ultrasonics*, vol. 32, no. 5, pp. 634–644, 1985.

[379] H. Zhang, Z. Wang, and S.-Y. Zhang, "Electrode effects on frequency spectra and electromechanical coupling factors of hbar," *IEEE Transactions on Ultrasonics, Ferroelectrics, and Frequency Control*, vol. 52, no. 6, pp. 1020–1025, 2005.

[380] C. L. Aardahl, J. W. Rogers, H. K. Yun, Y. Ono, D. J. Tweet, and S. T. Hsu, "Electrical properties of aln thin films deposited at low temperature on si(100)," *Thin Solid Films*, vol. 346, no. 1, pp. 174–180, 1999.

[381] I. Coddington, N. Newbury, and W. Swann, "Dual-comb spectroscopy," *Optica*, vol. 3, no. 4, p. 414, 2016.

[382] G. Piazza, P. J. Stephanou, and A. P. Pisano, "Piezoelectric aluminum nitride vibrating contour-mode mems resonators," *Journal of Microelectromechanical Systems*, vol. 15, no. 6, pp. 1406–1418, 2006.

[383] K.-J. Boller, A. van Rees, Y. Fan, J. Mak, R. E. Lammerink, C. A. Franken, P. J. van der Slot, D. A. Marpaung, C. Fallnich, J. P. Epping, R. M. Oldenbeuving, D. Geskus, R. Dekker, I. Visscher, R. Grootjans, C. G. Roelozen, M. Hoekman, E. J. Klein, A. Leinse, and R. G. Heideman, "Hybrid integrated semiconductor lasers with silicon nitride feedback circuits," *arXiv*, vol. 1911.10820.

[384] K. Umeda, H. Kawai, A. Honda, M. Akiyama, T. Kato, and T. Fukura, "Piezoelectric properties of scaln thin films for piezo-mems devices," in *2013 IEEE 26th International Conference on Micro Electro Mechanical Systems (MEMS)*, pp. 733–736, 2013.

[385] S. Fichtner, N. Wolff, F. Lofink, L. Kienle, and B. Wagner, "Alscn: A iii-v semiconductor based ferroelectric," *Journal of Applied Physics*, vol. 125, no. 11, p. 114103, 2019.

[386] W. Jin, D. John, J. Bauters, T. Bosch, B. Thibeault, and J. Bowers, "Deuterated silicon dioxide for heterogeneous integration of ultra low-loss waveguides," *Opt. Lett.*, 2020.

[387] M. Kawachi, "Recent progress in silica-based planar lightwave circuits on silicon," *IEE Proceedings - Optoelectronics*, vol. 143, no. 5, pp. 257–262, 1996.

[388] J. M. Ruano, V. Benoit, J. S. Aitchison, and J. M. Cooper, "Flame hydrolysis deposition of glass on silicon for the integration of optical and microfluidic devices," *Analytical Chemistry*, vol. 72, pp. 1093–1097, 03 2000.

[389] J. B. Spring, B. J. Metcalf, P. C. Humphreys, W. S. Kolthammer, X.-M. Jin, M. Barbieri, A. Datta, N. Thomas-Peter, N. K. Langford, D. Kundys, J. C. Gates, B. J. Smith, P. G. R. Smith, and I. A. Walmsley, "Boson sampling on a photonic chip," *Science*, vol. 339, no. 6121, pp. 798–801, 2013.

Curriculum Vitae

(updated on August 2020)

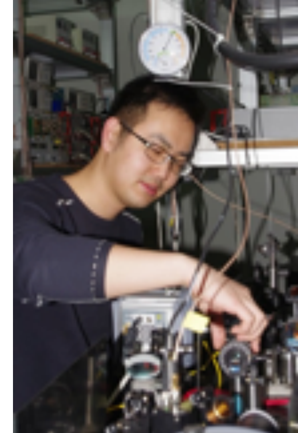

PERSONAL INFORMATION

Name: Junqiu Liu (刘骏秋)
Date of Birth: 08.08.1990
Nationality: China
E-mail: junqiu.liu@epfl.ch
Languages: Chinese Mandarin, English, French, German

EDUCATION

- **07.2016 – 07.2020**: *Doctoral Program on Photonics at École Polytechnique Fédérale de Lausanne* (*EPFL). **PhD** received. **Thesis title**: Nitride Integrated Nonlinear Photonics. **Advisor**: Prof. Tobias J. Kippenberg.
- **10.2013 – 04.2016**: *Master Program in Advanced Optical Technologies (MAOT,* DFG Excellence Initiative & Elite Network of Bavaria), *Friedrich-Alexander-Universität Erlangen-Nürnberg* (*FAU*). **Final Grade**: 1.1/1.0 (rank 1st in the department, top 1% among all university graduates), "**mit Auszeichnung bestanden (with highest distinction)**". **Master of Science with Honours** received.
- **08.2008 – 06.2012**: Undergraduate study at *School for the Gifted Young* (少年班), *University of Science and Technology of China* (*USTC*). Major in **Physics**. **Bachelor of Science** received.

WORKING EXPERIENCE

- **08.2020 – present**: Postdoc at *EPFL*. **Advisor**: Prof. Tobias J. Kippenberg.
- **07.2014 – 05.2016**: Master Thesis at *EPFL*. **Thesis Title**: Toward Octave-Spanning, Low-Power Microresonator Frequency Combs. **Advisor**: Prof. Tobias J. Kippenberg. **Co-Advisor**: Prof. Joachim von Zanthier.
- **08.2014 – 10.2014**: Summer research intern at *Physikalisches Institut, Universität Heidelberg.* **Advisor**: Prof. Shannon Whitlock.
- **02.2014 – 07.2014**: Student researcher at *Max-Planck-Institut für die Physik des Lichts* (*MPL*). **Advisor:** Prof. Vahid Sandoghdar.
- **11.2011 – 06.2013**: Bachelor Thesis and research intern at *Shanghai Branch, National Laboratory for Physical Sciences at Microscale, USTC*. **Advisor**: Prof. Shuai Chen (陈帅) and Prof. Jian-Wei Pan (潘建伟).
- **07.2011 – 10.2011**: Summer research intern at *Max-Planck-Institut für Quantenoptik* (*MPQ*). **Advisor**: Dr. Christoph Gohle and Prof. Immanuel Bloch.

RESEARCH INTERESTS

Silicon photonics, MEMS, integrated optics, frequency comb, quantum optics, microwave photonics.
Currently I am serving as an active reviewer for ***Optics Express**, **Optics Letter**, **Photonics Research***.

PUBLICATIONS (Google Scholar Link)

3 Nature, 3 Nature Photonics / Physics, *5 Nature Comm., 1 Science Adv., 4 Optica, 3 PRL / PRX / PRApplied*
(* equal contribution)

1. P. J. Marchand, J. C. Skehan, J. Riemensberger, J.-J. Ho, M. H. Pfeiffer, **J. Liu**, C. Hauger, T. Lasser, and T. J. Kippenberg, "*Soliton microcomb based spectral domain optical coherence tomography*", **Nature Communications** (in press, 2020).
2. J. Hu, J. He, **J. Liu**, A.S. Raja, M. Karpov, A. Lukashchuk, T. J. Kippenberg, and C.-S. Brès, "*Reconfigurable radiofrequency filters using versatile soliton microcombs*", **Nature Communications** (in press, 2020).
3. H. Guo*, W. Weng*, **J. Liu***, F. Yang, W. Hänsel, C. -S. Brès, L. Thévanaz, R. Holzwarth, and T. J. Kippenberg, "*Nanophotonic super continuum based mid-infrared dual-comb spectroscopy*", **Optica** (in press, 2020).
4. W. Weng, A. Kaszubowska-Anandarajah, **J. Liu**, P. M. Anandarajah, and T. J. Kippenberg, "*Frequency division using a soliton-injected semiconductor gain-switched frequency comb*", **Science Advances** (in press, 2020).
5. E. Nitiss, B. Zabelich, O. Yakar, **J. Liu**, R. N. Wang, T. J. Kippenberg, and C.-S. Brès, "*Broadband quasi-phase-matching in dispersion-engineered all-optically poled silicon nitride waveguides*", **Photonics Research** 8, 1475 (2020).
6. **J. Liu***, H. Tian*, E. Lucas*, A. S. Raja*, G. Likhachev, R. N. Wang, J. He, T. Liu, M. H. Anderson, W. Weng, S. A. Bhave, and T. J. Kippenberg, "*Monolithic piezoelectric control of soliton microcombs*", **Nature** 583, 385 (2020).
7. H. Tian, **J. Liu**, B. Dong, J. C. Skehan, M. Zervas, T. J. Kippenberg, and S. A. Bhave, "*Hybrid Integrated Photonics Using Bulk Acoustic Resonators*", **Nature Communications** 11, 3073 (2020).
8. B. Shen*, L. Chang*, **J. Liu***, H. Wang*, Q.-F. Yang*, C. Xiang, R. N. Wang, J. He, T. Liu, W. Xie, J. Guo, D. Kinghorn, L. Wu, Q.-X. Ji, T. J. Kippenberg, K. Vahala, and J. E. Bowers, "*Integrated turnkey soliton microcombs*", **Nature** 582, 365(2020).
9. **J. Liu***, E. Lucas*, A. S. Raja*, J. He*, J. Riemensberger, R. N. Wang, M. Karpov, H. Guo, R. Bouchand, and T. J. Kippenberg, "*Photonic microwave generation in the X- and K-band using integrated soliton microcombs*", **Nature Photonics** 14, 486 (2020).
10. J. Riemensberger, A. Lukashchuk, M. Karpov, W. Weng, E. Lucas, **J. Liu**, and T. J. Kippenberg, "*Massively parallel coherent laser ranging using a soliton microcomb*", **Nature** 581, 164 (2020). (***Cover Article*** of Volume 581, Issue 7807, 14th May 2020.)
11. A. S. Raja*, **J. Liu***, N. Volet, R. N. Wang, J. He, E. Lucas, R. Bouchand, P. Morton, J. Bowers, and T. J. Kippenberg, "*Chip-based soliton microcomb module using a hybrid semiconductor laser*", **Opt. Express** 28, 2714 (2020).
12. F. Gyger*, **J. Liu***, F. Yang*, J. He, A. S. Raja, R. N. Wang, S. A. Bhave, T. J. Kippenberg, and L. Thevanaz, "*Observation of stimulated Brillouin scattering in silicon nitride integrated waveguides*", **(Editors' Suggestion) Phys. Rev. Lett.** 124, 013902 (2020).
13. M. Karpov, M. H. Pfeiffer, H. Guo, W. Weng, **J. Liu**, and T. J. Kippenberg, "*Dynamics of soliton crystals in optical microresonators*", **Nature Physics** 15, 1071 (2019).
14. T. Wildi, V. Brasch, **J. Liu**, T. J. Kippenberg, and T. Herr, "*Thermally stable access to microresonator solitons via slow pump modulation*", **Opt. Lett.** 44, 4447 (2019).
15. G. Huang, E. Lucas, **J. Liu**, A. S. Raja, G. Lihachev, M. L. Gorodetsky, N. J. Engelsen, and T. J. Kippenberg, "*Thermal-refractive noise in silicon nitride microresonators*", (**Rapid Communications) Phys. Rev. A** 99, 061801 (2019).
16. D. Martyshkin, V. Fedorov, T. Kesterson, S. Vasilyev, H. Guo, **J. Liu**, W. Weng, K. Vodopyanov, T. J. Kippenberg, and S. Mirov, "*Visible-near-middle infrared spanning super continuum generation in a silicon nitride waveguide*", **Opt. Mater. Express** 9, 2553 (2019).
17. A. S. Raja*, A. Voloshin*, H. Guo*, S. Agafonova*, **J. Liu***, A. Gorodnitskiy, M. Karpov, N. Pavlov, E. Lucas, R. Galieve, A. Shitikov, J. Jost, M. L. Gorodetsky, and T. J. Kippenberg, "*Electrically pumped photonic integrated soliton microcomb*", **Nature Communications** 10, 680 (2019).

18. E. Obrzud, M. Rainer, A. Harutyunyan, M. Anderson, **J. Liu**, M. Geiselmann, B. Chazelas, S. Kundermann, S. Lecomte, M. Cecconi, A. Ghedina, E. Molinari, F. Pepe, F. Wildi, F. Bouchy, T. J. Kippenberg, and T. Herr, "*A microphotonic astrocomb*", **Nature Photonics** 13, 31 (2019).

19. **J. Liu***, A. S. Raja*, M. Karpov, B. Ghadiani, M. H. Pfeiffer, N. J. Engelsen, H. Guo, M. Zervas, and T. J. Kippenberg, "*Ultralow-power chip-based soliton frequency combs for photonic integration*", **Optica** 5, 1347 (2018).

20. M. H. Pfeiffer, **J. Liu**, A. S. Raja, T. Morais, B. Ghadiani, and T. J. Kippenberg, "*Ultra-smooth silicon nitride waveguides based on the Damascene reflow process: fabrication and loss origins*", **Optica** 5, 884 (2018).

21. **J. Liu***, A. S. Raja*, M. H. Pfeiffer, C. Herkommer, H. Guo, M. Zervas, M. Geiselmann, and T. J. Kippenberg, "*Double inverse nanotapers for efficient light coupling to integrated photonic devices*", **Opt. Lett.** 43, 3200 (2018).

22. M. H. Pfeiffer, C. Herkommer, **J. Liu**, T. Morais, M. Zervas, M. Geiselmann, and T. J. Kippenberg, "*Photonic Damascence process for low-loss, high-confinement silicon nitride waveguides*", **IEEE J. Sel. Top. Quantum Electron.** 24, 1 (2018).

23. M. Anderson, N. G. Pavlov, J. D. Jost, G. Lihachev, **J. Liu**, T. Morais, M. Zervas, M. L. Gorodetsky, and T. J. Kippenberg, "*Highly efficient coupling of crystalline microresonators to integrated photonic waveguides*", **Opt. Lett.** 43, 2106 (2018).

24. M. Karpov, M. H. Pfeiffer, **J. Liu**, A. Lukashchuk, and T. J. Kippenberg, "*Photonic chip-based soliton frequency combs covering the biological imaging window*", **Nature Communications** 9, 1146 (2018).

25. H. Guo, E. Lucas, M. H. Pfeiffer, M. Karpov, M. Anderson, **J. Liu**, M. Geiselmann, J. D. Jost, and T. J. Kippenberg, "*Inter-mode breather solitons in optical microresonators*", **Phys. Rev. X**. 7, 041055 (2017).

26. M. H. Pfeiffer, C. Herkommer, **J. Liu**, H. Guo, M. Karpov, E. Lucas, M. Zervas, and T. J. Kippenberg, "*Octave-spanning dissipative Kerr soliton frequency combs in Si_3N_4 microresonators*", **Optica** 4, 684 (2017).

27. M. H. Pfeiffer*, **J. Liu***, M. Geiselmann, and T. J. Kippenberg, "*Coupling ideality of integrated planar high-Q microresonators*", **Phys. Rev. Applied** 7, 024026 (2017).

28. **J. Liu**, V. Brasch, M. H. Pfeiffer, A. Kordts, A. N. Kamel, H. Guo, M. Geiselmann, and T. J. Kippenberg, "*Frequency-comb-assisted broadband precision spectroscopy with cascaded diode lasers*", **Opt. Lett.** 41, 3134 (2016).

29. M. H. Anderson, G. Lihachev, W. Weng, **J. Liu**, and T. J. Kippenberg, "*Zero-dispersion Kerr solitons in optical microresonators*", **arXiv**: 2007.14507 (2020).

30. W. Weng, A. Kaszubowska-Anandarajah, J. He, P. D. Lakshmijayasimha, E. Lucas, **J. Liu**, P. M. Anandarajah, and T. J. Kippenberg, "*Gain-switched semiconductor laser driven soliton microcombs*", **arXiv**: 2006.10662 (2020).

31. **J. Liu**, G. Huang, R. N. Wang, J. He, A. S. Raja, T. Liu, N. J. Engelsen, and T. J. Kippenberg, "*High-yield wafer-scale fabrication of ultralow-loss, dispersion-engineered silicon nitride photonic circuits*", **arXiv**: 2005.13949 (2020).

32. A. Tikan, J. Riemensberger, K. Komagata, S. Hönl, M. Churaev, C. Skehan, H. Guo, R. N. Wang, **J. Liu**, P. Seidler, and T. J. Kippenberg, "*Emergent Nonlinear Phenomena in a Driven Dissipative Photonic Dimer*", **arXiv**: 2005.06470 (2020).

33. J. Feldmann, N. Youngblood, M. Karpov, H. Gehring, X. Li, M. Le Gallo, X. Fu, A. Lukashchuk, A. S. Raja, **J. Liu**, C. D. Wright, A. Sebastian, T. J. Kippenberg, W. H. P. Pernice, and H. Bhaskaran, "*Parallel convolution processing using an integrated photonic tensor core*", **arXiv**: 2002.00281 (2020).

34. A. S. Voloshin*, **J. Liu***, N. M. Kondratiev*, G. V. Likhachev, T. J. Kippenberg, and I. A. Bilenko, "*Dynamics of laser self-injection locked soliton microcombs in integrated microresonators*", **arXiv**: 1912.11303 (2019).

35. M. H. Anderson, R. Bouchand, **J. Liu**, W. Weng, E. Obrzud, T. Herr, and T. J. Kippenberg, "*Photonic chip-based resonant supercontinuum*", **arXiv**: 1909.00022 (2019).

PATENTS

1. "*Coupled Optical waveguides*", T. J. Kippenberg (30%), H. Guo (30%), **J. Liu** (30%), W. Weng (10%), US patent pending, 2019.
2. "*Optical coupling device*", T. J. Kippenberg (25%), J. D. Jost (25%), M. Anderson (25%), **J. Liu** (25%), WO2019180655(A1), 2019.

HONOURS & AWARDS

- Chinese government award for outstanding self-finance students abroad, 2020
- Finalist of Best Student Paper Award in the joint conference of the IEEE IFCS-ISAF, 2020
- ECIO 2019 the Best Student Paper awarded by *Nature Photonics*, 2019
- IFCS-EFTF 2019 student travel grant, 2019

TALKS

1. (***Invited***) "Ultralow-Loss Silicon Nitride Photonics", **ACP/IPOC 2020** (online), China (2020).
2. "Monolithic piezoelectric control of integrated soliton microcombs", **Research and Applications of Photonics in Defense (RAPID) 2020** (online), US (2020).
3. (***Finalist of the Best Student Papers***) "Monolithic piezoelectric control of integrated soliton microcombs", **IFCS-ISAF** (online), US (2020).
4. (***Invited***) "Photonic integration of microresonator-based optical frequency combs", Optics and Photonics Workshop — a division of the Nanjing Tech week 2020 (online), China (2020)
5. "Monolithic piezoelectric control of integrated soliton microcombs", **ECIO 2020** (online), France (2020).
6. (***Invited***) "Monolithic piezoelectric control of integrated soliton microcombs", **CLEO** (online), US (2020).
7. (*Tutorial*) "Introduction to FDTD", *workshop "Computational methods for nonlinear photonics" within the Marie-Curie ITN MICROCOMB*, Switzerland (2020).
8. **(*Invited*)** "Microresonator frequency comb", *2019 Annual Meeting of Chinese Association of Science & Technology in Switzerland*, Zurich, Switzerland (2019).
9. "Photonic integrated microwave oscillator based on silicon nitride soliton microcomb", **CLEO**, US (2019).
10. "Electrically Driven Ultra-Compact Photonic Integrated Soliton Microcomb", **CLEO**, US (2019).
11. "Integrated Si_3N_4 Soliton Microcomb Driven by a Compact Ultra-low-noise Laser", **CLEO**, US (2019).
12. (***The Best Student Paper***) "Photonic integrated microwave oscillators based on silicon nitride soliton microcomb", **ECIO 2019**, Belgium (2019).
13. "Photonic integrated microwave oscillators based on silicon nitride soliton microcomb", **IFCS-EFTF 2019**, US (2019).
14. **(*Invited*)** "Ultralow-power photonic chip-based soliton frequency combs", *Keio Symposium on Microresonator Frequency Comb*, Japan (2018).
15. "Ultralow-power photonic chip-based soliton frequency combs", **ECOC**, Italy (2018).
16. "Ultralow-power photonic chip-based soliton frequency combs", **OMN 2019**, Switzerland (2018).
17. "Ultralow-power photonic chip-based soliton frequency combs", **Advanced Photonics Congress**, Switzerland (2018).
18. "Double-inverse tapers for efficient light coupling with arbitrary polarization", **CLEO**, US (2018).
19. "Photonic Damascene process with reflow step for ultra-smooth Si_3N_4 waveguide", **CLEO**, US (2018).
20. (*Tutorial*) "Study of Optical Mode Coupling in Nanophotonic Devices Using FDTD Methods", *workshop within the Marie-Curie ITN "Optomechanical Technologies (OMT)"*, Switzerland (2017).
21. "Dispersion Characterization of Microresonators for Broadband Kerr Frequency Comb Generation", **CLEO**, US (2017).

TEACHING

- Physique Générale II with Dr. Sylvain Bréchet, fall semester 2019-2020, EPFL.
- Physique Générale I with Dr. Jean-Marie Fuerbringer, spring semester 2019, EPFL.
- Physique Générale II with Prof. Tobias Kippenberg, fall semester 2018-2019, EPFL.

- Physique Générale I with Dr. Jean-Marie Fuerbringer, spring semester 2018, EPFL.
- Physique Générale II with Prof. Tobias Kippenberg, fall semester 2017-2018, EPFL.
- Physique Générale II with Prof. Tatsuya Nakada, spring semester 2017, EPFL.
- Physique Générale II with Prof. Hugo Dil, fall semester 2016-2017, EPFL.